

University of Nottingham
UK | CHINA | MALAYSIA

Asymptotic and Numerical Analysis of Nonlocal Reaction-Diffusion Equations

Jia Yin Lee

Thesis submitted to the University of Nottingham
for the degree of Doctor of Philosophy

September 2023

Dedicated to the loving memory of my grandmother and in honour of the soul of my father.

Abstract

This thesis consists of two parts. In the first part of the thesis, we study a local-nonlocal Fisher-Komogorov-Petrovskii-Piskunov equation, which contains a linear combination of local and nonlocal interaction terms in one spatial dimension. Similar to the local case, this equation admits two uniform steady states, one stable and the other unstable. In our study, we restrict our attention to kernels that are symmetric, strictly positive, and decreasing with distance to describe the nonlocal interaction over space. Using asymptotic and numerical analysis, we show that travelling wave solutions of this model have interesting properties when the diffusion length scale is much smaller than the interaction length scale, and the model is highly nonlocal. For example, we observe non-monotonic travelling waves behind the wavefront, connecting the two steady states. In particular, the solutions behave like Dirac delta functions where the height tends to infinity and the width tends to zero in the same limit before converging to the stable steady state.

In the second part of the thesis, we analyse the stability of the spatially-uniform, coexisting steady state of a diffusive nonlocal Lotka-Volterra system for two species in one spatial dimension, and include terms that model both nonlocal intraspecific and local interspecific competition. We find that the coexisting state of the system can lose stability once nonlocality is introduced. We use asymptotic and numerical analysis to find the neutral curve and also derive amplitude equations using weakly nonlinear analysis. These are used to determine bifurcation behaviour close to the neutral curve and confirmed to be consistent with behaviour observed in direct numerical simulations. Finally, we construct the asymptotic solution in the limit of weak diffusivity and find that the leading order periodic solution consists of disjoint regions where either one or the other species is absent.

Acknowledgements

First and foremost, I would like to express my deepest appreciation to my principal supervisor, Prof. John Billingham, and my co-supervisor, Prof. Stephen Coombes, for their invaluable support throughout my PhD journey. While Prof. John Billingham introduced me to this interesting and challenging research project, both supervisors provided insightful comments and guidance that played crucial roles in bringing this research to fruition.

I am also deeply thankful to my friends and colleagues at the University of Nottingham. Their camaraderie and shared experiences have made this academic journey all the more rewarding.

To my family in Malaysia, I owe an immeasurable debt of gratitude. Your continuous encouragement over these four years has been my driving force.

The realisation of this PhD would not have been possible without the generous funding provided by the University of Nottingham, particularly through the Vice Chancellor Scholarship and the School of Mathematical Sciences.

Lastly, I wish to express my gratitude to God for His grace and strength, which enable me to successfully complete this research work.

List of Planned Publications

- The results presented in Chapter 3 will be prepared for submission and publication in Proceedings of the Royal Society A in the near future.

- Some of the content presented in Chapter 4 will be integrated with the material from Chapter 5 to form a single, comprehensive research paper. This paper has been submitted to the IMA Journal of Applied Mathematics for peer review.

- The material presented in Chapter 6, combined with some additional results by my supervisor,Prof. John Billingham, will be prepared for submission and publication in Nonlinearity in the near future.

Contents

Abstract i

Acknowledgements ii

List of Planned Publications iii

List of Tables ix

List of Figures xi

1 Introduction 1

1.1 Background and motivation 1

1.2 Contributions 5

1.3 Literature Review 7

1.3.1 Nonlocal reaction-diffusion equation 7

1.3.2 Nonlocal Fisher-KPP model 9

1.3.3 Nonlocal Lotka-Volterra model 11

1.3.4 Turing instability 15

1.3.5 Weakly nonlinear analysis 17

1.4 Outline of the thesis 18

2 Preliminaries 20

2.1 Nonlocal kernel functions 20

2.1.1 Derivation of kernel functions 21

2.2 Multiple-scale analysis 22

2.2.1 Example 1 - Swift-Hohenberg equation 23

2.2.2 Example 2 - Neural field model 28

2.3 Mathieu equation 33

2.4 Numerical methods . . . 33
2.4.1 Finite difference method . . . 34
2.4.2 Two-point Gauss Quadrature rule . . . 37
2.4.3 Fast Fourier transform . . . 38

3 Travelling Waves of a Local-nonlocal Fisher-KPP Equation 39

3.1 Introduction . . . 39
3.2 Problem statement . . . 42
3.3 Numerical solution when $c \ll 1$ and $c = O(\alpha)$ . . . 45
3.3.1 Numerical solution when $\phi = \Phi_2$ . . . 45
3.3.2 Numerical solution when $\phi = \Phi_\infty$ . . . 48
3.4 Far-field asymptotic analysis . . . 50
3.4.1 Comparison between far-field solution and numerical solution . . . 54
3.5 Analysis of the first spike of the local-nonlocal Fisher-KPP . . . 56
3.5.1 Numerical analysis of the first spike . . . 56
3.5.2 Asymptotic analysis of the first spike . . . 57
3.5.3 Numerical method . . . 60
3.6 Asymptotic solution when $c \ll 1$ and $\alpha = O(1)$ . . . 62
3.6.1 Asymptotic solution when $\phi = \Phi_2$ . . . 64
3.6.2 Asymptotic solution when $\phi = \Phi_\infty$ . . . 67
3.6.3 Asymptotic solution when $\phi = \Phi_\infty$, $\alpha \ll 1$ and $c \ll \alpha$ . . . 68
3.7 Conclusion . . . 72

4 Linear Stability Analysis of a Nonlocal Lotka-Volterra (NLLV) System 74

4.1 Introduction . . . 74
4.2 Problem statement . . . 75
4.3 Nondimensionalisation . . . 76
4.4 Linear stability analysis . . . 77
4.5 Numerical solution . . . 80
4.5.1 Growth rate of numerical solution . . . 80

4.6 Asymptotic analysis when $\alpha = \beta$ . . . 82
4.7 Asymptotic analysis when $\alpha \neq \beta$ . . . 83
4.7.1 Asymptotic neutral curve when $\phi_1 = \phi_2 = \phi = \Phi_1$ . . . 85
4.7.2 Asymptotic neutral curve when $\phi_1 = \phi_2 = \phi = \Phi_\infty$ . . . 91
4.7.3 Asymptotic neutral curve when $\phi_1 = \phi_2 = \phi = \Phi_2$ . . . 95
4.7.4 Comparison between neutral curves when $\phi_1 = \phi_2 = \phi$. 97
4.7.5 Asymptotic neutral curve when $\phi_1 = \Phi_1$ and $\phi_2 = \Phi_\infty$ . . 99
4.7.6 Asymptotic neutral curve when $\phi_1 = \Phi_1$ and $\phi_2 = \Phi_2$ . . 102
4.7.7 Comparison between neutral curves when $\phi_1 \neq \phi_2$ . . . 104
4.8 Conclusion . . . 105

5 Weakly Nonlinear Analysis of a Nonlocal Lotka-Volterra System 107

5.1 Introduction . . . 107
5.2 Derivation of amplitude equation . . . 108
5.3 Analysis of amplitude equation . . . 120
5.3.1 Bifurcation type in terms of β . . . 121
5.4 Weakly nonlinear solution . . . 123
5.4.1 Weakly nonlinear amplitude . . . 123
5.4.2 Numerical amplitude . . . 123
5.4.3 Numerical amplitude away from bifurcation point . . . 129
5.5 Fully nonlinear numerical solution . . . 131
5.6 Conclusion . . . 138

6 Fully Nonlinear Pattern Formation in a Nonlocal Lotka-Volterra System with Small Diffusivity 140

6.1 Introduction . . . 140
6.2 Solution of IVP with random initial conditions . . . 142
6.3 Asymptotic structure of solution with small diffusivity . . . 149
6.4 Approximation of convolution term . . . 151
6.4.1 Effective periodic Gaussian kernel, Φ_∞, when $\lambda = 1$ . . . 151
6.4.2 Effective periodic Gaussian kernel, Φ_∞, when $\lambda \neq 1$ . . . 154

6.4.3 Effective periodic exponential kernel, Φ_1, when $\lambda = 1$ . . 155
6.4.4 Effective periodic exponential kernel, Φ_1, when $\lambda \neq 1$ . . 156
6.5 Inner region matching 156
6.5.1 Ratio of slopes 156
6.6 Asymptotic outer solution 158
6.6.1 Asymptotic outer solution when $\Phi = \Phi_\infty$ 159
6.6.2 Computation of asymptotic outer solutions when $\Phi = \Phi_\infty$ 162
6.6.3 Inner region solution 163
6.6.4 Comparison with numerical solution when $\Phi = \Phi_\infty$ . . . 164
6.6.5 Asymptotic outer solution when $\Phi = \Phi_1$ 171
6.6.6 Computation of asymptotic outer solution when $\Phi = \Phi_1$. 173
6.6.7 Comparison with numerical solution when $\Phi = \Phi_1$ 174
6.6.8 Comparison with numerical solution when $\phi_1 = \Phi_1$ and $\phi_2 = \Phi_\infty$ 177
6.6.9 Comparison with solution of IVP 180
6.7 Conclusion 184

7 Conclusion and Future Work **185**
7.1 Local-Nonlocal Fisher-KPP equation 185
7.2 Nonlocal Lotka-Volterra system 187
7.3 Future work 192

Appendices **194**

A Neural Field Model **194**
A.1 Bifurcation Point β_c at $D = 0$ 194

B Derivation of Amplitude Equation for NLLV System **196**
B.1 $\overline{a}(k_c)$ 196
B.2 Projections when $n = 3$ 196

C Numerical Amplitude Away from Bifurcation Point **200**
C.1 When $\beta = 0.5$ 200
C.2 When $\beta = 0.95$ 202

D Fully Nonlinear Numerical Solutions **204**

D.1 When $\phi_1 = \psi = \Phi_2$ 204

D.2 When $\phi_1 = \psi = \Phi_\infty$ 207

E Fully Nonlinear Pattern Formation in a NLLV System with Small Diffusivity **210**

E.1 Effective periodic kernel when $\Phi = \Phi_\infty$ and $\lambda \neq 1$ 210

E.2 Effective periodic kernel when $\Phi = \Phi_1$ and $\lambda \neq 1$ 211

E.3 Derivation of nonlinear Mathieu equation for v when $\phi_2 = \Phi_\infty$ and $\lambda \neq 1$ 212

E.4 Derivation of asymptotic equation for u when $\phi_1 = \Phi_1$ 213

E.5 Asymptotic equation for v when $\phi_2 = \Phi_1$ and $\lambda = 1$ 214

E.6 Derivation of asymptotic equation for v when $\phi_2 = \Phi_1$ and $\lambda \neq 1$ 214

E.6.1 Fifth order system for v when $\phi_2 = \Phi_1$ when $\lambda = 1$ . . . 216

Bibliography **217**

List of Tables

3.1 *Summary of k of different kernels and their corresponding far-field solutions $\overline{U} = Ae^{ikz}$.* 53

5.1 *Summary of α and k_c values of different kernels, $\phi_1 = \psi = \Phi_n$ where $n = 1, 2, \infty$, for $\beta = 0.25$ on the neutral curves from (4.9).* 124

5.2 *Summary of α and k_c values of different kernels, $\phi_1 = \psi = \Phi_n$ where $n = 1, 2, \infty$, for $\beta = 0.5$ on the neutral curves from (4.9).* 127

5.3 *Summary of α and k_c values of different kernels, $\phi_1 = \psi = \Phi_n$ where $n = 1, 2, \infty$, for $\beta = 0.95$ on the neutral curves from (4.9).* 127

6.1 *Parameter values for the solutions of IVP (6.1) when $\phi = \Phi_\infty$. The varying parameters based on case 1a are highlighted in red.* 144

6.2 *Parameter values for the solutions of IVP (6.1) when $\phi = \Phi_1$. The varying parameters based on case 2a are highlighted in red.* 146

6.3 *Parameter values for the solutions of IVP (6.1) when $\phi_1 = \Phi_1$ and $\phi_2 = \Phi_\infty$. The varying parameters based on case 3a are highlighted in red.* 148

6.4 *Parameter values for asymptotic solutions of u and v from solving (6.28) and (6.31) where $\phi_1 = \phi_2 = \phi = \Phi_\infty$ and $\alpha = \beta$. The asymptotic solutions can be found in Figure 6.8.* 165

6.5 *Parameter values for asymptotic solutions of u and v from solving (6.28) and (6.31) where $\phi_1 = \phi_2 = \phi = \Phi_\infty$ and $\lambda = 1$. The asymptotic solutions can be found in Figure 6.10.* 168

6.6 *Parameter values for asymptotic solutions of u and v from solving (6.28) and (E.8) where* $\phi_1 = \phi_2 = \phi = \Phi_\infty$ *and* $\lambda \neq 1$. *The asymptotic solutions can be found in Figure 6.11.* 170

6.7 λ, Λ, ϵ_u *and* ϵ_v *for asymptotic solutions in Figure 6.11* where $\phi_1 = \phi_2 = \phi = \Phi_\infty$ and $\lambda \neq 1$. 171

6.8 *Parameter values for asymptotic solutions of u and v from solving (6.44) and (E.13) where* $\phi_1 = \phi_2 = \phi = \Phi_1$ *and* $\lambda = 1$. *The asymptotic solutions can be found in Figure 6.12.* 174

6.9 *Parameter values for asymptotic solutions of u and v from solving (6.44) and (E.19) where* $\phi_1 = \phi_2 = \phi = \Phi_1$ *and* $\lambda \neq 1$. *The asymptotic solutions can be found in Figure 6.13.* 176

6.10 *Parameter values for asymptotic solutions of u and v from (6.44) and (6.31) where* $\phi_1 = \Phi_1$, *and* $\phi_2 = \Phi_\infty$ *and* $\lambda = 1$. *The asymptotic solutions can be found in Figure 6.14.* 177

6.11 *Parameter values for asymptotic solutions of u and v from (6.44) and (E.8) in Figure 6.15 where* $\phi_1 = \Phi_1$ *and* $\phi_2 = \Phi_\infty$ *and* $\lambda \neq 1$. *The asymptotic solutions can be found in Figure 6.15.* 179

6.12 *Amplitude and wavelength of the asymptotic and numerical solutions in Figure 6.16.* 180

6.13 *Amplitude and wavelength of the asymptotic and numerical solutions in Figure 6.17.* 182

6.14 *Amplitude and wavelength of the asymptotic and numerical solutions in Figure 6.18.* 183

List of Figures

2.1 The kernels Φ_1, Φ_2 and Φ_∞ from (2.2). 21

2.2 Supercritical bifurcation diagram for amplitude R_0 against δ, based on the linear stability analysis of the amplitude equation of the Swift-Hohenberg model (2.16). 27

2.3 Supercritical bifurcation diagram for amplitude R_0 against δ, based on the linear stability analysis of the amplitude equation of the neural field model (2.34). 32

2.4 Uniform grid spacing in x in the NLLV system (1.4). 34

2.5 Fitting a quadratic curve on three discrete points with uneven spacing. 35

3.1 Sketch of regions with TW solutions U when $\alpha_2 < \alpha \leq \alpha_1$. . . . 41

3.2 Sketch of regions with TW solutions U when $\alpha_{i+1} < \alpha \leq \alpha_i$. . . 42

3.3 The TW solution, $U = \mathrm{e}^L$, obtained by solving (3.5) with $\phi = \Phi_2$, $D_0 = 1/4$, $\alpha = 10^{-9}$ and $c = 10^{-10}$. These four plots highlight different views of the structure of the solution, with the bottom right panel showing the profile at the wavefront. 46

3.4 The heights of local maxima of spikes for $\phi = \Phi_2$ againt c in (a) and α in (b). The broken lines show the asymptotic approximations $U_{\max} \sim 0.8c^{-1/2}$ as $c \to 0$ in (a) and $U_{\max} \sim 2.5\alpha^{-1/2}$ as $\alpha \to 0$ in (b). Separation and weight of the spikes as a function of spike number m in (c). 47

3.5 The TW solution, $U = e^L$, obtained by solving (3.5) with $\phi = \Phi_\infty$, $D_0 = 1/4$, $\alpha = 10^{-9}$ and $c = 10^{-10}$. These four plots highlight different views of the structure of the solution, with the bottom right panel showing the profile at the wavefront. 48

3.6 The heights of local maxima of spikes for $\phi = \Phi_\infty$ against c in (a) and α in (b). The broken lines show the asymptotic approximations $U_{\max} \sim 0.8c^{-1/2}$ as $c \to 0$ in (a) and $U_{\max} \sim 2.5\alpha^{-1/2}$ as $\alpha \to 0$ in (b). Separation and weight of the spikes as a function of spike number m in (c). 50

3.7 Magnitudes of the real and imaginary parts of k for different kernels from Table 3.1 against α. 54

3.8 Numerical and far-field solutions from (3.20) for $\phi = \Phi_2$ with $\alpha = 0.0063$ and $D_0 = 0$. 55

3.9 Numerical and far-field solutions from (3.20) for $\phi = \Phi_\infty$ with $\alpha = 0.0186$ and $D_0 = 0$. 55

3.10 The first spikes of the numerical solutions (obtained by solving (3.5)) for various values of α are shown in (a) for $\phi = \Phi_2$ and (c) for $\phi = \Phi_\infty$. The corresponding scalings for their height, area and width are shown in (b) and (d). Note that the width of each spike is calculated at half the maximum of the spike. 57

3.11 The asymptotic spikes (broken lines) obtained from (3.26) and (3.30) and the numerical spikes (solid lines) obtained by solving (3.5) for (a) $\phi = \Phi_2$ at $A = -0.213$, (b) $\phi = \Phi_2$ at $B = 0.213$, (c) $\phi = \Phi_\infty$ at $A = -0.13$ and (d) $\phi = \Phi_\infty$ at $B = 0.13$. 62

3.12 $\tilde{L}$ and $\tilde{L}_z$ as a function of z for $\phi = \Phi_2$, with $D_0 = 1/4$, $\alpha = 10^{-9}$ and $c = 10^{-10}$. 63

3.13 (a) is the numerical solution, obtained by solving (3.5), for kernel $\phi = \Phi_2$, $D_0 = 0$ and $\alpha = 0.0063$. (b) is the magnified image of the first maximum of the wavefront of both numerical and asymptotic solutions (from (3.41)). 65

3.14 (a) is the numerical solution, obtained by solving (3.5), for kernel $\phi = \Phi_\infty$, $D_0 = 0$ and $\alpha = 0.0186$. (b) is the magnified image of the first maximum of the wavefront of both numerical and asymptotic solutions (from solving (3.45)). 68

3.15 Numerical and asymptotic solutions, obtained by solving (3.5) and (3.48), for $\phi = \Phi_\infty$ with $\alpha = 10^{-5}$ and $D_0 = 0$. The solutions in (a) are magnified in (b) and (c). 71

3.16 Weight and separation of the spikes of numerical and asymptotic solutions (obtained by solving (3.5) and (3.48)) for $\phi = \Phi_\infty$ as a function of spike number m. 72

4.1 The numerical solutions of the IVP (4.4) with $D = 0.025, \alpha = 0.6, \beta = 0.5$ and $R = \lambda = 1$ at different t values. 81

4.2 The growth rates of the amplitude of the numerical solutions of (4.4) for kernel $\phi = \Phi_1$ when $D = 0.025, \alpha = 0.6, \beta = 0.5$ and $R = \lambda = 1$ against t at $x = 0$. (a) The log of the amplitude of $u - u_e$ and (b) The log of the amplitude of $v - v_e$. 82

4.3 The comparison between the numerical and asymptotic σ in (4.13) as a function of k for $D = 0$. 83

4.4 (a) σ as a function of k from (4.9), plotted for $\alpha = 0.01$, $\beta = 0.02$, $R = \lambda = 1$, and $\phi = \Phi_\infty$. (b) is the magnified image of (a). . . . 85

4.5 The comparison between the numerical and asymptotic neutral curves for $\phi_1 = \phi_2 = \phi = \Phi_1$. The innermost curve is plotted with $D = 0.025$, whereas the outermost curve is plotted with $D = 0.001$. The broken lines show the asymptotic neutral curves obtained in (4.25). The solid lines are the numerical neutral curves obtained in (4.9). 88

4.6 The solutions of the IVP (4.4) for $\phi_1 = \phi_2 = \phi = \Phi_1$, where $D = 0.025$, $R = \lambda = 1$, $\beta = 0.5$. $\alpha = 0.3$ in (a), $\alpha = 0.6$ in (b). . 89

4.7 The solutions of the IVP (4.4) for $\phi_1 = \phi_2 = \phi = \Phi_1$ when the growth rate, σ, of the coexisting state is small and positive. The parameters are $D = 0.025, \alpha = 0.2366, \beta = 0.5, R = \lambda = 1$ (a) $t = 2000$ and (b) $t = 3000$. The initial condition is random across the spatial domain. . 90

4.8 (a) is the numerical and asymptotic neutral curves for kernel $\phi_1 = \phi_2 = \phi = \Phi_\infty$, where D decreases as the radius of the curve increases. The broken lines represent the asymptotic neutral curves obtained in (4.31). The solid lines are the numerical neutral curves obtained in (4.9). (b) is the magnified image of the numerical and asymptotic neutral curves where $\alpha, \beta \ll 1$. 94

4.9 The solutions of the IVP (4.4) for kernel $\phi_1 = \phi_2 = \phi = \Phi_\infty$, where $D = 0.025$, $R = \lambda = 1$, $\beta = 0.5$, and $\alpha = 0.6$. 94

4.10 The comparison between the numerical and asymptotic neutral curves for $\phi_1 = \phi_2 = \phi = \Phi_2$. The innermost curve is plotted with $D = 0.025$, whereas the outermost curve is plotted with $D = 0.001$. The broken lines show the asymptotic neutral curves obtained by solving (4.39) numerically. The solid lines are the numerical neutral curves obtained in (4.9). 96

4.11 The solutions of the IVP (4.4) for kernel $\phi_1 = \phi_2 = \phi = \Phi_2$, where $D = 0.025$, $R = \lambda = 1$, $\beta = 0.5$, and $\alpha = 0.6$. 97

4.12 The comparison between the numerical neutral curves obtained from (4.9) when both kernels are $\phi_1 = \phi_2 = \phi = \Phi_1, \Phi_2$ and Φ_∞, at $R = \lambda = 1$ and $D = 0.01$. 98

4.13 (a) The numerical and asymptotic neutral curves for kernel $\phi_1 = \Phi_1$ and $\phi_2 = \Phi_\infty$, where both D_1 and D_2 decrease as the curves approach the boundary of the axes. The broken lines represent the asymptotic neutral curves from (4.42) with k from (4.45). The solid lines are the numerical neutral curves obtained in (4.9). (b)-(d) highlight different views of the structure of the neutral curves. 101

4.14 The solutions of the IVP (4.4) for kernel $\phi_1 = \Phi_1$ and $\phi_2 = \Phi_\infty$, where $D = 0.025$, $R = \lambda = 1$, $\beta = 0.5$, and $\alpha = 0.6$. 102

4.15 The comparison between the numerical and asymptotic neutral curves for $\phi_1 = \Phi_1$ and $\phi_2 = \Phi_2$. The broken lines represent the asymptotic neutral curves obtained by solving (4.49) numerically.The solid lines are the numerical neutral curves obtained in (4.9). The innermost curve is plotted with $D = 0.025$, and the radius of the curves increases with decreasing D. The broken lines show the asymptotic neutral curves. 103

4.16 The solutions of the IVP (4.4) for kernel $\phi_1 = \Phi_1$ and $\phi_2 = \Phi_2$, where $D = 0.025$, $R = \lambda = 1$, $\beta = 0.5$, and $\alpha = 0.6$. 104

4.17 The comparison between the numerical neutral curves obtained from (4.9) for mixed kernels at $R = \lambda = 1$ and $D = 0.01$. 105

5.1 Plots of ν from (5.46) against β for three kernel pairs along the neutral curves from (4.9). 122

5.2 Bifurcation diagram from the analysis of the amplitude equation (5.45) for r_0 with no spatial variation ($\kappa = 0$). Solid lines represent the stable branches, and broken lines the unstable branches. The (α, β) values are (a) (0.23664,0.5) and (b) (0.39001,0.95). 123

5.3 Plot of neutral curves from (4.9), numerical amplitudes of u and v from (5.50) and weakly nonlinear (WN) amplitudes of u and v when $\beta = 0.25$. The values of α and k_c are summarised in Table 5.1. 125

5.4 Plot of neutral curves from (4.9), numerical amplitudes of u and v from (5.50) and weakly nonlinear (WN) amplitudes of u and v when $\beta = 0.5$. The values of α and k_c are summarised in Table 5.2. 126

5.5 Plot of neutral curves from (4.9), numerical amplitudes of u and v from (5.50) and weakly nonlinear (WN) amplitudes of u and v when $\beta = 0.5$. The values of α and k_c are summarised in Table 5.3. 128

5.6 (a) The numerical amplitudes (from (5.50)) and weakly nonlinear (WN) amplitudes of $\phi_1 = \psi = \Phi_1$ for large λ. (b) is the magnified image of (a). (c) The numerical solutions at $\lambda = 20$. 129

5.7 (a) The numerical amplitudes of u and v (from (5.50)) for $\phi_1 = \psi = \Phi_1$ solved by fixing amplitude. (b) The analytical and numerical amplitudes in a smaller λ domain. (c) The numerical solutions u and v solved by fixing amplitude. 130

5.8 Fully nonlinear solutions from (5.50) for $\phi_1 = \psi = \Phi_1$ for (a) decreasing D_1, (b) decreasing D_2 and (c) increasing α. 134

5.8 (cont.) Fully nonlinear solutions from (5.50) for $\phi_1 = \psi = \Phi_1$ for (d) increasing β, (e) increasing Λ, and (f) increasing λ. 135

5.9 Plots of the fully nonlinear solutions from (5.50) for $\phi_1 = \psi = \Phi_1$. (a) Solution u has two peaks due to $\Lambda = 2$. The maximum amplitude of v is larger than that of u as $\beta > \alpha$. (b) $D_2 < D_1$ results in higher peak in v. (c) The maximum amplitude of u is larger as $\alpha > \beta$, and $D_1 < D_2$ further amplifies the effect. (d) The effect of $D_2 < D_1$ is greater than $\alpha > \beta$, hence larger peak in v. (e) A larger peak of u due to $\alpha > \beta$ and $D_1, D_2 < 1$ leads to two peaks in u. (f) $D_1 < D_2$ and $\Lambda > 1$ generates larger $\max u$ with more than one peak. (g) $D_1 < D_2$ and $\alpha > \beta$ combined with $\Lambda > 1$ result in $\max u > \max v$ and three peaks in u. (h) The effect of $D_2 < D_1$ is greater than $\alpha > \beta$. 137

6.1 The random initial conditions from (6.3), for $a = 0.1$, $L = 2$, $\gamma = 0.025$ and $m = 200$. 143

6.2 IVP solutions from (6.1) at large t_{end} for $\phi = \Phi_\infty$. (a) $t_{end} = 4 \times 10^4$ from video 1a(i). (b) $t_{end} = 5000$ from video 1b(i). (c) $t_{end} = 8 \times 10^4$ from video 1c(i). (d) $t_{end} = 2 \times 10^4$ from video 1d(i). (e) $t_{end} = 2 \times 10^4$ from video 1e(i). (e) $t_{end} = 2 \times 10^4$ from video 1f(i). The parameter values can be found in Table 6.1. 145

6.3 IVP solutions from (6.1) at large t_{end} for $\phi = \Phi_1$. (a) $t_{end} = 9 \times 10^4$ from video 2a(i). (b) $t_{end} = 8 \times 10^4$ from video 2b(i). (c) $t_{end} = 5 \times 10^5$ from video 2c(i). (d) $t_{end} = 8 \times 10^4$ from video 2d(i). (e) $t_{end} = 8 \times 10^4$ from video 2e(i). (e) $t_{end} = 7 \times 10^4$ from video 2f(i). The parameter values can be found in Table 6.2. 147

6.4 IVP solutions from (6.1) at large t_{end} for $\phi_1 = \Phi_1$ and $\phi_2 = \Phi_\infty$. (a) $t_{end} = 9 \times 10^4$ from video 3a(i). (b) $t_{end} = 10^4$ from video 3b(i). (c) $t_{end} = 10^4$ from video 3c(i). (d) $t_{end} = 7.5 \times 10^5$ from video 3d(i). (e) $t_{end} = 6.5 \times 10^5$ from video 3e(i). (e) $t_{end} = 10^4$ from video 3f(i). The parameter values can be found in Table 6.3. 149

6.5 Numerical solutions of a steady-state problem when both $\phi = \Phi_1$. 150

6.6 Structure of asymptotic solutions. 150

6.7 Magnified inner region from solving (6.38) when both $\phi = \Phi = \Phi_\infty$. 164

6.8 Plots of asymptotic and numerical solutions u and v for $\phi_1 = \phi_2 = \phi = \Phi_\infty$ when $D_1 = D_2$, $\lambda = 1$ and $b = 0.5$. The details of the parameter values can be found in Table 6.4. (a) $D_1 = D_2 = 10^{-4}, \alpha = \beta = 0.1, \lambda = 1, \Lambda = 2, \hat{D}_1 = 0.242$, (b) $D_1 = D_2 = 10^{-5}, \alpha = \beta = 0.1, \lambda = 1, \Lambda = 2, \hat{D}_1 = 0.0242$, (c) $D_1 = D_2 = 10^{-4}, \alpha = \beta = 0.3667, \lambda = 1, \Lambda = 1, \hat{D}_1 = 6.99 \times 10^{12}$, (d) $D_1 = D_2 = 10^{-5}, \alpha = \beta = 0.3667, \lambda = 1, \Lambda = 1, \hat{D}_1 = 6.99 \times 10^{11}$, (e) $D_1 = D_2 = 10^{-3}, \alpha = \beta = 0.9, \lambda = 1, \Lambda = 3, \hat{D}_1 = 4.46 \times 10^{-3}$, and (f) $D_1 = D_2 = 10^{-4}, \alpha = \beta = 0.9, \lambda = 1, \Lambda = 3, \hat{D}_1 = 4.46 \times 10^{-4}$. 166

6.9 Plots of asymptotic and numerical solutions u and v for $\phi_1 = \phi_2 = \phi = \Phi_\infty$ when $D_1 = D_2 = 10^{-3}$, $\lambda = 1$, $\Lambda = 3$ and $b = 0.5$. The values of α and β decrease from (a) to (d). 167

6.10 Plots of asymptotic and numerical outer solutions u and v for $\phi_1 = \phi_2 = \phi = \Phi_\infty$ when $\lambda = 1$. The details of the parameter values can be found in Table 6.5. (a) $D_1 = D_2 = 10^{-5}, \alpha = 0.9, \beta = 0.427, \lambda = 1, \Lambda = 2, \hat{D}_1 = \hat{D}_2 = 0.0242, b = 0.4$, (b) $D_1 = D_2 = 10^{-5}, \alpha = 0.9, \beta = 0.01346, \lambda = 1, \Lambda = 2, \hat{D}_1 = \hat{D}_2 = 0.0242, b = 0.1$, (c) $D_1 = D_2 = 10^{-5}, \alpha = 0.02078, \beta = 0.1, \lambda = 1, \Lambda = 2, \hat{D}_1 = \hat{D}_2 = 0.0242, b = 0.7$, (d) $D_1 = D_2 = 10^{-4}, \alpha = 0.9, \beta = 0.2006, \lambda = 1, \Lambda = 3, \hat{D}_1 = \hat{D}_2 = 4.46 \times 10^{-4}, b = 0.2$. 169

6.11 Plots of asymptotic and numerical outer solutions u and v for $\phi_1 = \phi_2 = \phi = \Phi_\infty$ when $\lambda \neq 1$. The details of the parameter values can be found in Table 6.6. (a) $D_1 = D_2 = 10^{-5}, \alpha = 0.9, \beta = 0.164, \lambda = 1.2, \Lambda = 2, \hat{D}_1 = 0.0242, \hat{D}_2 = 1.8587, b = 0.4$, (b) $D_1 = D_2 = 10^{-5}, \alpha = 0.9, \beta = 0.321, \lambda = 0.9, \Lambda = 2, \hat{D}_1 = 0.0242, \hat{D}_2 = 3.7 \times 10^{-3}, b = 0.4$, (c) $D_1 = D_2 = 10^{-3}, \alpha = 0.9, \beta = 0.376, \lambda = 1.2, \Lambda = 3, \hat{D}_1 = 4.46 \times 10^{-3}, \hat{D}_2 = 0.0307, b = 0.4$, (d) $D_1 = D_2 = 10^{-4}, \alpha = 0.9, \beta = 0.1348, \lambda = 2, \Lambda = 3, \hat{D}_1 = 4.46 \times 10^{-4}, \hat{D}_2 = 231.65, b = 0.4$. 170

6.12 Plots of asymptotic and numerical outer solutions u and v for $\phi_1 = \phi_2 = \phi = \Phi_1$ when $\lambda = 1$. The details of the parameter values can be found in Table 6.8. (a) $D_1 = D_2 = 10^{-5}, \alpha = 0.9, \beta = 0.546, \lambda = 1, \Lambda = 0.5, \hat{D}_1 = \hat{D}_2 = 6.32 \times 10^{-3}, b = 0.4$, (b) $D_1 = D_2 = 10^{-5}, \alpha = 0.9, \beta = 0.604, \lambda = 1, \Lambda = 0.8, \hat{D}_1 = \hat{D}_2 = 9.6 \times 10^{-4}, b = 0.4$, (c) $D_1 = D_2 = 10^{-6}, \alpha = 0.9, \beta = 0.525, \lambda = 1, \Lambda = 0.9, \hat{D}_1 = \hat{D}_2 = 6 \times 10^{-5}, b = 0.4$, (d) $D_1 = D_2 = 10^{-5}, \alpha = 0.9, \beta = 0.546, \lambda = 1, \Lambda = 1.2, \hat{D}_1 = \hat{D}_2 = 1.9 \times 10^{-4}, b = 0.4$. . . 175

6.13 Plots of asymptotic and numerical outer solutions u and v for $\phi_1 = \phi_2 = \phi = \Phi_1$ when $\lambda \neq 1$. The details of the parameter values can be found in Table 6.9. (a) $D_1 = D_2 = 10^{-5}, \alpha = 0.9, \beta = 0.351, \lambda = 0.8, \Lambda = 0.5, \hat{D}_1 = 6.3 \times 10^{-3}, \hat{D}_2 = 4 \times 10^{-3}, b = 0.3$, (b) $D_1 = D_2 = 10^{-5}, \alpha = 0.9, \beta = 0.329, \lambda = 1.2, \Lambda = 0.8, \hat{D}_1 = 1.9 \times 10^{-4}, \hat{D}_2 = 1.22 \times 10^{-4}, b = 0.3$, (c) $D_1 = D_2 = 10^{-6}, \alpha = 0.9, \beta = 0.38, \lambda = 0.8, \Lambda = 0.9, \hat{D}_1 = 6 \times 10^{-5}, \hat{D}_2 = 3.85 \times 10^{-5}, b = 0.3$, (d) $D_1 = D_2 = 10^{-5}, \alpha = 0.9, \beta = 0.274, \lambda = 1.2, \Lambda = 1.2, \hat{D}_1 = 1.9 \times 10^{-4}, \hat{D}_2 = 2.74 \times 10^{-4}, b = 0.3$. 176

6.14 Plots of asymptotic and numerical outer solutions u and v for $\phi_1 = \Phi_1$, and $\phi_2 = \Phi_\infty$ when $\lambda = 1$. The details of the parameter values can be found in Table 6.10. (a) $D_1 = D_2 = 10^{-4}, \alpha = 6, \beta = 0.9, \lambda = 1, \Lambda = 1, \hat{D}_1 = 3.95 \times 10^{-3}, \hat{D}_2 = 6.99 \times 10^{12}, b = 0.3$, (b) $D_1 = D_2 = 10^{-5}, \alpha = 16.1, \beta = 0.9, \lambda = 1, \Lambda = 1, \hat{D}_1 = 3.95 \times 10^{-4}, \hat{D}_2 = 6.99 \times 10^{11}, b = 0.3$, (c) $D_1 = 10^{-5}, D_2 = 10^{-4}, \alpha = 3.58, \beta = 2, \lambda = 1, \Lambda = 1, \hat{D}_1 = 3.95 \times 10^{-4}, \hat{D}_2 = 6.99 \times 10^{12}, b = 0.3$, (d) $D_1 = 10^{-6}, D_2 = 10^{-5}, \alpha = 6.576, \beta = 0.9, \lambda = 1, \Lambda = 1, \hat{D}_1 = 3.95 \times 10^{-5}, \hat{D}_2 = 6.99 \times 10^{11}, b = 0.3$. 178

6.15 Plots of asymptotic and numerical outer solutions u and v for $\phi_1 = \Phi_1$ and $\phi_2 = \Phi_\infty$ when $\lambda \neq 1$. The details of the parameter values can be found in Table 6.11. (a) $D_1 = D_2 = 10^{-4}, \alpha = 5.62, \beta = 0.9, \lambda = 0.9, \Lambda = 0.9, \hat{D}_1 = 6 \times 10^{-3}, \hat{D}_2 = 8.62 \times 10^{12}, b = 0.3$, (b) $D_1 = D_2 = 10^{-5}, \alpha = 9.7, \beta = 0.9, \lambda = 0.8, \Lambda = 0.8, \hat{D}_1 = 9.64 \times 10^{-4}, \hat{D}_2 = 1.1 \times 10^{12}, b = 0.3$, (c) $D_1 = 10^{-5}, D_2 = 10^{-4}, \alpha = 2.79, \beta = 2, \lambda = 0.9, \Lambda = 0.9, \hat{D}_1 = 6 \times 10^{-4}, \hat{D}_2 = 8.6 \times 10^{12}, b = 0.3$, (d) $D_1 = 10^{-6}, D_2 = 10^{-5}, \alpha = 3.81, \beta = 0.9, \lambda = 0.8, \Lambda = 0.8, \hat{D}_1 = 9.64 \times 10^{-5}, \hat{D}_2 = 1.1 \times 10^{12}, b = 0.3$. 179

6.16 Plots of asymptotic solutions from (6.28) and (6.31) in (a), asymptotic solutions from (6.28) and (E.8) in (c) and IVP solutions from (6.1) in (b) and (d) for $\phi_1 = \phi_2 = \Phi_\infty$. 181

6.17 Plots of asymptotic solutions from (6.44) and (E.13) in (a), asymptotic solutions from (6.44) and (E.19) in (c) and IVP solutions from (6.1) in (b) and (d) for $\phi_1 = \phi_2 = \Phi_1$. 182

6.18 Plots of asymptotic solutions from (6.44) and (6.31) in (a), asymptotic solutions from (6.44) and (E.8) in (c) and IVP solutions from (6.1) in (b) and (d) for $\phi_1 = \Phi_1$ and $\phi_2 = \Phi_\infty$. . . 183

C.1 (a) The numerical amplitudes from (5.50) and weakly nonlinear (WN) amplitudes of $\phi_1 = \psi = \Phi_2$ for large λ. (b) is the magnified image of (a). (c) The numerical solutions at $\lambda = 20$. 200

C.2 (a) The numerical amplitudes from (5.50) and weakly nonlinear (WN) amplitudes of $\phi_1 = \psi = \Phi_\infty$ for large λ. (b) is the magnified image of (a). (c) The numerical solutions at $\lambda = 20$. 201

C.3 (a) The numerical amplitude of u and v from (5.50) for $\phi_1 = \psi = \Phi_2$ solved by fixing amplitude. (b) The analytical and numerical amplitudes in a smaller λ domain. (c) The numerical solutions u and v solved by fixing amplitude. 202

C.4 (a) The numerical amplitude of u and v from (5.50) for $\phi_1 = \psi = \Phi_\infty$ solved by fixing amplitude. (b) The analytical and numerical amplitudes in a smaller λ domain. (c) The numerical solutions u and v solved by fixing amplitude. 203

D.1 Fully nonlinear solutions from (5.50) for $\phi_1 = \psi = \Phi_2$ for (a) decreasing D_1 and (b) decreasing D_2. 204

D.1 (cont.) Fully nonlinear solutions from (5.50) for $\phi_1 = \psi = \Phi_2$ for (c) increasing α, (d) increasing β, (e) increasing Λ, and (f) increasing λ. 205

D.2 Plots of the fully nonlinear solutions from (5.50) for $\phi = \Phi_2$. (a) The maximum amplitude of v is greater than that of u as $D_2 < D_1$. (b) The effect of $\beta > \alpha$ is greater than $D_1 < D_2$, hence larger peak in v. More than two peaks due to $\Lambda = 5$. (c) $\alpha > \beta$ and therefore larger peak in u. (d) Larger peak in u as $D_1 < D_2$. (e) The effect of $D_2 < D_1$ is larger than $\alpha > \beta$. (f) $\max u > \max v$ as $\alpha > \beta$. Solution u has two peaks due to $\Lambda = 4$. (g) The effect of $D_2 < D_1$ is greater than $\alpha > \beta$. Solution v has more than two peaks. (h) $\alpha > \beta$ leads to larger amplitude in u. 206

D.3 Fully nonlinear solutions from (5.50) for $\phi_1 = \psi = \Phi_\infty$ for (a) decreasing D_1, (b) decreasing D_2 and (c) increasing α. 207

D.3 Fully nonlinear solutions from (5.50) for $\phi_1 = \psi = \Phi_\infty$ for (d) increasing β, (e) increasing Λ, and (f) increasing λ. 208

D.4 Plots of the fully nonlinear solutions from (5.50) for $\phi_1 = \psi = \Phi_\infty$. (a) $\beta > \alpha$ results in larger peak in v. $\Lambda = 4$ leads to two peaks in u. (b) $D_2 < D_1$ and hence $\max v > \max u$. (c) $\max u > \max v$ as $\alpha > \beta$.Solution v has more than two peaks as $\Lambda > 1$. (d) The maximum amplitude of u is larger as $\alpha > \beta$. (e) $\max u > \max v$ as $\alpha > \beta$. Solution u forms two peaks as $\Lambda > 1$. (f) The effect of $D_1 < D_2$ is larger than $\beta > \alpha$. (g) The effect of $D_2 < D_1$ is larger than $\alpha > \beta$. (h) Solution u has larger maximum amplitude than that of v as $D_1 < D_2$. 209

Chapter 1

Introduction

1.1 Background and motivation

Reaction-diffusion equations are mathematical models that describe the phenomenon of multiple substances interacting with each other while diffusing through a medium. In the context of population dynamics, the reaction terms correspond to interactions between the species, while the diffusion terms model the process of movement or dispersion [1, 2]. One of the simplest reaction-diffusion equations is the Fisher-Kolmogorov-Petrovskii-Piskunov (KPP) model [3]

$$\frac{\partial u}{\partial t} = D\frac{\partial^2 u}{\partial x^2} + u(1-u), \qquad t > 0, \qquad x \in \mathbb{R}, \tag{1.1}$$

where D is a diffusion coefficient and $u = u(x,t)$ is the population density. (Note that D can be scaled out of the equation (1.1), but we retain it here for compatibility with the literature review of the Fisher-KPP model later.) The model was initially proposed for the propagation of a mutant gene, resulting in travelling wavefronts that can also simulate events in biological invasion or population genetics [4]. The Fisher-KPP equation can be extended into a system with various modifications to model the interaction between two species.

A classic example of such a system in mathematical ecology is the diffusive Lotka-Volterra model [5]

$$\begin{aligned} \frac{\partial u}{\partial t} &= \frac{\partial^2 u}{\partial x^2} + u(1-u-av), \\ \frac{\partial v}{\partial t} &= D\frac{\partial^2 v}{\partial x^2} + rv(1-v-bu), \end{aligned} \tag{1.2}$$

which portrays the competition between two species. Here, D denotes the diffusivity of v relative to u, r is the relative intrinsic growth rate of v over u, a represents the competition coefficient of u multiplied by the carrying capacity of v and vice versa for b.

Three decades ago, nonlocal terms were first included in reaction-diffusion equations to model the intraspecific competition in a population where the strength of competition for resources between individuals depends on the distance between them [6, 7]. It is claimed in [7, 8] that the inclusion of nonlocality provides a higher level of realism when compared to the typical population models because the consumption of resources is rarely entirely local in populations. In the local models, populations are thoroughly blended, and any two individuals have an equal chance of interaction, irrespective of their geographical positions [9]. However, in reality, individuals compete not only at their own point in space but also with individuals in a neighbourhood of the original position. For instance, in a water-limited region, two neighbouring plants compete for water in areas where their root intersect. The closer the plants, the stronger the competition is [10]. Another possible factor of nonlocal competition arises when the distribution of resources is non-uniform; take the diffusion of nutrients in the case of bacteria, for example, [11, 12]. In such a scenario, individuals tend to saturate in regions where resources are more abundant [13]. Note that it is also possible to model the non-uniform distribution of resources with local reaction-diffusion equation with space-dependent carrying capacity (see [14] for more details).

Mathematically, reaction-diffusion systems have been widely proposed and analysed as chemical and biological pattern formation models over the past seven decades [15, 16]. When two interacting species diffuse at different rates in the local models, patterns that are stationary in time and periodic in space may arise. These are commonly known as the Turing patterns [17]. In nonlocal models, the nonlocal terms are integral operators with a kernel to describe how influence by an individual around the neighbourhood varies with distance. For a nonlocal model with sufficiently broad spatial spread, it has been shown that spatial patterns emerge differently from those associated with Turing instability [7, 11, 18]. For instance, it was demonstrated by a mathematical study in [10] that in water-limited regions, the highly nonlocal competition between plants alone can produce vegetation patterns without diffusivity.

Motivated by this mathematical interest, this thesis is centred around the analysis of two canonical examples of nonlocal reaction-diffusion models. The first model is a local-nonlocal Fisher-KPP equation

$$\frac{\partial u}{\partial t} = D\frac{\partial^2 u}{\partial x^2} + u\left(1 - \alpha u - (1-\alpha)\phi * u\right), \tag{1.3}$$

where $D > 0$, $0 \leq \alpha \leq 1$ and $\phi * u$ is the spatial convolution term such that $[\phi * u](x,t) = \int_{-\infty}^{\infty} \phi(x-y)u(y,t)\,\mathrm{d}y$. Note that our model is a combination of the classical Fisher-KPP with local interaction (when $\alpha = 1$ in (1.3)) and the nonlocal Fisher-KPP with nonlocal interaction (when $\alpha = 0$ in (1.3)). In the first part of our thesis, we intend to study the travelling wave (TW) solutions and pattern formation of (1.3) in detail. The second model is a competitive nonlocal Lotka-Volterra (NLLV) system

$$\begin{aligned} \frac{\partial u}{\partial t} &= D_1\frac{\partial^2 u}{\partial x^2} + u\left(1 - \int_{-\infty}^{\infty} \phi_1(x-y)u(y)\,\mathrm{d}y - \alpha v\right), \\ \frac{\partial v}{\partial t} &= D_2\frac{\partial^2 v}{\partial x^2} + Rv\left(1 - \frac{1}{\lambda}\int_{-\infty}^{\infty} \phi_2\left(\frac{x-y}{\lambda}\right)v(y)\,\mathrm{d}y - \beta u\right), \end{aligned} \tag{1.4}$$

where $D_1, D_2, R, \alpha, \beta, \lambda > 0$ are dimensionless constants. Here, λ is the ratio

of the length scale of ϕ_2 to the length scale of ϕ_1 and is obtained from the nondimensionalisation (more details can be found in Chapter 4 later). The NLLV system (1.4) consists of nonlocal intraspecific and local interspecific competitions. When the kernels are replaced by Dirac delta functions, the system is reduced to the classic diffusive Lotka-Volterra system such as (1.2). Our purpose is to gain more insight into the stability of the coexisting equilibrium state of this model, as well as how the solutions develop with time. To achieve these, we conduct linear and weakly nonlinear analyses of the stability of the coexisting state in the second part of the thesis. Finally, we look at pattern formation in solutions of the fully nonlinear model before moving on to study the structure of the solutions in a comprehensive manner. The study of nonlinear integro-differential equations poses a challenge due to the complexity of obtaining exact solutions. To shed analytical light on the patterns of the solutions of models (1.3) and (1.4), we employ asymptotic methods to develop asymptotic solutions and then compare the analysis with numerical simulations.

Since the introduction of a nonlocal reaction-diffusion equation by Britton [7] in 1990, many researchers have studied nonlocal Fisher-KPP equations with different modifications to the reaction terms. There are a lot of works that focus on proofs of the existence of TW solutions, e.g.,[4, 8, 19–21]. However, the number of studies devoted to the construction of asymptotic solutions and numerical analysis is relatively small. Among these papers, Britton [7] constructed an analytical expression for the solution of a nonlocal Fisher-KPP equation. He showed a prominent hump in the TW solutions that connects two steady states due to the nonlocal term. Fuentes et al. [11], on the other hand, studied the dependence of the patterns of steady-state solutions on kernel functions through numerical analysis. To the best of our knowledge, our model of the local-nonlocal Fisher-KPP equation, a mix of the classical local and nonlocal Fisher-KPP equations, has yet to be studied in the existing literature.

The nonlocal version of the Lotka-Volterra model has been a topic of great interest among researchers since the 1970s. Scholars like Segal et al. [22], Ni et al. [23], and Maciel and Martinez-Garcia [9], among many others, have included nonlocal intraspecific and nonlocal interspecific competitions into the local diffusive Lotka-Volterra competition model. The stability of the coexisting states of these models was examined in [9, 22], showing the formation of areas with dense and zero population, providing that the Fourier transform of the kernel function is negative. Our work focuses on a diffusive Lotka-Volterra model incorporating nonlocal intraspecific and local interspecific competitions. The model is the simplest tractable nonlocal modification of diffusive Lotka-Volterra that allows us to observe interesting qualitative behaviour in the solutions while characterising the structures of the solutions mathematically. For instance, we will later show the existence of oscillatory solutions with multiple peaks within a finite wavelength and solutions with local minima that are close to zero.

It is known that a neutral stability curve is a curve that is computed from the growth rates of a steady state to determine the stable and unstable regions in the space of some parameters. It is, therefore, the boundary between the stable and unstable regions (as determined by linear stability). Our work attempts to derive the neutral curves for the stability of coexisting states asymptotically to bridge the gap in the existing literature. In addition, we study the pattern formation of the solutions of the fully nonlinear system and investigate the structure of the solutions with small diffusivity, both asymptotically and numerically.

1.2 Contributions

This section describes the contributions of this thesis towards accomplishing the previously mentioned objectives. In Chapter 3, we include a parameter α in the local-nonlocal Fisher-KPP equation of interest (see (1.3)) to control

the nonlocality of its solution. As α decreases from one to zero, the equation transitions from the classical Fisher-KPP to the nonlocal case. The primary contributions from this chapter stem from the asymptotic analyses of the structure of the solutions as $\alpha \to 0$. For instance, we focus on TW solutions across the whole domain before concentrating on their first spikes (localised solutions that look like Dirac delta functions at $O(1)$ lengthscale) at the wavefront for further investigation. Moreover, we also consider the asymptotic far-field behaviour of the solutions for various kernel functions.

In Chapter 4, we consider the NLLV system (1.4) with eight dimensionless parameters. The main focus of this chapter is the linear stability analysis of the coexisting state of the system when the diffusion coefficients are small. The typical procedure is to derive the dispersion relation of the system to compute the neutral stability curve numerically. While some researchers have followed this procedure [9, 22], our study is the first to consider the solutions to the NLLV system for different kernel combinations from the Gaussian kernel, $\frac{1}{2\sqrt{\pi}}\mathrm{e}^{-x^2/4}$, the exponential kernel, $\frac{1}{2}\mathrm{e}^{-|x|}$, and the modified exponential kernel, $\frac{1}{4}\left(\sqrt{2}+2|x|\right)\mathrm{e}^{-\sqrt{2}|x|}$. All these analyses allow us to deduce the relationship between the stability of the coexisting state and the system's parameters, as well as the effect of different kernels on the stability of the coexisting state.

In Chapter 5, we examine the amplitude of the spatial patterns that emerge beyond the bifurcation point discussed in Chapter 4. We conduct a weakly nonlinear analysis to achieve this, where we introduce a new bifurcation parameter to the original system to derive a cubic amplitude equation. This investigation contributes to the limited work on weakly nonlinear analysis of NLLV systems available in the existing literature [24]. Additionally, further linear stability analysis of the amplitude equation provides insights into how the patterns bifurcate with respect to the parameters in the NLLV system.

Based on the conclusion drawn in the previous chapter, we notice the emergence

of intriguing patterns in the limit of small diffusivity. For instance, regions exist where either species is close to zero in the solutions. Therefore, Chapter 6 is devoted to studying fully nonlinear solutions with small diffusion coefficients. The main contribution of this chapter lies in the asymptotic approximation of effective periodic kernels, which provides a foundation for the subsequent construction of asymptotic solutions. This study broadens the scarce knowledge on understanding the structure of spatially oscillating patterns in NLLV models. Our analysis assumes periodic boundary conditions in the model, which means periodic solutions can be converted into effective periodic kernel functions within a finite domain. To a reasonable agreement, we can replicate the steady-state numerical solutions using matched asymptotic expansions.

1.3 Literature Review

1.3.1 Nonlocal reaction-diffusion equation

The theory of reaction-diffusion equations began in the first half of the twentieth century under the influence of a wide range of applications, including combustion theory, ecology, physiology and many other fields [1, 25]. A reaction-diffusion system, in its simplest form, may be written as

$$\frac{\partial U}{\partial T} = \nabla \cdot (D \nabla U) + F(U), \tag{1.5}$$

where $U = U(X, T) \in \mathbb{R}^m$ is the vector of dependent variables with $X \in \mathbb{R}^n$, $T \in \mathbb{R}^+$, $D \in \mathbb{R}^{n \times m}$ is the diffusion matrix and $F(U)$ is the vector source term. From (1.5), $\nabla \cdot (D \nabla U)$ is the diffusion term, whereas $F(U)$ is the reaction term. In the present work, we restrict our analysis to the one-dimensional setting $(n = 1)$.

The inclusion of nonlocal terms in the reaction-diffusion equations began approximately three decades ago when considering the nonlocal interaction

and competition in a population, and see, for example, [6, 7]. A typical nonlocal interaction involves a dependence on spatial convolution. This is commonly denoted as $\phi * U$ where U indicates the population density and $*$ represents the spatial convolution for a given kernel ϕ. Mathematically, $(\phi * U)(X) = \int_\Omega \phi(X - Y)U(Y)\,\mathrm{d}Y$ implies a weighted average of the values of U at all points in the domain Ω. From an ecological point of view, multiplying the nonlocal term by U, i.e. $U(\phi * U)$, is interpreted as intraspecific competition for resources, such as food or light. Take the intraspecific competition for water between plants with a finite length of roots for example. In this case, the kernel function accounts for the weighted mean vegetation density [10]. In particular, it defines how the influence of a plant decays with distance [10, 26] (see Section 2.1 for kernel assumptions). Therefore, the competition for water is stronger with increasing vegetation density in the surroundings of a plant.

In general, nonlocal reaction-diffusion equations arise in biological populations, and the interpretation of each model depends on the definition of the space variable X. The most common case is when X corresponds to the usual physical space, where the diffusion term describes the random motion of individuals, and the nonlocal reaction-diffusion model describes the evolution of the population density. If the variable X is treated as a morphological trait, such as the size of a bird's beak, the height and weight of an animal or the size of a plant [2, 27, 28], then the diffusion term models mutations and individuals with similar characteristics compete for the same resources. Consider an example of herbivores who consume leaves from bushes or trees at height X. For this particular example, the nonlocal interaction models the stronger competition for resources between individuals with similar heights and smaller competition between individuals with different heights [2, 29].

Suppose that individuals in a population do not move, and U is the wealth they possess. A nonlocal reaction-diffusion equation can describe the wealth's evolution by treating wealth as a function of the space variable X [25]. The

diffusion term in this context is interpreted as a local redistribution of wealth from rich to poor.

It is worth noting that the diffusion term in a nonlocal reaction-diffusion equation describes the slow change process. For plants that compete for light for growth, the diffusion term symbolises the process of offspring dispersal from the parental plant through pollen and seed [26].

Another interesting study is that by Berestycki et al. [30], who studied a two-dimensional nonlocal reaction-diffusion equation with two independent variables $X = (X_1, X_2)$, namely genetic traits, X_1 and spatial location, X_2. At a particular point X_2 and time T, each individual is subject to competition not only with all the individuals at the exact location but also with all values of traits.

Mathematically, nonlocal reaction-diffusion equations give rise to nontrivial spatial patterns in solutions. For example, the formation of non-monotonic TW behind the wavefronts [7], the presence of spikes and oscillating patterns in TW solutions [31], and the existence of islands and dead zones in steady-state solutions [22]. In the thesis, we will explore pattern formation in two nonlocal reaction-diffusion models in detail.

1.3.2 Nonlocal Fisher-KPP model

Another representation of the Fisher-KPP equation takes the form

$$\frac{\partial u}{\partial t} = \frac{\partial^2 u}{\partial x^2} + \mu u(1-u), \qquad t > 0, \qquad x \in \mathbb{R}, \tag{1.6}$$

where $\mu > 0$ denotes the growth rate of a population. Note that this is equivalent to the classical Fisher-KPP in (1.1) by defining $\mu = 1/D$ and scaling the time variable appropriately. We will employ this notation for the literature review of Fisher-KPP and nonlocal Fisher-KPP to ensure consistency with

some existing research work in the field [8, 19, 32].

By letting $u(x,t) = U(z)$ where $z = x - ct$, it is well known that the Fisher-KPP model admits TW solutions with a speed $c \geq 2\sqrt{\mu}$ that connect the unstable steady state $U = 0$ to the stable steady state $U = 1$ [19, 20]. The lower bound of the wave speed can be proven by studying the phase plane of the TW of (1.6) (see [33] for more details). Since the proposal of the model in (1.6), it has drawn much attention to the theory of reaction-diffusion equations due to their broad applicability in applied mathematics and physical fields such as mathematical modelling of wound healing [34] and bushfire invasion [35]

The Fisher-KPP equation (1.6) can be generalised into the nonlocal Fisher-KPP equation of the form

$$\frac{\partial u}{\partial t} = \frac{\partial^2 u}{\partial x^2} + \mu u(1 - \phi * u). \tag{1.7}$$

In other words, equation (1.6) is a particular case of equation (1.7) when $\phi(x) = \delta(x)$. Like the classical Fisher-KPP equation, the nonlocal Fisher-KPP equation admits TW solutions for $c \geq 2\sqrt{\mu}$. This equation has been studied extensively since Britton, [7], introduced a nonlocal reaction-diffusion equation in 1990, but most of the literature on the nonlocal Fisher-KPP equation focused on proofs of the existence of TW solutions [8, 19–21].

The existing literature shows that the behaviour of TW solutions, $u(x,t) = U(z)$, depends crucially on the value of μ and the functional form of the kernel function ϕ in (1.7). It has been proven that in the limit of highly nonlocal interactions (or μ sufficiently small), the TW that connects solutions with $U = 0$ and $U = 1$ is still monotonic. As μ increases (or D in (1.3) decreases when $\alpha = 0$), the TW loses monotonicity while connecting solutions from $U = 0$ to $U = 1$. Gourley has illustrated this [20] numerically as he showed that there exists a hump in the travelling front profile with $\phi(x) = \mathrm{e}^{-|x|}/2$. Another work by Billingham [31] showed that there exist spikes and oscillations behind the wavefront in TW solutions for different kernel functions. His work demonstrated both

asymptotically and numerically that properties of TW solutions of (1.7) behind the wavefront are strongly affected by the behaviour of the kernel functions around $x = 0$. In particular, kernels with higher smoothness around $x = 0$ generate a higher number of spikes and oscillations behind the wavefront.

In [19], Berestycki et al. proved that there exist TW solutions that connect $U = 0$ to $U = 1$ when the Fourier transform of ϕ is positive, regardless of the value of μ. However, when μ is sufficiently large, the TW that connects these two states may not be monotonic. Later, Hamel and Ryzhik [8] showed that when μ is large, and the Fourier transform of the kernel ϕ is not positive everywhere, $U = 1$ loses its stability and leads to the formation of stationary periodic solutions. This assertion has been verified in numerical simulations in [27] and [28] with an M-shaped competition kernel and a piece-wise constant function, respectively. This shows that the kernel ϕ plays a vital role in the behaviour of TW solutions of (1.7). Indeed, Nadin et al. [32] numerically showed that discontinuous kernels lead to periodic TW solutions when μ is large. However, periodic TW solutions are not the main concern of this thesis, and we focus on kernels such that $U = 1$ is a stable steady state.

There are also several works in which the authors incorporated a delay in both time and space in nonlocal terms. The reason for introducing temporal delay is to consider that individuals in a population are moving. Hence, they may be in a different position in space than at previous times. For more information regarding travelling wavefronts with spatial-temporal delays, readers are referred to [20, 36, 37] and the references therein.

1.3.3 Nonlocal Lotka-Volterra model

The Lotka-Volterra model was initially proposed by Alfred Lotka [38] in 1925 without the diffusion terms to study prey-predator interactions between a plant and a herbivore feeding on the plant in his book, *Elements of Physical*

Biology. Later, in 1926, Vito Volterra [39], an eminent Italian mathematician, published a short discussion on the analysis of prey-predator interactions in fish populations in the Adriatic Sea during World War One. A few years later, the model became known as the Lotka-Volterra model, which served as the pioneering equations for future work in mathematical ecology. Researchers later incorporated diffusion terms to consider the movement of two populations in space, leading to the well-known diffusive Lotka-Volterra model. Unlike the classical Lotka-Volterra model, which attracted scholarly interest earlier, the diffusive system only began to draw attention around the 1970s [40–42].

Over the past decades, generalisations and adaptations of the classical Lotka-Volterra model have been performed for a wide variety of applications. Apart from the well-known biological invasion phenomenon [43] and microbial interaction [44, 45], some researchers have applied the model in business applications to explore the competing species in the business ecosystem [46–48]. Take the work by Lee et al. [46] for example; the Lotka-Volterra model was adopted to analyse the dynamic relationship between two competing markets in the Korean stock market. In addition, Chiang et al. [47] analysed the competitive relationship between the shipments of desktops and notebooks in Taiwan using a different Lotka-Volterra model.

In this thesis, we focus on the diffusive Lotka-Volterra model, which can be written in the general dimensional form

$$\begin{aligned} \frac{\partial U}{\partial T} &= D_1 \nabla^2 U + U F(U,V), \\ \frac{\partial V}{\partial T} &= D_2 \nabla^2 V + V G(U,V), \end{aligned} \tag{1.8}$$

where $U(X,T) \in \mathbb{R}$ and $V(X,T) \in \mathbb{R}$, with $X \in \mathbb{R}^n$ and $T \in \mathbb{R}^+$, denote the population densities and D_1 and D_2 are diffusivities. In general, the diffusive Lotka-Volterra system can be categorised into three main types of interaction depending on the kinetic functions F and G [49].

(i) Prey-predator model [50]:

The growth rate of one species is decreased while the other increases from the interaction of the two species.

$$\frac{\partial F}{\partial V} < 0, \quad \frac{\partial G}{\partial U} > 0.$$

(ii) Competition model [51]:

The growth rate of each species is decreased by the interaction of the two species.

$$\frac{\partial F}{\partial V} < 0, \quad \frac{\partial G}{\partial U} < 0.$$

(iii) Symbiosis model [52]:

The growth rate of each species is enhanced by the interaction of the two species.

$$\frac{\partial F}{\partial V} > 0, \quad \frac{\partial G}{\partial U} > 0.$$

In 1937, Fisher [3], Kolmogorov, Petrovsky and Piscounov [53] found that a reaction-diffusion equation could give rise to a travelling wavefront between equilibrium states in one spatial dimension. This has motivated the study of the existence of TW solutions in diffusive Lotka-Volterra systems [52, 54, 55]. In [50], it was proven that the prey-predator system (1.8) admits non-monotonic TW solutions using a shooting argument, and the TW solution is equivalent to a heteroclinic orbit in 4-dimensional phase space. The minimum speed of the TW solutions of the competition diffusive Lotka-Volterra model has also been well studied in the literature [51, 56–58]. More recently, the analysis of (1.8) has been extended to multi-component cases to describe the interaction for more than two species. This allows the modelling of more practical applications, such as microbiological interactions in water bodies and multi-component chemical interactions. The study of pattern formation and the TW of a model consisting of three competitive species can be found in [59, 60]. In particular, the case

when a third species invades a system composed of two competing species has been studied by Chang et al. [61] and Mimura et al. [62]. The former examined the existence and stability of non-monotonic TW solutions of the system. In contrast, the latter discussed the dynamics of coexisting states of the system in three spatial dimensions. In essence, all of the Lotka-Volterra models (i)-(iii) have been studied extensively since it was developed in the mid-1920s.

Another way of defining the dimensional Fisher-KPP equation is

$$\frac{\partial U}{\partial T} = D\nabla^2 U + rU(1 - aU).$$

Here, U represents the population density, r denotes the growth rate of a population, $1/a$ is the carrying capacity of the environment, and D is the diffusion coefficient. Even though it was proposed to model the spatial spread of a mutant gene in a given population [3], this equation can also be applied to model the dynamics of a single species. When there are two interacting species, it can be easily generalised to the dimensional diffusive Lotka-Volterra competition model given by

$$\begin{aligned} \frac{\partial U}{\partial T} &= D_1\nabla^2 U + r_1 U(1 - a_1 U - b_1 V), \\ \frac{\partial V}{\partial T} &= D_2\nabla^2 V + r_2 V(1 - a_2 V - b_2 U). \end{aligned} \tag{1.9}$$

This is the same as (1.8) with $F = r_1(1-a_1U-b_1V)$ and $G = r_2(1-a_2V-b_2U)$. Here, r_1 and r_2 are the net birth rates, $1/a_1$ and $1/a_2$ are the carrying capacities, and b_1 and b_2 are the competition coefficients. Based on this model, Okubo et al. [43] studied the interaction between the externally introduced grey squirrels and the indigenous red squirrels in Britain. The estimation of model parameters that they obtained from field data predicted the speed of invasion of the grey squirrels through TW solutions of the system (1.9). It is straightforward to work out that the stability of the coexisting steady state of the diffusive Lotka-Volterra system (1.9) is stable when $b_1 < a_2$ and $b_2 < a_1$. The stability

of the equilibrium of prey-predator systems has received great attention since the incorporation of time delays into the systems [63–65]. Models involving delays are of interest as they consider the delay in predator maturation and the delay in predation.

The diffusive Lotka-Volterra system (1.9) above can be generalised into a model with nonlocal interactions between two species. It is also considered a generalisation of two nonlocal Fisher-KPP equations with different modifications. In [6], Britton showed that the coexistence of two species could be destabilised when the interactions are sufficiently nonlocal. Another study by Segal et al. [22] concentrated on a nonlocal model with nonlocal intraspecific and interspecific competitions. They examined the nonlinear behaviour of the solutions for a Gaussian kernel and a step function kernel. It was shown that the nonlocal interaction destabilises the coexisting steady state that is stable for local interaction. Numerical simulations for the fully nonlinear system illustrated patterns where a series of islands of nonzero population is separated by dead zones where the population is close to zero. They deduced from the linear stability analysis that the instability of the coexisting steady state requires that the Fourier transform of the kernel functions be negative for some band of wavenumbers, which aligned with the conclusion in [9]. Our research investigates a specific type of NLLV system derived from the general model in [22] with four kernels in four nonlocal competitions. We can recover our model by setting two of their kernels in the nonlocal interspecific competitions to delta functions. Our results show that pattern formation arises despite having positive values in the Fourier transform of our kernel functions in the nonlocal intraspecific competition.

1.3.4 Turing instability

From the spiral that originates from chemical reactions, [66] and the ripples on a sand dune [67] to the hair follicles of a mouse [68], patterns are

commonly found in nature. Over the past seven decades, reaction-diffusion systems have been widely proposed and analysed as models for chemical and biological pattern formation [15, 16]. Alan Turing proposed one of the most well-studied of such models in 1952 on the theory of morphogenesis - the biological process that causes an organism to develop its shape [17]. In his seminal work, the chemical reactions of morphogens were represented by a coupled system of reaction-diffusion equations with linear reaction kinetics. He predicted that two reacting and diffusing chemicals could generate patterns, provided the chemicals diffuse at a different rate. This phenomenon is now well known as diffusion-driven instability. Mathematically, inhomogeneous Turing patterns arise when the linearly stable, spatially homogeneous steady state becomes unstable to a spatially varying perturbation, provided that the diffusion coefficients of two reactants are different. Thirty years later, Gierer and Meinhardt introduced the terms activator and inhibitor in describing morphogens in [69]. They proposed that short-range activation and long-range inhibition, where the inhibitor diffuses faster than the activator, are necessary conditions for diffusion-driven instability. Later, in 1990, Turing's theory was confirmed by Castets, who produced the first experimental evidence of Turing patterns in the chloride-ionic-malonic-acid (CIMA) reaction [70].

Since Turing's paper, Turing instability that arises from reaction-diffusion models with various adaptation have been studied extensively. For more information regarding these studies, interested readers are referred to [15, 71] and the references therein.

In this thesis, we will later show that spatial patterns emerge due to the nonlocal terms in our nonlocal reaction-diffusion models, as opposed to diffusion-driven Turing instability.

1.3.5 Weakly nonlinear analysis

It is not trivial to derive analytical solutions for nonlinear partial differential equations (PDEs). However, we can study the behaviour of the solutions when the PDEs are weakly nonlinear by setting a small parameter that tends to zero at a bifurcation point. Near the threshold of nonlinearity, we can systematically approximate the solutions and describe the evolution of their patterns using amplitude equations.

The amplitude of the emerging patterns near the bifurcation point can be characterised using weakly nonlinear analysis, which was originally developed by Stuart [72] and Watson [73] in 1960 in a fluid mechanics context. While weakly nonlinear analysis is commonly employed in the field of fluid mechanics [74], it has also been applied in other areas such as dune formation [75], neural fields [76], ecology [77], and many others.

Close to the bifurcation point, the steady state has just lost stability, and therefore, the pattern evolves with a slowly varying amplitude. Due to this reason, one of the popular methods to derive the governing amplitude equations is multiple-scale perturbation theory. The implementation of this theory can be found in different contexts but mostly in fluid mechanics [74, 78, 79]. The general approach in weakly nonlinear analysis is to reduce the system of partial differential equations down to a specific type of Ginzburg-Landau amplitude equation that characterises the amplitude of the oscillatory patterning [79, 80]. The Ginzburg-Landau amplitude equation was first derived from simple models such as Rayleigh-Bénard convection or the Swift-Hohenberg equation [79]. More recently, studies have been carried out on the derivation of amplitude equations from models with nonlocal terms, such as the generalised Swift-Hohenberg model [81] and the nonlocal Fisher-KPP [82]. Both papers showed that the coefficients of the Ginzburg-Landau equation can be written in terms of the Fourier transform of the kernel function in the nonlocal intraspecific competition.

1.4 Outline of the thesis

The thesis is organised as follows. Asymptotic methods and numerical calculations constitute a large portion of this thesis. The background of the methods used and other mathematical backgrounds can be found in Chapter 2.

Chapter 3 is dedicated to investigating the behaviour of TW solutions of a local-nonlocal Fisher-KPP model (1.3) with a free parameter α, in the limit of small diffusivity. We will later show that the diffusivity correlates to the speed of the TW, c. We first analyse the numerical solutions when $c = O(\alpha)$, focusing on the Gaussian kernel and a modified exponential kernel. Numerical methods such as central finite differences and two-point Gaussian quadrature are used to discretise the TW equation numerically. Then, we venture into the far-field analysis of the solutions for various kernel functions by determining their decay rate and frequency of oscillation. Following this, we examine the first spikes of the solutions of two kernels. Finally, we compute the asymptotic solutions for these two kernels for $\alpha = O(1)$. Careful considerations must be taken when formulating asymptotic scalings, as we will later see that the structure of the spikes changes from a smoothed triangle to a Gaussian function as $\alpha \to 0$ and $c \to 0$.

Chapters 4 to 6 focus on a NLLV system (1.4) with nonlocal intraspecific and local interspecific competitions. In Chapter 4, we perform linear stability analysis for the coexisting state of the dimensionless system for different kernel combinations. For each combination, the neutral curves where the bifurcation of steady states occurs are studied asymptotically. Out of six parameters in the system, excluding those of the kernel functions, we choose to examine the stability of the coexisting state in relation to the two parameters that control the strength of local interspecific competition. The solutions of their respective initial value problems (IVPs) are computed using central finite differences and the Fast Fourier Transform method.

Chapter 5 details the derivation of the amplitude equation via weakly nonlinear analysis. To simplify the derivation process, we redefine one of the kernel functions in the system from Chapter 4. Then, a standard approach called the multiple-scale expansion is implemented to characterise the amplitude of the patterns at steady states. Following this, we present the analysis of the weakly nonlinear amplitudes in the neighbourhood of the bifurcation points obtained from Chapter 4 and compare them with the numerical amplitudes. The last section of this chapter presents the fully nonlinear steady-state solutions and how their behaviour changes with the parameters in the system.

In Chapter 6, we study pattern formation in the limit of small diffusivity, where segregated regions are expected. Numerical simulations of initial value problems are illustrated via some links to online animations. We then study the steady-state solutions asymptotically for different combinations of Gaussian and exponential kernels. It is found that we can obtain asymptotic solutions in a finite domain by solving boundary value problems, and they are in good agreement with the numerical solutions.

Finally, in Chapter 7, we briefly summarise the main findings from the thesis and propose some research ideas for future work.

Chapter 2

Preliminaries

This chapter presents some assumptions about the kernel functions needed in our nonlocal models. Additionally, we include some of the asymptotic and numerical methods used throughout the thesis. Lastly, some of the equations obtained in our results are briefly mentioned.

2.1 Nonlocal kernel functions

The kernel function $\phi(x)$ in the nonlocal term $\phi * u$ is assumed to satisfy [19, 21, 31, 32]

$$\phi(x) \geq 0, \quad \phi(x) = \phi(-x), \quad \phi(x) \to 0 \text{ as } x \to \pm\infty, \quad \text{and} \quad \int_{-\infty}^{\infty} \phi(x)\,\mathrm{d}x = 1. \tag{2.1}$$

Throughout this thesis, we use different kernel functions, with a primary focus on $\phi(x) = \Phi_1(x), \Phi_2(x)$ and $\Phi_\infty(x)$ in the form

$$\Phi_1(x) = \frac{1}{2}\mathrm{e}^{-|x|}, \qquad \Phi_2(x) = \frac{1}{4}\left(\sqrt{2} + 2|x|\right)\mathrm{e}^{-\sqrt{2}|x|}, \qquad \Phi_\infty(x) = \frac{1}{2\sqrt{\pi}}\mathrm{e}^{-\frac{1}{4}x^2}. \tag{2.2}$$

Here, Φ_1 is an exponential kernel, Φ_2 is a modified exponential kernel and Φ_∞ is a Gaussian kernel (see Figure 2.1). While the Gaussian kernel is a standard

kernel that has been used in much of the literature on the study of the nonlocal Fisher-KPP (see [11, 26, 29] for example), the choice of the kernels Φ_1 and Φ_2 are inspired by the work of Billingham ([31]).

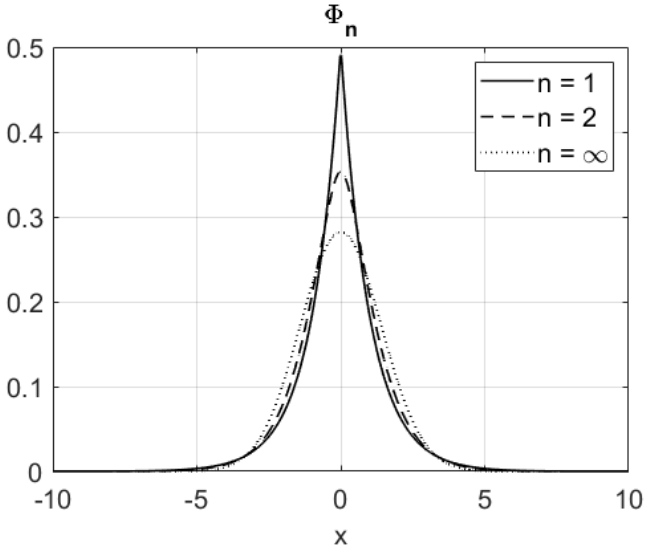


Figure 2.1: *The kernels Φ_1, Φ_2 and Φ_∞ from (2.2).*

2.1.1 Derivation of kernel functions

It is known that Green's function, G, is defined as $LG(x, x') = \delta(x - x')$ [83], where L is a linear differential operator acting on G and $\delta(x - x')$ is a Dirac delta function. For positive n, the bounded kernel $\Phi_n(z)$ from [31] that satisfies

$$\left(1 - \frac{1}{n}\frac{\mathrm{d}^2}{\mathrm{d}z^2}\right)^n \Phi_n = \delta(z), \tag{2.3}$$

is a Green's function of (2.3). Applying the Fourier transform on (2.3) returns

$$\mathcal{F}[\Phi_n] = \left(1 + \frac{1}{n}k^2\right)^{-n}, \tag{2.4}$$

where $\mathcal{F}[\Phi_n](k) = \int_{-\infty}^{\infty} \Phi_n(y)\mathrm{e}^{-iky}\,\mathrm{d}y$. For positive n, we can evaluate Φ_n analytically by applying the inverse Fourier transform to (2.4) to obtain $\Phi_1 = \mathrm{e}^{-|x|}/2$ and $\Phi_2 = \left(\sqrt{2} + 2|x|\right)\mathrm{e}^{-\sqrt{2}|x|}/4$. When $n \to \infty$, $\mathcal{F}[\Phi_\infty] \sim \mathrm{e}^{-k^2}$ as $\mathrm{e}^x = \lim_{i\to\infty}\left(1 + \frac{x}{i}\right)^i$. Therefore, the inverse Fourier transform returns a Gaussian kernel, i.e. $\Phi_\infty = \frac{1}{2\sqrt{\pi}}\mathrm{e}^{-x^2/4}$. This shows that the bounded function

defined in (2.3) connects Φ_1 to Φ_∞. Also, note that the Fourier transforms of Φ_1, Φ_2 and Φ_∞ are positive.

2.2 Multiple-scale analysis

According to Cross and Greenside [84], two key features underlie this theory. The first feature is the introduction of multiple scales, as the name suggested. The general idea is to uniformly expand the dependent variable(s) in terms of two or more independent variables, which are usually referred to as scales. The reason is that the spatial and temporal modulations of the patterns are slow when the nonlinearities of PDEs are weak, hence requiring slow time and slow space-independent variables to capture this behaviour. To obtain a weakly nonlinear model, we go beyond the linear analysis by including higher order terms in the expansion of the nonlinearity, say via a Taylor series that includes up to the cubic terms (see Subsections 2.2.1 and 2.2.2 for examples). The second feature is using solvability conditions (also known as resonance conditions [85]) in deriving amplitude equations.

Performing multiple-scale analysis for a weakly nonlinear behaviour near the instability of a spatially uniform state leads to a cubic amplitude equation. It is a well-known complex Ginzburg-Landau equation type, which is widely used in nonlinear wave phenomena [72, 73]. The simplest form can be written as [84]

$$\frac{\partial A}{\partial t} = A + (1 + ic_1)\nabla^2 A - (1 - ic_2)|A|^2 A, \tag{2.5}$$

where A is the complex amplitude, c_1 and c_2 are real numbers. In this section, we present two concrete examples of the multiple-scale regime, one concerning a nonlinear PDE and another about a nonlocal PDE. These techniques will be the foundation of the multiple-scale formalism for a system of two nonlocal PDEs later in Chapter 5.

2.2.1 Example 1 - Swift-Hohenberg equation

To illustrate the concept of weakly nonlinear analysis through multiple-scale expansion, we now present one of the simplest nonlinear PDEs that has been widely used in the study of pattern formation, namely the Swift-Hohenberg equation

$$\frac{\partial u}{\partial t} = \alpha u - \left(1 + \frac{\partial^2}{\partial x^2}\right)^2 u - u^3, \quad t \geq 0, \quad x \in \mathbb{R}, \quad u \in \mathbb{R}, \quad \alpha \in \mathbb{R}. \tag{2.6}$$

The model was introduced in 1977 for thermal fluctuations near the onset of Rayleigh-Bénard convection [86, 87]. Here, $u(x,t)$ represents the temperature field at point (x,t) of space and time, and $\alpha \in \mathbb{R}$ is a parameter.

We know that $u_0 = 0$ is a trivial solution for the nonlinear Swift-Hohenberg equation in (2.6). Therefore, we linearise (2.6) around $u_0 = 0$ by writing $u = \hat{u}\mathrm{e}^{\sigma t + ikx}$ for small amplitude $|\hat{u}| \ll 1$ to obtain the dispersion relation

$$\sigma = \alpha - (1 - k^2)^2. \tag{2.7}$$

When $\alpha < 0$, $\sigma < 0$ so $u_0 = 0$ is stable. When $\alpha > 0$, however, small amplitude perturbations of the form $\mathrm{e}^{\sigma t + ikx}$ grow with the maximum growth rate at $k = 1$. Therefore, $\alpha = 0$ is the bifurcation point where $\sigma(k_c) = 0, \sigma'(k_c) = 0$ and $\sigma''(k_c) < 0$ at the critical wavenumber $k_c = 1$. We then define the bifurcation parameter $\alpha = \epsilon^2\delta$ for $\delta = O(1)$ as $\epsilon \to 0$ to study the stability of the solution $u_0 = 0$ around the neighbourhood of $\alpha = 0$. The scaling of ϵ^2 is a natural choice as it does not affect the linear stability equation, which only depends on the terms of order ϵ. The δ term is included so that α can be made positive or negative with respect to the bifurcation point $\alpha = 0$.

It is natural to consider a multiple-scale analysis to understand the response properties of the system. To do so, we define the slow space variables, $\chi = \epsilon x$, and the slow time variable, $\tau = \epsilon^2 t$. Further, we consider the power series

expansion for $u = u_0 + \epsilon u_1 + \epsilon^2 u_2 + \epsilon^3 u_3 + \dots$ with unknown functions $u_n = u_n(x, t, \chi, \tau), n = 1, 2, 3, \dots$.

Then, we substitute

$$\frac{\partial}{\partial t} \to \frac{\partial}{\partial t} + \epsilon^2 \frac{\partial}{\partial \tau}, \qquad \frac{\partial}{\partial x} \to \frac{\partial}{\partial x} + \epsilon \frac{\partial}{\partial \chi}, \qquad \frac{\partial^2}{\partial x^2} \to \frac{\partial^2}{\partial x^2} + 2\epsilon \frac{\partial^2}{\partial x \partial \chi} + \epsilon^2 \frac{\partial^2}{\partial \chi^2}, \tag{2.8}$$

into (2.6) to obtain

$$\begin{aligned}
&\left(\frac{\partial u}{\partial t} + \epsilon^2 \frac{\partial}{\partial \tau}\right)\left(u_0 + \epsilon u_1 + \epsilon^2 u_2 + \epsilon^3 u_3 + \cdots\right) \\
&= \left(u_0 + \epsilon u_1 + \epsilon^2 u_2 + \epsilon^3 u_3 + \cdots\right)\left\{\epsilon^2 \delta - \left[\left(1 + \frac{\partial^2}{\partial x^2}\right)^2 + 4\epsilon \frac{\partial^2}{\partial x \partial \chi}\left(1 + \frac{\partial^2}{\partial x^2}\right)\right.\right. \\
&\quad + 2\epsilon^2 \frac{\partial^2}{\partial \chi^2}\left(1 + \frac{\partial^2}{\partial x^2}\right) + 4\epsilon^2 \left(\frac{\partial^2}{\partial x \partial \chi}\right)^2 + O(\epsilon^3)\left.\right]\left(u_0 + \epsilon u_1 + \epsilon^2 u_2 + \epsilon^3 u_3 + \cdots\right) \\
&\quad \left. - \left(u_0 + \epsilon u_1 + \epsilon^2 u_2 + \epsilon^3 u_3 + \cdots\right)^2\right\}.
\end{aligned} \tag{2.9}$$

Note that the scalings for χ and τ are chosen in order to balance the terms on both sides of (2.9).

Balancing the terms in the orders of ϵ in (2.9) gives:

$$u_0 = 0 \tag{2.10}$$

$$\left(\frac{\partial}{\partial t} + \mathcal{L}\right) u_1 = 0, \tag{2.11}$$

$$\left(\frac{\partial}{\partial t} + \mathcal{L}\right) u_2 = -4 \frac{\partial^2}{\partial x \partial \chi}\left(1 + \frac{\partial^2}{\partial x^2}\right) u_1, \tag{2.12}$$

$$\begin{aligned}
\left(\frac{\partial}{\partial t} + \mathcal{L}\right) u_3 = &-\frac{\partial u_1}{\partial \tau} + \delta u_1 - 2 \frac{\partial^2}{\partial \chi^2}\left(1 + \frac{\partial^2}{\partial x^2}\right) u_1 - 4 \left(\frac{\partial^2}{\partial x \partial \chi}\right)^2 u_1 \\
&- u_1^3 - 4 \frac{\partial^2}{\partial x \partial \chi}\left(1 + \frac{\partial^2}{\partial x^2}\right) u_2,
\end{aligned} \tag{2.13}$$

where the linear operator $\mathcal{L}$ is given by $\mathcal{L} = \left(1 + \frac{\partial^2}{\partial x^2}\right)^2$.

Note that in the multiple-scale method, both χ and τ are treated as independent variables. In essence, we have changed the independent variables from (x, t, ϵ) to $(x, t, \chi, \tau, \epsilon)$.

We then seek a weakly nonlinear solution u_n in the form $A(\chi, \tau)\mathrm{e}^{\pm ix}\mathrm{e}^{\sigma t}$, where A is the the complex amplitude. Therefore, at the bifurcation point where $\sigma = 0$, $\partial u_n/\partial t = 0$. Since each of the equations from (2.10) to (2.13) contains terms of the same order or lower, we can solve for u_n systematically from the first equation. The system above has the general form $\mathcal{L}u_n = g_n(u_0, u_1, u_2, \ldots, u_{n-1})$. Equation (2.11) returns a linear solution $u_1 = A(\chi, \tau)\mathrm{e}^{ix} + A^*(\chi, \tau)\mathrm{e}^{-ix}$, where $k_c = 1$, and A^* is the complex conjugate of A. Here the null space of $\mathcal{L}$ is spanned by $\mathrm{e}^{\pm ik_c x}$. Upon substituting u_1 into (2.12), we obtain $\mathcal{L}u_2 = 0$, suggesting that u_2 is a solution of the form $u_2 = B(\chi, \tau)\mathrm{e}^{ix} + c.c$ where c.c stands for complex conjugate. We can absorb u_2 into u_1 by $u_1 + \epsilon u_2 \to u_1$ so that the new u_1 will still be $O(1)$. This is the same as taking $B = 0$, and therefore $u_2 = 0$. Since the right-hand side of (2.13) is nontrivial, we need to derive a solvability condition using Fredholm alternative to obtain an equation for the complex amplitude $A(\chi, \tau)$.

We first define the inner product of two periodic functions U and V with periodicity $2\pi/k_c$ as

$$\langle U, V\rangle = \frac{k_c}{2\pi}\int_0^{\frac{2\pi}{k_c}} U^*(x)V(x)\,\mathrm{d}x, \tag{2.14}$$

where * denotes complex conjugation. For all $u \in \ker \mathcal{L}^\dagger$, we have $\langle u, g_n\rangle = \langle u, \mathcal{L}u_n\rangle = \langle \mathcal{L}^\dagger u, u_n\rangle = 0$ where $\mathcal{L}^\dagger$ is the adjoint of $\mathcal{L}$. Since $\mathcal{L}$ is self-adjoint, the solvability condition is $\langle \mathrm{e}^{ix}, \mathcal{L}u_3\rangle = 0$.

Next, we apply the solvability condition along with the result $\langle \mathrm{e}^{imx}, \mathrm{e}^{inx}\rangle = \delta_{m,n}$

to (2.13) that results in

$$\begin{aligned}\langle \mathrm{e}^{ix}, \mathcal{L}u_3\rangle = \left\langle \mathrm{e}^{ix}, -\frac{\partial u_1}{\partial \tau}\right\rangle + \langle \mathrm{e}^{ix}, \delta u_1\rangle + \left\langle \mathrm{e}^{ix}, -2\frac{\partial^2}{\partial \chi^2}\left(1+\frac{\partial^2}{\partial x^2}\right)u_1\right\rangle \\ \left\langle \mathrm{e}^{ix}, -4\left(\frac{\partial^2}{\partial x \partial \chi}\right)^2 u_1\right\rangle + \langle \mathrm{e}^{ix}, -u_1^3\rangle.\end{aligned} \tag{2.15}$$

Upon evaluating (2.15), we obtain the amplitude equation of (2.6) as

$$\frac{\partial A}{\partial \tau} = \delta A + 4\frac{\partial^2 A}{\partial \chi^2} - 3A|A|^2. \tag{2.16}$$

We now analyse the amplitude equation (2.16) by writing $A = R(\chi,\tau)\mathrm{e}^{i\theta(\chi,\tau)}$ where $R \in \mathbb{R}$ and $\theta \in [0, 2\pi)$. In (R,θ) coordinates, the real and imaginary parts of (2.16) lead to

$$\begin{aligned}\frac{\partial R}{\partial \tau} &= 4\frac{\partial^2 R}{\partial \chi^2} - 4R\left(\frac{\partial \theta}{\partial \chi}\right)^2 + R(\delta - 3R^2), \\ R\frac{\partial \theta}{\partial \tau} &= 8\frac{\partial R}{\partial \chi}\frac{\partial \theta}{\partial \chi} + 4R\frac{\partial^2 \theta}{\partial \chi^2},\end{aligned} \tag{2.17}$$

The spatially uniform steady states from (2.17) are $(R_0,\theta_0) = (0,\theta_c)$ and $(R_0,\theta_0) = \left(\sqrt{\delta/3},\theta_c\right)$, for arbitrary constant θ_c. We then linearise (2.17) around (R_0,θ_0) by writing $(R,\theta) = (R_0,\theta_0) + (\overline{R},\overline{\theta})$ for $|\overline{R}|,|\overline{\theta}| \ll 1$, which yields an uncoupled system

$$\begin{aligned}\frac{\partial \overline{R}}{\partial \tau} &= 4\frac{\partial^2 \overline{R}}{\partial \chi^2} + \overline{R}(\delta - 9R_0^2) \\ \frac{\partial \overline{\theta}}{\partial \tau} &= 4\frac{\partial^2 \overline{\theta}}{\partial \chi^2}.\end{aligned} \tag{2.18}$$

Substituting $\overline{\theta} = \hat{\theta}\mathrm{e}^{\lambda\tau + i\kappa\chi}$ (for constant $\hat{\theta}$) into (2.18) returns an eigenvalue $\lambda = -4\kappa^2$ which is always negative for all R_0. Hence, the phase of the amplitude is always stable. On the other hand, the eigenvalue for the $\overline{R}$ component with $\overline{R} = \hat{R}\mathrm{e}^{\lambda\tau + i\kappa\chi}$ is $\lambda = -4\kappa^2 + \delta - 9R_0^2$.

We are now ready to study the bifurcation of the amplitude, R_0, away from the

bifurcation point at $\alpha = 0$. We begin by looking at the case where the solutions are spatially uniform, i.e. when $\kappa = 0$. The eigenvalue of the $\overline{R}$ component is now $\lambda = \delta - 9R_0^2$. At $R_0 = 0$, bifurcation occurs at $\delta = 0$ where $\lambda < 0$ when $\delta < 0$, resulting in stable patterning of the solutions and unstable otherwise. At $R_0 = \sqrt{\delta/3}$, $\lambda = -2\delta$. Since $R_0 \geq 0$, we need $\delta > 0$ for this particular R_0 and therefore $\lambda < 0$. In conclusion, the amplitude of the solutions exhibits a supercritical bifurcation near the bifurcation point, as shown in Figure 2.2.

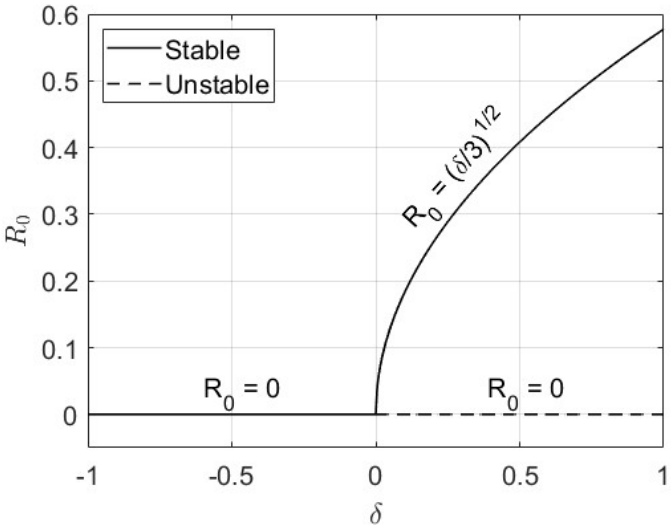


Figure 2.2: *Supercritical bifurcation diagram for amplitude R_0 against δ, based on the linear stability analysis of the amplitude equation of the Swift-Hohenberg model (2.16).*

The natural question that follows is whether another bifurcation point exists where the stable branches of R_0 will become unstable. To answer this question, we study the eigenvalue $\lambda = -4\kappa^2 + \delta - 9R_0^2$ when $\kappa \neq 0$. We first look at $R_0 = 0$, which gives $\lambda = -4\kappa^2 + \delta$. Since $\delta < 0$ in the stable branch, $\lambda < 0$ and hence the stable branch remains stable. At $R_0 = \sqrt{\delta/3}$, on the other hand, $\lambda = -4\kappa^2 - 2\delta$. Assuming that a secondary bifurcation occurs along the stable branch, it means $\lambda = 0$ and equivalently $\kappa = \sqrt{-2\delta/4}$. However, $\delta > 0$ in the stable branch suggests that κ is complex, which is not true. We, therefore, conclude that there is no secondary bifurcation such that λ becomes positive.

2.2.2 Example 2 - Neural field model

We now extend this analysis to cover a neural field model containing a nonlocal interaction. This is useful as it illustrates how to handle nonlocal terms in weakly nonlinear analysis. Consider the model

$$\frac{\partial u}{\partial t} = D\frac{\partial^2 u}{\partial x^2} - u + w * f(u). \tag{2.19}$$

Here, the diffusive term represents the effect of gap junction (electrical) coupling in the neural tissue [88], u is a scalar field representing neural activity, and the symbol $*$ denotes a spatial convolution defined by

$$[w * f(u)](x,t) = \int_{-\infty}^{\infty} w(x-y) f(u(y,t))\,\mathrm{d}y. \tag{2.20}$$

The nonlinear firing rate f is chosen as

$$f(u) = \frac{1}{1+\mathrm{e}^{-\beta u}}, \qquad \beta > 0. \tag{2.21}$$

We choose a symmetric kernel w in the form of

$$w(x) = (1-|x|)\mathrm{e}^{-|x|}, \tag{2.22}$$

to encode the spatial interactions between points in the tissue. This kernel has the balance property $\int_{-\infty}^{\infty} w(x)\,\mathrm{d}x = 0$. The spatially homogeneous steady is $u_0 = 0$ since $u_0 = f(u_0)\int_{-\infty}^{\infty} w(x-y)\,\mathrm{d}y = f(u_0)\int_{-\infty}^{\infty} w(y)\,\mathrm{d}y$. Linearising (2.19) around the spatially homogeneous steady state u_0 by writing $u = u_0 + \hat{u}\mathrm{e}^{\sigma t + ikx}$ for some small amplitude $|\hat{u}| \ll 1$, we obtain the dispersion relation

$$\sigma(k) = -Dk^2 - 1 + f'(u_0)\overline{w}(k). \tag{2.23}$$

When $\sigma = 0$, we have

$$\overline{w}(k_c) = \frac{1+Dk_c^2}{f'(u_0)}, \tag{2.24}$$

where k_c is the critical wavenumber defined by $\max_k f'(u_0)\overline{w}(k) - Dk^2 = 1$ and $\overline{w}$ is the Fourier transform of w. We now Taylor expand the nonlinear firing rate f around the steady state u_0 as

$$f(u) = f(u_0) + \beta_1(u - u_0) + \beta_2(u - u_0)^2 + \beta_3(u - u_0)^3, \tag{2.25}$$

where $\beta_2 = f''(u_0)/2$, $\beta_3 = f'''(u_0)/6$, and we treat β_1 as a bifurcation parameter and write $\beta_1 = \beta_c + \epsilon^2\delta$ (see Subsection 2.2.1 for the choice of scaling) where now β_c subject to

$$\beta_c = \begin{cases} \frac{4}{\overline{w}(k_c)} & \text{when } D = 0, \\ \frac{4(1+Dk_c^2)}{\overline{w}(k_c)} & \text{when } D \neq 0, \end{cases} \tag{2.26}$$

for critical wavenumber k_c. It can be shown that $\overline{w}(k_c) = 4k_c^2/(1 + k_c^2)^2$ and $\beta_c = 4$ when $D = 0$ (see Appendix A.1).

Next, we rescale $\chi = \epsilon x$ and $\tau = \epsilon^2 t$ and consider power series expansions for u as $u = u_0 + \epsilon u_1 + \epsilon^2 u_2 + \epsilon^3 u_3 + \ldots$. Then, we choose y and s to be the fast space and time variables and consider the Taylor series expansion of the functions u_n as

$$\begin{aligned} u_n(y, s, \epsilon y, \epsilon^2 s) &= u_n(y, s, \chi + \epsilon(y - x), \epsilon^2 s), \\ &\approx u_n(y, s, \chi, \tau) + \epsilon(y - x)\frac{\partial}{\partial \chi}u_n(y, s, \chi, \tau) \\ &\quad + \frac{\epsilon^2}{2}(y - x)^2\frac{\partial^2}{\partial \chi^2}u_n(y, s, \chi, \tau) + O(\epsilon^3), \end{aligned} \tag{2.27}$$

to facilitate the evaluation of the spatial convolution terms in (2.19). Upon substituting these into (2.19), we equate the powers of ϵ, which leads to a

hierarchy of equations:

$$u_0 = M_0(f(u_0)), \tag{2.28}$$

$$\frac{\partial u_1}{\partial t} = \mathcal{L}u_1, \tag{2.29}$$

$$\frac{\partial u_2}{\partial t} = \mathcal{L}u_2 + 2D\frac{\partial^2 u_1}{\partial x \partial \chi} + M_0(\beta_2 u_1^2) + M_1(\beta_c u_1), \tag{2.30}$$

$$\begin{aligned}\frac{\partial u_3}{\partial t}+\frac{\partial u_1}{\partial \tau} = \mathcal{L}u_3 + 2D\frac{\partial^2 u_2}{\partial x \partial \chi} + D\frac{\partial^2 u_1}{\partial \chi^2} + M_0(2\beta_2 u_1 u_2 + \beta_3 u_1^3 + \delta u_1) \\ + M_1(\beta_c u_2 + \beta_2 u_1^2) + M_2(\beta_c u_1),\end{aligned} \tag{2.31}$$

where the linear operators $\mathcal{L}$ and M_n are given by $\mathcal{L} = D\frac{\partial^2}{\partial x^2} - 1 + \beta_c w*$, $M_0 = w*$, $M_1 = W^x * \partial_\chi$, and $M_2 = \frac{1}{2}W^{xx} * \partial_{\chi\chi}$. We have introduced the new kernels $W^x(x) = -w(|x|)x$ and $W^{xx}(x) = w(|x|)x^2$.

We then seek a weakly nonlinear solution u_n in the form $A(\chi,\tau)\mathrm{e}^{\pm ik_c x}\mathrm{e}^{\sigma t}$. Therefore, at the bifurcation point where $\sigma = 0$, $\partial u_n/\partial t = 0$. The first equation in the system (2.28)-(2.31) fixes the steady state $u_0 = 0$ due to the balanced kernel w. The second equation (2.29) is linear with solutions $u_1 = A(\chi,\tau)\mathrm{e}^{ik_c x}$+c.c. Hence the null space of $\mathcal{L}$ is spanned by $\mathrm{e}^{\pm k_c x}$. The amplitude equation can be obtained by using Fredholm alternative to derive the solvability conditions for higher order equations, which have the general form $\mathcal{L}u_n = g_n(u_0, u_1, u_2, \ldots, u_{n-1})$. It is simple to show that $\mathcal{L}$ is self-adjoint and hence we obtain the set of solvability conditions $\langle \mathrm{e}^{ik_c x}, g_n\rangle = 0$ for $n \geq 2$, where inner products of U and V are defined earlier in (2.14) as $\langle U, V\rangle$.

Next, we evaluate each of the terms in the right-hand side of (2.30), with the use of the result $w * \mathrm{e}^{ikx} = \overline{w}(k)\mathrm{e}^{ikx}$ and the assumption that

$$u_2 = A_+\mathrm{e}^{2ik_c x} + A_-\mathrm{e}^{-2ik_c x} + A_0 + A_1\mathrm{e}^{ik_c x} + A_2\mathrm{e}^{-ik_c x}. \tag{2.32}$$

Balancing the powers of $\mathrm{e}^{ik_c x}$ gives

$$A_0 = \frac{2\beta_2|A|^2\overline{w}(o)}{1-\beta_c\overline{w}(0)}, \qquad A_+ = \frac{\beta_2\overline{w}(2k_c)A^2}{1+4Dk_c^2-\beta_c\overline{w}(2k_c)}, \qquad A_- = A_+^*, \quad (2.33)$$

where A_1 and A_2 are undetermined but do not appear in the amplitude equation for $A(\chi,\tau)$. Finally, by applying solvability condition on equation (2.31) and the result $\langle \mathrm{e}^{imk_c x}, \mathrm{e}^{ink_c x}\rangle = \delta_{m,n}$, we obtain the amplitude equation

$$\frac{\partial A}{\partial \tau} = \mu\frac{\partial^2 A}{\partial \chi^2} + A\overline{w}(k_c)(\delta+\gamma|A|^2), \quad (2.34)$$

where

$$\mu = -\frac{1}{2}\left.\frac{\mathrm{d}^2\sigma}{\mathrm{d}k^2}\right|_{k=k_c}, \quad \gamma = 2\beta_2 d + 3\beta_3, \quad d = \frac{2\beta_2\overline{w}(0)}{1-\beta_c\overline{w}(0)} + \frac{\beta_2\overline{w}(2k_c)}{1+4Dk_c^2-\beta_c\overline{w}(2k_c)}. \quad (2.35)$$

By letting $A = R\mathrm{e}^{i\theta}$ for real amplitude R and phase θ, the amplitude equation in (R,θ) coordinates can be written in the form

$$\begin{aligned} \frac{\partial R}{\partial \tau} &= \mu\left[\frac{\partial^2 R}{\partial \chi^2} - R\left(\frac{\partial \theta}{\partial \chi}\right)^2\right] + R\overline{w}(k_c)\left[\delta+\gamma R^2\right], \\ R\frac{\partial \theta}{\partial \tau} &= \mu\left(2\frac{\partial R}{\partial \chi}\frac{\partial \theta}{\partial \chi} + R\frac{\partial^2 \theta}{\partial \chi^2}\right) \end{aligned} \quad (2.36)$$

The spatially uniform system of (2.36) gives two steady states $(R_0,\theta_0) = (0,\theta_c)$ and $\left(\sqrt{-\delta/\gamma},\theta_c\right)$, for $\delta/\gamma < 0$ and arbitrary constant θ_c. Next, we linearise the system (2.36) around $(R(\chi,\tau),\theta(\chi,\tau)) = (R_0,\theta_0) + \left(\overline{R}(\chi,\tau),\overline{\theta}(\chi,\tau)\right)$ to obtain an uncoupled system. Letting $\overline{\theta}(\chi,\tau) = \hat{\theta}\mathrm{e}^{\lambda\tau+i\kappa\chi}$ for constant $\hat{\theta}$ returns an eigenvalue $\lambda = -\mu\kappa^2$ which is always negative. On the other hand, substituting $\overline{R}(\chi,\tau) = \hat{R}\mathrm{e}^{\lambda\tau+i\kappa\chi}$ for constant $\hat{R}$ gives

$$\lambda = -\mu\kappa^2 + \left(\delta + 3R_0^2\gamma\right)\overline{w}(k_c). \quad (2.37)$$

In the spatially uniform case ($\kappa = 0$), $\lambda = (\delta+3R_0^2\gamma)\overline{w}(k_c)$. Since $\overline{w}(k_c) =$

$4k_c^2/(1+k_c^2)^2 > 0$, bifurcation occurs at $\delta = 0$ when the amplitude is zero, i.e. $R_0 = 0$. Specifically, the amplitude is stable when $\delta < 0$ and unstable when $\delta > 0$. The positive amplitude $R_0 = \sqrt{-\delta/\gamma}$ exists only when $\delta > 0$ since $\gamma = -\beta^3/16 < 0$. Therefore, the eigenvalue $\lambda = -2\delta\overline{w}(k_c)$ gives stable amplitude branch for positive δ. The bifurcation is supercritical, as shown in Figure 2.3.

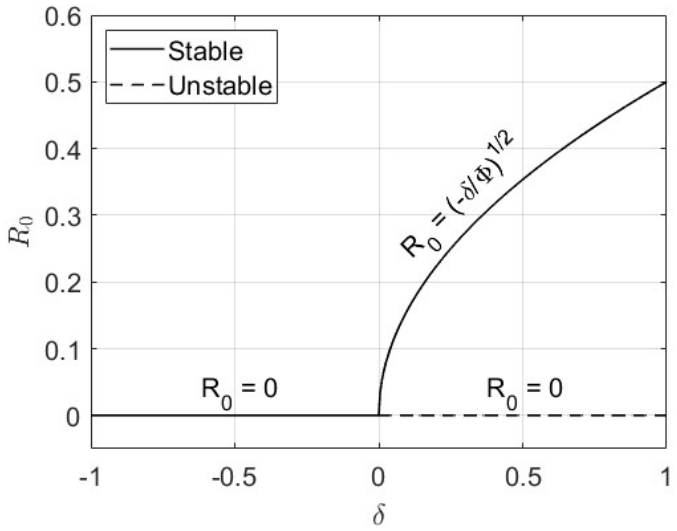


Figure 2.3: *Supercritical bifurcation diagram for amplitude R_0 against δ, based on the linear stability analysis of the amplitude equation of the neural field model (2.34).*

We are interested in whether a secondary bifurcation exists in the stable branch with positive amplitude when diffusion is considered. When $\kappa \neq 0$, the eigenvalue is now

$$\lambda = -\mu\kappa^2 - 2\delta\overline{w}(k_c), \tag{2.38}$$

which is always negative. Therefore, there is no secondary bifurcation in which the stable amplitude branch becomes unstable at κ_c.

In Chapter 5, we will investigate the weakly nonlinear analysis of the NLLV system, building on techniques developed for the neural field model, which also has nonlocal interaction.

2.3 Mathieu equation

In 1868, Mathieu studied the vibrations of an elliptical membrane through [89]

$$\frac{\mathrm{d}^2 y}{\mathrm{d}z^2} + (a - 2q\cos 2z)y = 0, \tag{2.39}$$

where $q \in \mathbb{R}$ is a free parameter, and $a \in \mathbb{R}$ is the eigenvalue of the equation. It was later named the Mathieu equation by Whittaker in 1912 in honour of its inventor [90]. This equation has generated much interest among researchers due to its applications in two main categories of physical phenomena. The first one involves the elliptical geometries such as the blood flow in elliptical cross sections of blood vessels under external pressure [91], and the water oscillations in an elliptical lake [92]. The second type is related to periodic motions, such as the oscillations of floating vessels and frequency modulation [93].

In general, the solutions of the Mathieu equation are not periodic. However, most literature focuses on the periodic solutions with period π and 2π. This specific type of solution is known as Mathieu functions [90], which can be written in terms of trigonometric series [93]. Readers interested in the technical aspects of Mathieu functions are referred to the work in [94, 95].

In Chapter 6, we will see that one of the asymptotic periodic solutions for our NLLV system turns out to be in the form of solutions of a Mathieu equation (2.39). The solutions can be easily obtained by solving the asymptotic equation numerically as a boundary value problem and hence do not involve Mathieu functions.

2.4 Numerical methods

In this section, we briefly introduce some of the numerical methods employed to solve the local-nonlocal Fisher-KPP (1.3) and the NLLV system (1.4) in this thesis.

2.4.1 Finite difference method

In general, we use the central finite difference approach to approximate the diffusion terms in both nonlocal reaction-diffusion models (1.3) and (1.4).

Uniform grid spacing (See [96])

For the NLLV system (1.4) that will later appear in Chapters 4 to 6, the diffusion term in the system is discretised uniformly in space. We first assume that the solution $u(x,t)$ is periodic and smooth in x. Take the interval $x \in [x_0, x_N] \in \mathbb{R}$ for instance; we first divide it into $N+1$ points with uniform grid spacing. Thus, $x_i = x_0 + i\Delta x$ for $i = 1, \ldots, N$ where $\Delta x = (x_N - x_0)/N$ is the spatial step size as shown in Figure 2.4. We then create a vector $u(t) = [u_0(t), \ldots, u_N(t)]^T \in \mathbb{R}^{N+1}$ where $u_i(t) = u(x_i, t)$ at x_i.

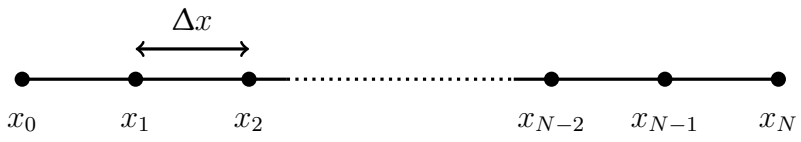


Figure 2.4: *Uniform grid spacing in x in the NLLV system (1.4).*

Next, we expand the solution u in a Taylor series at $x + \Delta x$ and $x - \Delta x$. Finally, adding the expansions and rearranging terms leads to the central finite difference approximation of the second derivative

$$\frac{D}{(\Delta x)^2}[u_{i+1}(t) - 2u_i(t) + u_{i-1}(t)] + O(\Delta x), \qquad i = 1, \ldots, N. \tag{2.40}$$

By imposing periodic boundary conditions on the spatial domain, we have $u_0(t) = u_N(t)$ and similarly $u_{-1} = u_{N-1}$. Therefore, for $N = 4$, a diffusion term, $D\frac{\partial^2 u}{\partial x^2}$, can be discretised as

$$\frac{D}{(\Delta x)^2}\begin{pmatrix} -2 & 1 & 0 & 0 & 1 \\ 1 & -2 & 1 & 0 & 0 \\ 0 & 1 & -2 & 1 & 0 \\ 0 & 0 & 1 & -2 & 1 \\ 1 & 0 & 0 & 1 & -2 \end{pmatrix} u(t), \tag{2.41}$$

that can be solved by using an appropriate numerical time integrator such as the Euler method or the midpoint method. This numerical integration in space will be employed to solve the NLLV system later.

Non-uniform grid spacing

Solving for TW solutions of the local-nonlocal Fisher KPP equation (1.3) is equivalent to solving a second-order ODE. Due to the behaviour of the solutions, which we will show in Chapter 3, TW solution is discretised into non-uniform grid points in space. This time, we discretise $x \in [x_0, x_N] \in \mathbb{R}$ into $N+1$ points with $x_i = x_0 + \sum_1^i \Delta x_i$ and $\Delta x_i = x_i - x_{i-1}$ for $i = 1, \ldots, N$. We then create a vector $u(x) = [u_0(x_0), \ldots, u_N(x_N)]^T \in \mathbb{R}^{N+1}$.

To evaluate the second derivative of unevenly spaced points, we use a three-point method. Figure 2.5 shows a simple illustration of three grid points and their corresponding solutions. To find the second derivative of the solution at

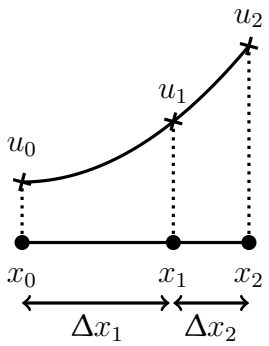


Figure 2.5: *Fitting a quadratic curve on three discrete points with uneven spacing.*

x_1, we first evaluate the derivatives at $(x_0 + x_1)/2$ and $(x_1 + x_2)/2$, and call them D_1 and D_2. Then, the second derivative will be the difference between D_2 and D_1 divided by $(x_2 - x_0)/2$. Substituting $D_1 = (u_1 - u_0)/\Delta x_1$ and $D_2 = (u_2 - u_1)/\Delta x_2$, we obtain

$$\left.\frac{\mathrm{d}^2 u}{\mathrm{d}x^2}\right|_{x_1} = \frac{2u_0}{\Delta x_1(\Delta x_1 + \Delta x_2)} - \frac{2u_1}{\Delta x_1 \Delta x_2} + \frac{2u_2}{\Delta x_2(\Delta x_1 + \Delta x_2)} \tag{2.42}$$

This calculation is equivalent to fitting a quadratic function through the three

points. To illustrate that mathematically, we assume that $u = u_0 + Ax + Bx^2$ for arbitrary constants A and B. It follows that

$$u_1 - u_0 = A\Delta x_1 + B(\Delta x_1)^2 \tag{2.43}$$

$$u_2 - u_0 = A(\Delta x_1 + \Delta x_2) + B(\Delta x_1 + \Delta x_2)^2. \tag{2.44}$$

The second derivative of u at x_1 is therefore $u_{xx} = 2B$. The constants A and B can be determined using the method of undetermined coefficients. To calculate B, we multiply (2.43) by $(\Delta x_1 + \Delta x_2)$ and (2.44) by (Δx_1) and subtract the latter from the former one to return the same second derivative approximation as (2.4.1).

By repeating the same process for the other grid points in the spatial domain $x \in [x_0, x_N]$, we have

$$\left.\frac{\mathrm{d}^2u}{\mathrm{d}x^2}\right|_{x=x_i} = \frac{2u_{i-1}}{\Delta x_i(\Delta x_i + \Delta x_{i+1})} - \frac{2u_i}{\Delta x_i \Delta x_{i+1}} + \frac{2u_{i+1}}{\Delta x_{i+1}(\Delta x_i + \Delta x_{i+1})}, \tag{2.45}$$

for $i = 1, \ldots, N-1$. Due to the finite number of grid points, the second derivative at x_0 is fitted by the curve from x_0 to x_2, whereas the second derivative at x_N is fitted by the curve from x_{N-2} to x_N. Hence, for $N = 4$, we approximate a diffusion term $D\frac{\mathrm{d}^2u}{\mathrm{d}x^2}$ as

$$2D \begin{pmatrix} [a(a+b)]^{-1} & -(ab)^{-1} & [b(a+b)]^{-1} & 0 & 0 \\ [a(a+b)]^{-1} & -(ab)^{-1} & [b(a+b)]^{-1} & 0 & 0 \\ 0 & [b(b+c)]^{-1} & -(bc)^{-1} & [c(b+c)]^{-1} & 0 \\ 0 & 0 & [c(c+d)]^{-1} & -(cd)^{-1} & [d(c+d)]^{-1} \\ 0 & 0 & [c(c+d)]^{-1} & -(cd)^{-1} & [d(c+d)]^{-1} \end{pmatrix} u(x), \tag{2.46}$$

where $(\Delta x_1, \Delta x_2, \Delta x_3, \Delta x_4, \Delta x_5)$ is represented by (a, b, c, d, e) for simplicity. The second derivative formula at any point can also be obtained by

differentiating the Lagrange Interpolation Polynomial twice (see [97, 98])

$$u(x) = \frac{(x-x_1)(x-x_2)\cdots(x-x_n)u_0}{(x_0-x_1)(x_0-x_2)\cdots(x_0-x_n)} + \frac{(x-x_0)(x-x_2)\cdots(x-x_n)u_1}{(x_1-x_0)(x_1-x_2)\cdots(x_1-x_n)} + \frac{(x-x_0)(x-x_1)\cdots(x-x_{n-1})u_n}{(x_n-x_0)(x_n-x_1)\cdots(x_n-x_{n-1})}. \tag{2.47}$$

2.4.2 Two-point Gauss Quadrature rule

The general framework in this subsection is adapted from the work in [99]. By definition, an $n-$point Gauss Quadrature rule is an approximation of the definite integral of a function $f : [0, 1] \in \mathbb{R}$ such that

$$\int_0^1 f(x)\,\mathrm{d}x \approx \sum_{i=1}^{n} w_i f(x_i), \tag{2.48}$$

where x_i are often called the Gauss points, and w_i the corresponding weights. An n-point quadrature rule yields the exact integration of polynomials up to $2n-1$ degree. A simple algorithm to determine the weights of Gauss Quadrature is to integrate the Lagrange polynomial through the roots of the Legendre polynomial between the interval (0,1) [99]. Another advantage of this scheme is that it avoids using endpoints in integration, which is desirable for functions with discontinuities in the endpoints [100].

Consider the mapping from $[a, b]$ to $[0, 1]$ by linear transformation $x = (b-a)\xi+a$. Then, by the change of variable, the required integral is given by

$$\begin{aligned}\int_a^b f(x)\,\mathrm{d}x &= (b-a)\int_0^1 f[(b-a)\xi + a]\,\mathrm{d}\xi, \\ &= (b-a)\sum_{i=1}^{n} w_i f[(b-a)\xi_i + a],\end{aligned} \tag{2.49}$$

for some points $\xi_i \in [0, 1]$ and w_i. The error estimate of the Gauss Quadrature rule is $O((b-a)^{2n+1})$ [101]. In our model, we employ the two-point Gauss

Quadrature rule with $n = 2$, $w_1, w_2 = 1/2$, $\xi_1 = (1 + 1/\sqrt{3})/2$ and $\xi_2 = 1 - \xi_1$. This method will later be used to discretise the nonlocal (or convolution) term in our local-nonlocal Fisher-KPP model in Chapter 3.

2.4.3 Fast Fourier transform

Another way to compute convolution terms numerically is via the convolution theorem, which will be used to solve the NLLV system in Chapters 4 to 6. First, let us consider the Fourier transform of a general function $f(x)$ to be $\mathcal{F}\{f\}(k) = F(k)$ where $\mathcal{F}$ denotes the Fourier transform operator. Its inverse Fourier transform is then

$$f(x) = \frac{1}{2\pi} \int_{-\infty}^{\infty} F(k) \mathrm{e}^{ikx} \, \mathrm{d}k,$$

where k is the frequency of $f(x)$.

The convolution theorem states that the Fourier transform of the convolution of two functions equals the product of their individual Fourier transforms. In other words, if $f(x)$ has the Fourier transform $F(k)$ and $g(x)$ has the Fourier transform $G(k)$, then $f(x) * g(x)$ has the Fourier transform $F(k)G(k)$ [102]. Each Fourier transform can be evaluated efficiently using Matlab's *fft* (Fast Fourier transform) function. Finally, the convolution of $f(x)$ and $g(x)$ is obtained by taking the inverse Fourier transform, $\mathcal{F}^{-1}$, of the product using *ifft* (Inverse Fast Fourier transform) function on Matlab, i.e. $f * g = \mathcal{F}^{-1}\{FG\}$.

Note that the Fast Fourier transform is an algorithm that became known in 1965 through Cooley and Tukey [103]. It is a method of computing the discrete Fourier transform of a sequence or its inverse much more efficiently than other algorithms. In 2000, it was nominated as one of the top ten algorithms of the 20th century by IEEE magazine *Computing in Science & Engineering* [104]. For more information about the computations and applications of Fast Fourier transform, please refer to the work by Bracewell [105].

Chapter 3

Travelling Waves of a Local-nonlocal Fisher-KPP Equation

3.1 Introduction

In this chapter, we focus on the TW solutions of a local-nonlocal Fisher-KPP equation (1.3) for two kernels, $\phi = \Phi_2$ and $\phi = \Phi_\infty$. The TW solutions can be written as $u(x,t) = U(z)$ where $z = x - ct$. The main objective of this chapter is to study the structure of the TW solutions of our model in the limit of small diffusivity, both asymptotically and numerically. It has been shown in [106] through some simulations that given localised initial conditions to a nonlocal Fisher-KPP equation, the solutions of such IVPs converge to two TWs propagating in opposite directions for t large. It is, therefore, of interest to study the structural change of the TW solutions in our model between $\alpha = 1$ and $\alpha = 0$, where the local-nonlocal Fisher-KPP reduces to the nonlocal Fisher-KPP (1.7). Since our model is a slight modification of the nonlocal Fisher-KPP equation, we expect the minimum speed to be $2\sqrt{D}$ [19, 20], the

same as the nonlocal case.

We will later show that the TW solutions of the nonlocal Fisher-KPP model (1.7) consist of more spikes and oscillations than that of our local-nonlocal Fisher-KPP model (1.3) [31]. In particular, when $\phi = \Phi_1$, Billingham showed that the TW solutions of (1.7) consist of only one spike with $O(1)$ weight behind the wavefront as $c \to 0$. Since we expect a similar structure in our solutions when $\alpha \to 0$ and $c \to 0$, it is not possible to analyse our solutions in terms of the appearance of spikes as $\alpha = O(1)$ decreases from one to zero. Therefore, we exclude $\phi = \Phi_1$ in our analysis of the pattern formation of TW solutions. On the other hand, he showed that the TW solutions with $\phi = \Phi_2$ generate an infinite number of spikes within a finite region behind the wavefront, while the solutions with $\phi = \Phi_\infty$ lead to infinitely many spikes for the whole domain behind the wavefront. Therefore, we expect that in the limit of $\alpha \to 0$, our model will generate spikes and oscillations for these two kernels for further investigation and comparison with the nonlocal Fisher-KPP when $\alpha = 0$.

We begin Section 3.2 by introducing the local-nonlocal Fisher-KPP (1.3) and its TW equation. In Section 3.3, we present the numerical TW solutions of this model for two different kernels, $\phi = \Phi_2$ and $\phi = \Phi_\infty$, when $c \ll 1$ and $c = O(\alpha)$. Section 3.4 details the study of the far-field behaviour of TW solutions for various kernels as $z \to -\infty$ in the limit of $c \to 0$. Appropriate comparisons between far-field solutions and numerical solutions are presented explicitly for the kernels $\phi = \Phi_2$ and $\phi = \Phi_\infty$. Then, we devote Section 3.5 to the asymptotic analysis of the structure of the first spike of the TW solutions for the two kernels in the distinguished limit $c = O(\alpha)$. Following this, we construct the asymptotic TW solutions for these two kernels in Section 3.6 for $c \ll 1$ and $\alpha = O(1)$ and compare them with numerical solutions. Finally, we conclude in Section 3.7 that the asymptotic solutions from the studies above agree well with the numerical solutions.

Summary

When $c \to 0$ and $\alpha = 0$ in the local-nonlocal Fisher-KPP equation (1.3), we obtain the results of the nonlocal Fisher-KPP in [31]. That is, there exist infinitely many spikes within a finite region behind the wavefront for $\phi = \Phi_2$ and an infinite number of spikes that fill the domain behind the wavefront for $\phi = \Phi_\infty$. Both of these solutions exhibit spikes in the shape of Gaussian functions.

However, as α increases from zero to one in our local-nonlocal Fisher-KPP equation (1.3), the number of spikes decreases behind the wavefront. Moreover, the presence of α changes the shape of the spikes in our TW solutions to smoothed triangles.

Before we present the numerical and asymptotic analyses in the next few sections, we will discuss the structure of the TW solutions of (1.3) as α decreases in the limit of $c \to 0$. When $\alpha_1 < \alpha \leq 1$, $U = O(1)$ behind the wavefront, and no spikes exist. For $\alpha_2 < \alpha \leq \alpha_1$, there exists a spike $U = O(1)$ at the wavefront, followed by one region in $z \in (z_2, z_1]$ where U is exponentially small and $U = O(1)$ as $z \to -\infty$, as shown in Figure 3.1.

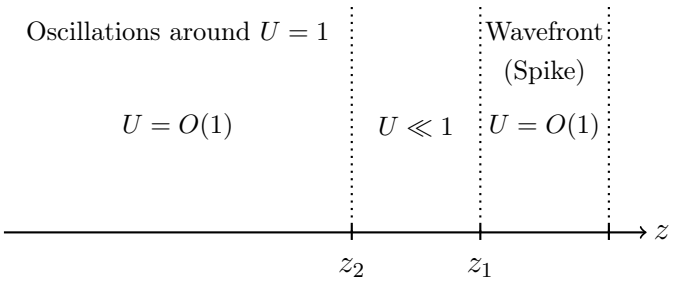


Figure 3.1: *Sketch of regions with TW solutions U when $\alpha_2 < \alpha \leq \alpha_1$.*

For $\alpha_3 < \alpha \leq \alpha_2$, the solution consists of two regions where U is exponentially small in $z \in (z_2, z_1]$ and $z \in (z_4, z_3]$ and $U = O(1)$ everywhere else behind the wavefront.

When α decreases further until $\alpha \ll 1$ but $c \ll \alpha$, the number of regions that with U exponentially small increases. In general, $\alpha_{i+1} < \alpha \leq \alpha_i$ leads

to a solution with i regions with $U \ll 1$ in the intervals $\bigcup_{j=1}^{i}(z_{2j}, z_{2j-1}]$, where $i \in \mathbb{Z}_+$ and $z_{2i} < z_{2i-1} < \ldots < z_2 < z_1$ (see Figure 3.2). In other words, if α is sufficiently small but $c \ll \alpha$, we observe finitely many spikes behind the wavefront.

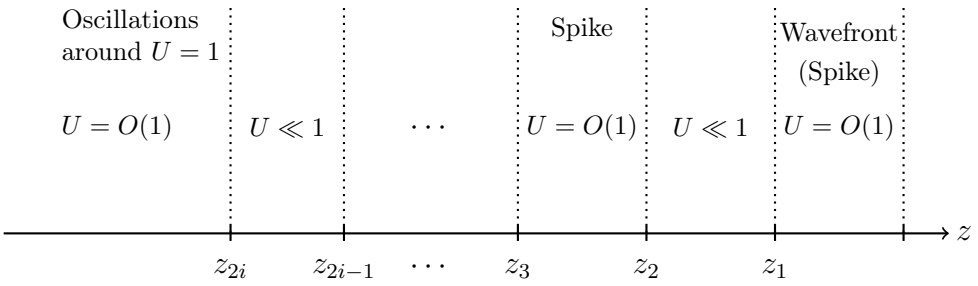


Figure 3.2: *Sketch of regions with TW solutions U when $\alpha_{i+1} < \alpha \leq \alpha_i$.*

It should be noted that for a fixed j, $(z_{2j}, z_{2j-1}]$ is different for each α because as α decreases, the distance between successive spikes decreases as well.

3.2 Problem statement

Consider the TW solutions of a local-nonlocal Fisher-KPP equation in one spatial dimension

$$u_t = Du_{xx} + u\left(1 - \alpha u - (1-\alpha)\phi * u\right), \tag{3.1}$$

where D is a positive constant, $0 \leq \alpha \leq 1$. The kernel function, ϕ, is assumed to satisfy the assumptions mentioned in Section 2.1. Equation (3.1) consists of local and nonlocal interactions of a single species. Similar to the classical Fisher-KPP (1.1) and the nonlocal Fisher-KPP equation (1.7), (3.1) admits two uniform steady states, an unstable one at $u = 0$ and a stable one at $u = 1$, provided that the Fourier transform of ϕ is positive. To investigate the stability of the steady states, we let $u = u_0 + \overline{u}$ for steady state u_0 and $\overline{u} \ll 1$ to obtain

$$\overline{u}_t = D\overline{u}_{xx} + (u_0 + \overline{u})\left(1 - \alpha(u_0 + \overline{u}) - (1-\alpha)\phi * (u_0 + \overline{u})\right). \tag{3.2}$$

Next, we rewrite (3.2) by letting $\overline{u} = \hat{u}e^{\sigma t+ikx}$ for $\sigma \in \mathbb{C}$ and $k \in \mathbb{R}$. At $u_0 = 0$, the linear terms from (3.2) return the eigenvalue $\sigma = -k^2D + 1$ which is positive when $k^2D < 1$. On the other hand, the steady state $u_0 = 1$ yields $\sigma = -k^2D - \alpha - (1-\alpha)\overline{\phi}(k)$ which is negative provided that $\overline{\phi}$, the Fourier transform of ϕ is positive. This implies that $u_0 = 0$ is unstable and $u_0 = 1$ is stable for $\overline{\phi} > 0$.

In the present work, we investigate TW solutions, $u = U(x - ct)$ with $D \ll 1$ (or μ sufficiently large in (1.7)) in which (3.1) can be interpreted as an equation with two different length scales in the diffusion and reaction terms. When $\alpha = 1$ for sufficiently small D, the classical Fisher-KPP admits monotonic TW solutions connecting $U = 0$ and $U = 1$. On the other hand, when $\alpha = 0$ and D is sufficiently small, non-monotonic TW solutions arise [20, 31]. For instance, Billingham [31] showed that kernels with discontinuous derivative at $x = 0$ such as $\phi(x) = \Phi_1(x) = e^{-|x|}/2$ can generate oscillations with a finite number of spikes behind the wavefront. On the other hand, smooth kernels such as a Gaussian kernel Φ_∞ can generate infinitely many spikes that fill the region behind the wavefront. Therefore, it is of interest to gain an understanding of how the properties of solutions of equation (3.1) vary with α.

While conducting numerical and asymptotic analysis in this chapter, we focus on the modified exponential kernel $\phi = \Phi_2$ and Gaussian kernel $\phi = \Phi_\infty$. However, some other kernels will also be briefly discussed when studying the far-field behaviour of TW solutions.

To investigate the behaviour of TW solutions of (3.1), we first substitute $u(x,t) = U(z)$ where $z = x - ct$ with unknown positive speed c. This gives a nonlocal ordinary differential equation (ODE) of the form.

$$-cU_z = DU_{zz} + U\left(1 - \alpha U - (1-\alpha)\int_{-\infty}^{\infty} \phi(z-y)U(y)\,\mathrm{d}y\right), \tag{3.3}$$

with boundary conditions

$$U \to 1 \quad \text{as} \quad z \to -\infty, \quad U \to 0 \quad \text{as} \quad z \to \infty. \tag{3.4}$$

From [31], we expect regions in the TW solutions from (3.3) where U is close to zero as α and $c \to 0$. Therefore, we introduce a new variable $L(z) = \log U(z)$ to the nonlocal ODE to reduce numerical errors. Hence, both (3.3) and (3.4) can be reformulated as

$$-cL_z = D\left(L_{zz} + L_z^2\right) + 1 - \alpha \mathrm{e}^{L(z)} - (1-\alpha)\int_{-\infty}^{\infty} \phi(z-y)\mathrm{e}^{L(y)}\,\mathrm{d}y, \tag{3.5}$$

subject to

$$L \to 0 \quad \text{as} \quad z \to -\infty, \qquad L \sim k_+ z \quad \text{as} \quad z \to \infty,$$

with

$$k_+ = \frac{-c + \sqrt{c^2 - 4D}}{2D}, \tag{3.6}$$

since αU^2 and $(1-\alpha)U\int_{-\infty}^{\infty}\phi(z-y)U(y)\,\mathrm{d}y$ from equation (3.3) tend to zero as $z \to \infty$. Here, k_+ is the dominant term that decays more slowly than k_- in the linearised solution.

From (3.6), TW solutions for non-negative U only exist for $c \geq 2\sqrt{D}$. This is also proven in [19] using weak boundary conditions where the limit of $\inf_{z\to\infty} U(z) = 0$. Henceforth, we will write $D = D_0 c^2$ with diffusion coefficient $D_0 \leq \frac{1}{4}$ and consider solutions of (3.5) with $c \ll 1$ to study cases when $D \ll 1$. Here, we fix D_0 (or D) and let c be the free parameter as it makes the numerical computation easier. When performing asymptotic analysis of solutions behind the wavefront, we assume that $D_0 = 0$ which will be explained in Section 3.6.

3.3 Numerical solution when $c \ll 1$ and $c = O(\alpha)$

One of the differences between Φ_2 and Φ_∞ is that the former is three-times differentiable whereas the latter is infinitely-differentiable at $x = 0$. In [31], it was shown that this particular feature affects the qualitative nature of TW solutions of the nonlocal Fisher-KPP equation. We will later show that $\phi = \Phi_2$ leads to solutions with a higher decay rate as $z \to -\infty$ in the analysis of the far-field behaviour of TW solutions.

To investigate the TW solutions of (3.5) behind the wavefront for $c \ll 1$ and $c = O(\alpha)$, we first truncate z to a finite domain and then evaluate L_z and L_{zz} using central finite differences (refer to Subsection 2.4.1 for non-uniform grid spacing). The integral term involving ϕ is computed using the two-point Gauss Quadrature rule (see Subsection 2.4.2) by collocating z at the midpoint of each interval between the grid points. Once we have discretised each term numerically, we then solve the resulting system of nonlinear equations using *fsolve* in MATLAB with the analytical Jacobian provided to enhance the computational speed of the solver. Starting from $\alpha = 1$, we decrease α down to 10^{-9} while letting $c = 0.1\alpha$ as it leads to a straightforward computation of the numerical solution. Note that c is an emergent property of the solution of an IVP. However, when studying the TW problem, c is merely a parameter, as is D. In fact, there is no equivalent of D in the local Fisher-KPP as it can be scaled out completely. As α and c decrease to smaller values, the curvature of the peaks of the spikes is resolved using adaptive regridding based on the size of $\sqrt{U/U_{zz}}$ by allowing non-uniform grid spacing in the spatial domain.

3.3.1 Numerical solution when $\phi = \Phi_2$

The TW solution of (3.5) with kernel $\Phi_2(x)$, diffusion coefficient $D_0 = 1/4$, $\alpha = 10^{-9}$ and $c = 10^{-10}$ is shown in Figure 3.3. In Figure 4.1(a), we observe a huge spike at the wavefront, followed by subsequent spikes with decreasing

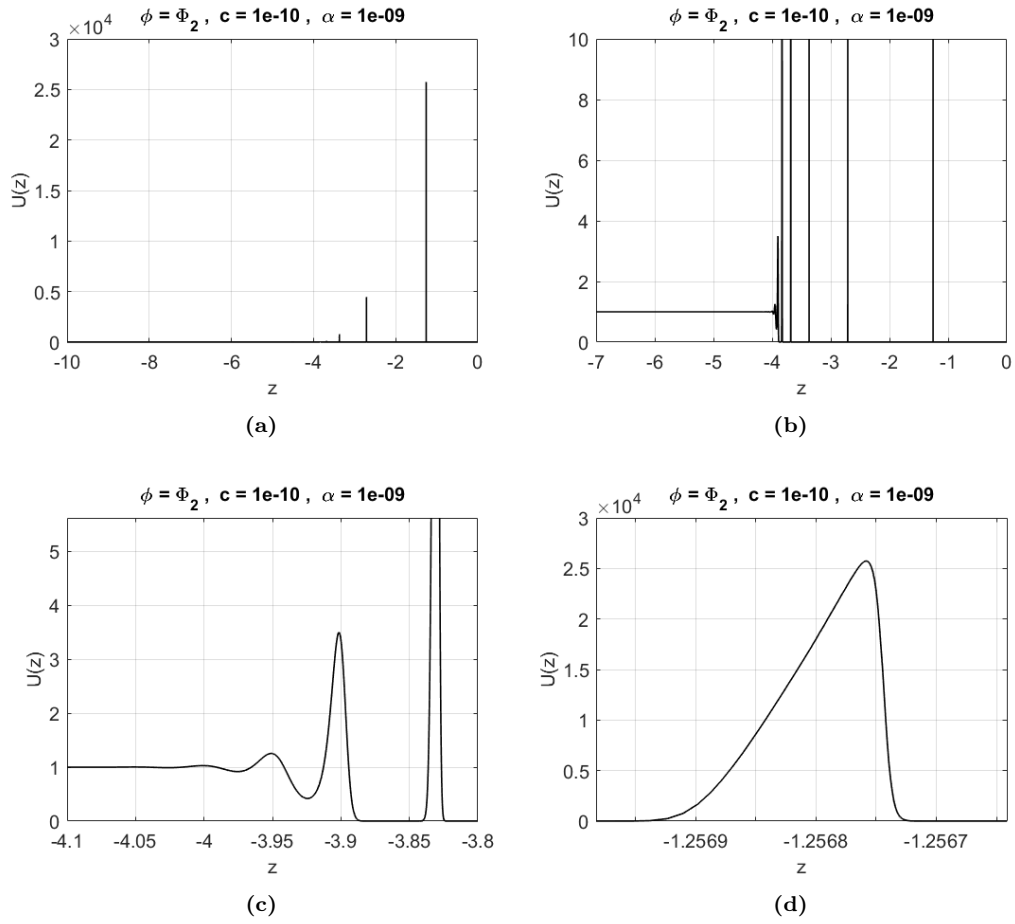


Figure 3.3: *The TW solution, $U = e^L$, obtained by solving (3.5) with $\phi = \Phi_2$, $D_0 = 1/4$, $\alpha = 10^{-9}$ and $c = 10^{-10}$. These four plots highlight different views of the structure of the solution, with the bottom right panel showing the profile at the wavefront.*

height as $z \to -\infty$. Each of these spikes seems like a Dirac delta function on this lengthscale. When $\alpha = 0$, it is shown in [31] that the nonlocal Fisher-KPP with Φ_2 leads to TW solutions with an infinite number of spikes within a finite region behind the wavefront. However, when α is sufficiently large, our model reduces the spikes to a finite number in the limit of small c. To study the structure of the spikes behind the wavefront, the full numerical solution is magnified in 4.1(b), 4.1(c) and 4.1(d). The distance between successive spikes behind the wavefront decreases with decreasing z. In Figure 4.1(c), the spikes decay rapidly to $U = 1$ for z less than -4.05. The first spike at the wavefront with a maximum value of $U = 25740$ is illustrated in Figure 4.1(d). Notice that the spike is a smoothed triangle, with U decaying more rapidly as z increases to the right than as z decreases to the left from the centre of the spike. This

is different from the results from the work of [31], which produced Gaussian spikes. From Figure 4.1(c), a smaller asymmetric spike is seen to lie to the left of each spike, with further oscillations as z decreases.

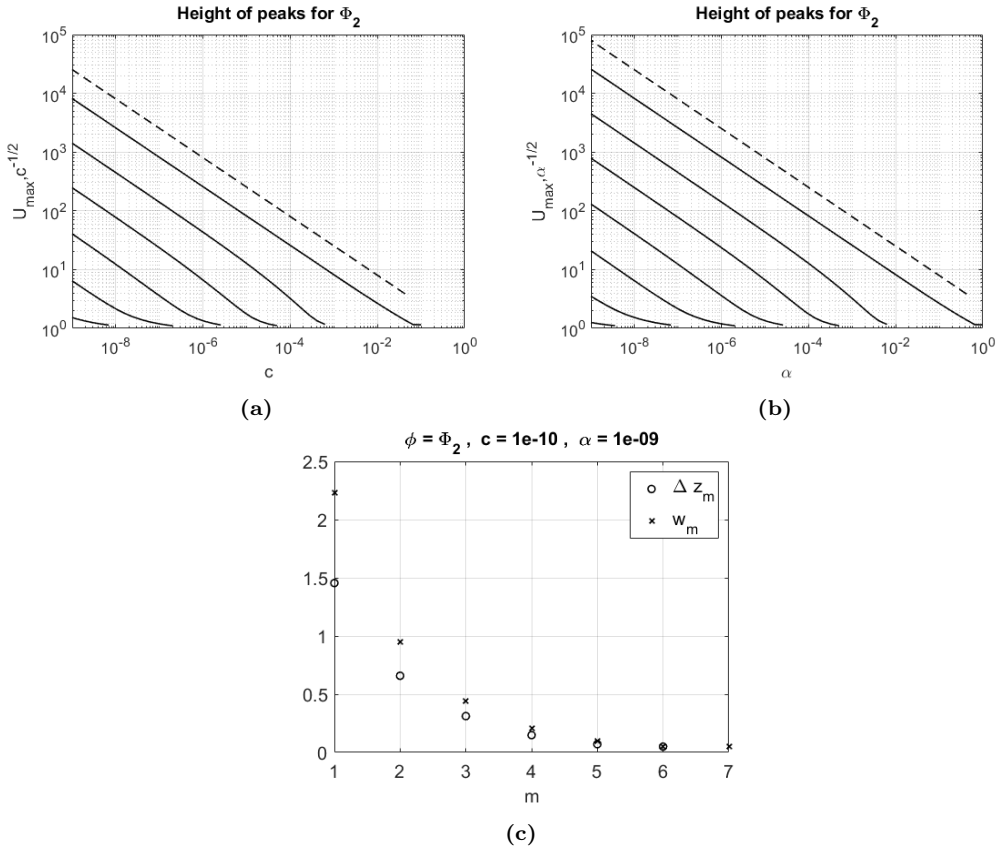


Figure 3.4: *The heights of local maxima of spikes for $\phi = \Phi_2$ against c in (a) and α in (b). The broken lines show the asymptotic approximations $U_{\max} \sim 0.8c^{-1/2}$ as $c \to 0$ in (a) and $U_{\max} \sim 2.5\alpha^{-1/2}$ as $\alpha \to 0$ in (b). Separation and weight of the spikes as a function of spike number m in (c).*

The heights of the spikes are plotted as a function of c in Figure 3.4(a). As c decreases from 0.1, the height of the first spike at the wavefront increases until c is small enough to form another spike behind the wavefront with a smaller height. As a result, a sequence of spikes is formed behind the wavefront, all of which have an amplitude that scales with $c^{-\frac{1}{2}}$ (represented by dashed line) as $c \to 0$. A similar pattern is also exhibited in Figure 3.4(b) where the heights of all spikes scale with $\alpha^{-\frac{1}{2}}$ (represented by dashed line) as $\alpha \to 0$. Figure 3.4(c) depicts how the spacings, Δz_m, between local maxima of the spikes and weights, w_m, which is computed as the area under the spike, vary with spike

number, m, with $m = 1$ at the wavefront. It appears that both Δz_m and w_m decrease with m and $\Delta z_m \sim w_m$ as $m \to \infty$, with $\Delta z_m < 0.1$ at $m = 6$.

Our results in Figure 3.4 are identical to those in the nonlocal Fisher-KPP in [31], i.e. when $\alpha = 0$ in (3.1). Hence, we would expect that as $c \to 0$ and $\alpha \to 0$, the TW solutions of the local-nonlocal Fisher-KPP generate an infinite number of spikes within a finite region behind the wavefront, with smoothed triangular spikes instead of Gaussian spikes.

In the next subsection, we will analyse the numerical solution of the TW equation (3.5) for kernel $\phi = \Phi_\infty$ with the same parameter values α, c and D_0 and compare with that of $\phi = \Phi_2$.

3.3.2 Numerical solution when $\phi = \Phi_\infty$

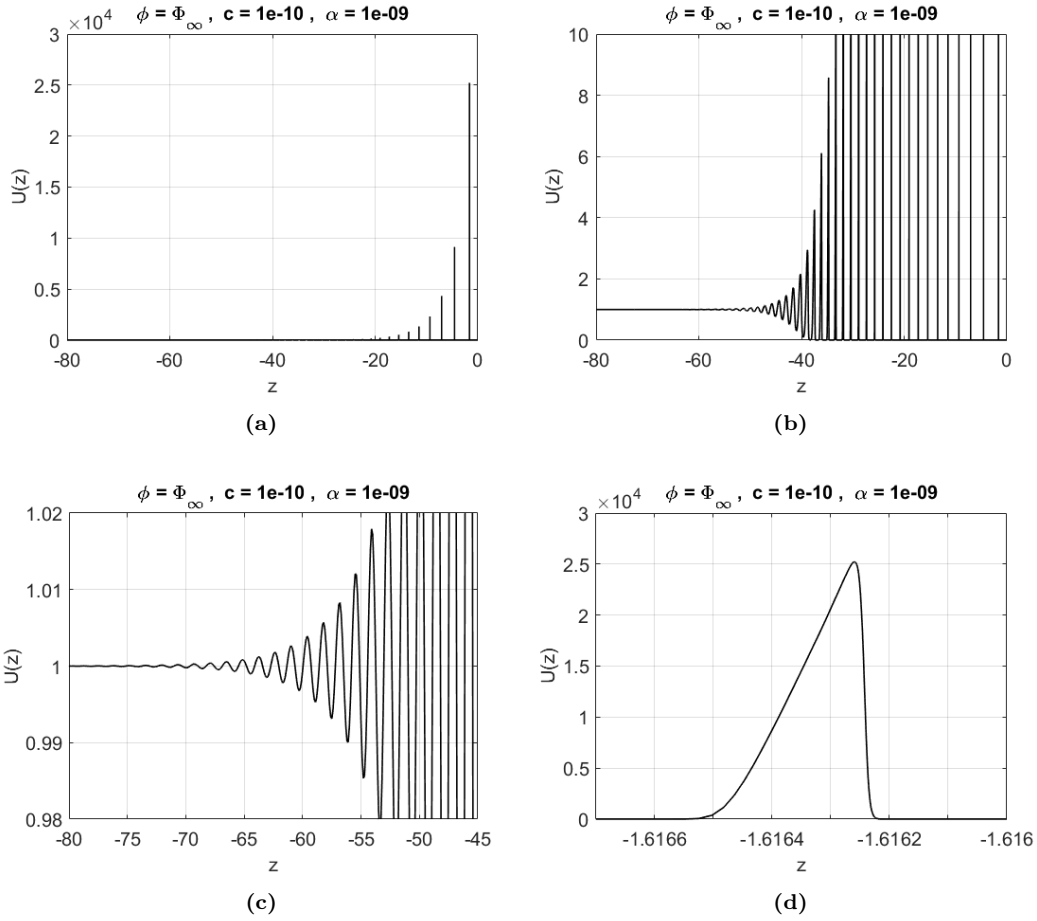


Figure 3.5: *The TW solution, $U = \mathrm{e}^L$, obtained by solving (3.5) with $\phi = \Phi_\infty$, $D_0 = 1/4$, $\alpha = 10^{-9}$ and $c = 10^{-10}$. These four plots highlight different views of the structure of the solution, with the bottom right panel showing the profile at the wavefront.*

The TW solution with Gaussian kernel $\phi = \Phi_\infty(x)$, diffusion coefficient $D_0 = 1/4$, $\alpha = 10^{-9}$ and $c = 10^{-10}$ is illustrated in Figure 3.5. Similar to the case of $\phi = \Phi_2$, the Gaussian kernel leads to a large spike at the wavefront and a sequence of narrow spikes behind the wavefront, followed by oscillatory decay as $z \to -\infty$. The spikes in 3.5(a) look like a sequence of decreasing Dirac delta functions on this lengthscale. It is noticeable that there are more spikes than when $\phi = \Phi_2$ and that the spikes decay in the direction of decreasing z at a slower rate. As shown in Figure 3.5(c), U still oscillates around one at small amplitude for z close to -80 whereas U for $\phi = \Phi_2$ converges to $U = 1$ around $z = -5$. Details of the decay rate for these kernels will be discussed in Section 3.4. Similar to the case of $\phi = \Phi_2$, the shape of the first spike is also a smoothed triangle, as shown in Figure 3.5(d). This is in contrast to the finding in [31] in which a Gaussian kernel leads to Gaussian spikes in the solution of the nonlocal Fisher-KPP equation when $\alpha = 0$. The difference is entirely due to the presence of the α term in our local-nonlocal reaction-diffusion equation, despite α being small.

Similar to the case $\phi = \Phi_2$, the heights of the spikes scale with $c^{-\frac{1}{2}}$ and $\alpha^{-\frac{1}{2}}$ as c and α tend to zero as shown in both Figure 3.6(a) and 3.6(b). At $c = 10^{-10}$ and $\alpha = 10^{-9}$, $\Delta z_m = O(w_m)$ as m increases. However, at $m = 19$, Δz_m is around 1.4, which is much larger than zero. This suggests that the solution oscillates around $U = 1$ as z decreases. Again, our observations are identical to those in the nonlocal Fisher-KPP in [31]. Even though we cannot compute solutions with smaller values of c or α numerically, we would expect an infinite number of spikes in the decreasing direction of z for $c \to 0$ and $\alpha \to 0$, same as the nonlocal Fisher-KPP, but with smoothed triangular shape. Note that the boundary condition of $U \to 1$ as $z \to -\infty$ does not satisfy $c = 0$ as it is a singular limit. However, for finite c and $-z$ large enough, $U \to 1$.

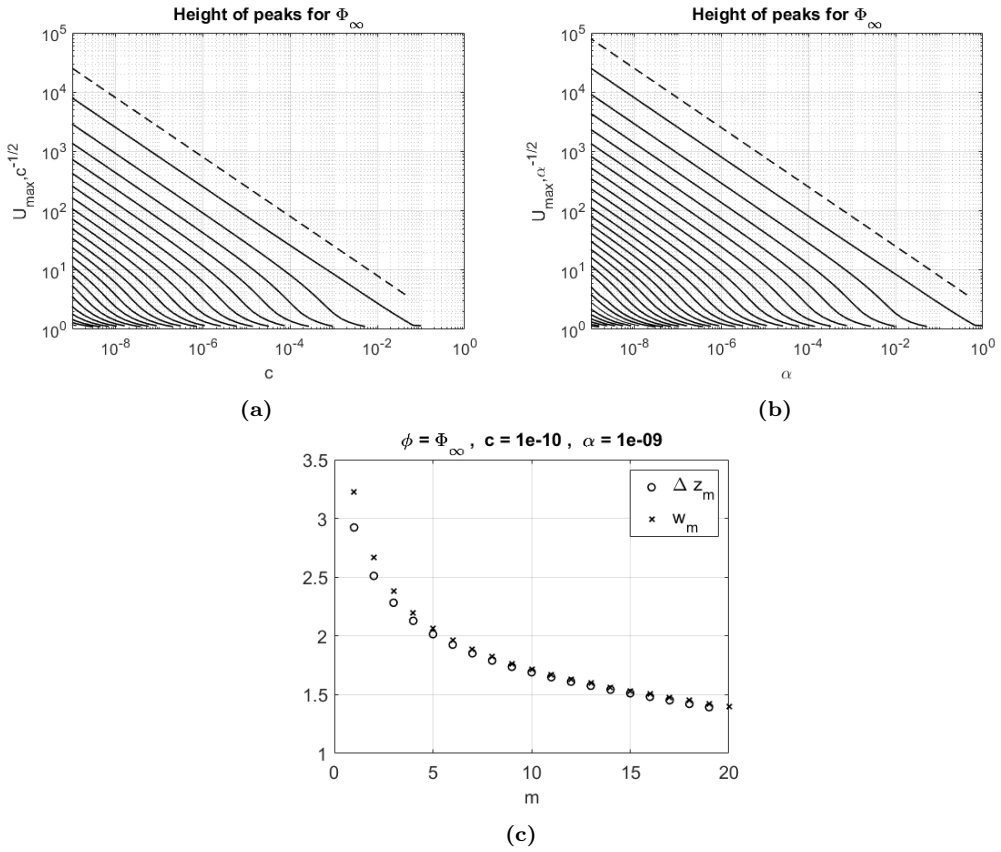


Figure 3.6: *The heights of local maxima of spikes for $\phi = \Phi_\infty$ against c in (a) and α in (b). The broken lines show the asymptotic approximations $U_{\max} \sim 0.8c^{-1/2}$ as $c \to 0$ in (a) and $U_{\max} \sim 2.5\alpha^{-1/2}$ as $\alpha \to 0$ in (b). Separation and weight of the spikes as a function of spike number m in (c).*

3.4 Far-field asymptotic analysis

From the numerical analysis in the preceding section, we have studied the behaviour of TW solutions and have shown that oscillations and (or) spikes are formed behind the wavefront as $U \to 1$. However, the decay rate and frequency of oscillation of TW solutions in the far field as $z \to -\infty$ remain unknown. To address this question, we proceed by conducting far-field analysis of asymptotic solutions when $U \to 1$ and study how oscillations of solutions behave in terms of α. The far-field analysis in this section is applicable for general kernel ϕ, and hence we will extend our study to other kernels apart from $\phi = \Phi_2$ and $\phi = \Phi_\infty$.

From Figures 4.1(c) and 3.5(c), solutions U behave like damped oscillations around $U = 1$ as z tends to minus infinity in the negative domain. Therefore,

to derive the asymptotic solution in the far field, we let $U = 1 + \overline{U}$ for $\overline{U}$ sufficiently small as $z \to -\infty$. In the limit of $c \to 0$, the linearisation of (3.3) about $U = 1$ yields an equation of the form

$$\alpha \overline{U} = (\alpha - 1) \int_{-\infty}^{\infty} \phi(z - y) \overline{U}(y) \, \mathrm{d}y. \tag{3.7}$$

We look for the solution of the form $\overline{U} = A\mathrm{e}^{ikz}$ so that the integral in (3.7) becomes a Fourier transform. Here, $A \in \mathbb{C}$ is an arbitrary constant, and k is a complex number. We are interested in evaluating k, which governs the decay rate and frequency of oscillation of solutions. If we write the real and imaginary parts of k as $k = k_R + ik_I$, then

$$\overline{U} = A\mathrm{e}^{i(k_R + ik_I)z} = A\mathrm{e}^{-k_I z}\mathrm{e}^{ik_R z} = R(z)\mathrm{e}^{i\theta(z)} \quad \text{as} \quad z \to -\infty, \tag{3.8}$$

where $R(z) = A\mathrm{e}^{-k_I z}$ and $\theta(z) = k_R z$. We conclude that the real part of k determines the oscillation frequency, whereas the imaginary part determines whether the oscillation amplitude increases or decreases with z. Based on our numerical and asymptotic analysis in the previous sections, we seek solutions with $k_I < 0$ to imply damping in the oscillation of the TW solution.

To work out k, we substitute $\overline{U} = A\mathrm{e}^{ikz}$ into (3.7) to obtain

$$\frac{\alpha}{\alpha - 1} = \int_{-\infty}^{\infty} \phi(s)\mathrm{e}^{-iks} \, \mathrm{d}s = \mathcal{F}[\phi], \tag{3.9}$$

where the integral term is a Fourier transform of general kernel ϕ.

For positive values of n, we can solve equation (3.9) using the Fourier transform of a general bounded kernel $\phi = \Phi_n$ from (2.4) to obtain a general expression for k in terms of α such that

$$k = -\sqrt{n\left(\left(\frac{\alpha - 1}{\alpha}\right)^{\frac{1}{n}} - 1\right)}. \tag{3.10}$$

The general expression (3.10) can be written as

$$k = -\sqrt{n\left((-1)^{\frac{1}{n}}\left(\frac{1}{\alpha}-1\right)^{\frac{1}{n}}-1\right)}. \tag{3.11}$$

For $\alpha \ll 1$, we can reduce (3.11) to

$$k = -\sqrt{n(-1)^{\frac{1}{n}}\left(\frac{1}{\alpha}\right)^{\frac{1}{n}}}, \tag{3.12}$$

and use the result of $-1 = \mathrm{e}^{i\pi}$ to obtain

$$k = -\sqrt{n}\cos\left(\frac{\pi}{2n}\right)\left(\frac{1}{\alpha}\right)^{\frac{1}{2n}} - i\sqrt{n}\sin\left(\frac{\pi}{2n}\right)\left(\frac{1}{\alpha}\right)^{\frac{1}{2n}}. \tag{3.13}$$

Consider the case when $n = 1$ where $\Phi_1 = e^{-|x|}/2$. In the limit of small α, we have

$$k = -i\sqrt{\frac{1}{\alpha}}, \tag{3.14}$$

and hence

$$\overline{U} \sim A\mathrm{e}^{\sqrt{\frac{1}{\alpha}}z} \quad \text{as} \quad z \to -\infty. \tag{3.15}$$

This implies that $\overline{U}$ decays exponentially without oscillation as $z \to -\infty$. When $\alpha \to 0$, the rate of decay of solution, $\sqrt{1/\alpha}$, increases, meaning that $\overline{U} \to 0$ or, equivalently, $U \to 1$ at a higher rate.

Similar analysis is carried out for $\phi = \Phi_2$ and $\phi = \Phi_3$, where

$$\Phi_3(x) = \frac{3\sqrt{3}}{16}(1 + \sqrt{3}|x| + x^2)\mathrm{e}^{-\sqrt{3}|x|}, \tag{3.16}$$

and it is found that their rate of decay and frequency of oscillation increase as $\alpha \to 0$.

Apart from that, smooth kernels such as $\phi = \Phi_\infty$ and an algebraically-decaying

Kernel	k
Φ_1	$-i\sqrt{\frac{1}{\alpha}}$
Φ_2	$-\left(\frac{1}{\alpha}\right)^{\frac{1}{4}} - i\left(\frac{1}{\alpha}\right)^{\frac{1}{4}}$
Φ_3	$-\frac{3}{2}\left(\frac{1}{\alpha}\right)^{\frac{1}{6}} - i\frac{3}{2}\left(\frac{1}{\alpha}\right)^{\frac{1}{6}}$
Φ_∞	$\sqrt{-\log\alpha} - i\frac{\pi}{2\sqrt{-\log\alpha}}$
Φ_{alg}	$-\log\alpha - i\pi$

Table 3.1: *Summary of k of different kernels and their corresponding far-field solutions $\overline{U} = Ae^{ikz}$.*

kernel

$$\Phi_{alg} = \frac{1}{\pi(1+x^2)}, \tag{3.17}$$

are also studied by evaluating the integral term in (3.9) analytically. It is found that the general expression for k for $\phi = \Phi_\infty$ and $\phi = \Phi_{alg}$ are

$$k = -\sqrt{-\log\left(\frac{\alpha}{\alpha-1}\right)}, \quad \text{and} \quad k = -\log\left(\frac{\alpha}{\alpha-1}\right). \tag{3.18}$$

As $\alpha \to 0$, (3.18) can be reformulated as

$$k = \sqrt{-\log\alpha} - i\frac{\pi}{2\sqrt{-\log\alpha}}, \quad \text{and} \quad k = -\log\alpha - i\pi, \tag{3.19}$$

by binomial expansion.

The expressions for k in the limit of $\alpha \to 0$ are summarised in Table 3.1. The magnitude of the real and imaginary parts of k is also illustrated in Figure 3.7 for more detailed analysis.

Other than $\phi = \Phi_1$ which returns imaginary k, which has zero real part, Figure 3.7(a) shows that all the other kernels have increasing oscillation frequency in the far field as $\alpha \to 0$. According to Table 3.1, the imaginary parts of k of all the kernels depend on α except for $\phi = \Phi_{alg}$. As a result, the decay rate of the solution with $\phi = \Phi_{alg}$ is constant while all the other kernels lead to increasing

decay rate as $\alpha \to 0$. Another important observation is that the decay rate of the solution with $\phi = \Phi_2$ is constantly above that of $\phi = \Phi_\infty$ in Figure 3.7(b). This is in great agreement with the numerical solutions for $\phi = \Phi_2$ and $\phi = \Phi_\infty$ in Section 3.3 where oscillations of U for $\phi = \Phi_2$ decay at a higher rate in the far field.

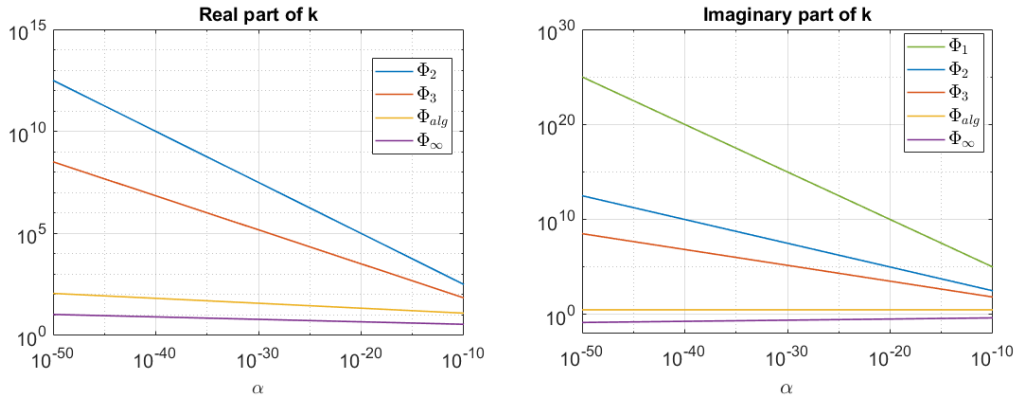


Figure 3.7: *Magnitudes of the real and imaginary parts of k for different kernels from Table 3.1 against α.*

3.4.1 Comparison between far-field solution and numerical solution

Now, we are able to plot $U = 1 + \overline{U}$ to verify the consistency of the far-field solutions with numerical solutions of the full TW problem as $z \to -\infty$. In this subsection, we will confine our attention to the comparison of solutions for $\phi = \Phi_2$ and $\phi = \Phi_\infty$ among the five kernels we have studied so far.

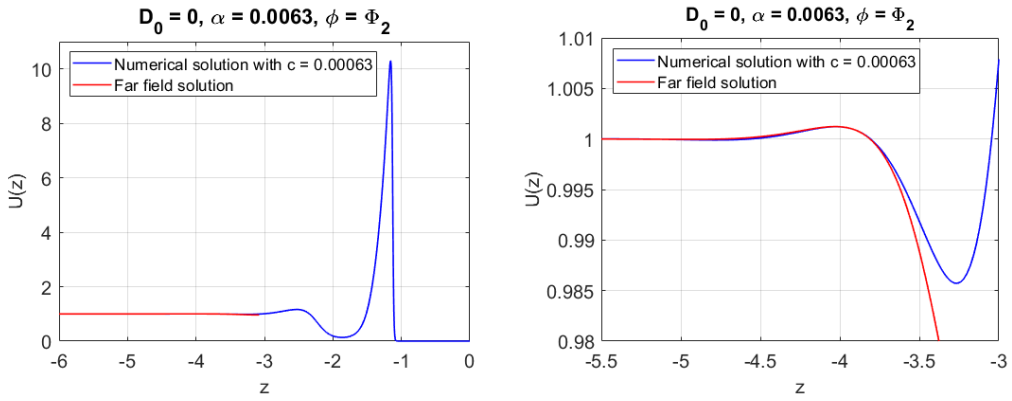
From (3.8), we can rewrite the U in terms of cos such that

$$U = 1 + Ae^{-k_I z}e^{ik_R z} = 1 + |A|e^{-k_I z}\cos\Big\{k_R(z - z_0)\Big\} \quad \text{as} \quad z \to -\infty, \quad (3.20)$$

with z_0 constant.

Note that there is no restriction on the choice of α and c values as long as they are consistent in both solutions. For $\phi = \Phi_2$, we choose $\alpha = 0.0063$ and $c = 0.1\alpha$. Note also that we choose $D_0 = 0$ as we will explain in Section 3.6

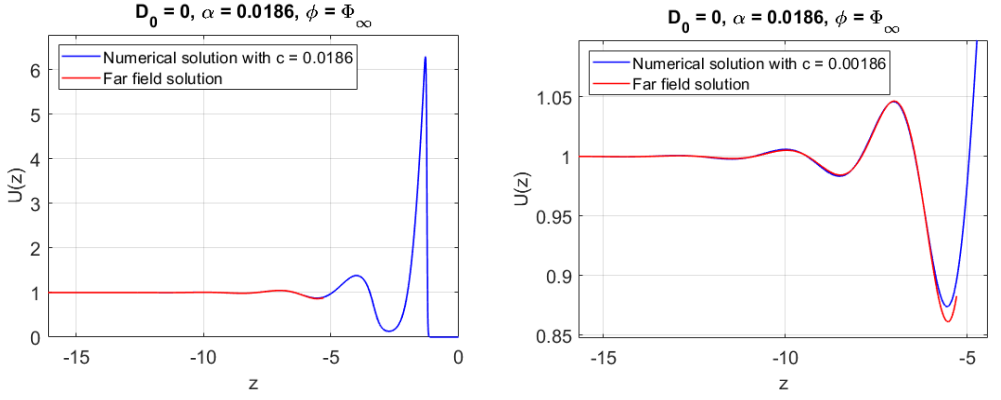
later that $D_0 = 0$ is sufficient to describe solutions behind the wavefront. By letting $n = 2$ in the general expression for k in (3.10), we plug in its real and imaginary part into equation (3.20) to plot the far-field solution in Figure 3.8. The structure of both numerical and asymptotic solutions are magnified in Figure 3.8(b), indicating a good agreement between both solutions when $\overline{U}$ is sufficiently small.



(a) (b)

Figure 3.8: *Numerical and far-field solutions from (3.20) for* $\phi = \Phi_2$ *with* $\alpha = 0.0063$ *and* $D_0 = 0$.

For $\phi = \Phi_\infty$, both numerical and far-field solutions are depicted in Figure 3.9, with $\alpha = 0.0186$ and k from (3.18). From Figure 3.9(b), the frequency and decay rate of the far-field solution matches the numerical solution when U oscillates towards one as z decreases. Therefore, we conclude that the far-field asymptotic analysis captures the behaviour of the solution as $z \to -\infty$.



(a) (b)

Figure 3.9: *Numerical and far-field solutions from (3.20) for* $\phi = \Phi_\infty$ *with* $\alpha = 0.0186$ *and* $D_0 = 0$.

3.5 Analysis of the first spike of the local-nonlocal Fisher-KPP

We have seen that the TW solutions of the local-nonlocal Fisher-KPP equation with kernels $\phi = \Phi_2$ and $\phi = \Phi_\infty$ contain a sequence of spikes with decreasing height behind the wavefront. It would be interesting to examine the structure of the spike at the wavefront and how it depends on the parameters c and α. In this section, we will investigate how the height, width and weight of the first spike of TW solutions with $\phi = \Phi_2$ and $\phi = \Phi_\infty$ change with α with a fixed c. In particular, we will derive asymptotic equations characterising the spikes and compare their solutions with the numerical simulations.

3.5.1 Numerical analysis of the first spike

Figures 3.10(a) and 3.10(c) show the first spikes of the numerical solutions for $\phi = \Phi_2$ and $\phi = \Phi_\infty$ with $D_0 = 0.25$, $c = 10^{-5}$ and $10^{-5} \leq \alpha \leq 10^{-3}$. Notice that when $c \ll \alpha$, the spikes resemble some smoothed triangles. As α decreases further, the height of the spikes increases while the base of the spikes becomes smaller. When $\alpha = c = 10^{-5}$, we see in Figures 3.10(a) and 3.10(c) that the spikes resemble skewed Gaussian functions. However, as $\alpha \ll c$, we expect the spikes to behave like Gaussian functions, as shown by the spikes in the nonlocal Fisher-KPP equation in [31].

As observed in Section 3.3, on an $O(1)$ length scale, the spikes of numerical solutions for $\phi = \Phi_2$ and $\phi = \Phi_\infty$ behave like Dirac delta functions in the limit of small α. We can see from Figures 3.10(b) and 3.10(d) that the weight (or area) of the first spike is of $O(1)$, the height of $O(\alpha^{-1/2})$ and the width (calculated at half the maximum of each spike) of $O(\alpha^{1/2})$, which agree with our observation.

To understand the structure of the spikes mathematically, we will study the

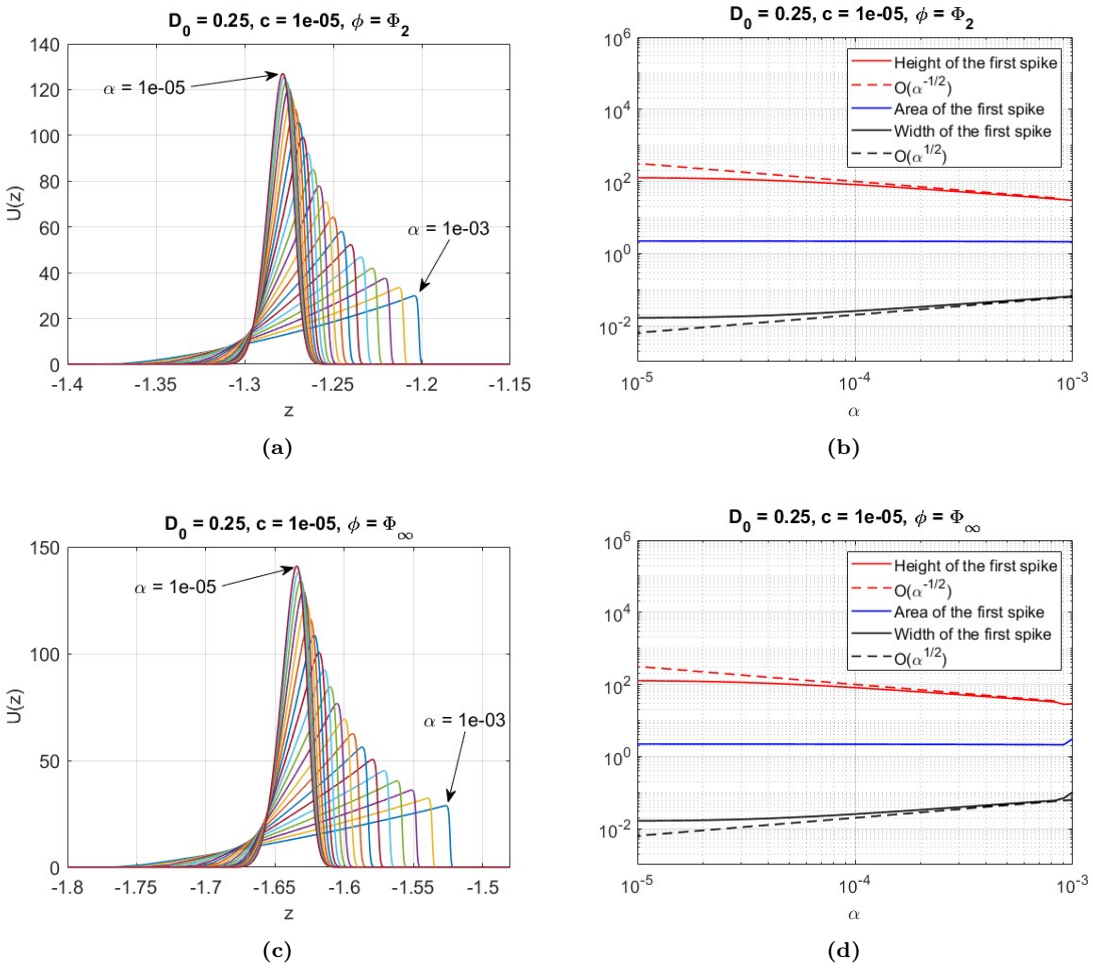


Figure 3.10: *The first spikes of the numerical solutions (obtained by solving (3.5)) for various values of α are shown in (a) for $\phi = \Phi_2$ and (c) for $\phi = \Phi_\infty$. The corresponding scalings for their height, area and width are shown in (b) and (d). Note that the width of each spike is calculated at half the maximum of the spike.*

inner structure of the spikes asymptotically in the next section. Once we have constructed the asymptotic solutions, they will be compared with the spikes in Figures 3.10(a) and 3.10(c), respectively.

3.5.2 Asymptotic analysis of the first spike

In the outer region, we deduced from Figure 3.10 that the base of spike scales with $O(\alpha^{1/2})$ while its height scales with $O(\alpha^{-1/2})$.

Suppose that the spike exists around the neighbourhood of z_0, we can write $z = z_0 + \alpha^{1/2}\overline{z}$ for inner scaling $\overline{z} = O(1)$ as $\alpha \to 0$. If we let $W(z) = \phi * U = \int_{-\infty}^{\infty} \phi(z-y)U(y)\,\mathrm{d}y$, W varies on the $O(1)$ length scale, and therefore we

can Taylor expand $W(z)$ to obtain $W(z) = W(z_0) + \alpha^{1/2}\overline{z}W'(z_0)$ in the outer region.

Asymptotic solutions when $c \ll 1$ and $\alpha \ll 1$

In the outer region, the TW equation of the nonlocal Fisher-KPP equation is

$$-cU_z = c^2 D_0 U_{zz} + U\left(1 - \alpha U - (1-\alpha)W\right), \tag{3.21}$$

where $W = \phi * U$.

In the spike region when $c \ll 1$ and $\alpha \ll 1$, we first rescale $U = \alpha^{-1/2}\overline{U}$ and $z = \alpha^{1/2}\overline{z}$. Without loss of generality, the origin is shifted such that $z_0 = 0$, and we are interested in what happens when $z \to \pm\infty$. We then substitute these into (3.21) to return

$$-\frac{c}{\alpha^{1/2}}\overline{U}_{\overline{z}} = \frac{c^2 D_0}{\alpha}\overline{U}_{\overline{z}\overline{z}} + \overline{U}\left(1 - \alpha\overline{U} - (1-\alpha)W\right). \tag{3.22}$$

To balance the outer and inner regions in (3.21) and (3.22) in the limit of $c \to 0$, we require $W = 1$ at the spike. We therefore assume that $W = 1 + \alpha^{1/2}A\overline{z}$ where $A = W'(z_0) < 0$ in the correction term.

Next, substituting $W = 1 + \alpha^{1/2}A\overline{z}$ into (3.22) further reduces it to

$$-\frac{c}{\alpha}\overline{U}_{\overline{z}} = \frac{c^2 D_0}{\alpha^{3/2}}\overline{U}_{\overline{z}\overline{z}} + \overline{U}\left(-\overline{U} - A\overline{z} + O(1)\right), \tag{3.23}$$

as $\alpha \to 0$.

Next, we study the spikes in the distinguished limit of $c = O(\alpha)$ by rescaling $c = c_0\alpha$ where $c_0 = O(1)$. At leading order (when $\alpha \to 0$), (3.23) becomes

$$-c_0\overline{U}_{\overline{z}} = \overline{U}\left(-\overline{U} - A\overline{z}\right), \qquad \text{for} \quad -\infty \le \overline{z} \le \infty, \tag{3.24}$$

such that $\overline{U} \to 0$ as $\overline{z} \to \pm\infty$ and $\int_{-\infty}^{\infty} \overline{U}(\overline{z})\,\mathrm{d}\overline{z} = w_n$ where w_n is the weight of the spike.

We are interested in the structure of the spikes in (3.24) when $c_0 = O(1)$ as $\alpha \to 0$ and when $c_0 \to 0$. To understand that, we fix $c = 10^{-5}$ and vary α in the rest of our analysis.

When $c_0 = O(1)$ as $\alpha \to 0$

By letting $\overline{U} = \mathrm{e}^{A\overline{z}^2/2c_0}\hat{U}$, we can rewrite (3.24) as $c_0\hat{U}_{\overline{z}} = \mathrm{e}^{A\overline{z}^2/2c_0}\hat{U}^2$. Upon integrating it with respect to $\overline{z}$, we obtain

$$-\frac{c_0}{\hat{U}} = \int_0^{\overline{z}} \mathrm{e}^{\frac{As^2}{2c_0}}\,\mathrm{d}s - \tilde{K}, \tag{3.25}$$

for constant $\tilde{K}$. Upon rearranging and rescaling $U = \alpha^{-1/2}\mathrm{e}^{Az^2/2\alpha c_0}\hat{U}$ and $z = \alpha^{1/2}\overline{z}$, we obtain the asymptotic solution

$$U(z) = \frac{c_0\mathrm{e}^{Az^2/2\alpha c_0}}{\sqrt{\alpha}}\left(\tilde{K} - \int_0^{z/\sqrt{\alpha}} \mathrm{e}^{\frac{As^2}{2c_0}}\,\mathrm{d}s\right)^{-1}, \qquad \text{where } -\infty \le z \le \infty, \tag{3.26}$$

with $\tilde{K}$ a constant to be determined.

When $c_0 \to 0$

When $\alpha \to 10^{-3}$, a rapid change in solution is spotted in the right end of the spikes in Figures 3.10(a) and 3.10(c), resulting in the numerical method that is used to evaluate the asymptotic solution from (3.26) failing to converge. We redefine (3.24) with $A = -B$, $\overline{z} = \sqrt{2c_0/B}\tilde{z}$, and $\overline{U} = \sqrt{2c_0B}\tilde{U}$ to obtain

$$\tilde{U}_{\tilde{z}} = 2\tilde{U}\left(\tilde{U} - \tilde{z}\right), \qquad \text{for} \quad -\infty \le \tilde{z} \le \infty, \tag{3.27}$$

such that $\tilde{U} \to 0$ as $\tilde{z} \to \pm\infty$ and $\int_{-\infty}^{\infty} \tilde{U}(\tilde{z})\,\mathrm{d}\tilde{z} = w_n/2c_0$. $\tilde{U}$ can be solved by

letting $\tilde{U} = \mathrm{e}^{-\tilde{z}^2}\hat{U}$ which becomes

$$-\frac{1}{\hat{U}} = 2\int_0^{\tilde{z}} \mathrm{e}^{-s^2}\,\mathrm{d}s + H, \tag{3.28}$$

for constant H. By using the result of $\int_0^{\infty} \mathrm{e}^{-s^2}\,\mathrm{d}s = \sqrt{\pi}/2$ and rewriting $-2M = \sqrt{\pi} + H$, (3.28) becomes

$$\tilde{U}(\tilde{z}) = \frac{1}{2}\mathrm{e}^{-\tilde{z}^2}\left(M + \int_{\tilde{z}}^{\infty} \mathrm{e}^{-s^2}\,\mathrm{d}s\right)^{-1}, \tag{3.29}$$

which can be further simplified to

$$\tilde{U}(\tilde{z}) = \frac{1}{\sqrt{\pi}}\mathrm{e}^{-\tilde{z}^2}\left[\mathrm{e}^{N} + (1 - \mathrm{erf}(\tilde{z}))\right]^{-1}, \tag{3.30}$$

where $N = \ln\left(M\sqrt{2/\pi}\right)$ is a constant.

3.5.3 Numerical method

When $c_0 = O(1)$ as $\alpha \to 0$

To compute the solution of (3.26), we must first determine the constants A and $\tilde{K}$ where $A = W'(0)$ at the left end of the spike. However, it is not so straightforward to determine $W'(0)$. Therefore, we will fit A to the numerical solution instead. To determine $\tilde{K}$, we need to solve $\int_{-\infty}^{\infty} \overline{U}(\overline{z})\,\mathrm{d}\overline{z} = w_n$. This is equivalent to $\int_{-\infty}^{\infty} \mathrm{e}^{A\overline{z}^2/2c_0}\hat{U}(\overline{z})\,\mathrm{d}\overline{z} = w_n$ which yields

$$w_n = \int_{-\infty}^{\infty} \frac{c_0 \mathrm{e}^{\frac{A\overline{z}^2}{2c_0}}}{\tilde{K} - \int_0^{\overline{z}} \mathrm{e}^{\frac{As^2}{2c_0}}\,\mathrm{d}s}\,\mathrm{d}\overline{z}. \tag{3.31}$$

Finally, we can simplify the relation above by applying the scalings of $s = \sqrt{-c_0/A}\hat{s}$ and $\overline{z} = \sqrt{-c_0/A}\hat{z}$ to simplify the exponential terms, $\tilde{K} = \sqrt{-c_0/A}\hat{K}$ to get rid of the constant terms $\sqrt{-c_0/A}$, and $\hat{s} = \sqrt{2}t$ to simplify

the integral term in the denominator to obtain

$$\frac{w_n}{c_0} = \int_{-\infty}^{\infty} \frac{\mathrm{e}^{-\hat{z}^2/2}}{\hat{K} - \sqrt{\frac{\pi}{2}}\,\mathrm{erf}\left(\frac{\hat{z}}{\sqrt{2}}\right)}\,\mathrm{d}\hat{z}. \tag{3.32}$$

We find w_n from the outer solution, and then (3.32) gives $\hat{K}$. Finally, we substitute the values of A and $\tilde{K}$ into (3.26) to plot the asymptotic solution of U for $\phi = \Phi_2$ and $\phi = \Phi_\infty$ in Figures 3.11(a) and 3.11(c).

When $c_0 \to 0$

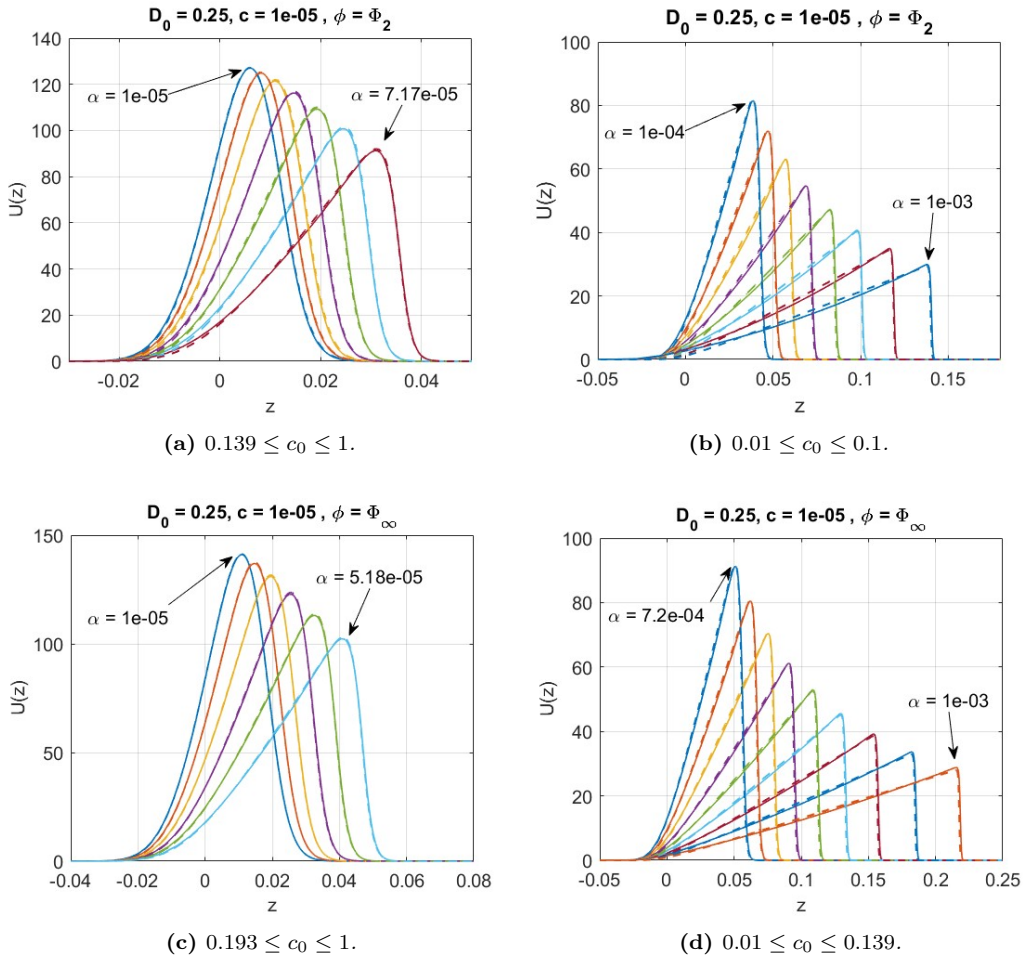
To compute the asymptotic solution $\tilde{U}$ from (3.30) when $c_0 \to 0$, we solve for N by computing $\int_{-\infty}^{\infty} \tilde{U}(\tilde{z})\,\mathrm{d}\tilde{z} = w_n/(2c_0)$ and substitute the value of N into (3.30). Finally, we plot the solutions in terms of U and z by rescaling $U = \sqrt{2c_0B/\alpha}\tilde{U}$ and $z = \sqrt{2c_0\alpha/B}\tilde{z}$ and compare them with the numerical solutions in Figures 3.11(b) and 3.11(d).

Comparison between asymptotic and numerical solutions

The asymptotic solutions are compared with the shifted numerical solutions from Figures 3.10(a) and 3.10(c) for various α values.

In Figure 3.11(a), when α increases from 10^{-5} to 7.17×10^{-5}, c_0 decreases from 1 to 0.139 for $\phi = \Phi_2$. Similarly in Figure 3.11(c), c_0 decreases from 1 to 0.193 as α increases from 10^{-5} to 5.18×10^{-5} for $\phi = \Phi_\infty$. We see that both of the asymptotic solutions for $\phi = \Phi_2$ and $\phi = \Phi_\infty$ are able to capture the behaviour of the first spikes to a good extent. Note that we fixed $A = -0.213$ for $\phi = \Phi_2$ and $A = -0.13$ for $\phi = \Phi_\infty$ for the best agreement in the solutions.

As c_0 decreases further for each kernel down to 0.01, we plot their corresponding asymptotic and numerical spikes in Figures 3.11(b) and 3.11(d). Since $A = -B$, we use the same A value for each kernel as before, which gives $B = 0.213$ for $\phi = \Phi_1$ and $B = 0.13$ for $\phi = \Phi_\infty$. Notice that there are some discrepancies



(a) $0.139 \leq c_0 \leq 1$. **(b)** $0.01 \leq c_0 \leq 0.1$.

(c) $0.193 \leq c_0 \leq 1$. **(d)** $0.01 \leq c_0 \leq 0.139$.

Figure 3.11: *The asymptotic spikes (broken lines) obtained from (3.26) and (3.30) and the numerical spikes (solid lines) obtained by solving (3.5) for (a) $\phi = \Phi_2$ at $A = -0.213$, (b) $\phi = \Phi_2$ at $B = 0.213$, (c) $\phi = \Phi_\infty$ at $A = -0.13$ and (d) $\phi = \Phi_\infty$ at $B = 0.13$.*

between the solutions regarding the slope leading to the local maxima of the spikes. Nevertheless, the asymptotic solutions from (3.30) managed to capture the sharp change in the right end of the spikes from the local maxima to $U \ll 1$ as $z \to \infty$.

3.6 Asymptotic solution when $c \ll 1$ and $\alpha = O(1)$

In this section, we construct asymptotic solutions for the modified exponential kernel $\phi = \Phi_2$ and Gaussian kernel $\phi = \Phi_\infty$ at leading order as $c \to 0$. The asymptotic analysis in this section takes α in the range of $\alpha_1 < \alpha \leq 1$ for $\alpha_1 > 0$ so there is no spike formation behind the wavefront. Then, the asymptotic solutions will be compared with numerical solutions at the same α value and

$c \ll \alpha$.

Throughout the section, we will assume D_0 as zero at leading order. To justify this, we first consider the asymptotic solution in the regions between spikes where $U \ll 1$ at $c \ll 1$. We know that $U = \mathrm{e}^L$, and since U is exponentially small in these regions, we expect L to be a large negative number. Therefore, we define $L = \tilde{L}/c$ with $\tilde{L} = O(1)$ as $c \to 0$. At leading order, equation (3.5) can be reformulated as

$$-\tilde{L}_z = D_0 \tilde{L}_z^2 + 1 - (1-\alpha) \int_{-\infty}^{\infty} \phi(z-y) \mathrm{e}^{\frac{\tilde{L}(y)}{c}} \, \mathrm{d}y. \tag{3.33}$$

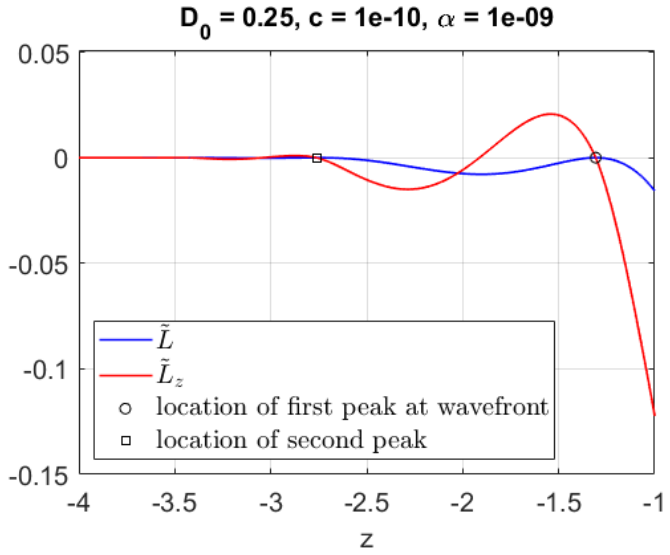


Figure 3.12: *$\tilde{L}$ and $\tilde{L}_z$ as a function of z for $\phi = \Phi_2$, with $D_0 = 1/4$, $\alpha = 10^{-9}$ and $c = 10^{-10}$.*

To study $\tilde{L}$ and $\tilde{L}_z$ in detail, we plot the numerical solution for $\phi = \Phi_2$ with $c \ll 1$ and $\alpha \ll 1$ in Figure 3.12. In agreement with our assumption, $\tilde{L} = O(1)$ as it oscillates between 0 and -0.008 in the region between the local maxima of first and second spikes when $U \ll 1$. Also, notice that $\tilde{L}_z$ is between -0.015 and 0.02 for the solution behind the wavefront, resulting in $D_0 \tilde{L}_z = 0.005$ at the maximum value of $D_0 = 1/4$. On the other hand, the absolute value of $\tilde{L}_z$ increases in the region to the right of the wavefront. Hence, we conclude that $D_0 \tilde{L}_z$ is numerically small and only plays an important role in the analysis of the solution ahead of the wavefront and that $D_0 = 0$ is sufficient to describe

solutions behind the wavefront with $0 < D_0 \leq 1/4$ and general kernel ϕ.

3.6.1 Asymptotic solution when $\phi = \Phi_2$

In this subsection, we study the asymptotic solution for $\phi = \Phi_2$ when $c \ll 1$ and $\alpha_1 < \alpha \leq 1$ such that $U = O(1)$ behind the wavefront. When $\phi = \Phi_2$, the TW equation

$$-cU_z = DU_{zz} + U\left(1 - \alpha U - (1-\alpha)\int_{-\infty}^{\infty} \phi(z-y)U(y)\,\mathrm{d}y\right),$$

becomes

$$-cU_z = D_0 c^2 U_{zz} + U(1 - \alpha U - (1-\alpha)W), \tag{3.34}$$

where $W = \phi * U = \int_{-\infty}^{\infty} \phi(z-y)U(y)\,\mathrm{d}y$.

Upon expanding the bounded function Φ_n in

$$\left(1 - \frac{1}{n}\frac{\mathrm{d}^2}{\mathrm{d}z^2}\right)^n \Phi_n = \delta(z), \tag{3.35}$$

by $n = 2$ and convolving it with U, we obtain

$$\begin{aligned}\int_{-\infty}^{\infty} \Phi_2(z-y)U(y)\,\mathrm{d}y - \int_{-\infty}^{\infty} \Phi_{2_{zz}}(z-y)U(y)\,\mathrm{d}y + \frac{1}{4}\int_{-\infty}^{\infty} \Phi_{2_{zzzz}}(z-y)U(y)\,\mathrm{d}y \\ = \int_{-\infty}^{\infty} \delta(z-y)U(y)\,\mathrm{d}y.\end{aligned} \tag{3.36}$$

By employing the translation property of the Dirac delta function and the differentiation property of the convolution term, i.e. $(f * g)' = f' * g = f * g'$, we obtain the coupled equations for the asymptotic solutions as

$$-cU_z = D_0 c^2 U_{zz} + U(1 - \alpha U - (1-\alpha)W), \tag{3.37}$$

$$0 = \frac{1}{4}W_{zzzz} - W_{zz} + W - U, \tag{3.38}$$

subject to boundary conditions (3.4) along with

$$W \to 1 \quad \text{as} \quad z \to -\infty, \qquad W \to 0 \quad \text{as} \quad z \to \infty. \tag{3.39}$$

When $D_0 = 0$ and $c \to 0$, we obtain the leading order solutions

$$U = 0, \qquad W = (A + Bz)\mathrm{e}^{-\sqrt{2}z} \quad \text{for} \quad z > 0, \tag{3.40}$$

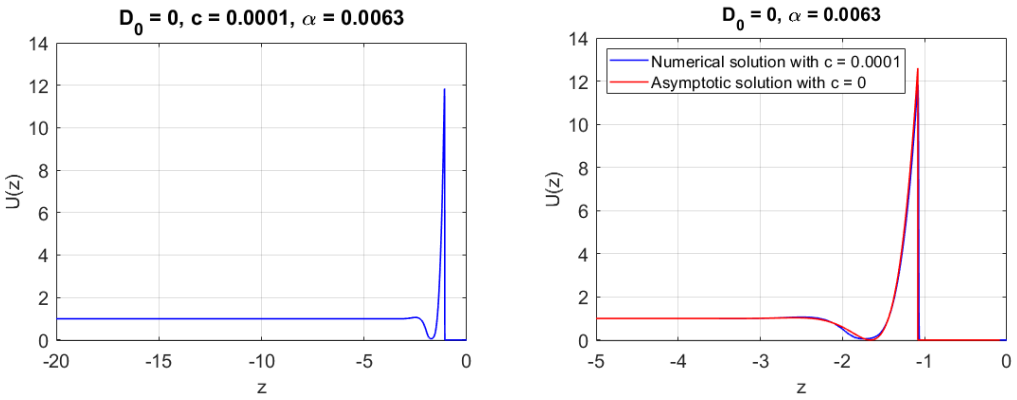
and

$$U = 1 + \left(C\cos\left(z\sqrt{\sqrt{\frac{1}{\alpha}} - 1} \right) + D\sin\left(z\sqrt{\sqrt{\frac{1}{\alpha}} - 1} \right) \right) \mathrm{e}^{\left(\sqrt{1+\sqrt{\frac{1}{\alpha}}}\right)z}, \tag{3.41}$$

$$W = \frac{1 - \alpha U_2}{1 - \alpha} \quad \text{for} \quad z < 0, \tag{3.42}$$

where A, B, C and D are four unknown constants. Since both of the W in (3.40) and (3.42) are three times differentiable at $z = 0$, the four unknowns can be solved by equating the derivatives of both W at $z = 0$. Once we evaluate the constants C and D, we can compare the asymptotic solution (3.41) with its numerical solution in a finite domain of $z \in [L_1, 0)$ for $L_1 < 0$.

Comparison between asymptotic and numerical solutions when $\phi = \Phi_2$



(a) **(b)**

Figure 3.13: *(a) is the numerical solution, obtained by solving (3.5), for kernel $\phi = \Phi_2$, $D_0 = 0$ and $\alpha = 0.0063$. (b) is the magnified image of the first maximum of the wavefront of both numerical and asymptotic solutions (from (3.41)).*

For $\phi = \Phi_2$, $U = O(1)$ for both numerical and asymptotic solutions when $0.006295 < \alpha \leq 1$. Therefore, $\alpha_1 = 0.006295$ and we choose $\alpha = 0.0063$ so that U remains positive and does not cross the $z-$axis behind the wavefront. For comparison, the numerical solution requires $c \ll 1$ since $c \to 0$ and $\alpha = O(1)$ in asymptotic solution. Therefore, we choose $D_0 = 0$, $\alpha = 0.0063$ and $c = 0.0001$ for numerical solution shown in Figure 3.13(a). The numerical solution U is large at the wavefront and rapidly decreases while remaining positive as z decreases. As z decreases further, it converges to $U = 1$, which satisfies the boundary condition (3.4).

The asymptotic solution is represented by a red line in Figure 3.13(b) with $c = 0$ at the leading order. Even though it was computed within the domain of $[L_1, 0)$, the maximum of the wavefront at $z = 0$ is shifted to the left to match with the numerical solution for comparison. The asymptotic solution shows good agreement with the numerical solution at the wavefront, as both wavefronts are asymmetric. However, the height of the wavefront in the asymptotic solution is larger than that of the numerical solution due to a smaller value of c. This strongly supports the assertion in Subsection 3.3.1 that the height of the spike of solution scales with $c^{-\frac{1}{2}}$. As z decreases, both numerical and asymptotic solutions converge to $U = 1$ at around $z = -3.6$, suggesting that the asymptotic solution agrees with the numerical solution for the Φ_2 kernel for α of $O(1)$.

For $\alpha_2 < \alpha \leq 0.006295$, the structure must be modified to contain two additional regions, i.e. $U \ll 1$ in $(z_2, z_1]$ and $U = O(1)$ in $(-\infty, z_2]$. To study the asymptotic solution for $\alpha_2 < \alpha \leq 0.006295$, we have to match the solutions W in four different regions, i.e., $(-\infty, z_2]$, $(z_2, z_1]$, $(z_1, 0)$ and $z > 0$ at three continuity points, i.e. $z = 0, z_1$ and z_2, which is equivalent to a system of 14 equations and 14 unknowns. In the interest of brevity, we will not study this asymptotic solution in our thesis. In the following subsection, we will look at the asymptotic solution for $\phi = \Phi_\infty$ and compare it with its corresponding numerical solution.

3.6.2 Asymptotic solution when $\phi = \Phi_\infty$

To study the asymptotic solution for $\phi = \Phi_\infty$ when $U = O(1)$ behind the wavefront, we use two different expressions for W defined earlier in Subsection 3.6.1. Recall that

$$W = \frac{1 - \alpha U}{1 - \alpha} \quad \text{for} \quad z < 0, \tag{3.43}$$

and

$$W = \int_{-\infty}^{\infty} \phi(z - y) U(y)\, \mathrm{d}y \quad \text{for all } z. \tag{3.44}$$

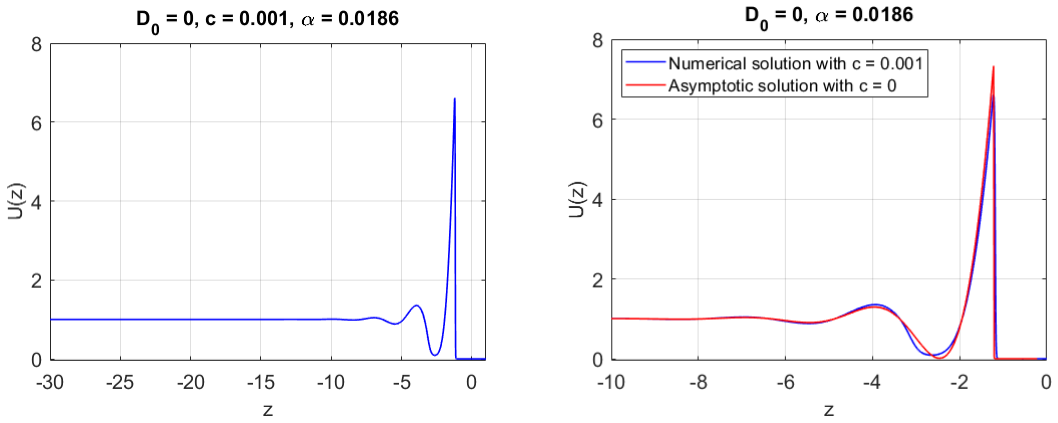
The equation for U in $z < 0$ can be obtained by equating (3.43) and (3.44) to give

$$\frac{1 - \alpha U(z)}{1 - \alpha} = \int_{-\infty}^{0} \phi(z - y) U(y)\, \mathrm{d}y \qquad \text{for} \quad z < 0. \tag{3.45}$$

It is straightforward to numerically solve for U in (3.45) as it is linear and $\phi = \Phi_\infty$ is a smooth kernel. We first truncate z to a finite domain, $[L_1, 0)$ for $L_1 < 0$ with uniform grid spacing. Then, we collocate z at the midpoint of each interval between the grid points before discretising the integral term using the midpoint rule. Finally, we solve the resulting linear system using *linsolve* in MATLAB to return U. Since U is evaluated at the midpoint of elements of the domain, we extrapolate to obtain the value of U at the wavefront and treat it as the local maximum, as shown in Figure 3.14(b).

Comparison between asymptotic and numerical solutions when $\phi = \Phi_\infty$

For both numerical and asymptotic solutions for $\phi = \Phi_\infty$, $0.0183 < \alpha \leq 1$ generates a solution that is positive everywhere behind the wavefront. Therefore, we choose $\alpha = 0.0186$ to proceed with the asymptotic analysis. For the numerical solution with $\phi = \Phi_\infty$, c is chosen to be 0.001 as we cannot access smaller values of c numerically for $\alpha = 0.0186$. The numerical solution in Figure 3.14(a) consists of a large value at the wavefront, followed by further oscillations around $U = 1$ as z decreases and finally converges to $U = 1$ when



(a) (b)

Figure 3.14: *(a) is the numerical solution, obtained by solving (3.5), for kernel* $\phi = \Phi_\infty$, $D_0 = 0$ *and* $\alpha = 0.0186$. *(b) is the magnified image of the first maximum of the wavefront of both numerical and asymptotic solutions (from solving (3.45)).*

$z < -15$.

Note that both numerical and asymptotic solutions have asymmetric wavefronts, as shown in Figure 3.14. The maximum value of U from the numerical solution is around 6.6, while the asymptotic solution gives a slightly higher maximum value of 7.3 due to the smaller c value. Despite having different maximum values at the wavefront, both solutions continue to oscillate around $U = 1$ behind the wavefront at a similar frequency and amplitude. This suggests that the asymptotic solution matches the numerical solution for $\alpha = 0.0186$ for this particular kernel. For $\alpha \leq 0.0183$, the asymptotic solution U forms regions where $U \ll 1$ and therefore, U in (3.45) must be modified to incorporate such regions.

3.6.3 Asymptotic solution when $\phi = \Phi_\infty$, $\alpha \ll 1$ and $c \ll \alpha$

The numerical solution with $\phi = \Phi_\infty$ suggests that there exists a finite number of spikes followed by an infinite number of oscillations behind the wavefront when $c \ll 1$, $\alpha \ll 1$ and $c \ll \alpha$. To analyse the asymptotic solution with more spikes, we extend our asymptotic analysis to consider smaller α values with $c \ll \alpha$ for $\phi = \Phi_\infty$ in particular. In Section 3.6, we take α from the interval $(\alpha_1, 1]$. In this section, we require α to be sufficiently small, i.e. $\alpha_{i+1} < \alpha \leq \alpha_i$

such that the solution consists of i regions where $U \ll 1$, in the intervals $\bigcup_{j=1}^{i}(z_{2j}, z_{2j-1}]$, for $i \in \mathbb{Z}_+$ and $z_{2j} < z_{2j-1} < \ldots < z_2 < z_1$.

Recall that in Section 3.6, we defined $L = \tilde{L}/c$ with $\tilde{L} = O(1)$ as $c \to 0$ in the regions between spikes where $U \ll 1$. Since U is exponentially small between spikes, we can write $U = 0$ in these regions. At leading order where $c \to 0$, the TW equation (3.33) can be rewritten as

$$D_0 \tilde{L}_z^2 + \tilde{L}_z + 1 - (1-\alpha)\phi * U = 0. \tag{3.46}$$

In the regions where U is of order $O(1)$, we have $L = \log U$ and hence L is of order $O(1)$. By defining $\tilde{L} = cL$, we get $\tilde{L} = O(c)$ or, equivalently, $\tilde{L} \ll 1$ as $c \to 0$. At leading order, we have from (3.5) that

$$\tilde{L} = 0 \quad \text{and} \quad 1 - \alpha U - (1-\alpha)\phi * U = 0. \tag{3.47}$$

By letting $D_0 = 0$, $\tilde{L}_z$ from (3.46) can be written as

$$\begin{aligned} \tilde{L}_z &= -1 + \alpha U + (1-\alpha)\phi * U \\ &= -1 + \alpha U + (1-\alpha)\int_{-\infty}^{0} \phi(z-y)U(y)\,\mathrm{d}y, \end{aligned} \tag{3.48}$$

subject to the boundary conditions $U \to 0$ as $z \to \infty$ and $U \to 1$ as $z \to -\infty$. Once we work out $\tilde{L}_z = 0$, we can then solve for U in the regions where $U = O(1)$ in (3.47).

Numerical method

To work out the solution U numerically, we first truncate $\tilde{L}_z$ into a finite domain and collocate z at the midpoint of each interval between the grid points. Using the midpoint rule, we then discretise the $(1-\alpha)\int_{-\infty}^{0}\phi(z-y)U(y)\,\mathrm{d}y$ from (3.48) into a matrix-vector multiplication. Therefore, $\tilde{L}_z$ in (3.48) can be discretised into $\widetilde{\mathbf{L}}_z = A\mathbf{U} - b$, for matrix A and vector b.

We first let α in the asymptotic solution decrease from $\alpha = 1$ until $U \ll 1$ in $z \in (z_2, z_1]$ behind the wavefront. Then, we construct a vector z in a finite domain, $[L_1, 0)$ which consists of z_1 and z_2, i.e. $L_1 < z_2 < z_1 < 0$. Next, we solve for $\widetilde{\mathbf{L}} = 0$, i.e. $A\mathbf{U} = b$ in $[z_1, 0)$ and $[L_1, z_2]$ where $U = O(1)$ while assuming U in $(z_2, z_1]$ is zero. Then, we proceed by computing $\widetilde{\mathbf{L}}_z = A\mathbf{U} - b$ using the final $\mathbf{U}$ for the whole domain, and compute $\tilde{L}$ by finite difference. Finally, we force U and $\tilde{L}$ at the left edge of the spike, i.e. z_1 to be zero and use $fsolve$ to solve for z values of the next interval, i.e. $(z_4, z_3]$ where $U \ll 1$. The new interval will then be incorporated in the next z vector to solve for successive regions where $U \ll 1$ while α decreases. A regridding method is applied in this problem to ensure that the grid spacing of each spike is finer than those in the regions where $U \ll 1$.

Comparison between asymptotic and numerical solutions when $\phi = \Phi_\infty$

Using the numerical method described above, we can decrease the value of α to $\alpha = 1.102 \times 10^{-9}$ to obtain the asymptotic solution shown in Figure 3.15. For comparison, the corresponding numerical solution is plotted on the same figure with $c = 0.1\alpha$.

It is noticeable from Figure 3.15(a) that the maximum values of U in the asymptotic solution are larger than those of the numerical solution due to the smaller value of c in the asymptotic solution, which is zero. This is in accordance with the finding earlier that the heights of the spikes scale with $c^{-\frac{1}{2}}$ as $c \to 0$. By taking a closer look at the solutions in Figure 3.15(b), it appears that there are 21 regions where $U \ll 1$, with the first region $(z_2, z_1]$ located around $(-2.92, -3 \times 10^{-4}]$. It is also found in Figure 3.15(c) that the final few spikes of the asymptotic solution have a good agreement with the numerical solution in terms of width and the location of the spikes. However, as $z \to -\infty$, the differences between the width of both oscillating solutions start to increase.

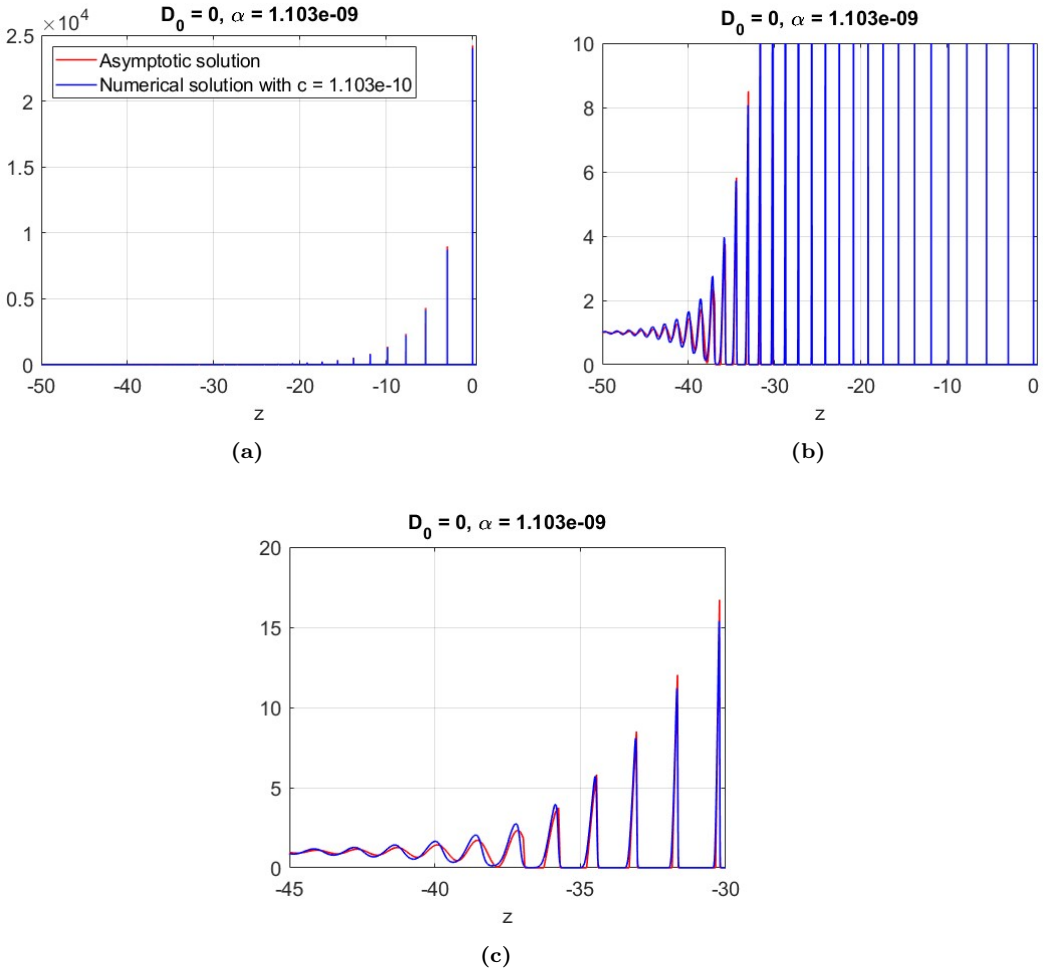


Figure 3.15: *Numerical and asymptotic solutions, obtained by solving (3.5) and (3.48), for $\phi = \Phi_\infty$ with $\alpha = 10^{-5}$ and $D_0 = 0$. The solutions in (a) are magnified in (b) and (c).*

By integrating U between successive minima of each spike, we obtain the weights, w_m, with respect to its spike number m. Although the maximum values of the first few spikes are larger in the asymptotic solution, Figure 3.16(a) shows that both asymptotic and numerical solutions have almost identical weights in the first 19 spikes. However, as the number of spikes increases in the decreasing direction of z, the weights of the numerical solution become smaller than the asymptotic solution. As for the distance between the local maxima of spikes, Figure 3.16(b) shows that the first 19 separations of spikes in the asymptotic solution are almost identical to that of the numerical solution, with a slight deviation at the 20th separation.

In short, the asymptotic solution captures the behaviour of the numerical solution of the full TW problem up to a finite number of spikes behind the

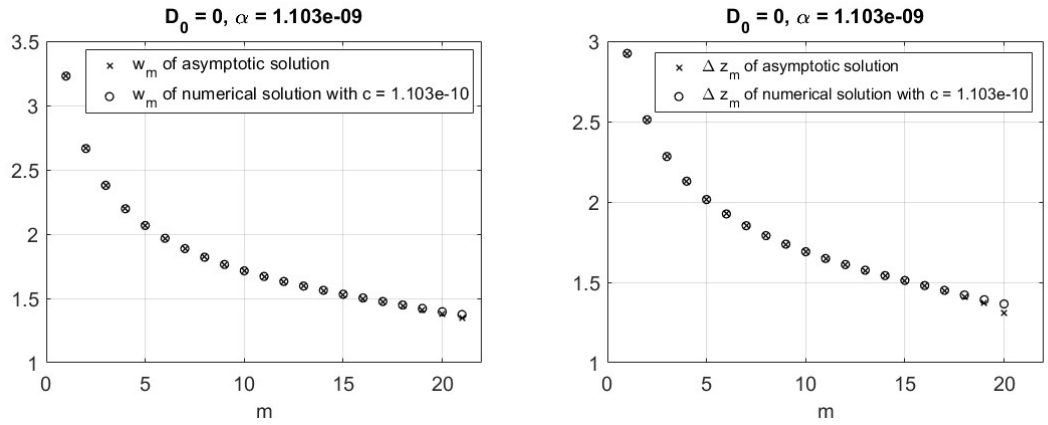


Figure 3.16: *Weight and separation of the spikes of numerical and asymptotic solutions (obtained by solving (3.5) and (3.48)) for $\phi = \Phi_\infty$ as a function of spike number m.*

wavefront.

3.7 Conclusion

We have shown that in the limit of small diffusivity (or small c), the TW solutions of the local-nonlocal Fisher-KPP equation (3.1) have fewer spikes behind the wavefront compared to the nonlocal Fisher-KPP (1.7) due to the presence of α in (3.1). Besides, the spikes of the TW solutions of our model resemble a smoothed triangle compared to the Gaussian structure in the nonlocal Fisher-KPP where $\alpha = 0$, as shown in [31]. By linearising the TW equation (3.3) around $U = 1$ as $z \to -\infty$, we have deduced the relationship between decay rate and frequency of oscillations and α. These agree well with numerical solutions in the far field.

We have analysed the numerical solutions of the first spikes for both $\phi = \Phi_2$ and $\phi = \Phi_\infty$ and have shown that the spikes have weights of $O(1)$ in the outer region. In particular, the height of the spikes scales with $O(\alpha^{-1/2})$ and the width of the spikes scales with $O(\alpha^{1/2})$ for $c \ll \alpha \ll 1$. We have studied the inner region of the spikes and have constructed the asymptotic solutions by fixing c and varying α. It is shown that $c = O(\alpha)$ is the distinguished limit where the shape of the spikes changes from a smoothed triangle to a Gaussian

function. With appropriate scalings, the shape of the numerical spikes can be predicted by asymptotic solutions to a good agreement.

Moreover, we have studied the asymptotic solutions for $\alpha = O(1)$ for $\phi = \Phi_2$ and $\phi = \Phi_\infty$. In general, the number of spikes increases as $\alpha \to 0$ and $c \to 0$. We have shown that they behave as expected compared to numerical solutions. Since the heights of the spikes of TW solutions scale with $c^{-1/2}$, we have seen that the asymptotic solutions with smaller c generally give a larger local maximum of spikes compared to the numerical solutions. Despite the differences in heights, the weights of the spikes tend to a constant as the spikes behave like Dirac delta functions in the limit of $\alpha \to 0$ and $c \to 0$.

In conclusion, our observations of the TW solutions behaviour agree with nonlocal Fisher-KPP [31] in the limit of $\alpha \to 0$ and $c \to 0$, except that our spikes transition from Gaussian functions to smoothed triangles as α gradually increases from zero to one as $c \to 0$.

Chapter 4

Linear Stability Analysis of a Nonlocal Lotka-Volterra (NLLV) System

4.1 Introduction

In Chapter 3, we studied the asymptotic and numerical behaviour of the TW solutions of a local-nonlocal Fisher-KPP equation (3.1). One of the key points that we deduced from the study is that for $D \ll 1$ (or $c \ll 1$) and $\alpha \ll 1$, the nonlocal intraspecific interaction leads to the formation of spikes and oscillations in the TW. In particular, we focused on the modified exponential kernel $\phi = \Phi_2$ and Gaussian kernel $\phi = \Phi_\infty$ and showed that the latter generates more distinct spikes and oscillations at the same c and α due to its smoothness at $x = 0$.

The natural next step is to extend our analysis to a system of two coupled nonlocal reaction-diffusion equations and investigate the interesting patterning properties that the system supports. In this chapter, we examine the stability of the coexisting state of a particular system of nonlocal reaction-diffusion equations. We begin by setting up the problem in Sections 4.2 and 4.3. We

then study the linear stability of the coexisting state in Section 4.4, which serves as the starting point of the analysis of this chapter. In Section 4.5, we investigate the numerical solutions of the system and their growth rates, σ, obtained in the linear stability analysis. Then, we perform an asymptotic analysis of the dispersion relation and the neutral curve for different kernels in Sections 4.6 and 4.7. Neutral curves are constructed when the two kernels in the system are identical, as well as when they are different. Appropriate comparisons between the asymptotic and numerical neutral curves are also presented. We then discuss the differences among the numerical neutral curves for each combination of kernels. For each of the cases, numerical simulations are shown in an attempt to study the stability and behaviour of the coexisting state of the initial value problem. Finally, we conclude in Section 4.8 that the coexisting state can lose its stability once nonlocality is introduced into the local system and that the higher the smoothness of the kernel function at $x = 0$, the larger the instability region in parameter space.

4.2 Problem statement

In this chapter, we focus on a system of two nonlocal Fisher-KPP equations with local coupling

$$\begin{aligned} \frac{\partial u}{\partial t} &= d_1 \frac{\partial^2 u}{\partial x^2} + r_1 u \left(1 - \frac{\phi_1 * u}{K_1} - \frac{\rho_1 v}{K_1}\right), \\ \frac{\partial v}{\partial t} &= d_2 \frac{\partial^2 v}{\partial x^2} + r_2 v \left(1 - \frac{\phi_2 * v}{K_2} - \frac{\rho_2 u}{K_2}\right). \end{aligned} \tag{4.1}$$

For $n = 1, 2$,

$$[\phi_n * v](x,t) = \int_{-\infty}^{\infty} \phi_n \left(\frac{x-y}{l_n}\right) v(y,t)\, \mathrm{d}y,$$

where l_n is the length scale of the kernel ϕ_n, d_n are the diffusion coefficients, r_n are the net birth rates, K_n are the carrying capacities and ρ_n measure the strength of the interspecific competition, all of which are assumed to be nonnegative. Again, the same kernel assumptions from Section 2.1 apply to

the kernels, ϕ_n, in (4.1).

The presence of two kernels in the system above allows us to study different combinations of kernels that might lead to interesting nonlinear behaviour in the system. In Sections 4.6 and 4.7 later, we will conduct both asymptotic and numerical analysis for the cases when $\phi_1 = \phi_2$ and $\phi_1 \neq \phi_2$.

4.3 Nondimensionalisation

Before analysing the system (4.1), it is helpful to rewrite it in nondimensional terms to reduce the number of parameters in the system. By adopting the scaling

$$\overline{u} = \frac{ul_1}{K_1}, \quad \overline{v} = \frac{vl_2}{K_2}, \quad \overline{t} = r_1 t, \quad \overline{x} = \frac{x}{l_1}, \quad \lambda = \frac{l_2}{l_1}, \tag{4.2}$$

$$R = \frac{r_2}{r_1}, \quad \alpha = \frac{K_2\rho_1}{K_1 l_2}, \quad \beta = \frac{K_1\rho_2}{K_2 l_1}, \quad D_1 = \frac{d_1}{r_1 l_1^2}, \quad D_2 = \frac{d_2}{r_1 l_1^2}, \tag{4.3}$$

and replacing $\overline{u}, \overline{v}, \overline{t}, \overline{x}$ by u, v, t, x, system (4.1) is transformed into the dimensionless form of nonlocal Lotka-Volterra (NLLV) system

$$\begin{aligned} \frac{\partial u}{\partial t} &= D_1 \frac{\partial^2 u}{\partial x^2} + u\left(1 - \int_{-\infty}^{\infty} \phi_1(x-y)u(y)\,\mathrm{d}y - \alpha v\right), \\ \frac{\partial v}{\partial t} &= D_2 \frac{\partial^2 v}{\partial x^2} + Rv\left(1 - \frac{1}{\lambda}\int_{-\infty}^{\infty} \phi_2\left(\frac{x-y}{\lambda}\right) v(y)\,\mathrm{d}y - \beta u\right), \end{aligned} \tag{4.4}$$

with D_1, D_2, R, α and β defined as above.

Note that when $\alpha = \beta = 0$, (4.4) becomes two uncoupled nonlocal Fisher-KPP equations. On the other hand, when $\phi_1(x) = \phi_2(x) = \delta(x)$, the fact that we have used the length scale of ϕ_1 to nondimensionalise the problem notwithstanding, we recover the local diffusive Lotka-Volterra system [43, 51].

4.4 Linear stability analysis

To derive the steady states of the dimensionless system (4.4), we study the spatially uniform or homogeneous, local Lotka-Volterra problem

$$\begin{aligned} \frac{\mathrm{d}u}{\mathrm{d}t} &= u\left(1-u-\alpha v\right), \\ \frac{\mathrm{d}v}{\mathrm{d}t} &= Rv\left(1-v-\beta u\right). \end{aligned} \tag{4.5}$$

Here, the steady states, (u^*, v^*), of (4.5) are the solutions of $\mathrm{d}u/\mathrm{d}t = \mathrm{d}v/\mathrm{d}t = 0$. The four steady states are $(0,0), (1,0), (0,1)$ and $\left(\frac{1-\alpha}{1-\alpha\beta}, \frac{1-\beta}{1-\alpha\beta}\right)$. For simplicity, we denote the coexisting steady state $\left(\frac{1-\alpha}{1-\alpha\beta}, \frac{1-\beta}{1-\alpha\beta}\right)$ as (u_e, v_e) throughout the rest of the thesis. In the local system, the stability of the steady states has been well studied for four cases, as shown below, with $(0,0)$ being an unstable node in all cases.

Stability of u and v in the local diffusive Lotka-Volterra system

Case (i): When $\alpha < 1$ and $\beta < 1$

Steady states $(0,1)$ and $(1,0)$ are both saddle points whereas the coexisting steady state, (u_e, v_e) is a stable node. As $t \to \infty$, both u and v coexist at a lower population than their respective carrying capacities, which is one in the dimensionless case.

Case (ii): When $\alpha > 1$ and $\beta > 1$

Both $(0,1)$ and $(1,0)$ are stable nodes whereas (u_e, v_e) is an unstable node. Depending on the initial population of each species, the species that prevails will reach its carrying capacity at one, while the other species will be driven to extinction.

Case (iii): When $\alpha < 1$ and $\beta > 1$

There is a saddle point at $(0,1)$ and a stable node at $(1,0)$. Interspecific

competition of u dominates regardless of the initial population of both species, driving v to extinction.

Case (iv): When $\alpha > 1$ and $\beta < 1$

As opposed to case (iii), There is a saddle point at $(1, 0)$ and a stable node at $(0, 1)$. Regardless of the initial population of both species, v prevails and drives u to extinction.

In this chapter, we are interested in the stability of the coexisting state and its dependence on the parameters, $\alpha, \beta, R, \lambda, D_1, D_2$ and different kernels. According to Turing's theory [107], if we have a linearly stable spatially uniform steady state, the uniform steady state becomes unstable in the presence of spatially varying perturbation, leading to pattern formation (see the literature review in Subsection 1.3.4). Therefore, we restrict our attention to the case when $\alpha < 1$ and $\beta < 1$, i.e. when the intraspecific effects are greater than the interspecific effects for both species, as the coexisting state is stable in the local system in this case.

To begin with, we first let $u = u_e + \overline{u}$ and $v = v_e + \overline{v}$ for $\overline{u}$ and $\overline{v}$ small. On substituting these into (4.4), the system is linearised to

$$\begin{aligned} \frac{\partial \overline{u}}{\partial t} &= D_1 \frac{\partial^2 \overline{u}}{\partial x^2} - u_e \left(\int_{-\infty}^{\infty} \phi_1(x-y)\overline{u}(y)\,\mathrm{d}y + \alpha \overline{v} \right), \\ \frac{\partial \overline{v}}{\partial t} &= D_2 \frac{\partial^2 \overline{v}}{\partial x^2} - R v_e \left(\frac{1}{\lambda} \int_{-\infty}^{\infty} \phi_2 \left(\frac{x-y}{\lambda} \right) \overline{v}(y)\,\mathrm{d}y + \beta \overline{u} \right). \end{aligned} \tag{4.6}$$

Next, we consider perturbations of the form $\overline{u} = \hat{u}\mathrm{e}^{\sigma t + ikx}$ and $\overline{v} = \hat{v}\mathrm{e}^{\sigma t + ikx}$ where $\sigma \in \mathbb{C}$ and $k \in \mathbb{R}$. We find that

$$\begin{aligned} \sigma \hat{u} &= \left(-D_1 k^2 - u_e \overline{\phi}_1(k) \right) \hat{u} - \alpha u_e \hat{v}, \\ \sigma \hat{v} &= \left(-D_2 k^2 - R v_e \overline{\phi}_2(\lambda k) \right) \hat{v} - R\beta v_e \hat{u}, \end{aligned} \tag{4.7}$$

where $\overline{\phi}(k) = F[\phi(y)](k)$. Note that the Fourier transform of ϕ is defined as

$$\overline{\phi}(k) = \int_{-\infty}^{\infty} \phi(y) \mathrm{e}^{-iky} \, \mathrm{d}y.$$

Non-trivial solutions of (4.7) for $(\hat{u}, \hat{v})$ require that $\sigma = \sigma(k)$, where

$$\begin{aligned} \sigma^2 + \Big[(D_1 + D_2)k^2 + u_e\overline{\phi}_1(k) + Rv_e\overline{\phi}_2(\lambda k)\Big]\sigma \\ + \left(D_1k^2 + u_e\overline{\phi}_1(k)\right)\left(D_2k^2 + Rv_e\overline{\phi}_2(\lambda k)\right) - R\alpha\beta u_e v_e = 0, \end{aligned} \tag{4.8}$$

which gives an implicit dispersion relation between σ and k.

By writing $B = (D_1 + D_2)k^2 + u_e\overline{\phi}_1(k) + Rv_e\overline{\phi}_2(\lambda k)$, the larger of the two solutions of (4.8) is, therefore

$$2\sigma = -B + \left\{B^2 - 4\Big[\left(D_1k^2 + u_e\overline{\phi}_1(k)\right)\left(D_2k^2 + Rv_e\overline{\phi}_2(\lambda k)\right) - R\alpha\beta u_e v_e\Big]\right\}^{\frac{1}{2}}. \tag{4.9}$$

In fact, σ is real for all D_1, D_2, R and λ as the square root term in (4.9) can be simplified to

$$\left\{\left(D_1 - D_2\right)k^2 + u_e\overline{\phi}_1(k) - Rv_e\overline{\phi}_2(\lambda k)\right\}^2 + 4R\alpha\beta u_e v_e, \tag{4.10}$$

where both of the terms are positive. To find the stationary points of σ, we take the derivative of the quadratic function (4.8) with respect to k to get

$$\begin{aligned} 0 = &\frac{\mathrm{d}\sigma}{\mathrm{d}k}\left\{2\sigma + \Big[(D_1 + D_2)k^2 + u_e\overline{\phi}_1(k) + Rv_e\overline{\phi}_2(\lambda k)\Big]\right\} \\ &+ \Big[2(D_1 + D_2)k + u_e\overline{\phi}_1'(k) + R\lambda v_e\overline{\phi}_2'(\lambda k)\Big]\sigma \\ &+ \left(D_1k^2 + u_e\overline{\phi}_1(k)\right)\left(2D_2k + Rv_e\lambda\overline{\phi}_2'(\lambda k)\right) \\ &+ \left(2D_1k + u_e\overline{\phi}_1'(k)\right)\left(D_2k^2 + Rv_e\overline{\phi}_2(\lambda k)\right), \end{aligned} \tag{4.11}$$

and let $\mathrm{d}\sigma/\mathrm{d}k = 0$ in (4.11). We will later see that it is useful to know where $\sigma(k) = 0$ when $d\sigma/dk = 0$ in order to locate the critical wavenumber, $k = k_c$, at which the bifurcation occurs in the coexisting state.

4.5 Numerical solution

It is helpful to plot some numerical solutions of the IVP (4.4) with some initial conditions to investigate the solutions' behaviour. First, we discretise the diffusion terms into uniform grid spacing using central finite differences (see Subsection 2.4.1) and apply periodic boundary conditions at $x = \pm L$. This is due to the periodic input in the convolution theorem that we will employ to discretise the convolution terms. To compute the convolution $\phi * u$, we use the *fft* and *ifft* functions in MATLAB as described in Subsection 2.4.3. Finally, the time-dependent nonlinear system is solved numerically using the *ode45* solver in MATLAB.

Later in Section 4.7, the solutions to the IVP will be plotted to examine the stability of the coexisting state for different kernel combinations in more detail.

4.5.1 Growth rate of numerical solution

In the linear stability analysis in Section 4.4, we let $u = u_e + \hat{u}\mathrm{e}^{\sigma t+ikx}$ and $v = v_e + \hat{v}\mathrm{e}^{\sigma t+ikx}$. To verify the growth rates of the amplitudes, we plot $\log(u - u_e)$ (similarly for v) and compare it with the analytical amplitude, $\log(\hat{u}\mathrm{e}^{\sigma t})$, as well as the growth rates, σt, we obtained numerically.

First, we choose $D = 0.025, \alpha = 0.6, \beta = 0.5, R = \lambda = 1$ and solve (4.9) for $k = k_{max}$, the most unstable wavenumber when $\sigma(k)$ in (4.9) is maximum. Then, we introduce a small perturbation, $0.1\cos(k_{max}x)$, to the coexisting state of the system at $t = 0$. Then, we substitute all the parameters into (4.8), which gives $\sigma = -0.57879$ and 0.12165, respectively. The domain length is chosen to be $x \in [-\pi/k_{max}, \pi/k_{max}]$ which is exactly one period. The numerical solutions

of the IVP (4.4) are plotted in Figure 4.1 for $t = 1, 3, 8$ and 20. As $t \to \infty$, we expect that the logarithm of both $u - u_e$ and $v - v_e$ scale with the larger value of σ which is 0.12165, as shown in Figure 4.2. The accuracy of the amplitudes is confirmed by the agreement between the amplitudes and their corresponding analytical solutions by solving the linearised system in (4.6).

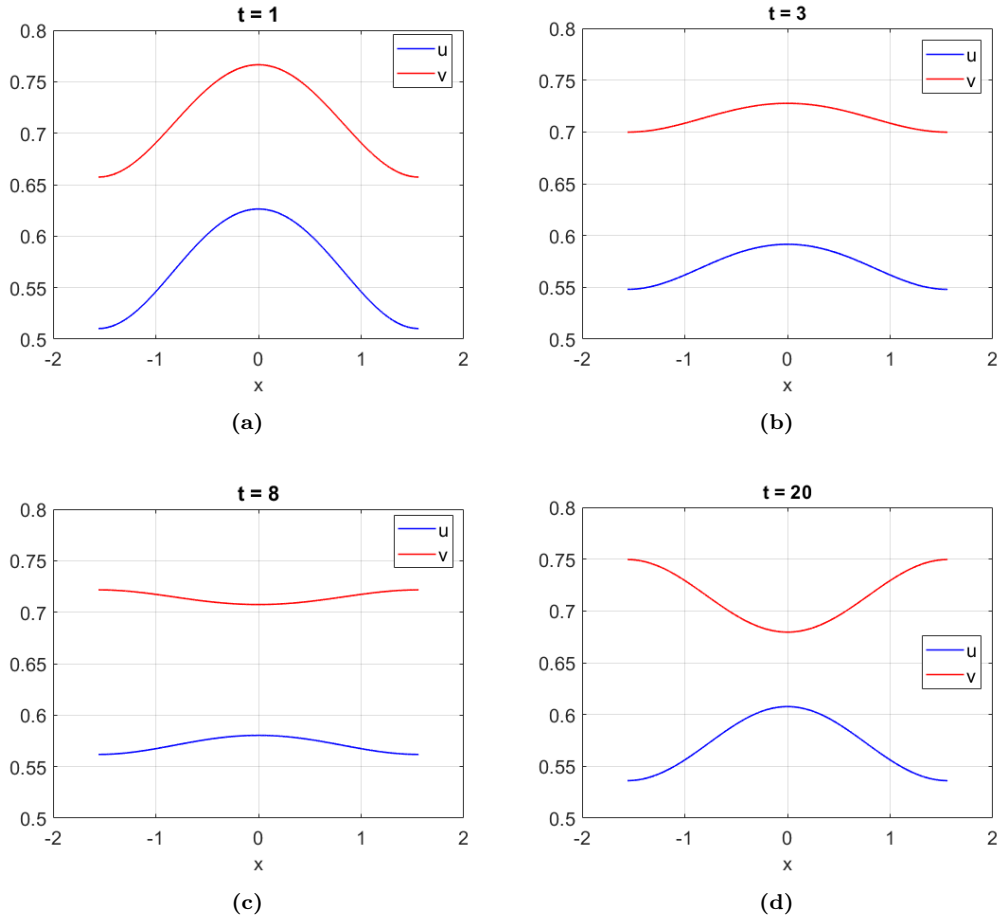
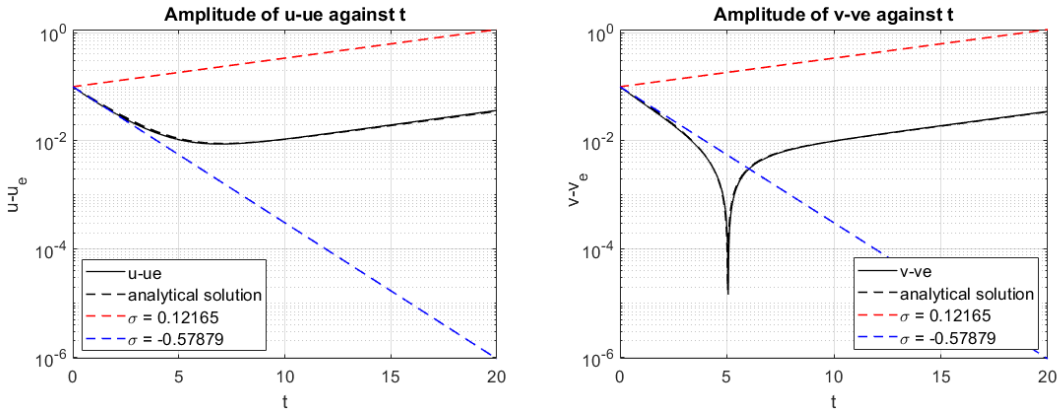


Figure 4.1: *The numerical solutions of the IVP (4.4) with* $D = 0.025, \alpha = 0.6, \beta = 0.5$ *and* $R = \lambda = 1$ *at different* t *values.*



(a) (b)

Figure 4.2: *The growth rates of the amplitude of the numerical solutions of (4.4) for kernel* $\phi = \Phi_1$ *when* $D = 0.025, \alpha = 0.6, \beta = 0.5$ *and* $R = \lambda = 1$ *against* t *at* $x = 0$. *(a) The log of the amplitude of* $u - u_e$ *and (b) The log of the amplitude of* $v - v_e$.

4.6 Asymptotic analysis when $\alpha = \beta$

Next, we analyse the dispersion relation (4.8) asymptotically by first considering the simplest case. Suppose $D_1 = D_2 = D$, $R = \lambda = 1$, $\alpha = \beta$ and $\phi_1 = \phi_2 = \phi$, the relation can be simplified as

$$\sigma^2 + \left[2Dk^2 + 2\left(\frac{1-\alpha}{1-\alpha^2}\right)\overline{\phi}(k)\right]\sigma + \left[Dk^2 + \left(\frac{1-\alpha}{1-\alpha^2}\right)\overline{\phi}(k)\right]^2 - \frac{\alpha^2(1-\alpha)^2}{(1-\alpha^2)^2} = 0. \tag{4.12}$$

Then, σ can be solved using the quadratic formula to obtain the larger value of σ, i.e. $\sigma = -Dk^2 + (\alpha - \overline{\phi}(k))/(1+\alpha)$. As $D \to 0$, we have

$$\begin{aligned} \sigma &\to \frac{\alpha - (1+k^2)^{-1}}{1+\alpha} \quad \text{for} \quad \phi = \Phi_1, \\ \sigma &\to \frac{\alpha - (1+k^2/2)^{-2}}{1+\alpha} \quad \text{for} \quad \phi = \Phi_2, \\ \sigma &\to \frac{\alpha - e^{-k^2}}{1+\alpha} \quad \text{for} \quad \phi = \Phi_\infty. \end{aligned} \tag{4.13}$$

If $k \to \infty$, then all of the expressions for σ above tend to $\alpha/(1+\alpha)$, meaning that $\left(\frac{1-\alpha}{1-\alpha^2}, \frac{1-\alpha}{1-\alpha^2}\right)$ is unstable. This is depicted in Figure 4.3 where the σ value converges to the broken lines for $\phi = \Phi_1, \Phi_2$ and Φ_∞ with $D = 0$ and $\alpha = 0.1$. The agreement between the numerical σ and the asymptotic solution increases from $\phi = \Phi_1$ to $\phi = \Phi_\infty$, as shown in Figure 4.3. The agreement for all the

kernels is expected to improve further if we decrease the value of D further. The most unstable wavenumber, $k = k_{max}$, that gives the maximum value of $\sigma(k)$ in (4.9) can be easily determined from the figure or by using a numerical method.

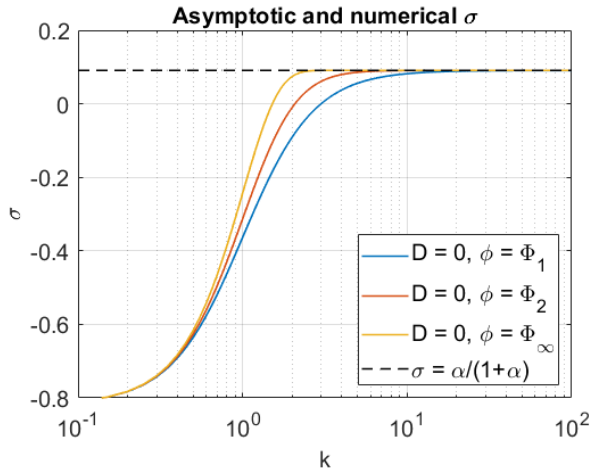


Figure 4.3: *The comparison between the numerical and asymptotic σ in (4.13) as a function of k for $D = 0$.*

If $k = O(D^{-1/2})$, or equivalently $k = \overline{k}D^{-1/2}$ where $\overline{k} = O(1)$, then σ is reduced to

$$\sigma = -\overline{k}^2 + \frac{\alpha}{1+\alpha}, \tag{4.14}$$

for all three of the kernels. When $\sigma = 0$,

$$k = \sqrt{\frac{\alpha}{D(1+\alpha)}}. \tag{4.15}$$

Therefore, at leading order as $D \to 0$, $\left(\frac{1-\alpha}{1-\alpha^2}, \frac{1-\alpha}{1-\alpha^2}\right)$ is stable when k is greater than the expression on the right-hand side of (4.15) and unstable otherwise.

4.7 Asymptotic analysis when $\alpha \neq \beta$

The asymptotic analysis of the dispersion relation (4.8) when $\alpha \neq \beta$ is not as straightforward. In this section, we will construct the neutral curve for different combinations of kernels and deduce the stability of each combination, respectively. Before deriving the asymptotic neutral curves analytically, we will

first study the existence of the neutral curve of the NLLV system (4.4) when $\alpha \neq \beta$ and its dependence on the diffusion term.

Existence of neutral curves

Case (i): $D_1 = D_2 = 0$

First, we assume that both D_1 and D_2 are zero. It is important to note that the system is nonlinear and spatially inhomogeneous, even without diffusion terms. Hence, we shall not assume that the coexisting steady state is stable. As $k \to \infty$, the Fourier transform of kernel $\overline{\phi} \to 0$. Therefore, $\sigma \to \sqrt{4R\alpha\beta u_e v_e}/2$ from (4.9), which is positive. On the other hand, when $k = 0$, we have

$$2\sigma = -(u_e + Rv_e) + \left((u_e + Rv_e)^2 - 4(1 - \alpha\beta)Ru_e v_e\right)^{\frac{1}{2}}. \tag{4.16}$$

Here, $\sigma < 0$ since $4(1 - \alpha\beta)Ru_e v_e$ is positive. To illustrate this, σ from (4.9) is plotted against k in Figure 4.4, with $R = \lambda = 1$, $\alpha = 0.01$, and $\beta = 0.02$ for $\phi = \Phi_\infty$ and is represented by the solid line. From Figure 4.4(a), it is clear that σ is negative at $k = 0$. At $k = 100$, the magnified image in Figure 4.4(b) shows that $\sigma \sim 0.01$, which agrees with our earlier approximation. Therefore, σ is an increasing function of k. We conclude that in the absence of diffusion terms in the NLLV system (4.4), there is no local maximum in σ that will lead to the existence of a neutral curve for the coexisting state.

Case (ii): $D_1 \neq 0$ **and** $D_2 \neq 0$

In Chapter 3, we showed that there exist some spikes and oscillations behind the wavefront in the local-nonlocal Fisher-KPP equation (3.1) when the diffusion coefficient is small. Therefore, let us now slightly increase D_1 and D_2 to introduce diffusion into the system. As $k \to \infty$,

we have $\sigma \to -2\min\{D_1, D_2\}k^2$ when $\alpha, \beta \ll 1$ from (4.9) which is less than zero. Like the above case, we have $\sigma < 0$ when $k = 0$. We then plot the function of σ in terms of k in Figure 4.4, represented as the broken line. From Figure 4.4(b), $\sigma \sim -0.09$ at $k = 100$ which is very close to the asymptotic approximation of -0.1. It can also be seen that there is a local maximum in σ, suggesting that there exists a neutral curve where $\sigma = 0$ and $\mathrm{d}\sigma/\mathrm{d}k = 0$ at some critical wavenumber $k = k_c \gg 1$ for appropriate parameter values.

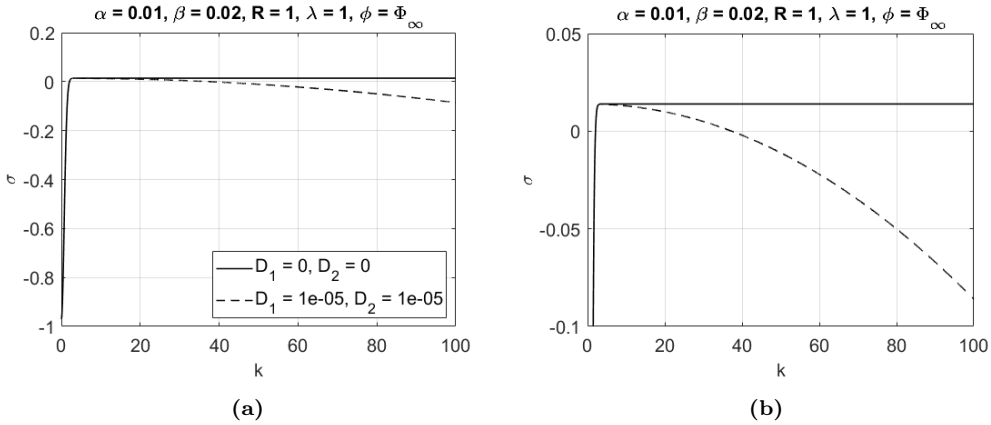


Figure 4.4: *(a) σ as a function of k from (4.9), plotted for $\alpha = 0.01$, $\beta = 0.02$, $R = \lambda = 1$, and $\phi = \Phi_\infty$. (b) is the magnified image of (a).*

Based on the analysis above, we can now investigate the neutral curves for D_1, $D_2 \ll 1$ for different kernels. Throughout the chapter, we will confine our attention to three kernels, Φ_1, Φ_2 and Φ_∞. In addition, we will work on the cases where $\phi_1 = \phi_2$ as well as $\phi_1 \neq \phi_2$ using the combination of these kernels. By studying the neutral curves in detail, we can then determine the relation between the stability of the coexisting state (u_e, v_e) and other parameters such as $R, \lambda, D_1, D_2, \alpha$ and β, as well as the kernels being used. We will analyse the asymptotic neutral curves and compare them with the numerical neutral curves by plotting the contour at the bifurcation point, $k = k_c$ when $\sigma(k_c) = 0$.

4.7.1 Asymptotic neutral curve when $\phi_1 = \phi_2 = \phi = \Phi_1$

We begin by looking at the case when both kernels are $\phi = \Phi_1 = \mathrm{e}^{-|x|}/2$, which has a discontinuous derivative at $x = 0$. Recalling that neutral curves exist

under the conditions that $\mathrm{d}\sigma/\mathrm{d}k = 0$ and $\sigma = 0$. By replacing $\mathrm{d}\sigma/\mathrm{d}k$ and σ with zero in (4.8) and (4.11), we obtain

$$\begin{aligned}\left(D_1k^2 + u_e\overline{\phi}_1(k)\right)\left(2D_2k + Rv_e\lambda\overline{\phi}_2'(\lambda k)\right)\\ + \left(2D_1k + u_e\overline{\phi}_1'(k)\right)\left(D_2k^2 + Rv_e\overline{\phi}_2(\lambda k)\right) = 0,\end{aligned} \tag{4.17}$$

and

$$\left(D_1k^2 + u_e\overline{\phi}_1(k)\right)\left(D_2k^2 + Rv_e\overline{\phi}_2(\lambda k)\right) - R\alpha\beta u_e v_e = 0, \tag{4.18}$$

which are the governing equations that we will be using to formulate the neutral curves for different combinations of kernels later.

To introduce small diffusivity into the system, we rescale $D_1 = \epsilon^2\hat{D}_1$ and $D_2 = \epsilon^2\hat{D}_2$ with $\hat{D}_1,\ \hat{D}_2 = O(1)$ as $\epsilon \to 0$. Since both of the kernels are Φ_1, their respective Fourier transform are therefore $\overline{\phi}_1(k) = (1+k^2)^{-1} \sim k^{-2}$ and $\overline{\phi}_2(\lambda k) = (1+(\lambda k)^2)^{-1} \sim (\lambda k)^{-2}$ as $k \to \infty$. Next, we find the derivatives of these Fourier transforms and substitute them into (4.17) and (4.18) above to get

$$\begin{aligned}\left(\epsilon^2\hat{D}_1k^2 + u_ek^{-2}\right)\left(2\epsilon^2\hat{D}_2k - 2Rv_e\lambda(\lambda k)^{-3}\right)\\ + \left(2\epsilon^2\hat{D}_1k - 2u_ek^{-3}\right)\left(\epsilon^2\hat{D}_2k^2 + Rv_e(\lambda k)^{-2}\right) = 0,\end{aligned} \tag{4.19}$$

and

$$\left(\epsilon^2\hat{D}_1k^2 + u_ek^{-2}\right)\left(\epsilon^2\hat{D}_2k^2 + Rv_e(\lambda k)^{-2}\right) - R\alpha\beta u_e v_e = 0. \tag{4.20}$$

In order to retain the terms involving $\hat{D}_1, \hat{D}_2, \alpha$ and β in (4.20), we need $R\alpha\beta u_e v_e = O(\epsilon^4k^4)$. The most general case is to let $\alpha\beta \ll 1$ and $R, u_e, v_e = O(1)$. In (4.19), an obvious scaling would be $\epsilon^2k^2 = O(k^{-2})$, which keeps the first two terms in the first bracket. Following the assumption that $R, u_e, v_e = O(1)$, we have $\alpha\beta = O(\epsilon^2)$. Finally, we rescale $k = \epsilon^{-1/2}\hat{k}$ and $\alpha\beta = \epsilon^2\hat{\alpha}\hat{\beta}$, with

$\hat{k}, \hat{\alpha}, \hat{\beta} = O(1)$ and rewrite equations (4.19) and (4.20) as

$$\begin{aligned}\left(\hat{D}_1\hat{k}^2 + u_e\hat{k}^{-2}\right)\left(\hat{D}_2\hat{k}^2 - Rv_e(\lambda\hat{k})^{-2}\right) \\ + \left(\hat{D}_1\hat{k}^2 - u_e\hat{k}^{-2}\right)\left(\hat{D}_2\hat{k}^2 + Rv_e(\lambda\hat{k})^{-2}\right) = 0,\end{aligned} \tag{4.21}$$

and

$$\left(\hat{D}_1\hat{k}^2 + u_e\hat{k}^{-2}\right)\left(\hat{D}_2\hat{k}^2 + Rv_e(\lambda\hat{k})^{-2}\right) - R\hat{\alpha}\hat{\beta}u_ev_e = 0. \tag{4.22}$$

If we expand (4.21), some of the terms cancel out each other. Upon scaling back the remaining terms to the original parameters, we find that the explicit function of k is

$$k = \left(\frac{Ru_ev_e}{\lambda^2 D_1 D_2}\right)^{1/8}. \tag{4.23}$$

Next, we expand the bracket in (4.22) to obtain.

$$\hat{D}_1\hat{D}_2\hat{k}^4 + u_e\hat{D}_2 + \hat{D}_1Rv_e\lambda^{-2} + Rv_eu_e\lambda^{-2}\hat{k}^{-4} = R\hat{\alpha}\hat{\beta}u_ev_e. \tag{4.24}$$

We then substitute the expression of k into the original scaling of (4.24) to get

$$R\alpha\beta u_ev_e = 2\lambda^{-1}(Rv_eu_eD_1D_2)^{1/2} + u_eD_2 + Rv_eD_1\lambda^{-2}.$$

It can be further simplified by letting $D_1 = D_2 = D$ to yield the asymptotic neutral curve as

$$\frac{R\alpha\beta(1-\alpha)(1-\beta)}{(1-\alpha\beta)^2} - D\left(\frac{2\sqrt{R(1-\alpha)(1-\beta)}}{\lambda(1-\alpha\beta)} + \frac{1-\alpha}{1-\alpha\beta} + \frac{R(1-\beta)}{\lambda^2(1-\alpha\beta)}\right) = 0. \tag{4.25}$$

Note that k in (4.23) is the asymptotic critical wavenumber where bifurcation occurs along the asymptotic neutral curve. The asymptotic neutral curve (4.25) is plotted for $R = \lambda = 1$ and $D = 0.025, 0.01$ and 0.001 in Figure 4.5 below to compare with the numerical neutral curve when $\sigma = 0$ in (4.9).

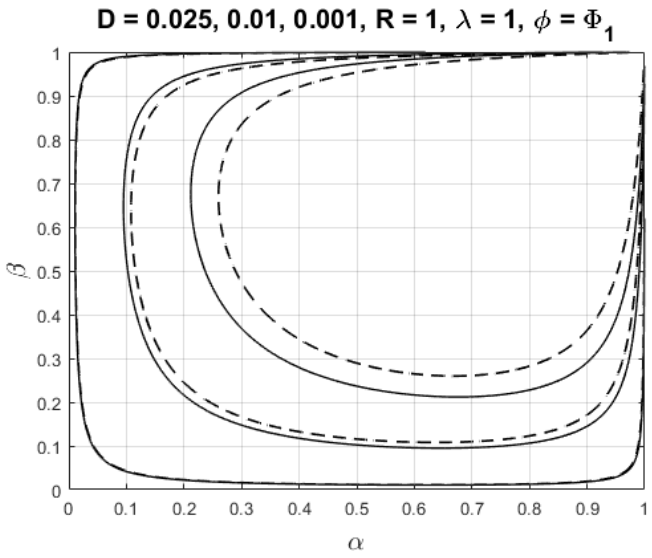


Figure 4.5: *The comparison between the numerical and asymptotic neutral curves for* $\phi_1 = \phi_2 = \phi = \Phi_1$. *The innermost curve is plotted with* $D = 0.025$, *whereas the outermost curve is plotted with* $D = 0.001$. *The broken lines show the asymptotic neutral curves obtained in (4.25). The solid lines are the numerical neutral curves obtained in (4.9).*

Observations

The asymptotic neutral curves that we construct are shown as broken lines in Figure 4.5. Notice that as D decreases from 0.025 to 0.001, the broken lines are in better agreement with the numerical neutral curves, shown as solid lines. In fact, the solid line is in excellent agreement with the broken line at $D = 0.001$. This supports our earlier assertion that D has to be sufficiently small in the asymptotic neutral curve (4.25). Recalling that, we imposed the condition that $\alpha\beta \ll 1$ before constructing the neutral curve asymptotically. It means that we have so far studied the cases for i) $\alpha \to 0$ and $\beta \to 1$, ii) $\alpha \to 1$ and $\beta \to 0$, and iii) $\alpha \to 0$ and $\beta \to 0$, all of which are reflected in Figure 4.5. The case where both $\alpha \to 1$ and $\beta \to 1$ are not captured in the figure as $(1 - \alpha\beta)$ tends to zero in the denominator, resulting in a much bigger value for the terms involving $(1 - \alpha\beta)^2$, and hence getting a nonzero value in the neutral curve (4.25).

Stability of (u_e, v_e)

For each D value, σ is positive inside the neutral curve (not a closed curve) and negative on the outside of the curve. Therefore, (u_e, v_e) is unstable for

any (α, β) pair inside the neutral curve and stable otherwise. To illustrate the stability of the coexisting state, we plot the solutions of an IVP for the NLLV system (4.4) with localised initial conditions and study the behaviour of the solutions. First, we fix $D = 0.025$ and $\beta = 0.5$ whilst varying α to increase σ. By referring to the innermost numerical neutral curve in Figure 4.5, we choose $\alpha = 0.3$ and 0.6 to represent the cases where the coexisting state is unstable. At $t = 0$, small perturbation terms are added to the coexisting state, i.e. $u_e + 0.01\mathrm{e}^{-x^2}$ and $v_e + 0.01\mathrm{e}^{-x^2}$, to perform the stability test for all wavenumbers, k.

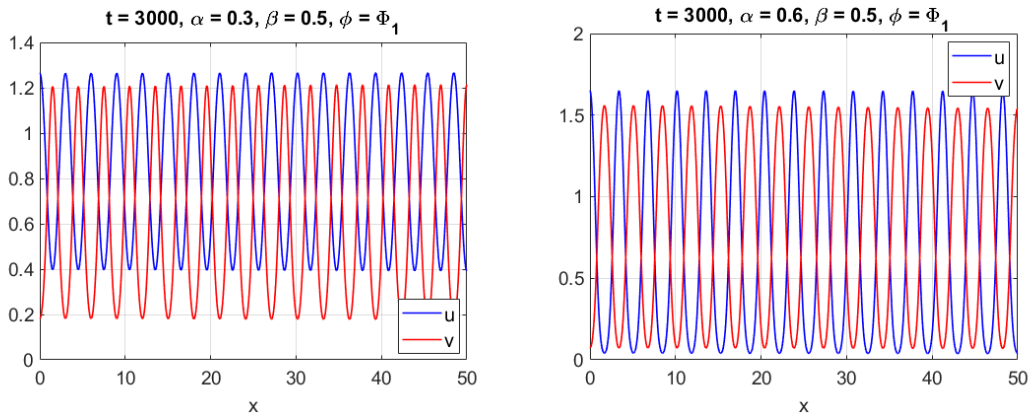


Figure 4.6: *The solutions of the IVP (4.4) for $\phi_1 = \phi_2 = \phi = \Phi_1$, where $D = 0.025$, $R = \lambda = 1$, $\beta = 0.5$. $\alpha = 0.3$ in (a), $\alpha = 0.6$ in (b).*

The first observation from Figures 4.6(a) and 4.6(b) is that the solutions oscillate in space around their respective coexisting states at $(0.82, 0.59)$ and $(0.57, 0.71)$. Moreover, u is at its local maximum when v is at its local minimum, and this oscillation is consistent in terms of its period across the spatial domain. As α increases from 0.3 to 0.6, the amplitudes of the oscillations in both u and v increase by about 0.3. This is in agreement with the fact that σ is more positive at $\alpha = 0.6$, and therefore, the solutions grow at a higher rate. Despite the increase in amplitude and, subsequently, the lower local minimum value in u and v, both species still survive and coexist across the spatial domain.

The value of σ can be determined numerically by first solving for the most unstable wavenumber, k_{max}, that gives the maximum value of σ in (4.9). At

$\alpha = 0.3$, we have $\sigma = 0.03$ with $k_{max} = 2.07$. The solutions oscillate at the wavelength of 3.03, which is very close to the most unstable wavelength predicted by linear stability analysis at $2\pi/k_{max} = 3.04$. On the other hand, when $\alpha = 0.6$, $\sigma = 0.12$ with $k_{max} = 2.01$. The solutions oscillate at the wavelength of 3.42, whereas the predicted wavelength is $2\pi/k_{max} = 3.12$. Therefore, the further σ is from the neutral curve, the further the wavelength is from its predicted most unstable wavelength.

Another interesting analysis can be drawn on the case where σ is small and positive when it is close to the neutral curve. For this kernel combination, such a case occurs at $\alpha = 0.2366$ and $\beta = 0.5$. Instead of assuming a sufficiently localised initial condition, we now introduce a random noise, i.e. a vector of random numbers in the interval (-0.01,0.01), to the coexisting state and study how the solutions behave at large times. At this (α, β) pair, the solutions grow at an extremely slow rate of 1.3×10^{-6}. By letting the simulation run up to $t = 2000$, we can see from Figure 4.7(a) that the solutions oscillate with small and varying amplitude. As t increases further, the solutions in Figure 4.7(b) settle down to a stable and spatially-oscillatory state. This observation will be analysed in more detail when we use a weakly nonlinear analysis in the next chapter.

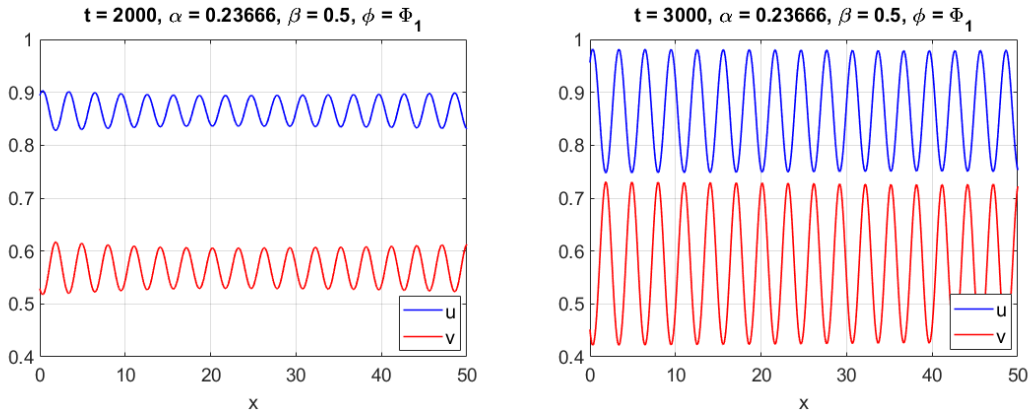


Figure 4.7: *The solutions of the IVP (4.4) for $\phi_1 = \phi_2 = \phi = \Phi_1$ when the growth rate, σ, of the coexisting state is small and positive. The parameters are $D = 0.025, \alpha = 0.2366, \beta = 0.5, R = \lambda = 1$ (a) $t = 2000$ and (b) $t = 3000$. The initial condition is random across the spatial domain.*

Next, we examine the case when both kernels are $\phi = \Phi_\infty$ and $\phi = \Phi_2$. We find that these two cases produce similar results, and therefore, we will derive the asymptotic neutral curve and present the results with only a brief analysis.

4.7.2 Asymptotic neutral curve when $\phi_1 = \phi_2 = \phi = \Phi_\infty$

In this subsection, we examine the case when both of the kernels are Gaussian, i.e. $\phi = \Phi_\infty = \mathrm{e}^{-\frac{1}{4}x^2}/(2\sqrt{\pi})$ which is a smooth kernel that is infinitely-differentiable at $x = 0$.

Again, we rescale $D_1 = \epsilon^2 \hat{D}_1$ and $D_2 = \epsilon^2 \hat{D}_2$ with $\hat{D}_1$, $\hat{D}_2 = O(1)$ as $\epsilon \to 0$. For Gaussian kernel, the Fourier transforms are $\overline{\phi}_1(k) = \mathrm{e}^{-k^2}$ and $\overline{\phi}_2(\lambda k) = \mathrm{e}^{-\lambda^2 k^2}$. From the general equations (4.17) and (4.18), we find that

$$\begin{aligned}\left(\epsilon^2 \hat{D}_1 k^2 + u_e \mathrm{e}^{-k^2}\right)\left(2\epsilon^2 \hat{D}_2 k - 2R v_e \lambda^2 k \mathrm{e}^{-\lambda^2 k^2}\right) \\ + \left(2\epsilon^2 \hat{D}_1 k - 2u_e k \mathrm{e}^{-k^2}\right)\left(\epsilon^2 \hat{D}_2 k^2 + R v_e \mathrm{e}^{-\lambda^2 k^2}\right) = 0,\end{aligned} \tag{4.26}$$

and

$$\left(\epsilon^2 \hat{D}_1 k^2 + u_e \mathrm{e}^{-k^2}\right)\left(\epsilon^2 \hat{D}_2 k^2 + R v_e \mathrm{e}^{-\lambda^2 k^2}\right) - R\alpha\beta u_e v_e = 0. \tag{4.27}$$

The richest balance can be obtained when $\lambda = 1$ in both (4.26) and (4.27). (Note that λ is not necessarily one, but we focus only on the cases when $\lambda = 1$ for the rest of this chapter.) To balance the terms in both brackets that have a difference in (4.26), we need $\mathrm{e}^{-k^2} = O(\epsilon^2)$. As $k \to \infty$, we have $\epsilon^2 k^2 \gg \mathrm{e}^{-k^2}$ at leading order. Therefore, we can discard the exponential terms in the first and the last brackets in (4.26) and rearrange the equation to obtain

$$k = \left[\ln\left(\frac{\hat{D}_1 R v_e + \hat{D}_2 u_e}{2\epsilon^2 \hat{D}_1 \hat{D}_2}\right)\right]^{1/2}. \tag{4.28}$$

Proceeding as before, (4.27) can be simplified to

$$\epsilon^2 k^2 = \left(\frac{R\alpha\beta u_e v_e}{\hat{D}_1 \hat{D}_2} \right)^{1/2}. \tag{4.29}$$

Finally, we substitute the expression of k from (4.28) into (4.29) and rescale it back to the original parameters to yield

$$\ln\left(\frac{D_1 R v_e + D_2 u_e}{2D_1 D_2} \right) = \left(\frac{R\alpha\beta u_e v_e}{D_1 D_2} \right)^{1/2}. \tag{4.30}$$

By letting $D_1 = D_2 = D$, the general formula for the asymptotic neutral curve is then

$$\frac{\sqrt{R\alpha\beta(1-\alpha)(1-\beta)}}{D(1-\alpha\beta)} - \ln\left(\frac{R(1-\beta)+(1-\alpha)}{2D(1-\alpha\beta)} \right) = 0. \tag{4.31}$$

It is also possible to study the general neutral curve above for various combinations of α and β limits.

Case (i): If $\alpha \to 0$ and $\beta \to 1$

First, let us look at the case when $\alpha \to 0$ and $\beta \to 1$. From the expression of coexisting state, it can be easily deduced that $u_e \sim 1$ and $v_e \sim 1 - \beta$. By replacing u_e and v_e with the new limits while neglecting all the small terms in (4.30), it is straightforward to work out that

$$R\alpha(1-\beta) \sim (D \ln 2D)^2. \tag{4.32}$$

Case (ii): If $\beta \to 0$ and $\alpha \to 1$

By repeating a similar process, we obtain the relation

$$R\beta(1-\alpha) \sim \left[D \ln\left(\frac{R}{2D} \right) \right]^2. \tag{4.33}$$

Case (iii): If $\alpha \to 0$ and $\beta \to 0$

As $\alpha \to 0$ and $\beta \to 0$, both u_e and v_e are approximately one. Therefore, the remaining terms are

$$R\alpha\beta \sim \left[D \ln \left(\frac{R+1}{2D} \right) \right]^2. \tag{4.34}$$

Case (iv): If $\alpha \to 1$ and $\beta \to 1$

Finally, let us look at the case where both $\alpha \to 1$ and $\beta \to 1$. In this case, $(u_e, v_e) \sim \left(\frac{1-\alpha}{2-\alpha-\beta}, \frac{1-\beta}{2-\alpha-\beta} \right)$, where we substitute $\alpha = 1-(1-\alpha)$ and $\beta = 1-(1-\beta)$ in the denominators and make use of the fact that $1-\alpha \ll 1$ and $1-\beta \ll 1$. From (4.30), we have

$$\frac{R(1-\alpha)(1-\beta)}{(2-\alpha-\beta)^2} \sim \left[D \ln \left(\frac{R(1-\beta)+(1-\alpha)}{2D(2-\alpha-\beta)} \right) \right]^2. \tag{4.35}$$

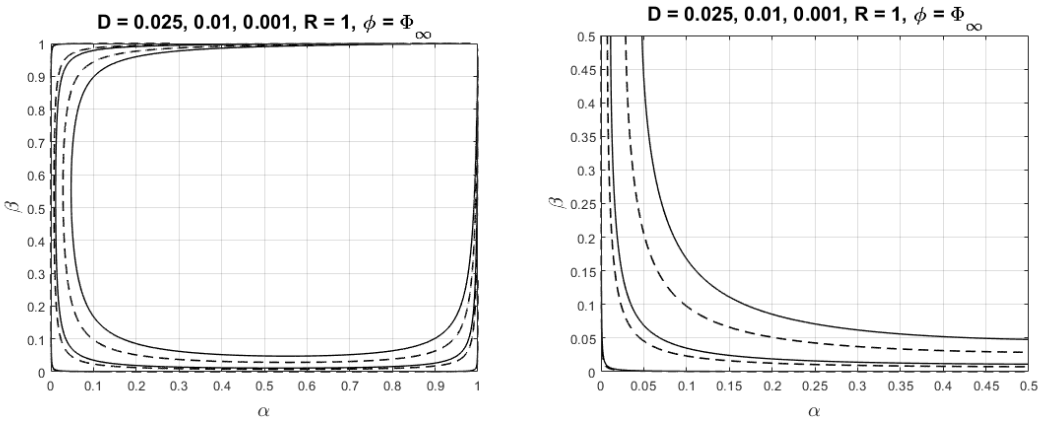
We are now ready to plot the general asymptotic neutral curve in (4.31) and compare it with the numerical neutral curve that is obtained by letting $\sigma = 0$ in (4.9). If we fix $R = 1$ and $D_1 = D_2 = D$ where $D = 0.025, 0.01$ and 0.001, the neutral curves can be plotted in Figure 4.8.

Observations

Like the previous case, the asymptotic neutral curve in Figure 4.8(a) better agrees with the neutral curve with decreasing D.

Stability of (u_e, v_e)

The solutions in Figure 4.9 are plotted for $\beta = 0.5$ and $\alpha = 0.6$, where the coexisting state is unstable as seen in the neutral curve in Figure 4.8(a). The solutions oscillate with a growth rate of $\sigma = 0.244$ and the most unstable wavenumber of $k_{max} = 1.8$ around the coexisting state, $(0.57, 0.71)$. The



(a) **(b)**

Figure 4.8: *(a) is the numerical and asymptotic neutral curves for kernel* $\phi_1 = \phi_2 = \phi = \Phi_\infty$*, where* D *decreases as the radius of the curve increases. The broken lines represent the asymptotic neutral curves obtained in (4.31). The solid lines are the numerical neutral curves obtained in (4.9). (b) is the magnified image of the numerical and asymptotic neutral curves where* $\alpha, \beta \ll 1$*.*

wavelength of the oscillations is approximately 3.95, while the predicted wavelength from the linear stability analysis is $2\pi/k_{max} = 3.49$. The oscillatory pattern is similar to the one we observe earlier when $\phi = \Phi_1$. However, at each local minimum, u and v are 0.0037 and 0.008, respectively. It appears that one species is locally extinct when the other species is at its peak population.

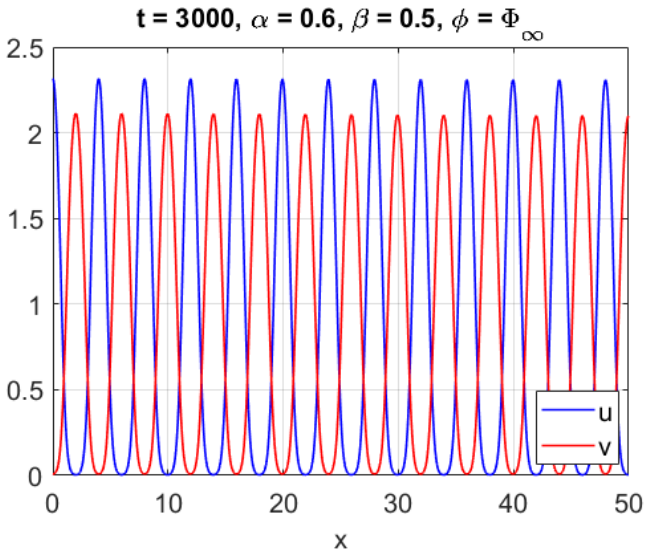


Figure 4.9: *The solutions of the IVP (4.4) for kernel* $\phi_1 = \phi_2 = \phi = \Phi_\infty$*, where* $D = 0.025$*,* $R = \lambda = 1$*,* $\beta = 0.5$*, and* $\alpha = 0.6$*.*

4.7.3 Asymptotic neutral curve when $\phi_1 = \phi_2 = \phi = \Phi_2$

Having studied the cases where both of the kernels are $\phi = \Phi_1$ and $\phi = \Phi_\infty$, we are interested in the case where $\phi = \Phi_2$, which is the intermediate kernel between the two. Note that $\Phi_2 = \left(\sqrt{2} + 2|x|\right) \mathrm{e}^{-\sqrt{2}|x|}/4$ is differentiable, but not infinitely differentiable at $x = 0$.

We employ a slightly different approach for this particular case than the asymptotic methods presented above for $\phi = \Phi_1$ and $\phi = \Phi_\infty$. Instead of rescaling D_1 and D_2, we apply the binomial expansion to the Fourier transforms of $\phi = \Phi_2$ which are $\overline{\phi}_1(k) = (1 + k^2/2)^{-2}$ and $\overline{\phi}_2(\lambda k) = (1 + \lambda^2 k^2/2)^{-2}$ respectively. Keeping only the first two terms of each binomial expansion, we substitute the Fourier transforms and their corresponding derivatives into the governing equations (4.17) and (4.18) to obtain

$$\left(D_1 k^2 + \frac{4u_e}{k^4} - \frac{16u_e}{k^6}\right)\left(2D_2 k - \frac{16\lambda R v_e}{\lambda^5 k^5} + \frac{96\lambda R v_e}{\lambda^7 k^7}\right) + \left(2D_1 k - \frac{16u_e}{k^5} + \frac{96u_e}{k^7}\right)\left(D_2 k^2 + \frac{4Rv_e}{\lambda^4 k^4} - \frac{16Rv_e}{\lambda^6 k^6}\right) = 0, \tag{4.36}$$

and

$$\left(D_1 k^2 + \frac{4u_e}{k^4} - \frac{16u_e}{k^6}\right)\left(D_2 k^2 + \frac{4Rv_e}{\lambda^4 k^4} - \frac{16Rv_e}{\lambda^6 k^6}\right) - R\alpha\beta u_e v_e = 0. \tag{4.37}$$

Next, we multiply (4.36) through by $\lambda^7 k^{14}$ and rearrange it to get

$$D_2\left(4D_1\lambda^7 k^{17} - 8u_e\lambda^7 k^{11} + 64u_e\lambda^7 k^9\right) + Rv_e\lambda^2 k^2\left(-8D_1\lambda k^9 - 128u_e\lambda k^3 + 640u_e\lambda k\right) + Rv_e\lambda\left(64D_1 k^9 + 640u_e k^3 - 3072u_e k\right) = 0. \tag{4.38}$$

At leading order when $k \to \infty$, (4.38) is reduced to

$$4D_1 D_2\lambda^7 k^{17} - 8D_2 u_e\lambda^7 k^{11} - 8D_1 R v_e\lambda^3 k^{11} - 128R v_e u_e\lambda^3 k^5 = 0, \tag{4.39}$$

while both of the k^{-6} terms in (4.37) can be eliminated.

On simplifying, (4.39) can be written as a quadratic function of m where $m = k^6$. Then, we solve for m using the quadratic formula and rewrite k as $m^{1/6}$. Finally, we substitute the k we obtained into (4.37) at leading order and plot the resulting neutral curves below. At the leading order where $k \to \infty$, the analytical expression for k is only valid under the condition that

$$32Ru_ev_e \gg D_1D_2\lambda^4 - 2D_2u_e\lambda^4 - 2D_1Rv_e, \tag{4.40}$$

which is valid as long as α and β are not approaching one.

By setting $D_1 = D_2 = D = 0.025, 0.01$ and 0.001, the asymptotic and numerical neutral curves are plotted in Figure 4.10.

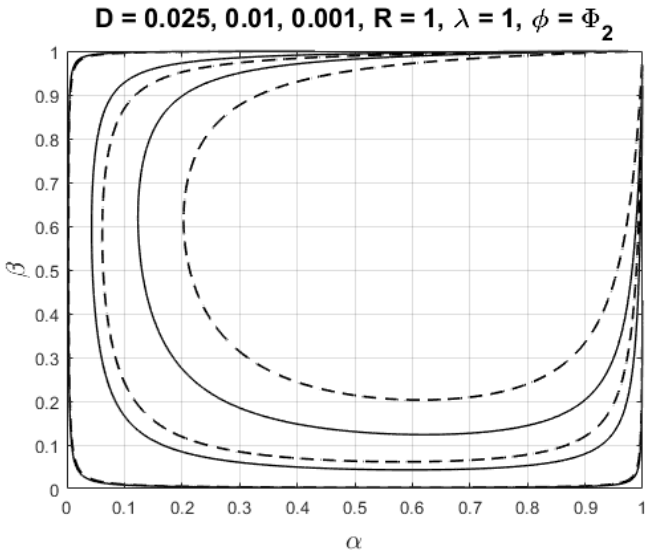


Figure 4.10: *The comparison between the numerical and asymptotic neutral curves for $\phi_1 = \phi_2 = \phi = \Phi_2$. The innermost curve is plotted with $D = 0.025$, whereas the outermost curve is plotted with $D = 0.001$. The broken lines show the asymptotic neutral curves obtained by solving (4.39) numerically. The solid lines are the numerical neutral curves obtained in (4.9).*

Observations

Again, Figure 4.10 illustrates that the asymptotic neutral curve is in excellent agreement with the neutral curve for sufficiently small D.

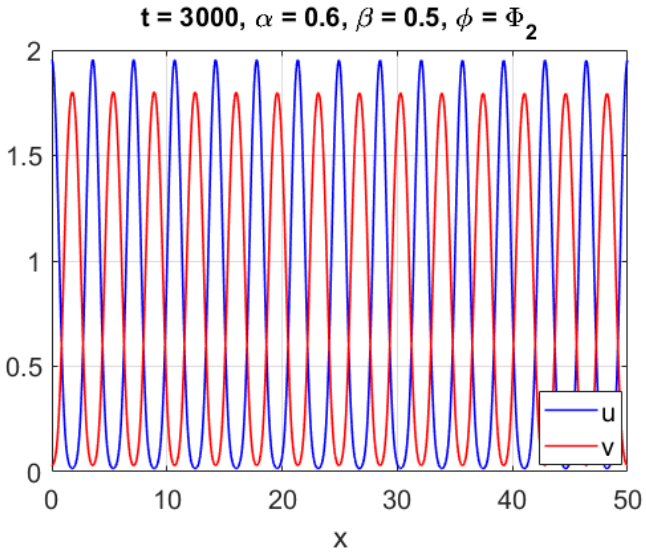


Figure 4.11: *The solutions of the IVP (4.4) for kernel* $\phi_1 = \phi_2 = \phi = \Phi_2$*, where* $D = 0.025$*,* $R = \lambda = 1$*,* $\beta = 0.5$*, and* $\alpha = 0.6$*.*

Stability of (u_e, v_e)

In Figure 4.11, the solutions at $\beta = 0.5$ and $\alpha = 0.6$ oscillate with a growth rate of $\sigma = 0.18$ with its most unstable wavenumber of $k_{max} = 1.97$ around the coexisting state, $(0.57, 0.71)$. The predicted wavelength is $2\pi/k_{max} = 3.18$ while the wavelength observed in the solutions is around 3.5. Again, the oscillatory pattern is similar to the two cases above.

So far, we have studied three different cases when both ϕ_1 and ϕ_2 are identical, with ϕ_1 as a function of k and ϕ_2 as a function of λk, and we have employed a slightly different method to derive the neutral curve analytically for each case.

4.7.4 Comparison between neutral curves when $\phi_1 = \phi_2 = \phi$

The next step is to understand the effect of the kernels on the stability of the coexisting state. In the previous subsections, we use the same values of

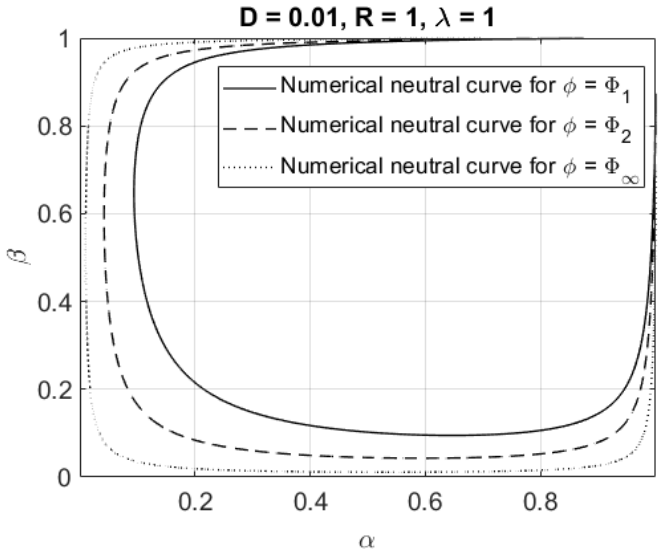


Figure 4.12: *The comparison between the numerical neutral curves obtained from (4.9) when both kernels are* $\phi_1 = \phi_2 = \phi = \Phi_1, \Phi_2$ *and* Φ_∞*, at* $R = \lambda = 1$ *and* $D = 0.01$*.*

$D = 0.025, 0.01$ and 0.001 to plot the neutral curves for $\phi = \Phi_1, \Phi_2$ and Φ_∞. For comparison purposes, we now fix $D = 0.01$ and plot the numerical neutral curves of all three kernels in Figure 4.12. It can be seen from the figure that the neutral curve approaches the boundary when the kernel Φ_n increases in n. Hence, the coexisting state of the nonlocal Lokta-Volterra system (4.4) for $\phi = \Phi_\infty$ has positive σ in the highest proportion of (α, β) pair, followed by that of $\phi = \Phi_2$ and lastly $\phi = \Phi_1$. In other words, for the same α and β, σ is the largest in $\phi = \Phi_\infty$, and hence the coexisting state has the highest growth rate.

The smoothness of the kernel functions increases from $\phi = \Phi_1$ to $\phi = \Phi_\infty$. At $x = 0$, $\phi = \Phi_1$ has a discontinuous derivative (see Figure 2.1) whereas $\phi = \Phi_\infty$ is infinitely-differentiable (see Figure 2.1). Therefore, we deduce that the coexisting state has a larger instability region in (α, β) parameter space when the regularity of the kernel function at $x = 0$ is higher.

In the following subsections, we will derive the asymptotic neutral curves when ϕ_1 differs from ϕ_2 and compare them with the corresponding numerical neutral curves.

4.7.5 Asymptotic neutral curve when $\phi_1 = \Phi_1$ and $\phi_2 = \Phi_\infty$

We begin by looking at the most extreme case when ϕ_1 has a discontinuous derivative at $x = 0$, and ϕ_2 is smooth. By letting $\phi_1 = \Phi_1$ and $\phi_2 = \Phi_\infty$ and taking the Fourier transform of both kernels, we can rewrite the governing equations (4.17) and (4.18) as

$$\begin{aligned}\left(D_1k^2(1+k^2)+u_e\right)\left(D_2 - Rv_e\lambda^2 k\mathrm{e}^{-\lambda^2k^2}\right)\\ + \left(D_1(1+k^2) - \frac{u_e}{1+k^2}\right)\left(D_2k^2 + Rv_e\mathrm{e}^{-\lambda^2k^2}\right) = 0,\end{aligned} \tag{4.41}$$

and

$$\left(D_1k^2 + \frac{u_e}{1+k^2}\right)\left(D_2k^2 + Rv_e\mathrm{e}^{-\lambda^2k^2}\right) - R\alpha\beta u_e v_e = 0. \tag{4.42}$$

From (4.42), $R\alpha\beta u_e v_e = O(D_1D_2k^4)$. If we take $R, u_e, v_e = O(1)$, it requires that $\alpha\beta = O(D_1D_2k^4)$. For $R\alpha\beta u_e v_e \ll 1$, we need $D_1D_2 \gg 1/k^4$ at leading order. Next, we expand (4.41) to get

$$\begin{aligned}D_2\left[2D_1k^2(1+k^2)^2 + u_e\right]\\ + Rv_e\mathrm{e}^{-\lambda^2k^2}\left\{D_1(1+k^2)^2(1-\lambda^2k^2) - u_e\left[1+\lambda(1+k^2)\right]\right\} = 0.\end{aligned} \tag{4.43}$$

To establish the leading order balance, we neglect the terms in (4.43) that are not of $O(1)$ as $k \to \infty$, and rearrange the equation as

$$Rv_e\mathrm{e}^{-\lambda^2k^2} = \frac{D_2(2D_1k^6 + u_e)}{\lambda^2k^2(D_1k^4 + u_e)}. \tag{4.44}$$

Then, we substitute (4.44) into (4.42) and eliminate the small terms at leading order. As a result, the second term in the second bracket in (4.42) vanishes so that

$$k = \left[\frac{u_e}{D_1}\left(\frac{R\alpha\beta v_e}{D_2} - 1\right)\right]^{1/4}. \tag{4.45}$$

As we require that $k \gg 1$ in the neutral curve, the expression above is only valid under the condition that

$$R\alpha\beta u_e v_e \gg (D_1 + u_e)D_2. \tag{4.46}$$

Let us closely inspect the condition (4.46) for different combinations of α and β limits whilst assuming that $R = 1$ for simplicity.

Conditions at leading order for $\alpha\beta \ll 1$

(i) When $\alpha, \beta \to 0$, condition (4.46) tends to $\alpha\beta \gg D_2(D_1 + 1)$.

(ii) When $\alpha \to 0$ and $\beta \to 1$, condition (4.46) tends to $\alpha v_e \gg (D_1 + 1)D_2$.

(iii) When $\alpha \to 1$ and $\beta \to 0$, condition (4.46) tends to $\beta u_e \gg D_1 D_2$.

Hence, to ensure that expression (4.45) is valid, D_2 has to be sufficiently small. Finally, we are now ready to plot the neutral curves by substituting k in (4.45) into (4.42) and compare them with the ones we obtained numerically. We set $D_1 = 10, 5$ and 2.5, $D_2 = 10^{-8}D_1$ and $R = 1$ in MATLAB to produce the figure below. It is worth noting that even though we have been focusing on cases when both D_1 and D_2 are small, it is not necessary for either asymptotic or numerical analysis. It is well known that a small diffusion coefficient leads to the instability of the local Lotka-Volterra model and the nonlocal Fisher equations. However, the asymptotic analysis above remains valid as long as D_1 and D_2 are positive provided that D_2 is sufficiently small.

Observations

It can be seen from Figure 4.13 that the neutral curves exhibit similar properties as the previous cases, where the asymptotic neutral curves are getting closer to the numerical neutral curves for decreasing diffusion coefficients.

Stability of (u_e, v_e)

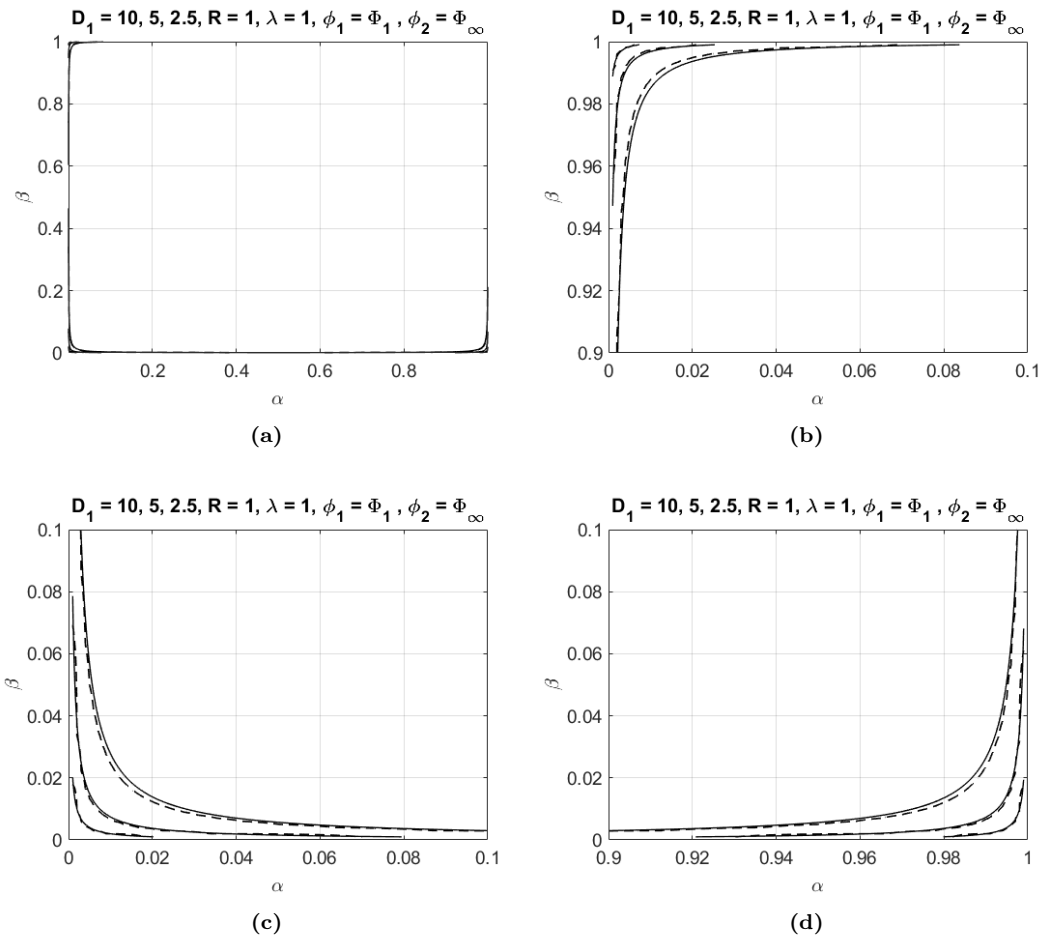


Figure 4.13: *(a) The numerical and asymptotic neutral curves for kernel $\phi_1 = \Phi_1$ and $\phi_2 = \Phi_\infty$, where both D_1 and D_2 decrease as the curves approach the boundary of the axes. The broken lines represent the asymptotic neutral curves from (4.42) with k from (4.45). The solid lines are the numerical neutral curves obtained in (4.9). (b)-(d) highlight different views of the structure of the neutral curves.*

We choose $D_1 = D_2 = D = 0.025$ to be consistent with the solutions for other kernel combinations. At $\alpha = 0.6$ and $\beta = 0.5$, the growth rate of (u_e, v_e) is $\sigma = 0.19$. From Figure 4.14, the wavelength of the solutions is around 3.7 compared to the predicted wavelength of $2\pi/k_{max} = 3.4$. At $t = 3000$, the solutions exhibit a similar spatial pattern to the cases when both kernels are Φ_1 or Φ_∞. However, the maximum value of oscillations in v is much larger than that of u compared to the solutions in Figures 4.6(b) and Figure 4.9.

It is worth noting that this combination of the kernel is considered as a particular case of all the cases we have studied so far, as Φ_1 and Φ_∞ are very different in terms of their regularity around $x = 0$ and their smoothness in general. On

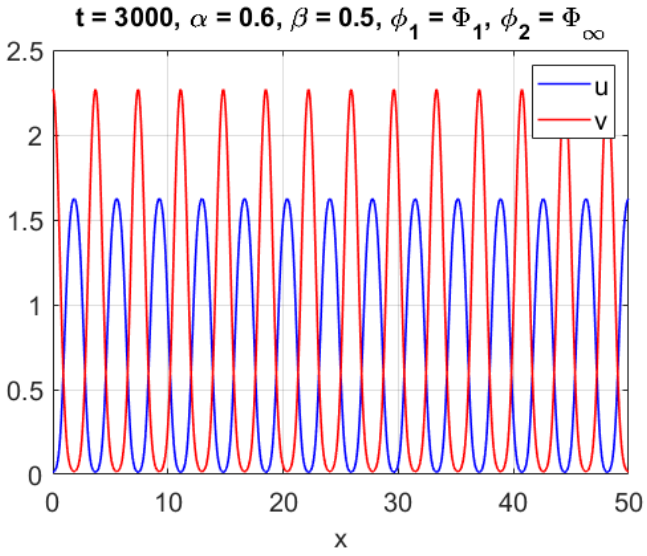


Figure 4.14: *The solutions of the IVP (4.4) for kernel $\phi_1 = \Phi_1$ and $\phi_2 = \Phi_\infty$, where $D = 0.025$, $R = \lambda = 1$, $\beta = 0.5$, and $\alpha = 0.6$.*

top of that, the asymptotic neutral curve is only valid under the condition that $D_2 \ll 1$, restricting the study of the neutral curves for more general diffusion coefficients. Next, we will look at a final combination of kernel when $\phi_1 = \Phi_1$ and $\phi_2 = \Phi_2$.

4.7.6 Asymptotic neutral curve when $\phi_1 = \Phi_1$ and $\phi_2 = \Phi_2$

Since both Φ_1 and Φ_2 are polynomials in terms of k, the derivation of the asymptotic neutral curve is very similar to the case when $\phi_1 = \phi_2 = \phi = \Phi_2$. By using binomial expansion in the Fourier transforms of Φ_1 and Φ_2, (4.17) and (4.18) become

$$\left(D_1k^2 + \frac{u_e}{k^2} - \frac{u_e}{k^4}\right)\left(2D_2k - \frac{16\lambda R v_e}{\lambda^5 k^5} + \frac{96\lambda R v_e}{\lambda^7 k^7}\right) + \left(2D_1k - \frac{2u_e}{k^3} + \frac{4u_e}{k^5}\right)\left(D_2k^2 + \frac{4Rv_e}{\lambda^4 k^4} - \frac{16Rv_e}{\lambda^6 k^6}\right) = 0, \tag{4.47}$$

and

$$\left(D_1k^2 + \frac{u_e}{k^2} - \frac{u_e}{k^4}\right)\left(D_2k^2 + \frac{4Rv_e}{\lambda^4 k^4} - \frac{16Rv_e}{\lambda^6 k^6}\right) - R\alpha\beta u_e v_e = 0. \tag{4.48}$$

Multiplying (4.47) by $\lambda^7 k^{12}$ and neglecting the terms of $O(1)$ at leading order as $k \to \infty$, the equation can be simplified to

$$4D_1 D_2 \lambda^7 k^{15} + 2D_2 u_e \lambda^7 k^9 - 8D_1 R v_e \lambda^3 k^9 - 24 R u_e v_e \lambda^3 k^5 = 0. \tag{4.49}$$

Although this does not allow us to solve for k analytically, we can solve (4.49) numerically and substitute the resulting k into (4.48) at leading order where the k^{-6} terms are eliminated. By doing so, we can plot the asymptotic neutral curves for this specific combination of kernels and compare them with the numerical neutral curves where $R = \lambda = 1$ and $D_1 = D_2 = D = 0.025, 0.01$ and 0.001.

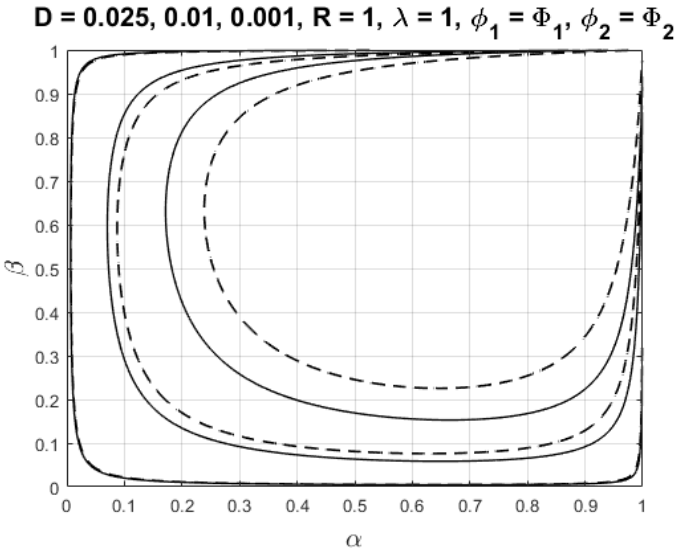


Figure 4.15: *The comparison between the numerical and asymptotic neutral curves for $\phi_1 = \Phi_1$ and $\phi_2 = \Phi_2$. The broken lines represent the asymptotic neutral curves obtained by solving (4.49) numerically.The solid lines are the numerical neutral curves obtained in (4.9). The innermost curve is plotted with $D = 0.025$, and the radius of the curves increases with decreasing D. The broken lines show the asymptotic neutral curves.*

Observations

Figure 4.15 shows that the asymptotic neutral curves approach the numerical neutral curves as D decreases, consistent with all the other cases above.

Stability of (u_e, v_e)

The behaviour of the solutions of the IVP in Figure 4.16 is similar to the cases

when both kernels are $\phi = \Phi_1$ and $\phi = \Phi_2$. The growth rate of the solutions is $\sigma = 0.15$ with the most unstable wavenumber of $k_{max} = 1.99$. From the linear stability analysis, the predicted wavelength is $2\pi/k_{max} = 3.15$, while the actual wavelength in the solutions is 3.4. At $\alpha = 0.6$, however, there is a noticeable difference between the solutions for this particular kernel combination and the kernels mentioned above as v oscillates at a larger amplitude compared to u, compared to the solutions in Figure 4.6(b) and Figure 4.11.

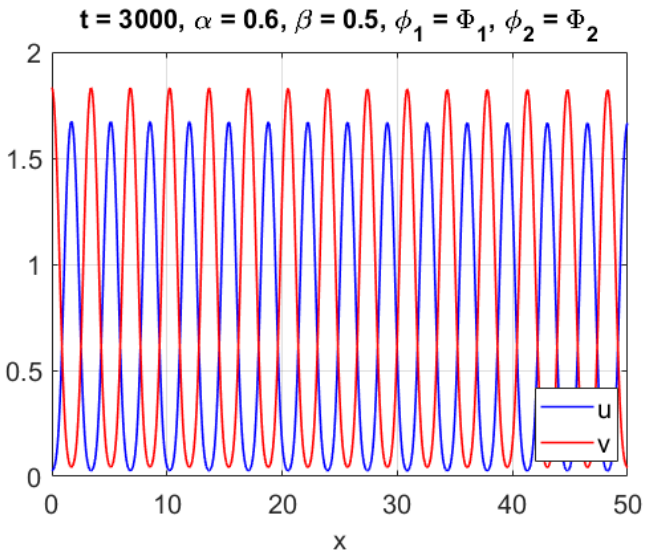


Figure 4.16: *The solutions of the IVP (4.4) for kernel $\phi_1 = \Phi_1$ and $\phi_2 = \Phi_2$, where $D = 0.025$, $R = \lambda = 1$, $\beta = 0.5$, and $\alpha = 0.6$.*

4.7.7 Comparison between neutral curves when $\phi_1 \neq \phi_2$

Next, we compare the effect of the mixed kernels on the stability of the coexisting state by analysing the numerical neutral curves in Figure 4.17. By fixing $D = 0.01, R = \lambda = 1$, we can see from the figure that a combination of Φ_1 and Φ_∞ results in a neutral curve that is closer to the boundary of the axes, represented by the broken line. This means that there exists a more significant proportion of (α, β) that results in the instability of (u_e, v_e) for such kernel pair, as compared to the Φ_1 and Φ_2 combination that is shown by the solid line. The controlling factor of these two kernel pairs lies in the second kernel, i.e. Φ_2 and Φ_∞ and the result is consistent with the analysis of the neutral curves in subsection 4.7.4. The Gaussian kernel, Φ_∞, which is smooth, leads to the

solutions of higher growth rate for the same α and β value.

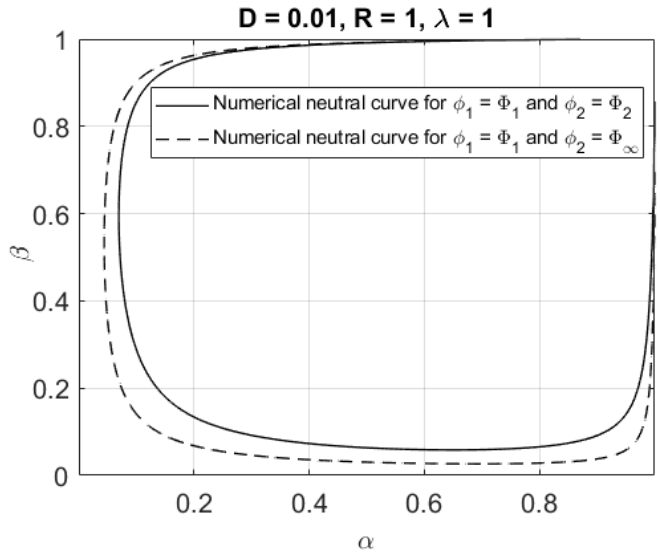


Figure 4.17: *The comparison between the numerical neutral curves obtained from (4.9) for mixed kernels at* $R = \lambda = 1$ *and* $D = 0.01$.

4.8 Conclusion

In this chapter, we have studied the linear stability of the coexisting state of the NLLV system (4.4) and its dependence on the parameters of the system. Such a steady state exists only when $\alpha, \beta < 1$. We have constructed the asymptotic neutral curves for different kernel combinations among Φ_1, Φ_2 and Φ_∞ in the (α, β) parameter space. Cases where $\phi_1 = \phi_2$, as well as $\phi_1 \neq \phi_2$, have been considered. We have shown that bifurcation occurs at the critical wave number, $k = k_c$, where $\sigma(k_c) = 0$ and $\frac{\mathrm{d}\sigma}{\mathrm{d}k}\big|_{k=k_c} = 0$. In our asymptotic analysis of the dispersion relation between the growth rate σ and the wavenumber k, the diffusion coefficients are assumed to be sufficiently small and equal, i.e. $D_1 = D_2 = D$. The asymptotic neutral curves are found to better agree with the numerical neutral curves as $D \to 0$. Despite assuming that $D_1 = D_2$ instead of $D_1 \neq D_2$ according to Turing's theory, instability in the coexisting state was observed due to the nonlocal intraspecific competition in the model.

Apart from that, we have also observed that the instability region of the coexisting state in (α, β) parameter space is larger for kernel combinations

that involve Φ_∞, followed by kernel combinations involving Φ_2 and then for Φ_1. We have also verified our linear stability analysis with the solutions of IVP (4.4) with localised initial conditions. The initial conditions converge to spatially oscillatory patterns for all the combination pairs by introducing a small initial perturbation to the unstable coexisting state. Besides, the asymptotic wavelength from linear stability analysis can predict the wavelength of the solutions of IVP at steady state, provided that the (α, β) values are close to the neutral curves.

Chapter 5

Weakly Nonlinear Analysis of a Nonlocal Lotka-Volterra System

5.1 Introduction

In Chapter 4, we linearised the NLLV system (4.4) around the coexisting state, allowing us to study how the nonlinear system behaves in the neighbourhood of the coexisting state. We have seen how the stability of these solutions changes as we fix β and vary α, provided that the other parameters are fixed. In the linear stability analysis, we have observed that a small initial perturbation to the coexisting state leads to the formation of oscillations in the solutions. However, we do not have further information about the amplitude of the emergent oscillations. Therefore, the next step is to study the amplitude of the emerging patterns in the neighbourhood of a bifurcation point.

In this chapter, we investigate the governing amplitude equation of the nonlinear system by carrying out a weakly nonlinear analysis near the bifurcation point, using the techniques developed for the Swift-Hohenberg equation and the neural field model in Subsections 2.2.1 and 2.2.2. Even though weakly nonlinear analysis works for any kernel with a well-defined Fourier transform, we restrict

our attention to the same kernel choices as the ones in Chapter 4, and focus only on the cases where both kernels are the same. In this chapter, we choose λ, the ratio of the length scale of the kernels, as our bifurcation parameter. We begin by deriving the amplitude equation in Section 5.2 using a multiple-scale method. Then, we analyse the amplitude equation using bifurcation theory in Section 5.3. In Section 5.4, the weakly nonlinear amplitude is compared against the numerical amplitude around the bifurcation point, $\lambda_c = 1$, for different β values. In all cases, good agreement is found between the amplitudes and simulations. In Section 5.5, we investigate the relation between the patterning of the fully nonlinear solutions and the system parameters numerically. We conclude in Section 5.6 that the amplitudes of the oscillations that emerge from the coexisting state exhibit supercritical and subcritical bifurcations around the bifurcation point, and no secondary bifurcations are observed. For the fully nonlinear solutions, the solutions u and v are segregated when D_1 or D_2 are sufficiently small. More specifically, regions exist where one species is close to extinction while the other is thriving in the spatial domain, which will be examined in more detail in the next chapter.

5.2 Derivation of amplitude equation

In this section, we employ some standard approaches in wealy nonlinear analysis (see examples in Subsections 2.2.1 and 2.2.2) to derive the amplitude equation of the NLLV system (4.4). To simplify the derivation process, we redefine the NLLV system (4.4) as

$$\begin{aligned} \frac{\partial u}{\partial t} &= D_1 \frac{\partial^2 u}{\partial x^2} + u\left(1 - \int_{-\infty}^{\infty} \phi_1(x-y)u(y)\,\mathrm{d}y - \alpha v\right), \\ \frac{\partial v}{\partial t} &= D_2 \frac{\partial^2 v}{\partial x^2} + Rv\left(1 - \int_{-\infty}^{\infty} \phi_2\left(x-y\right)v(y)\,\mathrm{d}y - \beta u\right), \end{aligned} \tag{5.1}$$

such that $\phi_2 = \phi_2(x;\lambda)$ and define

$$\phi_2(x;\lambda) = \frac{1}{\lambda}\psi\left(\frac{x}{\lambda}\right). \tag{5.2}$$

The spatial convolutions for the two kernels ϕ_1 and ϕ_2 are

$$[\phi_n * u](x,t) = \int_{-\infty}^{\infty} \phi_n(x-y)u(y,t)\,\mathrm{d}y,$$

where $\int_{-\infty}^{\infty}\phi_n(x)\,\mathrm{d}x = 1$ for $n = 1, 2$ and ϕ_2 has a length scale λ relative to ϕ_1.

Linearising (5.1) around the coexisting state, $(u_e, v_e) = \left(\frac{1-\alpha}{1-\alpha\beta}, \frac{1-\beta}{1-\alpha\beta}\right)$, by letting $u(t) = u_e + \overline{u}(t)$ and $v(t) = v_e + \overline{v}(t)$ for $\overline{u}$ and $\overline{v}$ small, leads to the linearised system

$$\begin{aligned}
\frac{\partial \overline{u}}{\partial t} &= D_1\frac{\partial^2\overline{u}}{\partial x^2} - u_e\left(\int_{-\infty}^{\infty}\phi_1(x-y)\overline{u}(y)\,\mathrm{d}y + \alpha\overline{v}\right),\\
\frac{\partial \overline{v}}{\partial t} &= D_2\frac{\partial^2\overline{v}}{\partial x^2} - Rv_e\left(\int_{-\infty}^{\infty}\phi_2(x-y)\overline{v}(y)\,\mathrm{d}y + \beta\overline{u}\right).
\end{aligned} \tag{5.3}$$

System (5.3) can then be written as

$$\frac{\partial}{\partial t}\begin{bmatrix}\overline{u}\\ \overline{v}\end{bmatrix} = \mathcal{L}\begin{bmatrix}\overline{u}\\ \overline{v}\end{bmatrix}, \tag{5.4}$$

where $\mathcal{L}$ is the linear operator

$$\mathcal{L} = \begin{bmatrix}D_1 & 0\\ 0 & D_2\end{bmatrix}\frac{\partial^2}{\partial x^2} + \begin{bmatrix}0 & -\alpha u_e\\ -Rv_e\beta & 0\end{bmatrix} + \begin{bmatrix}-u_e\phi_1 & 0\\ 0 & -Rv_e\phi_2\end{bmatrix} * . \tag{5.5}$$

Next, we seek solutions of the form $(\overline{u}, \overline{v}) = \mathrm{e}^{\sigma t}\mathrm{e}^{ikx}(\hat{u}, \hat{v})$ where the dispersion relation between k and σ can be written implicitly in the form $\mathcal{E}(k,\sigma) = 0$ with

$$\mathcal{E}(k,\sigma) = \det(A(k) - \sigma I_2), \tag{5.6}$$

where $A(k) = -Dk^2 + J_0 - J_1(k)$, and

$$D = \begin{bmatrix} D_1 & 0 \\ 0 & D_2 \end{bmatrix}, \quad J_0 = \begin{bmatrix} 0 & -\alpha u_e \\ -Rv_e\beta & 0 \end{bmatrix}, \quad J_1(k) = \begin{bmatrix} u_e\overline{\phi}_1(k) & 0 \\ 0 & Rv_e\overline{\phi}_2(k) \end{bmatrix}. \tag{5.7}$$

To obtain the above, we use the result that $\phi * \mathrm{e}^{ikx} = \overline{\phi}(k)\mathrm{e}^{ikx}$, for Fourier transform $\overline{\phi}$. Then, we equate (5.6) to zero to yield the characteristic equation

$$\sigma^2 - \mathrm{Tr}\left(A(k)\right)\sigma + \mathrm{Det}\left(A(k)\right) = 0. \tag{5.8}$$

This quadratic equation in σ has the specific form

$$\begin{aligned} \sigma^2 + \Big[(D_1 + D_2)k^2 + u_e\overline{\phi}_1(k) + Rv_e\overline{\phi}_2(k)\Big]\sigma \\ + \left(D_1k^2 + u_e\overline{\phi}_1(k)\right)\left(D_2k^2 + Rv_e\overline{\phi}_2(k)\right) - R\alpha\beta u_e v_e = 0. \end{aligned} \tag{5.9}$$

Next, we choose to use λ as the bifurcation parameter for the NLLV system (5.1) and write (as explained in Subsection 2.2.1 earlier)

$$\lambda = \lambda_c + \epsilon^2\delta, \tag{5.10}$$

where $\lambda = \lambda_c$ is the bifurcation point, $|\epsilon| \ll 1$ and $\delta = O(1)$ as $\epsilon \to 0$. Intuitively, δ measures the distance from the bifurcation point, λ_c. As explained in Section 2.2, we anticipate that the solution will involve a slow space variable, $\chi = \epsilon x$, and a slow time variable, $\tau = \epsilon^2 t$. We then consider power series expansions for u and v as

$$(u(x,t), v(x,t)) = (u_e, v_e) + \sum_{n=1}^{\infty} \epsilon^n \left(u_n(x,\chi,t,\tau), v_n(x,\chi,t,\tau)\right), \tag{5.11}$$

for unknown functions $u_n = u_n(x,\chi,t,\tau)$ and $v_n = v_n(x,\chi,t,\tau)$. The next step is to find the Taylor series expansion of the functions u_n and v_n using the same method as (2.27) in Subsection 2.2.2. For a general kernel ϕ and a function w that represents u or v, the spatial convolution between these two functions

is $\int_{-\infty}^{\infty} \phi(x-y)w(y)\,\mathrm{d}y = \int_{-\infty}^{\infty} \phi(y)w(x-y)\,\mathrm{d}y$. In a multiple-scale approach, $w(x) = w(x, \epsilon x)$ and hence, the spatial convolution becomes

$$\begin{aligned} &\int_{-\infty}^{\infty} \phi(y) w\left(x-y, \epsilon(x-y)\right)\,\mathrm{d}y \\ &= \int_{-\infty}^{\infty} \phi(y) w\left(x-y, \chi-\epsilon y\right)\,\mathrm{d}y \\ &\approx \int_{-\infty}^{\infty} \mathrm{d}y\, \phi(y) \left(1 - \epsilon y \frac{\partial}{\partial \chi} + \frac{\epsilon^2 y^2}{2}\frac{\partial^2}{\partial \chi^2} + \cdots\right) w\left(x-y, \chi\right). \end{aligned} \tag{5.12}$$

Finally, we substitute the derivatives

$$\frac{\partial}{\partial t} \to \frac{\partial}{\partial t} + \epsilon^2 \frac{\partial}{\partial \tau}, \qquad \frac{\partial}{\partial x} \to \frac{\partial}{\partial x} + \epsilon \frac{\partial}{\partial \chi}, \qquad \frac{\partial^2}{\partial x^2} \to \frac{\partial^2}{\partial x^2} + 2\epsilon \frac{\partial^2}{\partial x \partial \chi} + \epsilon^2 \frac{\partial^2}{\partial \chi^2}, \tag{5.13}$$

into the system (5.1) to obtain

$$\begin{aligned} &\left(\frac{\partial}{\partial t} + \epsilon^2 \frac{\partial}{\partial \tau} - D_1 \frac{\partial^2}{\partial x^2} - 2\epsilon D_1 \frac{\partial^2}{\partial x \partial \chi} - \epsilon^2 D_1 \frac{\partial^2}{\partial \chi^2}\right)\left(u_e + \epsilon u_1 + \epsilon^2 u_2 + \epsilon^3 u_3 + \cdots\right) \\ &= \left(u_e + \epsilon u_1 + \epsilon^2 u_2 + \epsilon^3 u_3 + \cdots\right)\Big[1 - \phi_1 * (u_e + \epsilon u_1 + \epsilon^2 u_2 + \epsilon^3 u_3 + \cdots) \\ &\quad + \epsilon \phi_1^y * \frac{\partial}{\partial \chi}(u_e + \epsilon u_1 + \epsilon^2 u_2 + \cdots) - \frac{\epsilon^2}{2}\phi_1^{yy} * \frac{\partial^2}{\partial \chi^2}(u_e + \epsilon u_1 + \cdots) \\ &\quad - \alpha(v_e + \epsilon v_1 + \epsilon^2 v_2 + \epsilon^3 v_3 + \cdots)\Big], \end{aligned} \tag{5.14}$$

where $\phi_1^y = y\phi_1(y)$ and $\phi_1^{yy} = y^2\phi_1(y)$.

Similarly,

$$\begin{aligned} &\left(\frac{\partial}{\partial t} + \epsilon^2 \frac{\partial}{\partial \tau} - D_1 \frac{\partial^2}{\partial x^2} - 2\epsilon D_1 \frac{\partial^2}{\partial x \partial \chi} - \epsilon^2 D_2 \frac{\partial^2}{\partial \chi^2}\right)\left(v_e + \epsilon v_1 + \epsilon^2 v_2 + \epsilon^3 v_3 + \cdots\right) \\ &= R\left(v_e + \epsilon v_1 + \epsilon^2 v_2 + \epsilon^3 v_3 + \cdots\right)\Big[1 - \phi_2 * (v_e + \epsilon v_1 + \epsilon^2 v_2 + \epsilon^3 v_3 + \cdots) \\ &\quad + \epsilon \phi_2^y * \frac{\partial}{\partial \chi}(v_e + \epsilon v_1 + \epsilon^2 v_2 + \cdots) - \frac{\epsilon^2}{2}\phi_2^{yy} * \frac{\partial^2}{\partial \chi^2}(v_e + \epsilon v_1 + \cdots) \\ &\quad - \beta(u_e + \epsilon u_1 + \epsilon^2 u_2 + \epsilon^3 u_3 + \cdots)\Big]. \end{aligned} \tag{5.15}$$

Balancing terms at $O(1)$ in (5.14) and (5.15) yields

$$\begin{aligned} 0 &= u_e - u_e^2 - u_e \alpha v_e, \\ 0 &= v_e - v_e^2 - \beta u_e v_e, \end{aligned} \tag{5.16}$$

which returns the four steady states, including the coexisting state (u_e, v_e). Before we proceed to higher powers of ϵ, we first Taylor expand ϕ_2 such that

$$\begin{aligned} \phi_2(x) = \phi_2(x;\lambda) &\approx \phi_2(x;\lambda_c) + \frac{\partial \phi_2}{\partial \lambda}(x;\lambda_c)(\lambda - \lambda_c), \\ &= \frac{1}{\lambda_c}\psi\left(\frac{x}{\lambda_c}\right) + \frac{\partial}{\partial \lambda}\left[\frac{1}{\lambda}\psi\left(\frac{x}{\lambda}\right)\right]\Bigg|_{\lambda=\lambda_c} \epsilon^2\delta. \end{aligned} \tag{5.17}$$

By defining $\phi_c = \frac{1}{\lambda_c}\psi\left(\frac{x}{\lambda_c}\right)$, the right hand side of (5.17) can be simplified as

$$\phi_c + \frac{\partial \phi_c}{\partial \lambda}\bigg|_{\lambda=\lambda_c} \epsilon^2\delta = \phi_c + \phi_c^{'}\epsilon^2\delta. \tag{5.18}$$

We now balance the terms at $O(\epsilon)$ in (5.14) and (5.15) such that

$$\begin{aligned} \left(\frac{\partial}{\partial t} - D_1\frac{\partial^2}{\partial x^2}\right) u_1 &= u_e(-\phi_1 * u_1 - \alpha v_1) + u_1(1 - u_e - \alpha v_e), \\ \left(\frac{\partial}{\partial t} - D_2\frac{\partial^2}{\partial x^2}\right) v_1 &= R v_e(-\phi_c * v_1 - \beta u_1) + v_1(1 - v_e - \beta u_e). \end{aligned} \tag{5.19}$$

Note that $1 - u_e - \alpha v_e$ and $1 - v_e - \beta u_e$ from (5.19) are zero according to (5.16). Next, we introduce $\omega_n = (u_n, v_n)$ and rewrite (5.19) as

$$\frac{\partial \omega_1}{\partial t} = \mathcal{L} w_1, \tag{5.20}$$

where $\mathcal{L}$ is the linear operator given by (5.5). We then seek a weakly nonlinear solution ω_n in the form

$$Z(\chi,\tau)\mathrm{e}^{\pm ikx}\mathrm{e}^{\sigma t}\begin{bmatrix} u_c^{\pm} \\ v_c^{\pm} \end{bmatrix}, \tag{5.21}$$

where $u_c^{\pm}$ and $v_c^{\pm}$ are constants and $Z \in \mathbb{C}$ is the complex amplitude. Using

the result that

$$\begin{aligned}\mathcal{L}\left(\mathrm{e}^{ikx}\mathrm{e}^{\sigma t}\right) &= \mathrm{e}^{ikx}\mathrm{e}^{\sigma t}\big[-Dk^2 + J_0 - J_1(k)\big] \\ &= \mathrm{e}^{ikx}\mathrm{e}^{\sigma t}A(k),\end{aligned} \tag{5.22}$$

a substitution of (5.21) into (5.20) returns $\big[A(\pm k) - \sigma I_2\big]\omega_c^{\pm} = 0$ where $\omega_c^{\pm} = \begin{bmatrix} u_c^{\pm} \\ v_c^{\pm} \end{bmatrix}$. Hence, at the bifurcation point where $\mathrm{Re}(\sigma) = 0$ or $\mathcal{L}\omega_1 = 0$, we have $\lambda = \lambda_c$ and $k = k_c$. Therefore, $\omega_c^{\pm}$ is a null vector of $A(\pm k_c)$, i.e. $A(\pm k_c)\omega_c^{\pm} = 0$, where

$$\omega_c^{\pm} = \begin{bmatrix} \frac{-A_{12}(\pm k_c)}{A_{11}(\pm k_c)} \\ 1 \end{bmatrix}. \tag{5.23}$$

For even kernels, $A(k) = A(-k)$ is symmetric. Therefore, $\omega_c^{\pm} = \omega_c$ and $A(k_c)\omega_c = 0$. Finally, we write the weakly nonlinear solution of $\mathcal{L}\omega_1 = 0$ as

$$\omega_1(x, t, \chi, \tau) = \big[Z(\chi, \tau)\mathrm{e}^{ik_c x} + \text{c.c.}\big]\omega_c = \begin{bmatrix} u_1 \\ v_1 \end{bmatrix}, \tag{5.24}$$

where $\omega_c \in \mathbb{R}^2$. Equation (5.24) means that the null space of $\mathcal{L}$ is spanned by $\mathrm{e}^{\pm ik_c x}\omega_c$.

Next, we balance the terms at $O(\epsilon^2)$ in (5.14) and (5.15) to yield a system

$$\begin{aligned}\left(\frac{\partial}{\partial t} - D_1\frac{\partial^2}{\partial x^2}\right)u_2 - 2D_1\frac{\partial^2 u_1}{\partial x \partial \chi} &= u_e\left(-\phi_1 * u_2 + \phi_1^y * \frac{\partial u_1}{\partial \chi} - \alpha v_2\right) \\ &\quad + u_1(-\phi_1 * u_1 - \alpha v_1), \\ \left(\frac{\partial}{\partial t} - D_2\frac{\partial^2}{\partial x^2}\right)v_2 - 2D_2\frac{\partial^2 v_1}{\partial x \partial \chi} &= Rv_e\left(-\phi_c * v_2 + \phi_c^y * \frac{\partial v_1}{\partial \chi} - \beta u_2 - \phi_c'\delta * v_e\right) \\ &\quad + Rv_1(-\phi_c * v_1 - \beta u_1).\end{aligned} \tag{5.25}$$

Note that the convolution term $\phi_c'\delta * v_e$ in (5.25) vanishes by the Leibniz integral

rule since

$$\begin{aligned}\int_{-\infty}^{\infty}\phi_c^{'}\,\mathrm{d}x &= \int_{-\infty}^{\infty}\frac{\partial\phi_c}{\partial\lambda}\bigg|_{\lambda=\lambda_c}\mathrm{d}x = \frac{\partial}{\partial\lambda}\int_{-\infty}^{\infty}\phi_c\,\mathrm{d}x\bigg|_{\lambda=\lambda_c}\\ &= \frac{\partial}{\partial\lambda}\int_{-\infty}^{\infty}\left[\frac{1}{\lambda}\psi\left(\frac{x}{\lambda}\right)\right]\mathrm{d}x\bigg|_{\lambda=\lambda_c} = \frac{\partial}{\partial\lambda}1\bigg|_{\lambda=\lambda_c} = 0,\end{aligned} \tag{5.26}$$

due to the kernel assumption mentioned earlier. We can now rewrite the system (5.25) in the form

$$\begin{aligned}\left(\frac{\partial}{\partial t}-\mathcal{L}\right)\omega_2 = 2D\frac{\partial^2\omega_1}{\partial x\partial\chi} + \begin{bmatrix} u_e\phi_1^y* & 0\\ 0 & Rv_e\phi_c^y* \end{bmatrix}\frac{\partial\omega_1}{\partial\chi}\\ - \begin{bmatrix} u_1\phi_1 * u_1 + \alpha u_1 v_1\\ Rv_1\phi_c * v_1 + R\beta u_1 v_1 \end{bmatrix}.\end{aligned} \tag{5.27}$$

On the left-hand side of (5.27), we know that $\partial\omega_2/\partial t = 0$ for solutions in the form of $\mathrm{e}^{ikx+\sigma t}$ when $\sigma = 0$. To simplify the expression on the right-hand side, we use the property of the bifurcation that requires $\mathrm{d}\sigma/\mathrm{d}k = 0$ at $k = k_c$. Differentiating the characteristic polynomial (5.8) with respect to k and setting $\sigma = 0$ yields

$$\frac{\mathrm{d}\sigma}{\mathrm{d}k} = \frac{\frac{\mathrm{d}}{\mathrm{d}k}\mathrm{Det(A(k))}}{\mathrm{Tr(A(k))}} = \frac{\mathrm{Tr}\left[\mathrm{adj}(A(k))\frac{\mathrm{d}}{\mathrm{d}k}A(k)\right]}{\mathrm{Tr(A(k))}}, \tag{5.28}$$

by Jacobi's formula. Therefore, the neutral condition requires that $\mathrm{d}A/\mathrm{d}k = 0$ to enforce $\mathrm{d}\sigma/\mathrm{d}k = 0$ at $k = k_c$. Recall that $A(k) = -Dk^2 + J_0 - J_1(k)$ and thus

$$\frac{\mathrm{d}A}{\mathrm{d}k} = -2Dk - \begin{bmatrix} u_e\overline{\phi}_1^{\prime}(k) & 0\\ 0 & Rv_e\overline{\phi}_c^{\prime}(k) \end{bmatrix}. \tag{5.29}$$

Since the first two terms on the right-hand side of (5.27) involve

$$\left\{2D\frac{\partial}{\partial x} + \begin{bmatrix} u_e\phi_1^y* & 0\\ 0 & Rv_e\phi_1^y* \end{bmatrix}\right\}\mathrm{e}^{ikx} = -i\frac{\mathrm{d}A}{\mathrm{d}k}, \tag{5.30}$$

which is equal to zero, the system (5.27) (at bifurcation) can be further reduced to the form

$$\mathcal{L}\omega_2 = \begin{bmatrix} u_1\phi_1 * u_1 + \alpha u_1 v_1 \\ R v_1 \phi_c * v_1 + R\beta u_1 v_1 \end{bmatrix}. \tag{5.31}$$

We now set

$$\omega_2 = \omega_+ \mathrm{e}^{2ik_c x} + \omega_- \mathrm{e}^{-2ik_c x} + \omega_0 + \xi\omega_1. \tag{5.32}$$

Here, the constant, ξ, remains undetermined at this order of perturbation but does not appear in the amplitude equation for $Z(\chi,\tau)$. Upon substituting (5.32) into (5.31), we obtain

$$\begin{aligned} &A(2k_c)\omega_+ \mathrm{e}^{2ik_c x} + A(-2k_c)\omega_- \mathrm{e}^{-2ik_c x} + A(0)\omega_0 + \xi\mathcal{L}\omega_1 \\ &= \begin{bmatrix} \left(Z\mathrm{e}^{ik_c x} + Z^*\mathrm{e}^{-ik_c x}\right)\left(Z\overline{\phi}_1(k_c)\mathrm{e}^{ik_c x} + Z^*\overline{\phi}_1(-k_c)\mathrm{e}^{-ik_c x}\right) u_c^2 \\ R\left(Z\mathrm{e}^{ik_c x} + Z^*\mathrm{e}^{-ik_c x}\right)\left(Z\overline{\phi}_c(k_c)\mathrm{e}^{ik_c x} + Z^*\overline{\phi}_c(-k_c)\mathrm{e}^{-ik_c x}\right) v_c^2 \end{bmatrix} \\ &+ \begin{bmatrix} \alpha\left(Z\mathrm{e}^{ik_c x} + Z^*\mathrm{e}^{-ik_c x}\right)\left(Z\mathrm{e}^{ik_c x} + Z^*\mathrm{e}^{-ik_c x}\right) u_c v_c \\ R\beta\left(Z\mathrm{e}^{ik_c x} + Z^*\mathrm{e}^{-ik_c x}\right)\left(Z\mathrm{e}^{ik_c x} + Z^*\mathrm{e}^{-ik_c x}\right) u_c v_c \end{bmatrix}. \end{aligned} \tag{5.33}$$

Note that the Fourier transform of even kernels ϕ is symmetric, i.e. $\overline{\phi}(k_c) = \overline{\phi}(-k_c)$. Balancing terms at powers of $\mathrm{e}^{ik_c x}$ therefore yields the equations

$$\begin{aligned} A(0)\omega_0 &= 2|Z|^2 \begin{bmatrix} \overline{\phi}_1(k_c)u_c^2 + \alpha u_c v_c \\ R\overline{\phi}_c(k_c)v_c^2 + R\beta u_c v_c \end{bmatrix}, \\ A(2k_c)\omega_+ &= Z^2 \begin{bmatrix} \overline{\phi}_1(k_c)u_c^2 + \alpha u_c v_c \\ R\overline{\phi}_c(k_c)v_c^2 + R\beta u_c v_c \end{bmatrix}, \\ A(-2k_c)\omega_- &= (Z^*)^2 \begin{bmatrix} \overline{\phi}_1(-k_c)u_c^2 + \alpha u_c v_c \\ R\overline{\phi}_c(-k_c)v_c^2 + R\beta u_c v_c \end{bmatrix}, \end{aligned} \tag{5.34}$$

where $\omega_+ = \omega_-^*$.

Finally, we balance the terms of $O(\epsilon^3)$ in (5.1) to obtain

$$\begin{aligned}
&\left(\frac{\partial}{\partial t} - D_1\frac{\partial^2}{\partial x^2}\right)u_3 + \left(\frac{\partial}{\partial \tau} - D_1\frac{\partial^2}{\partial \chi^2}\right)u_1 - 2D_1\frac{\partial^2 u_2}{\partial x \partial \chi} \\
&= u_e\left(-\phi_1 * u_3 + \phi_1^y * \frac{\partial u_2}{\partial \chi} - \frac{1}{2}\phi_1^{yy} * \frac{\partial^2 u_1}{\partial \chi^2} - \alpha v_3\right) \\
&\quad + u_1\left(-\phi_1 * u_2 + \phi_1^y * \frac{\partial u_1}{\partial \chi} - \alpha v_2\right) + u_2(-\phi_1 * u_1 - \alpha v_1) + u_3(1 - u_e - \alpha v_e), \\
&\left(\frac{\partial}{\partial t} - D_2\frac{\partial^2}{\partial x^2}\right)v_3 + \left(\frac{\partial}{\partial \tau} - D_2\frac{\partial^2}{\partial \chi^2}\right)v_1 - 2D_2\frac{\partial^2 v_2}{\partial x \partial \chi} \\
&= Rv_e\left(-\phi_c * v_3 + \phi_c^y * \frac{\partial v_2}{\partial \chi} - \frac{1}{2}\phi_c^{yy} * \frac{\partial^2 v_1}{\partial \chi^2} - \beta u_3\right) \\
&\quad + Rv_1\left(-\phi_c * v_2 + \phi_c^y * \frac{\partial v_1}{\partial \chi} - \beta u_2\right) + Rv_2(\phi_c * v_1 - \beta u_1) + Rv_3(1 - v_e - \beta u_e) \\
&\quad - Rv_e\phi_c'\delta * v_1 - Rv_1\phi_c'\delta * v_e.
\end{aligned} \tag{5.35}$$

Using the property that $\phi_c' * v_e = 0$ in (5.26) and the results of balancing terms at $O(1)$, the system (5.35) is simplified to

$$\begin{aligned}
&\left(\frac{\partial}{\partial t} - \mathcal{L}\right)\omega_3 + \left(\frac{\partial}{\partial \tau} - D\frac{\partial^2}{\partial \chi^2}\right)\omega_1 \\
&= \left(2D\frac{\partial^2}{\partial x \partial \chi} + \begin{bmatrix} u_e\phi_1^y * & 0 \\ 0 & Rv_e\phi_c^y * \end{bmatrix}\frac{\partial}{\partial \chi}\right)\omega_2 - \frac{1}{2}\begin{bmatrix} u_e\phi_1^{yy} * & 0 \\ 0 & Rv_e\phi_c^{yy} * \end{bmatrix}\frac{\partial^2 \omega_1}{\partial \chi^2} \\
&+ \begin{bmatrix} -u_1\phi_1 * u_2 + u_1\phi_1^y * \frac{\partial u_1}{\partial \chi} - \alpha u_1 v_2 - u_2\phi_1 * u_1 - \alpha u_2 v_1 \\ -Rv_1\phi_c * v_2 + Rv_1\phi_c^y * \frac{\partial v_1}{\partial \chi} - R\beta v_1 u_2 - Rv_2\phi_c * v_1 - R\beta v_2 u_1 - \delta Rv_e\phi_c' * v_1 \end{bmatrix}.
\end{aligned} \tag{5.36}$$

Notice that the systems obtained from balancing terms at powers of ϵ, i.e. (5.16), (5.20), (5.31) and (5.36) have the general form $\mathcal{L}\omega_n = g_n(\omega_1, \omega_2, \ldots, \omega_{n-1})$(with $\mathcal{L}\omega_1 = 0$) and the right-hand side ω_n will always contain known quantities. The first system (5.16) in the hierarchy fixes the coexisting steady-state (u_e, v_e). The second system (5.31) returns the linear solution $\omega_1 = \left[Z(\chi, \tau)\mathrm{e}^{ik_c x} + \text{c.c.}\right]\omega_c$.

By assuming that ω_2 is a linear combination of terms present in ω_1^2, we use substitution to find the particular solution of ω_2. For higher orders (5.36), we use Fredholm alternative to determine ω_2. By deriving and applying solvability conditions to the system, we can form a dynamical equation for the complex amplitude $Z(\chi, \tau)$.

To achieve this, we first define the Euclidean dot product of two vectors consisting of two periodic functions using the same idea as the formula (2.14) in Subsection 2.2.2 by replacing the inner product with the standard vector dot product. Then, the Fredholm alternative states that for all $f \in \ker \mathcal{L}^\dagger$, then $\langle f, \mathcal{L}\omega_n \rangle = \langle \mathcal{L}^\dagger f, \omega_n \rangle = 0$ where $\mathcal{L}^\dagger$ is the adjoint of $\mathcal{L}$. Clearly, $\mathcal{L}$ is not self-adjoint as the linear operator is not symmetric (see (5.5)). Therefore, we have to evaluate the vector b such that $\mathcal{L}^\dagger(\mathrm{e}^{ikx}b) = 0$ which yields $A^\dagger(k)b = 0$ from (5.22). Since the adjoint of a square matrix is the same as its conjugate transpose, and $A(k)$ is real (see (5.7)), we have that $A^\dagger = (A^*)^T = A^T$. For $k = k_c$, $A^T(k_c)b = 0$ gives

$$b = \begin{bmatrix} \frac{-A_{21}(k_c)}{A_{11}(k_c)} \\ 1 \end{bmatrix}. \tag{5.37}$$

Hence, the set of solvability conditions are $\langle \mathrm{e}^{\pm ik_c x}b, \mathcal{L}\omega_3 \rangle = 0$. To evaluate the solvability condition at $n = 3$, we make use of the result $\langle \mathrm{e}^{imk_c x}b, \mathrm{e}^{ink_c x}\omega_c \rangle = \delta_{m,n} b \cdot \omega_c$ and then choose the scale of b and ω_c such that $b \cdot \omega_c = 1$. Next, we project all the terms in (5.36) onto $\mathrm{e}^{ik_c x}b$ and make use of the results

$$\begin{gathered} \frac{\partial \omega_3}{\partial t} = 0, \qquad \langle \mathrm{e}^{ik_c x}b, \mathcal{L}\omega_3 \rangle = 0, \qquad \left\langle \mathrm{e}^{ik_c x}b, \begin{bmatrix} u_1 \phi_1^y * \frac{\partial u_1}{\partial \chi} \\ R v_1 \phi_c^y * \frac{\partial v_1}{\partial \chi} \end{bmatrix} \right\rangle = 0, \\ \left\langle \mathrm{e}^{ik_c x}b, \left(2D \frac{\partial^2}{\partial x \partial \chi} + \begin{bmatrix} u_e \phi_1^y * & 0 \\ 0 & R v_e \phi_c^y * \end{bmatrix} \frac{\partial}{\partial \chi} \right) \omega_2 \right\rangle = 0, \end{gathered} \tag{5.38}$$

to obtain

$$\begin{aligned}
&\left\langle \mathrm{e}^{ik_c x} b, \left(\frac{\partial}{\partial \tau} - D\frac{\partial^2}{\partial \chi^2}\right)\right\rangle \omega_1 \\
&= \left\langle \mathrm{e}^{ik_c x} b, -\frac{1}{2}\begin{bmatrix} u_e \phi_1^{yy} * & 0 \\ 0 & R v_e \phi_c^{yy} * \end{bmatrix} \frac{\partial^2 \omega_1}{\partial \chi^2}\right\rangle \\
&+ \left\langle \mathrm{e}^{ik_c x} b, \begin{bmatrix} -u_1\phi_1 * u_2 - \alpha u_1 v_2 - u_2 \phi_1 * u_1 - \alpha u_2 v_1 \\ -Rv_1\phi_c * v_2 - R\beta v_1 u_2 - Rv_2\phi_c * v_1 - R\beta v_2 u_1 \end{bmatrix}\right\rangle \\
&+ \left\langle \mathrm{e}^{ik_c x} b, \begin{bmatrix} 0 \\ -\delta R v_e \phi_c' * v_1 \end{bmatrix}\right\rangle.
\end{aligned} \tag{5.39}$$

By substituting ω_1 into (5.39), it is simple to show that

$$\left\langle \mathrm{e}^{ikx} b, \left(\frac{\partial}{\partial \tau} - D\frac{\partial^2}{\partial \chi^2}\right)\right\rangle \omega_1 = b \cdot \left(\frac{\partial Z}{\partial \tau} - D\frac{\partial^2 Z}{\partial \chi^2}\right)\omega_c, \tag{5.40}$$

$$\left\langle \mathrm{e}^{ikx} b, -\frac{1}{2}\begin{bmatrix} u_e \phi_1^{yy} * & 0 \\ 0 & R v_e \phi_c^{yy} * \end{bmatrix} \frac{\partial^2 \omega_1}{\partial \chi^2}\right\rangle = \frac{1}{2}\left(b \cdot \begin{bmatrix} u_e \overline{\phi}_1''(k_c) & 0 \\ 0 & R v_e \overline{\phi}_c''(k_c) \end{bmatrix} \omega_c\right) \frac{\partial^2 Z}{\partial \chi^2}. \tag{5.41}$$

On the other hand, the last term on the right-hand side of (5.39) becomes

$$\left\langle \mathrm{e}^{ikx} b, \begin{bmatrix} 0 \\ -\delta R v_e \phi_c' * v_1 \end{bmatrix}\right\rangle = -R v_e \delta \overline{a}(k_c)\left(b \cdot \begin{bmatrix} 0 & 0 \\ 0 & 1 \end{bmatrix} \omega_c\right) Z, \tag{5.42}$$

where $\overline{a}(k_c)$ is the Fourier transform of ϕ_c' such that (see Appendix B.1 for detailed workings)

$$\overline{a}(k_c) = \int_{-\infty}^{\infty} \frac{\partial \phi_c(y)}{\partial \lambda}\bigg|_{\lambda=\lambda_c} \mathrm{e}^{-ik_c y}\,\mathrm{d}y = k_c \overline{\psi}'(k_c \lambda_c). \tag{5.43}$$

Finally, the remaining projection (see Appendix B.1 for detailed workings)

results in the cubic term

$$
\begin{aligned}
&\left\langle \mathrm{e}^{ik_c x} b, \begin{bmatrix} -u_1\phi_1 * u_2 - \alpha u_1 v_2 - u_2\phi_1 * u_1 - \alpha u_2 v_1 \\ -Rv_1\phi_c * v_2 - R\beta v_1 u_2 - Rv_2\phi_c * v_1 - R\beta v_2 u_1 \end{bmatrix} \right\rangle \\
&= -b \cdot \left\{ Z \begin{bmatrix} u_c\left(\overline{\phi}_1(0) + \overline{\phi}_1(k_c)\right) + \alpha v_c & \alpha u_c \\ R\beta v_c & v_c R\left[\overline{\phi}_c(0) + \overline{\phi}_c(k_c)\right] + R\beta c u_c \end{bmatrix} \omega_0 \right. \\
&\qquad \left. + Z^* \begin{bmatrix} u_c\left(\overline{\phi}_1(2k_c) + \overline{\phi}_1(k_c)\right) + \alpha v_c & \alpha u_c \\ R\beta v_c & v_c R\left[\overline{\phi}_c(2k_c) + \overline{\phi}_c(k_c)\right] + R\beta u_c \end{bmatrix} \omega_+ \right\} \\
&= -b \cdot \left\{ Z|Z|^2 \left\{ 2P_1 \left[A(0)\right]^{-1} + P_2 \left[A(2k_c)\right]^{-1} \right\} \begin{bmatrix} \overline{\phi}_1(k_c) u_c^2 + \alpha u_c v_c \\ R\overline{\phi}_c(k_c) v_c^2 + R\beta u_c v_c \end{bmatrix} \right\} \\
&\equiv CZ|Z|^2,
\end{aligned}
\tag{5.44}
$$

where P_1 and P_2 denote the matrices in the second line of (B.13), and ω_0 and ω_+ are obtained from the system (5.34).

Combining, (5.40), (5.41), (5.42) and (5.44), we obtain the amplitude equation or envelope equation in the form of a Ginzburg-Landau equation:

$$
\frac{\partial Z}{\partial \tau} = \gamma \frac{\partial^2 Z}{\partial \chi^2} + Z(\eta - \nu|Z|^2), \tag{5.45}
$$

where

$$
\begin{aligned}
\gamma &= b \cdot \left\{ \left(D + \frac{1}{2} \begin{bmatrix} u_e \overline{\phi}_1''(k_c) & 0 \\ 0 & Rv_e \overline{\phi}_c''(k_c) \end{bmatrix} \right) \omega_c \right\}, \\
\eta &= -Rv_e \delta\overline{a}(k_c) \left(b \cdot \begin{bmatrix} 0 & 0 \\ 0 & 1 \end{bmatrix} \omega_c \right), \\
\nu &= -C.
\end{aligned}
\tag{5.46}
$$

Here, the amplitude Z is complex in general but the coefficients are real.

5.3 Analysis of amplitude equation

We now begin the analysis of the amplitude equation (5.45) by considering the spatially uniform case of the equation. By introducing $Z = re^{i\theta}$, we may rewrite the equation as

$$\frac{\mathrm{d}r}{\mathrm{d}\tau} = r(\eta - \nu r^2), \qquad \frac{\mathrm{d}\theta}{\mathrm{d}\tau} = 0, \tag{5.47}$$

which returns the steady states $(r_0, \theta_0) = (0, \theta_c)$ and $(r_0, \theta_0) = \left(\sqrt{\eta/\nu}, \theta_c\right)$ if $\eta/\nu > 0$, where θ_c is an arbitrary constant.

The full amplitude equation can be written in (r, θ) parameter space as

$$\begin{aligned} \frac{\partial r}{\partial \tau} &= \gamma\left[\frac{\partial^2 r}{\partial \chi^2} - r\left(\frac{\partial \theta}{\partial \chi}\right)^2\right] + r(\eta - \nu r^2) \\ r\frac{\partial \theta}{\partial \tau} &= \gamma\left(2\frac{\partial r}{\partial \chi}\frac{\partial \theta}{\partial \chi} + r\frac{\partial^2 \theta}{\partial \chi^2}\right). \end{aligned} \tag{5.48}$$

To study the linear stability of the steady states, we linearise the system (5.48) by writing $(r(\chi, \tau), \theta(\chi, \tau)) = (r_0, \theta_0) + \left(\overline{r}, \overline{\theta}\right)$ for $\overline{r}$ and $\overline{\theta}$ small to give

$$\begin{aligned} \frac{\partial r}{\partial \tau} &= \gamma\frac{\partial^2 \overline{r}}{\partial \chi^2} + \overline{r}(\eta - 3r_0^2\nu) \\ \frac{\partial \overline{\theta}}{\partial \tau} &= \gamma\frac{\partial^2 \overline{\theta}}{\partial \chi^2}. \end{aligned} \tag{5.49}$$

Notice that (5.49) is an uncoupled system that can be solved separately. By substituting $\overline{\theta} = \hat{\theta}e^{\rho\tau + i\kappa\chi}$ ($\hat{\theta}$ = constant) into the system, we get $\rho = -\gamma\kappa^2$ which is stable for $\gamma > 0$. Next, we let $\overline{r} = \hat{r}e^{\rho\tau + i\kappa\chi}$ and substitute it into the system (5.49) to return $\rho = -\gamma\kappa^2 + \eta - 3r_0\nu$, which is the eigenvalue for the r component. In the absence of spatial variation, i.e. $\kappa = 0$, the eigenvalue becomes $\rho = \eta - 3r_0^2\nu$. At $r_0 = 0$, bifurcation occurs at $\rho = 0$ or $\eta = 0$. Therefore, the steady state $(0, \theta_c)$ is stable when $\eta < 0$ and is unstable when $\eta > 0$. At $r_0 = \sqrt{\eta/\nu}$, $\rho = -2\eta$ and hence bifurcation occurs at $\eta = 0$. Since

this steady state only exists when $\eta/\nu > 0$, the stability of the steady state $\left(\sqrt{\eta/\nu}, \theta_c\right)$ in terms of η depends on the sign of ν.

5.3.1 Bifurcation type in terms of β

We now take a closer look at how ν, the coefficient of the cubic term in the amplitude equation (5.45), changes sign with respect to β. This will, in turn, give us an insight into how the solutions bifurcate along the neutral curve in (α, β) parameter space.

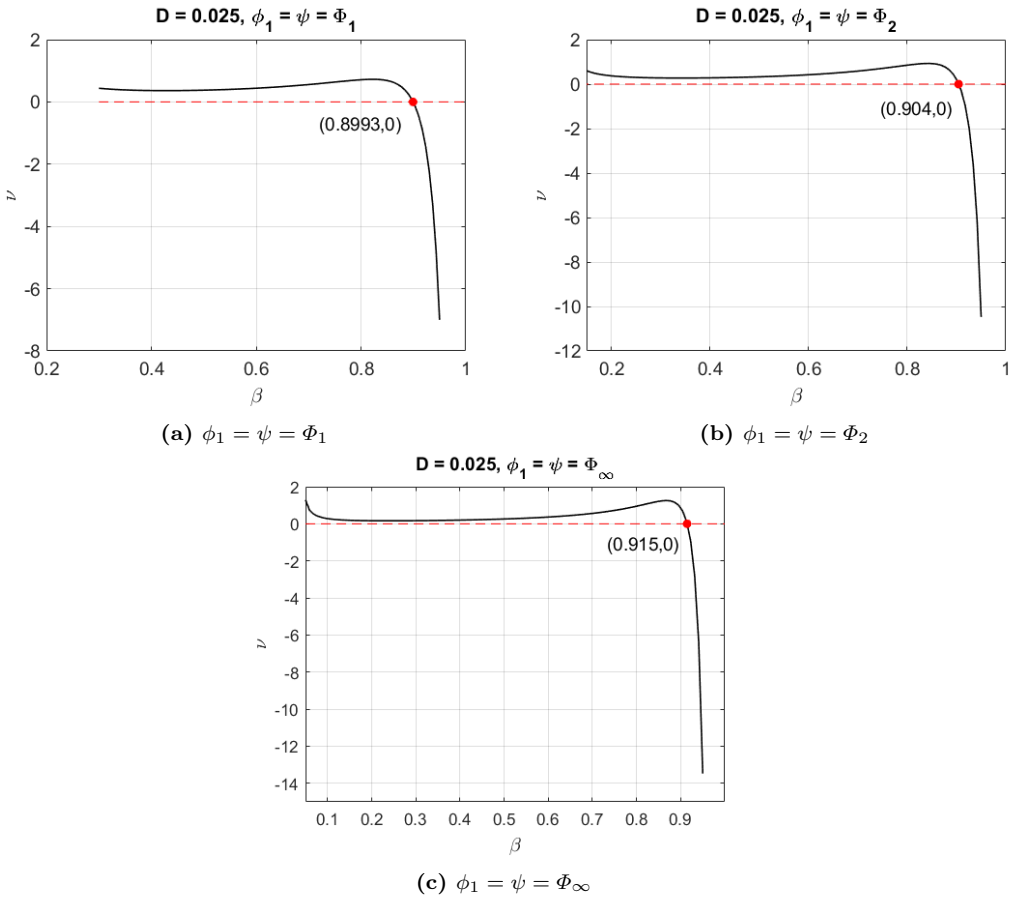
In the time-independent problem

$$\begin{aligned} 0 &= D_1 \frac{\mathrm{d}^2 u}{\mathrm{d}x^2} + u\left(1 - \int_{-\infty}^{\infty} \phi_1(x-y)u(y)\,\mathrm{d}y - \alpha v\right), \\ 0 &= D_2 \frac{\mathrm{d}^2 v}{\mathrm{d}x^2} + Rv\left(1 - \int_{-\infty}^{\infty} \phi_2(x-y)v(y)\,\mathrm{d}y - \beta u\right), \end{aligned} \tag{5.50}$$

the second equation in the NLLV system (5.50) depends only on the ratio D_2/R. Increasing R has the same effect as decreasing D_2 and vice versa. Hence, we will let $R = 1$ throughout this chapter for simplicity. For each of the kernel pairs, we fix $D = 0.025$, $\lambda = 1$ and $\beta \in (0.05, 0.99)$ and solve for α and k_c on the neutral curve. These values are then used to compute ν, plotted against β in Figure 5.1.

Notice that ν changes from positive to negative at $\beta = 0.8993$ when both kernels are $\phi_1 = \psi = \Phi_1$, at $\beta = 0.904$ when both kernels are $\phi_1 = \psi = \Phi_2$, and at $\beta = 0.915$ when both kernels are $\phi_1 = \psi = \Phi_\infty$. Therefore, in general, for $\beta < 0.89$, η/ν is positive when $\eta > 0$, and the steady state $\sqrt{\eta/\nu}$ is stable as $\rho = -2\eta$. On the other hand, when $\beta > 0.92$, $\sqrt{\eta/\nu}$ is only real when $\eta < 0$, indicating that $r_0 = \sqrt{\eta/\nu}$ is unstable. Therefore, we expect the bifurcation to be supercritical when $\beta < 0.89$ and subcritical when $\beta > 0.92$ for all the kernel pairs.

The bifurcation diagrams of r_0 against η for $\phi_1 = \psi = \Phi_1$ are shown in Figure



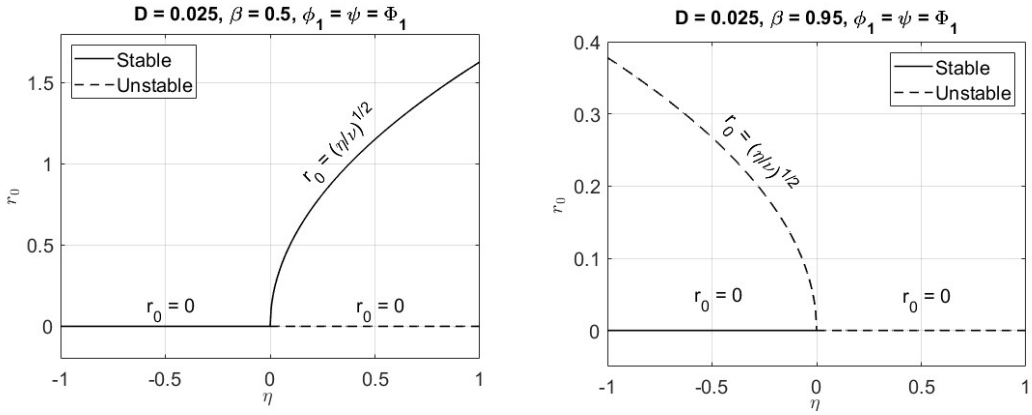
(a) $\phi_1 = \psi = \Phi_1$ **(b)** $\phi_1 = \psi = \Phi_2$

(c) $\phi_1 = \psi = \Phi_\infty$

Figure 5.1: *Plots of ν from (5.46) against β for three kernel pairs along the neutral curves from (4.9).*

5.2. We observe a supercritical bifurcation when $\beta = 0.25$ and a subcritical bifurcation when $\beta = 0.95$, which is in agreement with the analysis above. Similar bifurcations are expected for the two other kernel pairs and will not be shown here.

When $\kappa \neq 0$, we are interested in the presence of another bifurcation point, κ_c, where the stable solutions become unstable at $\rho = 0$. At $r_0 = 0$, $\rho = -\gamma\kappa^2 + \eta$. For $\eta > 0$, the solutions are already unstable when $\kappa = 0$. When $\eta < 0$, $\kappa = (\eta/\nu)$ is complex when $\gamma > 0$ and hence no real κ_c exists . At $r_0 = \sqrt{\eta/\nu}$, the stable branch only exists when $\eta > 0$ and $\beta < 0.89$. For $\rho = -\gamma\kappa^2 - 2\eta$, $\rho < 0$ for $\eta > 0$ and hence the solutions remain stable. Therefore, no secondary bifurcation or long wavelength instability is observed.



(a) *Supercritical bifurcation* **(b)** *Subcritical bifurcation*

Figure 5.2: *Bifurcation diagram from the analysis of the amplitude equation (5.45) for r_0 with no spatial variation ($\kappa = 0$). Solid lines represent the stable branches, and broken lines the unstable branches. The (α, β) values are (a) (0.23664,0.5) and (b) (0.39001,0.95).*

5.4 Weakly nonlinear solution

This section compares the analytical amplitudes obtained from weakly nonlinear analysis with the numerical amplitudes of the steady-state problem (5.50).

5.4.1 Weakly nonlinear amplitude

We define the weakly nonlinear amplitude for the solution around the bifurcation point as $\|2\,\mathrm{Re}(\omega_1)\|$ to consider the complex conjugate term.

5.4.2 Numerical amplitude

In this section, we use a continuation method to numerically obtain the amplitudes of the solutions of the steady-state problem (5.50) and compare them with the theoretical predictions from the weakly nonlinear analysis. The details of the numerical discretisation can be found in Section 4.5. The only difference is that we now solve the time-independent system using *fsolve* instead of *ode45* in MATLAB.

For each of the kernel pairs, $\phi_1 = \psi = \Phi_1$, $\phi_1 = \psi = \Phi_2$ and $\phi_1 = \psi = \Phi_\infty$, we fix $D_1 = D_2 = 0.025$, $\lambda_c = 1$, $\beta = 0.25, 0.5, 0.95$, and solve for the corresponding α and k_c on the neutral curve using *fsolve* in MATLAB. Then, we obtain the

weakly nonlinear amplitude for the initial value of λ, λ_0, and use it as the initial guess for the *fsolve* for numerical u and v. The solution will then be used as the next initial guess for the next λ. The numerical amplitude for u is defined as $(\max u - \min u)/2$ and similarly for v. From the weakly nonlinear solution, $\eta \propto \lambda - \lambda_c$, therefore plotting the weakly nonlinear amplitude against λ is equivalent to transforming the bifurcation diagram in Figure 5.2 by λ_c to the right (as $\lambda \propto \eta + \lambda_c$) along with some stretch factor in the x or y direction.

When $\beta = 0.25$

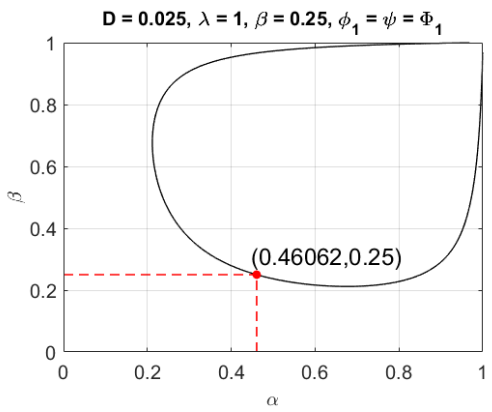
From subsection (5.3.1), we expect a supercritical bifurcation to occur for $\beta < 0.89$. Therefore, we choose $\lambda_0 = 1.04$ ($> \lambda_c$) to compute the numerical amplitude in the continuation method. Using λ_0, we first compute the weakly nonlinear amplitude y_0 and let $(u(x,0), v(x,0)) = (u_e, v_e) + y_0 \cos(k_c x)$ to be our initial guess for the numerical solution. From there, we evaluate the numerical solutions, which will then be used as the initial guess for decreasing λ down to $\lambda = 0.95$. The α and k_c values for each kernel combination on the neutral curves (obtained in Chapter 4) are summarised in Table 5.1. For each of these kernel pairs, the weakly nonlinear amplitude is plotted against λ and is compared with its numerical amplitude in Figure 5.3.

Kernel	α	k_c
Φ_1	0.46062	2.08767
Φ_2	0.21804	2.09187
Φ_∞	0.07106	1.87864

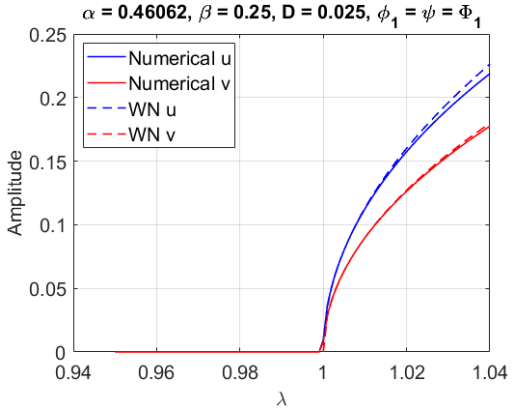
Table 5.1: *Summary of α and k_c values of different kernels, $\phi_1 = \psi = \Phi_n$ where $n = 1, 2, \infty$, for $\beta = 0.25$ on the neutral curves from (4.9).*

As λ increases beyond $\lambda_c = 1$, the steady state becomes unstable, and a stable, spatially periodic pattern emerges. The larger the value of λ, the larger the amplitude of the solutions. From Figure 5.3, the weakly nonlinear amplitude of each kernel pair is in good agreement with the numerical amplitude around the bifurcation point $\lambda_c = 1$. However, the difference between analytical and numerical amplitudes increases with $|\lambda - \lambda_c|$, and the numerical amplitude is

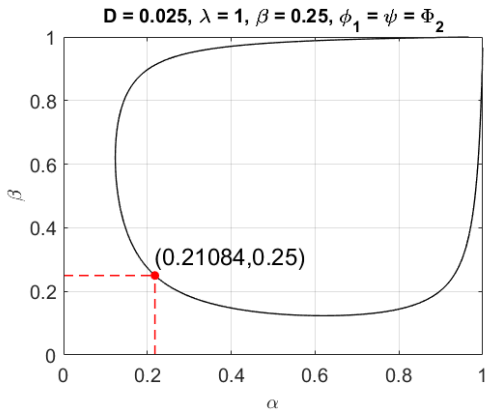
slightly smaller than the weakly nonlinear amplitude. Note that the bifurcation for the amplitudes is supercritical. Despite the coexisting state being unstable for $\lambda > 1$, the solution oscillates in space at a stable amplitude with uniform wavelength.



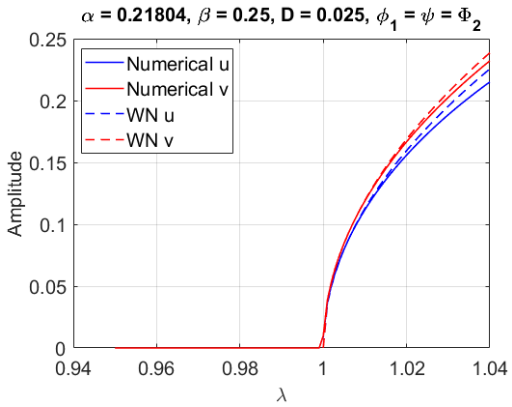
(a) *Neutral curve for* $\phi_1 = \psi = \Phi_1$.



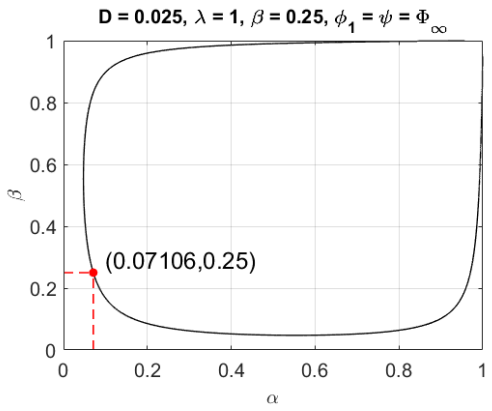
(b) *Amplitude vs* λ *for* $\phi_1 = \psi = \Phi_1$.



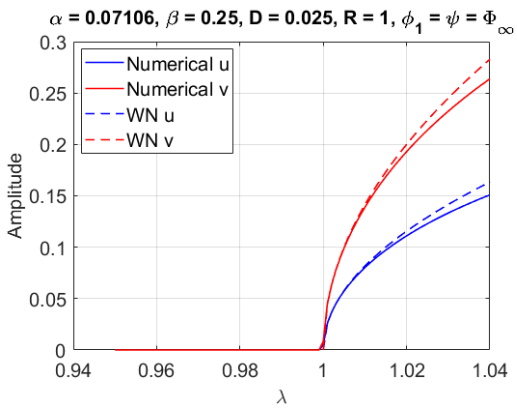
(c) *Neutral curve for* $\phi_1 = \psi = \Phi_2$.



(d) *Amplitude vs* λ *for* $\phi_1 = \psi = \Phi_2$.



(e) *Neutral curve for* $\phi_1 = \psi = \Phi_\infty$.

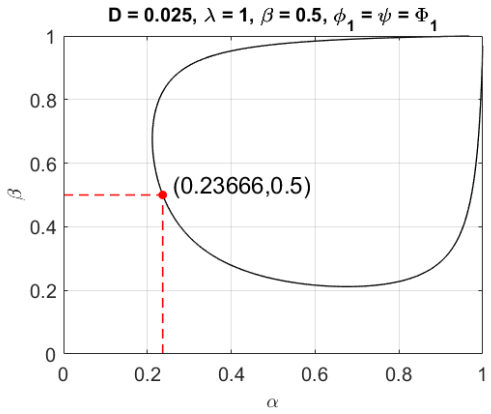


(f) *Amplitude vs* λ *for* $\phi_1 = \psi = \Phi_\infty$.

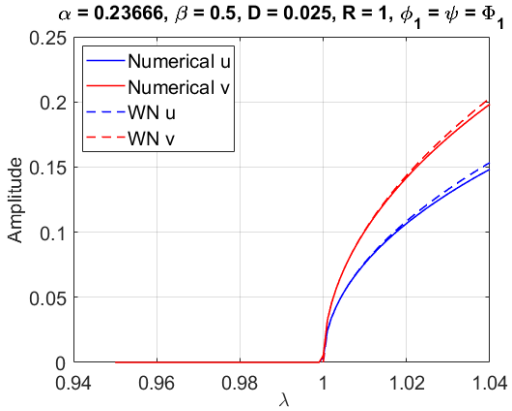
Figure 5.3: *Plot of neutral curves from (4.9), numerical amplitudes of* u *and* v *from (5.50) and weakly nonlinear (WN) amplitudes of* u *and* v *when* $\beta = 0.25$. *The values of* α *and* k_c *are summarised in Table 5.1.*

When $\beta = 0.5$

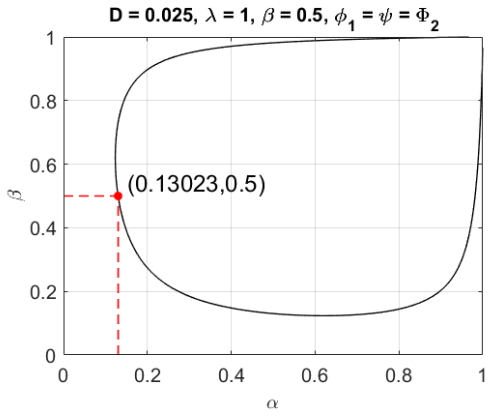
Table 5.2 shows the α and k_c values for each kernel combination on the neutral curves. The weakly nonlinear and numerical amplitudes for each kernel pair are plotted against λ in Figure 5.4.



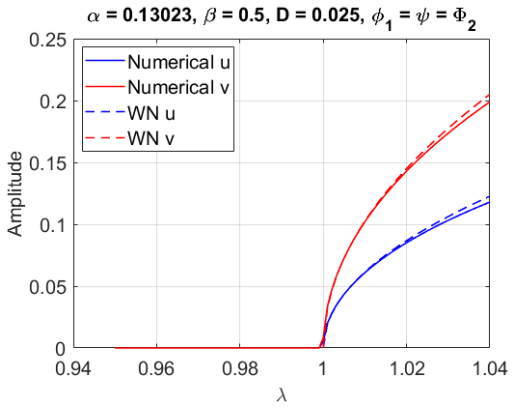
(a) *Neutral curve for* $\phi_1 = \psi = \Phi_1$.



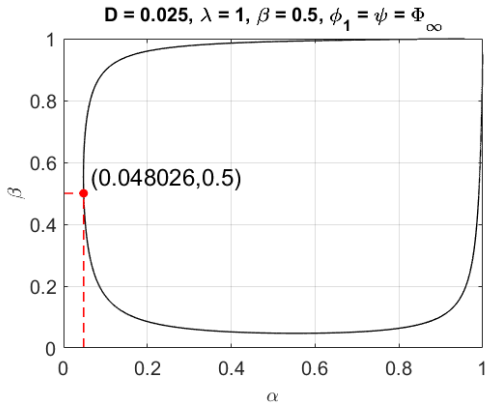
(b) *Amplitude vs* λ *for* $\phi_1 = \psi = \Phi_1$.



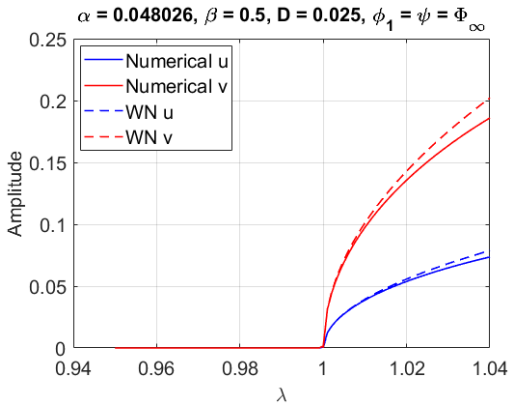
(c) *Neutral curve for* $\phi_1 = \psi = \Phi_2$.



(d) *Amplitude vs* λ *for* $\phi_1 = \psi = \Phi_2$.



(e) *Neutral curve for* $\phi_1 = \psi = \Phi_\infty$.



(f) *Amplitude vs* λ *for* $\phi_1 = \psi = \Phi_\infty$.

Figure 5.4: *Plot of neutral curves from (4.9), numerical amplitudes of* u *and* v *from (5.50) and weakly nonlinear (WN) amplitudes of* u *and* v *when* $\beta = 0.5$. *The values of* α *and* k_c *are summarised in Table 5.2.*

Similar to the case of $\beta = 0.25$, the weakly nonlinear amplitude for each kernel pair agrees with the numerical amplitude at $\lambda = 1$. As λ increases, the agreement decreases as expected. For all the kernel pairs, a supercritical bifurcation is observed.

Kernel	α	k_c
Φ_1	0.23666	2.07074
Φ_2	0.13023	2.0249
Φ_∞	0.048027	1.83579

Table 5.2: *Summary of α and k_c values of different kernels, $\phi_1 = \psi = \Phi_n$ where $n = 1, 2, \infty$, for $\beta = 0.5$ on the neutral curves from (4.9).*

When $\beta = 0.95$

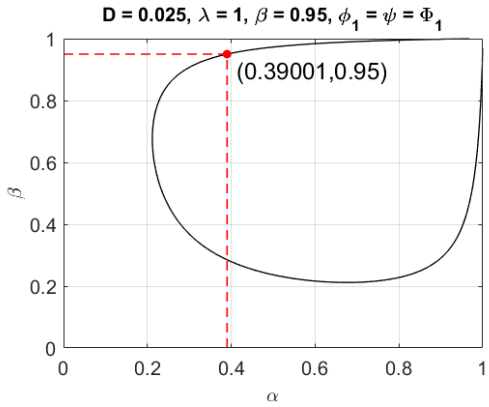
As we expect a subcritical bifurcation in the amplitude for this β value, we now choose $\lambda_0 = 0.95$ ($< \lambda_c$) and gradually increase λ up to 1.04 in the continuation method when computing numerical amplitude. Using the α and k_c values from Table 5.3 below, the weakly nonlinear and numerical amplitudes are plotted in Figure 5.5.

Kernel	α	k_c
Φ_1	0.39001	1.43514
Φ_2	0.30013	1.56372
Φ_∞	0.17072	1.65663

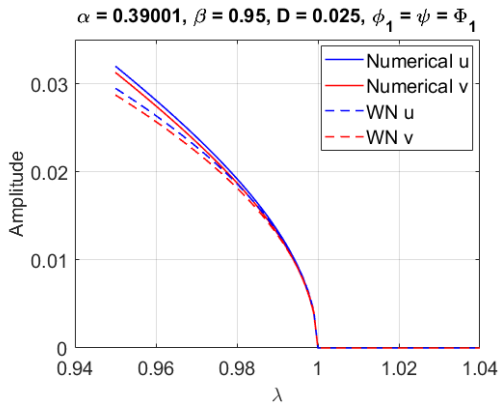
Table 5.3: *Summary of α and k_c values of different kernels, $\phi_1 = \psi = \Phi_n$ where $n = 1, 2, \infty$, for $\beta = 0.95$ on the neutral curves from (4.9).*

The bifurcation is now subcritical, with both positive and zero amplitude branches unstable. Similar results are obtained where the agreement between the analytical and numerical amplitudes decreases as λ decreases from 1 to 0.95.

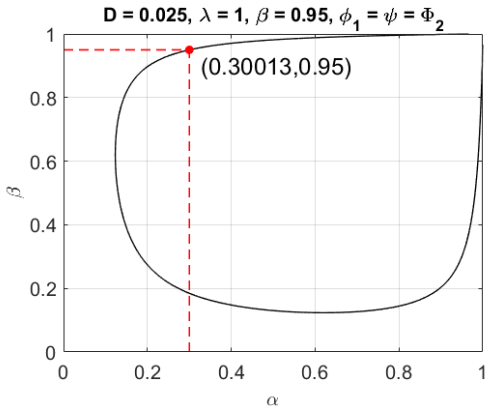
In conclusion, the amplitude of the solutions that bifurcate from the coexisting state changes from supercritical bifurcation to subcritical bifurcation as β increases from 0.25 to 0.95 along the neutral curve. The natural next step would be to study how the amplitudes evolve when the parameter λ moves away from the neutral curve, which will be discussed in the next subsection.



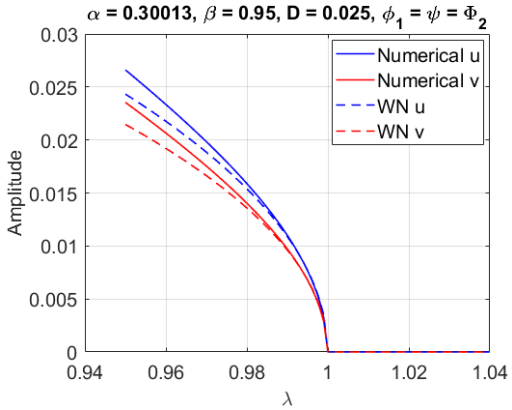
(a) *Neutral curve for* $\phi_1 = \psi = \Phi_1$.



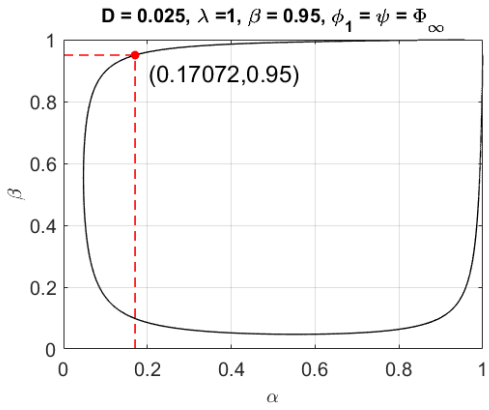
(b) *Amplitude vs* λ *for* $\phi_1 = \psi = \Phi_1$.



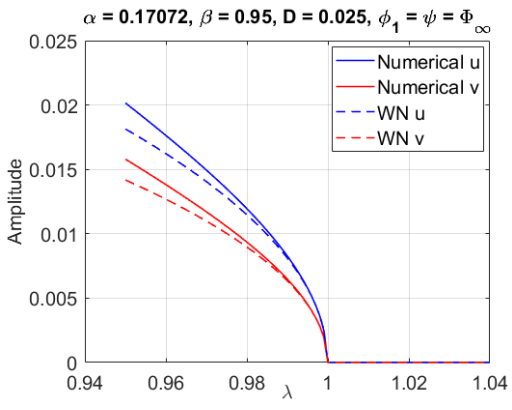
(c) *Neutral curve for* $\phi_1 = \psi = \Phi_2$.



(d) *Amplitude vs* λ *for* $\phi_1 = \psi = \Phi_2$.



(e) *Neutral curve for* $\phi_1 = \psi = \Phi_\infty$.



(f) *Amplitude vs* λ *for* $\phi_1 = \psi = \Phi_\infty$.

Figure 5.5: *Plot of neutral curves from (4.9), numerical amplitudes of* u *and* v *from (5.50) and weakly nonlinear (WN) amplitudes of* u *and* v *when* $\beta = 0.5$. *The values of* α *and* k_c *are summarised in Table 5.3.*

5.4.3 Numerical amplitude away from bifurcation point

We begin by looking at the case when $\beta < 0.89$ where a supercritical bifurcation occurs near the bifurcation point $\lambda_c = 1$. For $\phi_1 = \psi = \Phi_1$, we use the same parameters as the ones used in Figure 5.4(b) to plot both numerical and weakly nonlinear amplitudes against λ for $\lambda = 1.04$ to $\lambda = 20$. The numerical solutions u and v at $\lambda = 20$ are shown in Figure 5.6(c) for one wavelength since the solutions are periodic. The numerical amplitudes are measured by half the difference between the maximum and minimum points across one wavelength.

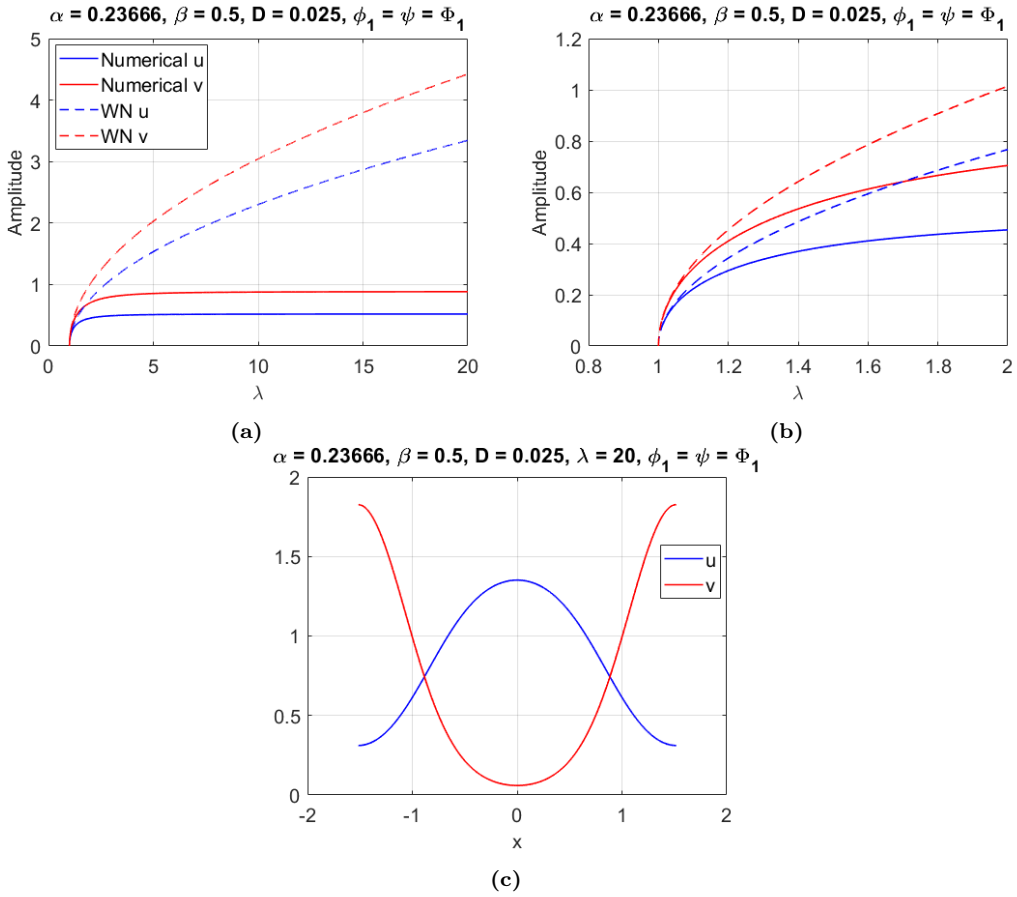


Figure 5.6: *(a) The numerical amplitudes (from (5.50)) and weakly nonlinear (WN) amplitudes of $\phi_1 = \psi = \Phi_1$ for large λ. (b) is the magnified image of (a). (c) The numerical solutions at $\lambda = 20$.*

Figure 5.4(b) shows that the weakly nonlinear amplitudes agree with the numerical amplitudes to a reasonable extent up to $\lambda = 1.04$. From Figures 5.6(a) and 5.6(b), we see that the agreement is still close as λ increases to 1.1, after which the weakly nonlinear amplitudes no longer capture the behaviour of

the numerical amplitudes. The latter grows with a lower rate before converging to 0.52 for u and 0.88 for v as $\lambda \to 20$. On the other hand, the amplitudes predicted by the weakly nonlinear analysis scale with $\sqrt{\lambda - \lambda_c}$ and grow up to 3.3 for u and 4.4 for v at $\lambda = 20$.

We now consider the case when $\beta = 0.95$ for $\phi_1 = \psi = \Phi_1$. Recall that in subsection 5.4.2, both numerical and weakly nonlinear amplitudes exhibit subcritical bifurcation near the bifurcation point. Using the same parameters as the ones in Figure 5.5(b), we plot the amplitudes of the emergent oscillations against λ. In Figure 5.7(c), we extrapolate the weakly nonlinear amplitudes, which scale with $\sqrt{-(\lambda - \lambda_c)}$, from $\lambda = 1$ down to $\lambda = 0.5$, as shown in the blue and red broken lines.

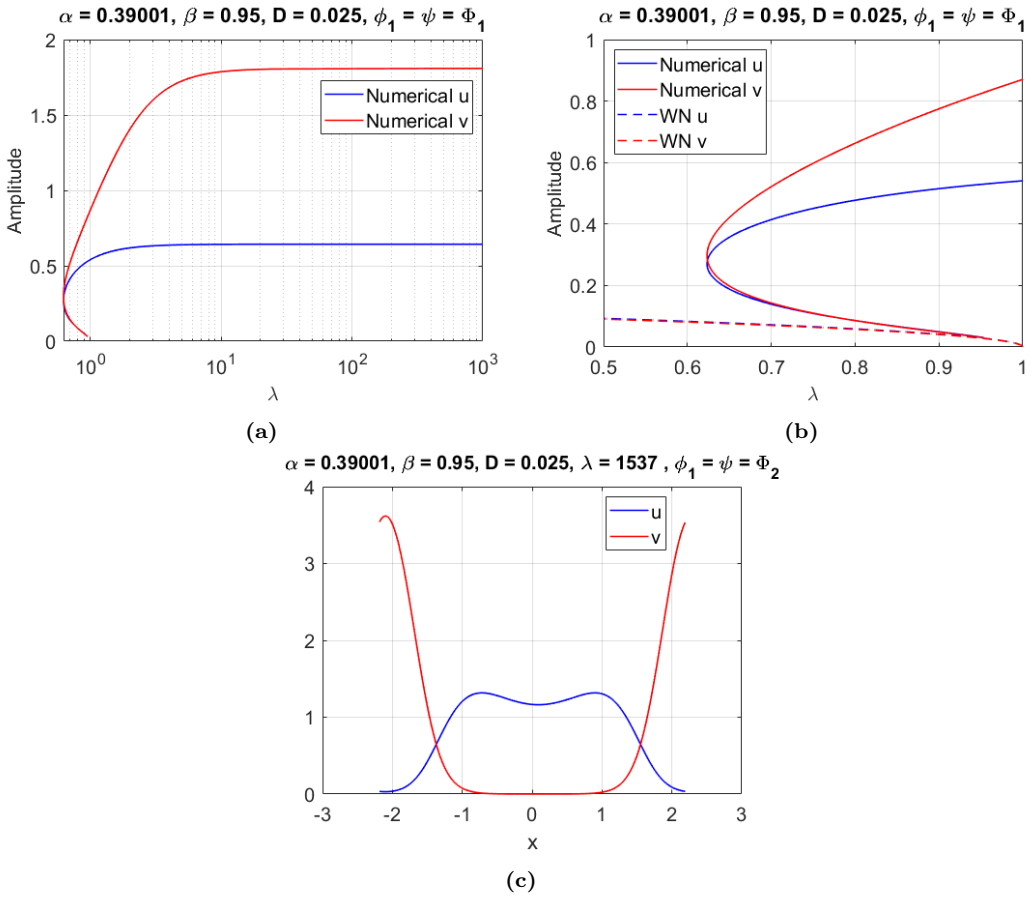


Figure 5.7: *(a) The numerical amplitudes of u and v (from (5.50)) for $\phi_1 = \psi = \Phi_1$ solved by fixing amplitude. (b) The analytical and numerical amplitudes in a smaller λ domain. (c) The numerical solutions u and v solved by fixing amplitude.*

The numerical amplitudes are also plotted in the same figure for $\lambda \leq 0.98$ as

solid lines. However, using the continuation method, the solver for solving u and v stalled prematurely for $\lambda \leq 0.62$. Therefore, we use an alternative approach by adding another condition to fix the amplitude and solve for u, v and λ instead. By increasing amplitudes from 0.03 to 1.9, we managed to solve for the numerical amplitude of u and v as shown in the blue and red lines in Figure 5.7(b)

In Figure 5.5(b), the nonzero weakly nonlinear amplitudes agree with the numerical amplitudes down to $\lambda = 0.98$. When λ decreases from 0.98, the numerical amplitudes bifurcate away from the amplitudes predicted by the weakly nonlinear analysis, as shown in Figure 5.7(c). In fact, the numerical amplitudes of u and v increase when λ decreases from 1 to 0.62 and then increases further when $\lambda \geq 0.62$.

The full structure of the numerical solutions u and v solved by fixing amplitude is shown in Figure 5.7(a). Note that the amplitude of v converges to 1.8 when $\lambda \geq 25$, whereas the amplitude of u converges to 0.64 beyond $\lambda = 10$. Figure 5.7(c) illustrates the numerical amplitudes of u and v at $\lambda = 1537$.

The same study is conducted when both kernels, ϕ_1 and ψ, are Φ_2 and Φ_∞ for $\beta = 0.5$ and $\beta = 0.95$, respectively. The resulting figures can be found in Appendix C, from Figures C.1 to C.4. It has been found that the amplitudes of both of these kernel pairs demonstrate similar behaviour to that of $\phi_1 = \psi = \Phi_1$.

5.5 Fully nonlinear numerical solution

In this section, we aim to understand the fully nonlinear problem and not just the coexisting state of the system. More specifically, we would like to study how the numerical solutions change with parameters D_1, D_2, α, β, λ, and wavelength, Λ. We will focus on the case when $\phi_1 = \psi = \Phi_1$ and briefly summarise the behaviour of the solutions for $\phi_1 = \psi = \Phi_2$ and $\phi_1 = \psi = \Phi_\infty$,

in which the figures can be found in Appendix D.

Numerical method

First, we initialise the parameters in these ranges, i.e. $D_1, D_2 \in [10^{-6}, 10^{-3}]$, $\alpha, \beta \in [0.1, 0.9]$, $\lambda \in [0.8, 1.2]$, and $\Lambda \in [1, 5]$. Then, we define the initial condition as $(u_0, v_0) = \left(10\mathrm{e}^{-25x^2/\Lambda^2}, 10\mathrm{e}^{-25x^2/\Lambda^2}\right)$ for the first set of parameters, $[D_1, D_2, \alpha, \beta, \lambda, \Lambda] = [10^{-3}, 10^{-3}, 0.1, 0.1, 0.8, 1]$, when solving the steady-state problem (5.50) using *fsolve* in MATLAB. The resulting solutions u and v will be used as the initial conditions for the next set of parameters. To achieve that, we first construct a lattice using all the data points of the parameters. Then, an algorithm moves the lattice point randomly through the parameter space by identifying the adjacent empty point. The process is repeated until all the points in the parameter space have been filled or no solutions have been found in all six parameters in the new parameter set.

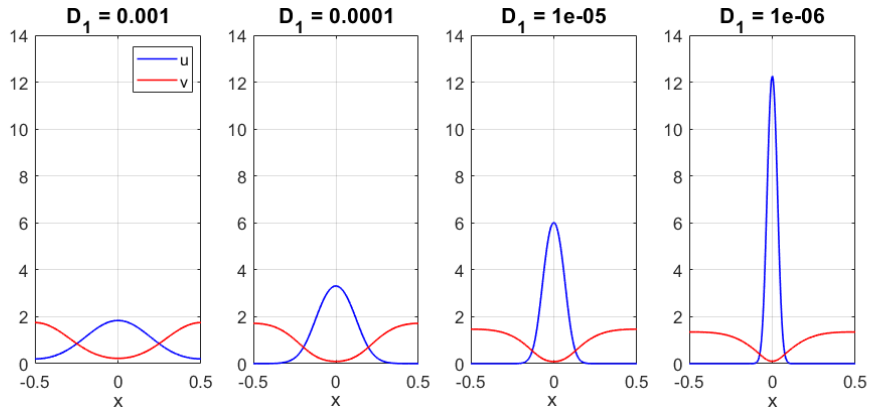
Observations

To understand the behaviour of the steady-state solutions in $[D_1, D_2, \alpha, \beta, \lambda, \Lambda]$ parameter space, we vary one of the six parameters at a time while fixing the rest. The plots in Figure 5.8 illustrate how the solutions depend on each parameter. Figure 5.8(a) shows that as $D_1 \to 0$, the amplitude of u increases from 0.82 to 6 and the peak gets sharper when D_1 is sufficiently small. Besides, the difference between the maximum value of u and the minimum value of v increases as D_1 decreases. It is also worth noting that the minimum value of u decreases from 0.226 to 2.18×10^{-29}, which is very close to zero.

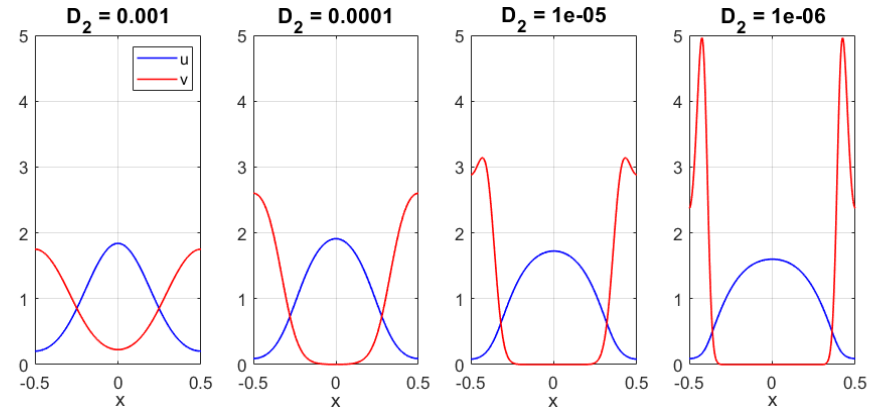
A reverse effect is observed when we decrease D_2 in Figure 5.8(b), where v increases in amplitude and forms sharper peaks. As expected, the difference between the maximum value of v and the minimum value of u increases with decreasing D_2. In the meantime, the minimum value of v decreases from 0.227 to 8.17×10^{-24}.

The solutions in Figure 5.8(c) are plotted for increasing α from 0.1 to 0.9. The general pattern is similar to when we decrease D_1, i.e. increase in the amplitude of u and the difference between a maximum of u and a minimum of v. The minimum value of u decreases from 0.204 to 5.78×10^{-5}. An equal but opposite effect is spotted when we increase β from 0.1 to 0.9 in Figure 5.8(d). The minimum value of v decreases from 0.227 to 5.29×10^{-5}.

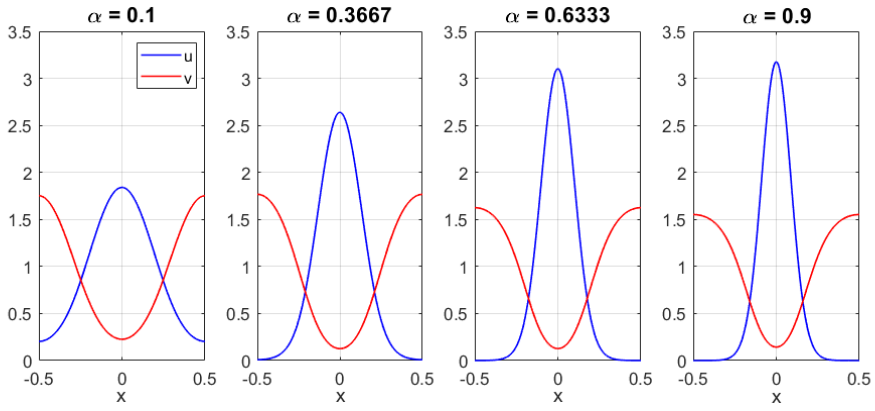
When we increase the wavelength of the solutions from one to two in Figure 5.8(e), the number of peaks of u also increases from one to two. Finally, increasing λ from 0.8 to 1.2 increases the amplitude of u slightly from 0.82 to 0.875 and the amplitude of v from 0.76 to 0.915, as shown in Figure 5.8(f).



(a) $D_2 = 0.001$, $\alpha = \beta = 0.1$, $\lambda = 0.8$, $\Lambda = 1$.

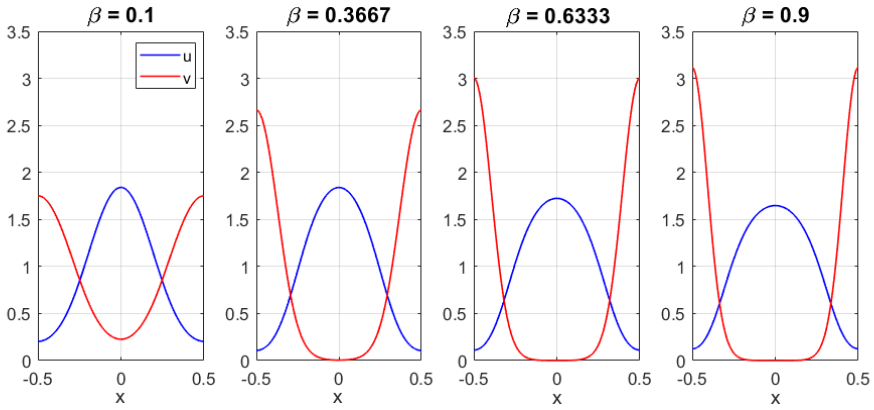


(b) $D_1 = 0.001$, $\alpha = \beta = 0.1$, $\lambda = 0.8$, $\Lambda = 1$.

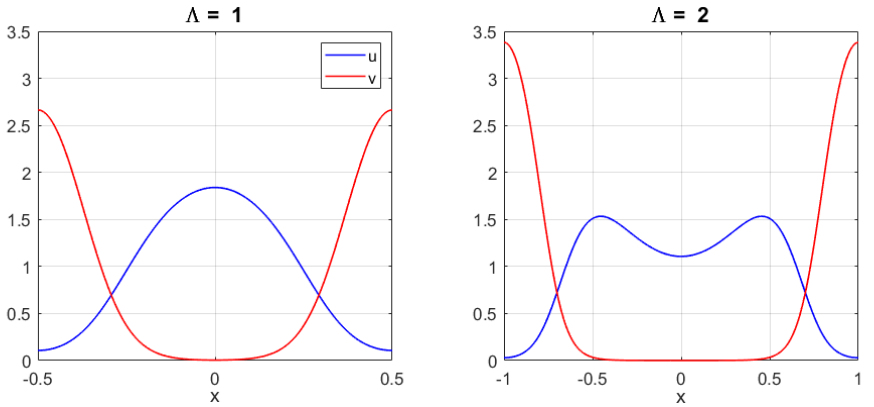


(c) $D_1 = D_2 = 0.001$, $\beta = 0.1$, $\lambda = 0.8$, $\Lambda = 1$.

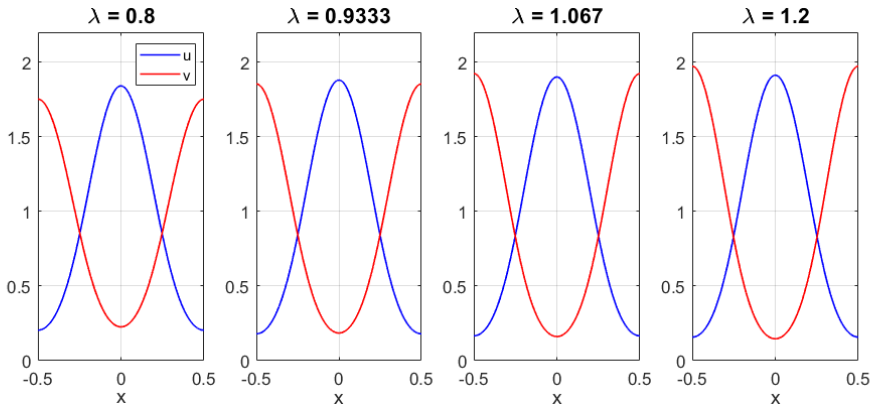
Figure 5.8: *Fully nonlinear solutions from (5.50) for $\phi_1 = \psi = \Phi_1$ for (a) decreasing D_1, (b) decreasing D_2 and (c) increasing α.*



(d) $D_1 = D_2 = 0.001$, $\alpha = 0.1$, $\lambda = 0.8$, $\Lambda = 1$.



(e) $D_1 = D_2 = 0.001$, $\alpha = 0.1$, $\beta = 0.3667$, $\lambda = 0.8$, $\Lambda = 1$.



(f) $D_1 = D_2 = 0.001$, $\alpha = \beta = 0.1$, $\Lambda = 1$.

Figure 5.8: *(cont.) Fully nonlinear solutions from (5.50) for $\phi_1 = \psi = \Phi_1$ for (d) increasing β, (e) increasing Λ, and (f) increasing λ.*

After running the solver across all the parameters, we obtained 1391 sets of solutions out of 5120 combinations of parameters. Some solutions that exhibit interesting features are plotted in Figure 5.9. Note that Figures 5.9(a) to 5.9(h) are not arranged in order according to any of the parameters.

The qualitative feature of each subfigure is described in terms of its parameter values in the caption of Figure 5.9. In short, we could deduce some general patterns based on the observations of the plots. In all cases, we observe the formation of either one peak in u and two peaks in v or two peaks in both u and v. Another observation is that sharp peaks are formed when D_1 or D_2 is as small as 10^{-6} (see Figures 5.9(g) and 5.9(h)). When both D_1 and D_2 are sufficiently small, there exist regions where u is positive and v is very close to zero and vice versa. For instance, in Figure 5.9(g), the minimum value of u is 6.27×10^{-181} when v is 1.01. In the same figure, the minimum value of v is 4.49×10^{-28} when u is 0.955. This feature will be studied in detail in Chapter 6.

The figures of the fully nonlinear numerical solutions when both kernels are Φ_2 and Φ_∞ are included in Appendix D. Changing each parameter results in similar behaviour in the solutions with $\phi_1 = \psi = \Phi_2$ and $\phi_1 = \psi = \Phi_\infty$ compared to that of $\phi_1 = \psi = \Phi_1$. The only difference is that increasing λ does not change much of the amplitudes of u or v, as shown in Figures D.1(f) and D.3(f). From Figures D.2 and D.4, the solutions with $\phi_1 = \psi = \Phi_2$ and $\phi_1 = \psi = \Phi_\infty$ have similar features to that of $\phi_1 = \psi = \Phi_1$. However, the peaks of the former kernel combinations are less sharp, and more than two peaks can be found in either u or v.

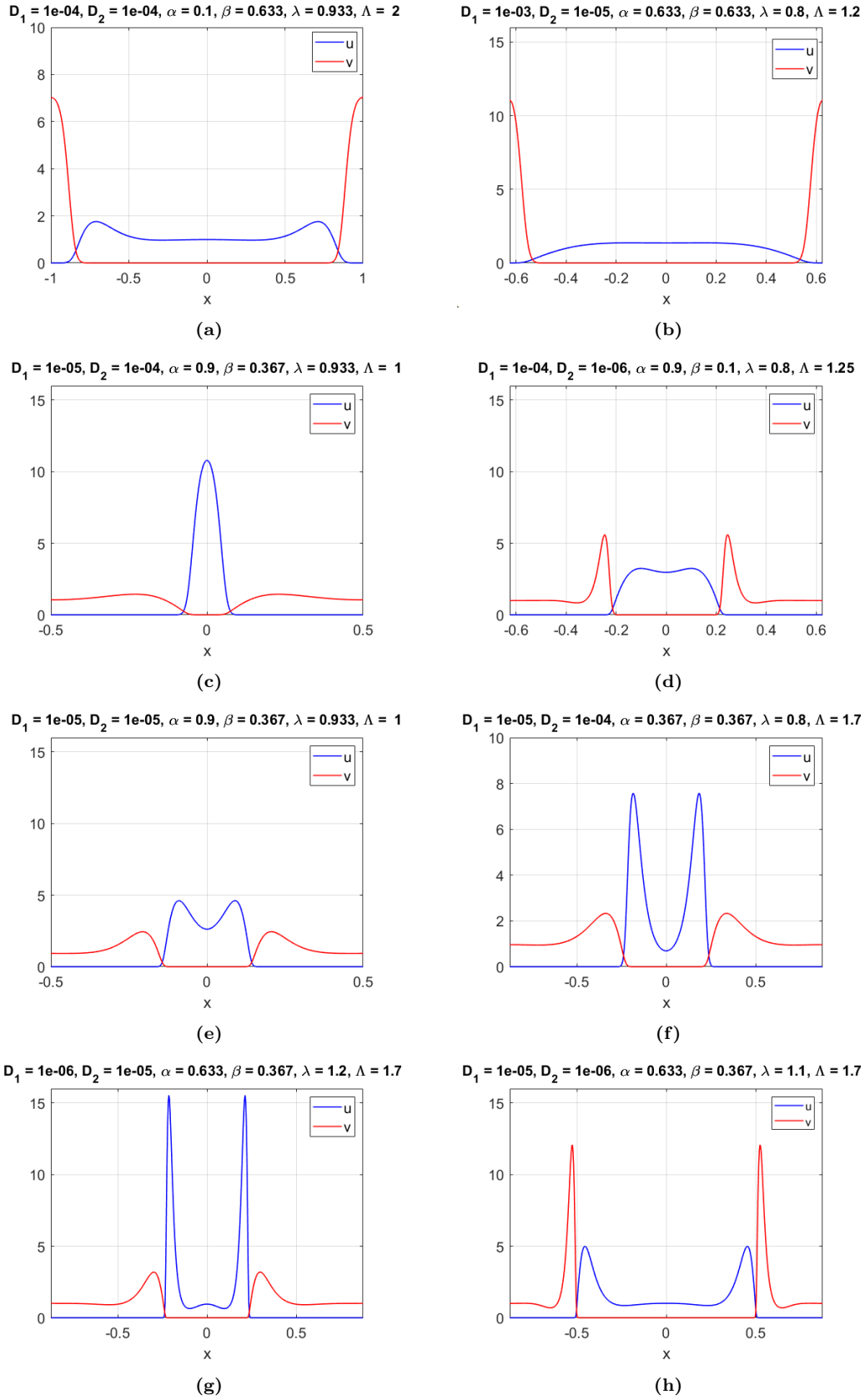


Figure 5.9: *Plots of the fully nonlinear solutions from (5.50) for $\phi_1 = \psi = \Phi_1$. (a) Solution u has two peaks due to $\Lambda = 2$. The maximum amplitude of v is larger than that of u as $\beta > \alpha$. (b) $D_2 < D_1$ results in higher peak in v. (c) The maximum amplitude of u is larger as $\alpha > \beta$, and $D_1 < D_2$ further amplifies the effect. (d) The effect of $D_2 < D_1$ is greater than $\alpha > \beta$, hence larger peak in v. (e) A larger peak of u due to $\alpha > \beta$ and $D_1, D_2 < 1$ leads to two peaks in u. (f) $D_1 < D_2$ and $\Lambda > 1$ generates larger $\max u$ with more than one peak. (g) $D_1 < D_2$ and $\alpha > \beta$ combined with $\Lambda > 1$ result in $\max u > \max v$ and three peaks in u. (h) The effect of $D_2 < D_1$ is greater than $\alpha > \beta$.*

5.6 Conclusion

We have constructed a cubic amplitude equation analytically by employing multiple-scale analysis and the techniques built upon the examples for a neural field model and the Swift Hohenberg equation in 2.2. We have focused on the kernel pairs where $\phi_1 = \psi = \Phi_1, \Phi_2$ and Φ_∞. Since the coefficient of the cubic term in the amplitude equation, ν, changes sign as β increases from zero to one, we expect the patterns of the solutions to change from supercritical bifurcation to subcritical bifurcation with increasing β along the neutral curves from Chapter 4.

By studying the amplitudes of the steady-state solutions around the bifurcation point $\lambda_c = 1$, we have verified that the asymptotic or weakly nonlinear amplitudes for all three kernel pairs only agree with the numerical ones when they are very close to the bifurcation point. For instance, the weakly nonlinear amplitudes of the solutions with $\phi_1 = \psi = \Phi_1$ kernels agree with the numerical amplitudes from $\lambda_c = 1$ to $\lambda = 1.1$ at $\beta = 0.5$, and from $\lambda_c = 1$ to $\lambda = 0.98$ at $\beta = 0.95$. As λ increases further beyond $\lambda = 1.1$ at $\beta = 0.5$, the numerical amplitudes continue to increase with a smaller growth rate than those predicted by weakly nonlinear analysis. However, we have observed an interesting bifurcation in the numerical amplitudes for $\beta = 0.95$. Initially, both amplitudes increase with decreasing λ down to $\lambda = 0.62$, but the numerical amplitudes continue to increase when $\lambda \geq 0.62$ by fixing amplitudes in the numerical solver. Though we are not able to verify the stability of the amplitude branch for $\lambda > 0.62$, we suspect there exists a hysteresis bifurcation in the numerical amplitudes. While we have not looked into the cases when the solutions bifurcate away from $\lambda_c = 1$ for $\phi_1 = \psi = \Phi_2$ and $\phi_1 = \psi = \Phi_\infty$ in detail, some figures are plotted in Appendix C and similar observations to Φ_1 are found.

Finally, we have studied how the behaviour of the fully nonlinear steady-state

solutions changes with parameters $D_1, D_2, \alpha, \beta, \lambda$ and the wavelength, Λ of the solutions for $\phi_1 = \psi = \Phi_1$. One key takeaway from this study is that when either one or both of the diffusion coefficients are sufficiently small, the solutions are highly segregated, leading to interesting features in the solutions. Again, interested readers can refer to the solutions for $\phi_1 = \psi = \Phi_2$ and $\phi_1 = \psi = \Phi_\infty$ in Appendix D.

Chapter 6

Fully Nonlinear Pattern Formation in a Nonlocal Lotka-Volterra System with Small Diffusivity

6.1 Introduction

In this chapter, we study the fully nonlinear solutions of the same NLLV problem as the ones in Chapters 4 and 5 before

$$\begin{aligned} \frac{\partial u}{\partial t} &= D_1 \frac{\partial^2 u}{\partial x^2} + u\left(1 - \int_{-\infty}^{\infty} \phi_1(x-y)u(y)\,\mathrm{d}y - \alpha v\right), \\ \frac{\partial v}{\partial t} &= D_2 \frac{\partial^2 v}{\partial x^2} + Rv\left(1 - \frac{1}{\lambda}\int_{-\infty}^{\infty} \phi_2\left(\frac{x-y}{\lambda}\right) v(y)\,\mathrm{d}y - \beta u\right), \end{aligned} \tag{6.1}$$

but in the limit of small diffusivity. In particular, we aim to understand the structure of the solutions where either one or the other species is absent in disjoint regions at leading order as D_1 and/or $D_2 \to 0$, as seen in the numerical solutions in Section 5.5. Henceforth, we regard system (6.1) with an initial condition

$$(u(x,0), v(x,0)) = (u_0, v_0), \tag{6.2}$$

as an IVP.

In Section 6.2, we begin by showing some links to online videos of solutions of the IVP with random initial conditions (see (6.3)) that showcase the evolution of numerical solutions towards their steady states, where segregated regions are formed. The results motivate us to study the solutions asymptotically to gain an insight into the behaviour of such solutions. We do so by assuming periodicity in our solutions (u, v). It is later found that such an assumption leads to the representation of convolution terms in terms of effective periodic kernels within a finite domain. In Section 6.3, it is shown that the structure of the asymptotic solutions consists of outer solutions in two distinct regions, where $u = O(1)$ and $v = O(1)$, with inner regions at the junctions. In Section 6.4, we approximate the effective periodic kernels using truncated Fourier series. Then, we derive the slope condition in the inner region in Section 6.5 and use it to derive the asymptotic outer solutions in Section 6.6. Finally, the asymptotic outer solutions will be compared with the numerical solutions of the fully nonlinear system at a steady state and the IVP solutions with small initial perturbation in the spatial domain.

Throughout this chapter, we restrict our attention to the combination of Φ_1 and Φ_∞ kernels in the asymptotic analysis of segregated solutions. For all the cases, we analytically derive the asymptotic outer solutions and find that they agree with the numerical solutions in those disjoint regions to a reasonable extent. In addition, the asymptotic outer solutions tend to be one of the fully nonlinear solutions in IVP as $t \to \infty$.

6.2 Solution of IVP with random initial conditions

In this section, we simulate some numerical solutions of the IVP (6.1) with random initial conditions [108] by introducing a smooth random function $f(x) = \sum_{j=-m}^{m} c_j \cos\left(\frac{2\pi jx}{L}\right)$ for u_0, where each c_j is an independent sample from $N_1(0, 1/(2m+1))$ and $m = \lfloor L/\gamma \rfloor$ with $\gamma > 0$ as a wavelength parameter. Similarly, we set another smooth random function $g(x) = \sum_{j=-m}^{m} c_j \cos\left(\frac{2\pi jx}{L}\right)$, where each c_j is an independent sample from $N_2(0, 1/(2m+1))$. As shown in [108], the resulting distribution of the summation series does not depend on the support. In particular, for any $x \in \mathbb{R}$, $f(x)$ and $g(x)$ are distributed as $N(0, 1)$ distributions.

The random initial conditions (6.2) for (u, v) are

$$(u_0, v_0) = (1, 1) + a\left(\frac{f(x)}{\max|f(x)|}, \frac{g(x)}{\max|g(x)|}\right), \tag{6.3}$$

for constant a. To ensure that the perturbations in the initial conditions are small, we choose $a = 0.1$. The IVP solutions for this section are computed using the Euler method in MATLAB for time-stepping for $x \in [-L, L]$ domain where $L = 5$, $\gamma = 0.025$ and $m = 200$. Figure 6.1 shows an example of the random initial conditions in (6.3) with $L = 2$, $\gamma = 0.025$ and $m = 200$.

We are interested in the patterning of the solutions, which evolve with time from $t = 0$ to $t = t_{end}$, where the numerical solutions of the IVP tend to time-independent spatially structured solutions. The structure of the steady solutions at large t will also be observed. The solutions are presented as animations with different parameter values from the parameter set $[D_1, D_2, \alpha, \beta, \lambda, \phi_1, \phi_2]$.

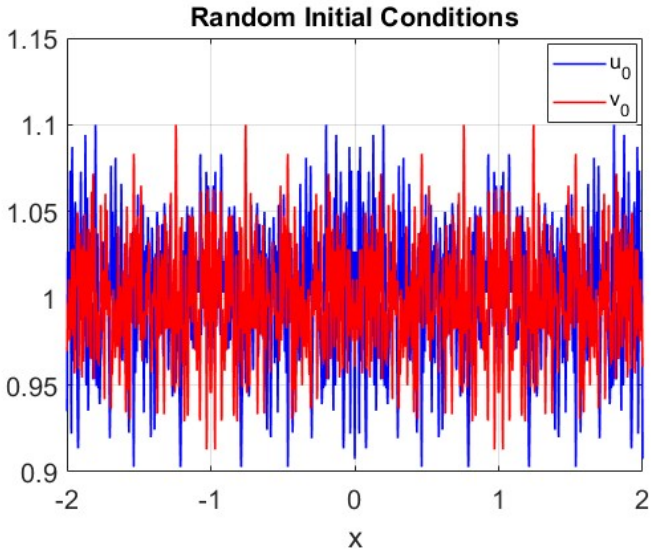


Figure 6.1: *The random initial conditions from (6.3), for* $a = 0.1$, $L = 2$, $\gamma = 0.025$ *and* $m = 200$.

When $\phi_1 = \phi_2 = \phi = \Phi_\infty$

Table 6.1 shows the parameter values for videos 1a to 1f. Each video can be accessed via the links in blue in the table. We demonstrate small and large-time IVP solutions for the six cases in parts (i) and (ii). The solutions at $t = t_{end}$ from part (i) are illustrated in Figure 6.2. In Table 6.1, the amplitude and wavelength, Λ, at the large-time steady-state solutions are tabulated in the last two columns in the same table. Based on case 1a, we vary one of the parameters from $(D_1, D_2, \alpha, \beta, \lambda, \phi_1, \phi_2)$ in the subsequent cases to understand better the effect of changing parameters on the behaviour of the solutions.

The videos show that all initial conditions with random wavelengths and amplitudes evolve into periodic oscillatory patterns with fixed amplitudes. At the steady state, the solutions are segregated into regions with $u = O(1)$ or $v = O(1)$. When $D_2 = 10^{-6}$, the solutions in video 1c(i) converge to a steady state slower compared to the case when $D_1 = D_2 = 10^{-5}$. Another observation is that in both 1b and 1c, $D_2 < D_1$, resulting in a larger amplitude in v and a smaller amplitude in u at steady state compared to 1a. In contrast, increasing α in 1d and decreasing β in 1e lead to smaller peaks in v and larger peaks in u. Decreasing λ from 1 to 0.8, on the other hand, decreases v and increases u

Videos	t_{end}	D_1	D_2	α	β	λ	Amplitude in (i)	Λ in (i)
1a(i)	4×10^4	10^{-5}	10^{-5}	0.2	0.9	1	$u = 2.17$ $v = 7.47$	2.5
1a(ii)	200							
1b(i)	5000	10^{-4}	10^{-5}	0.2	0.9	1	$u = 1.41$ $v = 15.47$	2.5
1b(ii)	200							
1c(i)	8×10^4	10^{-5}	10^{-6}	0.2	0.9	1	$u = 1.8$ $v = 12$	1.67
1c(ii)	1000							
1d(i)	2×10^4	10^{-5}	10^{-5}	0.6	0.9	1	$u = 2.85$ $v = 3.49$	1.67
1d(ii)	500							
1e(i)	2×10^4	10^{-5}	10^{-5}	0.2	0.3	1	$u = 2.85$ $v = 3.48$	1.67
1e(ii)	500							
1f(i)	2×10^4	10^{-5}	10^{-5}	0.2	0.9	0.8	$u = 2.31$ $v = 4.82$	1.67
1f(ii)	300							

Table 6.1: *Parameter values for the solutions of IVP (6.1) when $\phi = \Phi_\infty$. The varying parameters based on case 1a are highlighted in red.*

slightly in video 1f(i). All these observations have also been observed in the steady-state solutions of the fully nonlinear problem in Section 5.5. Overall, we observe smaller wavelength and therefore higher number of oscillations in the solutions when $D \leq 10^{-6}$, $\alpha \approx \beta$, and $\lambda < 1$.

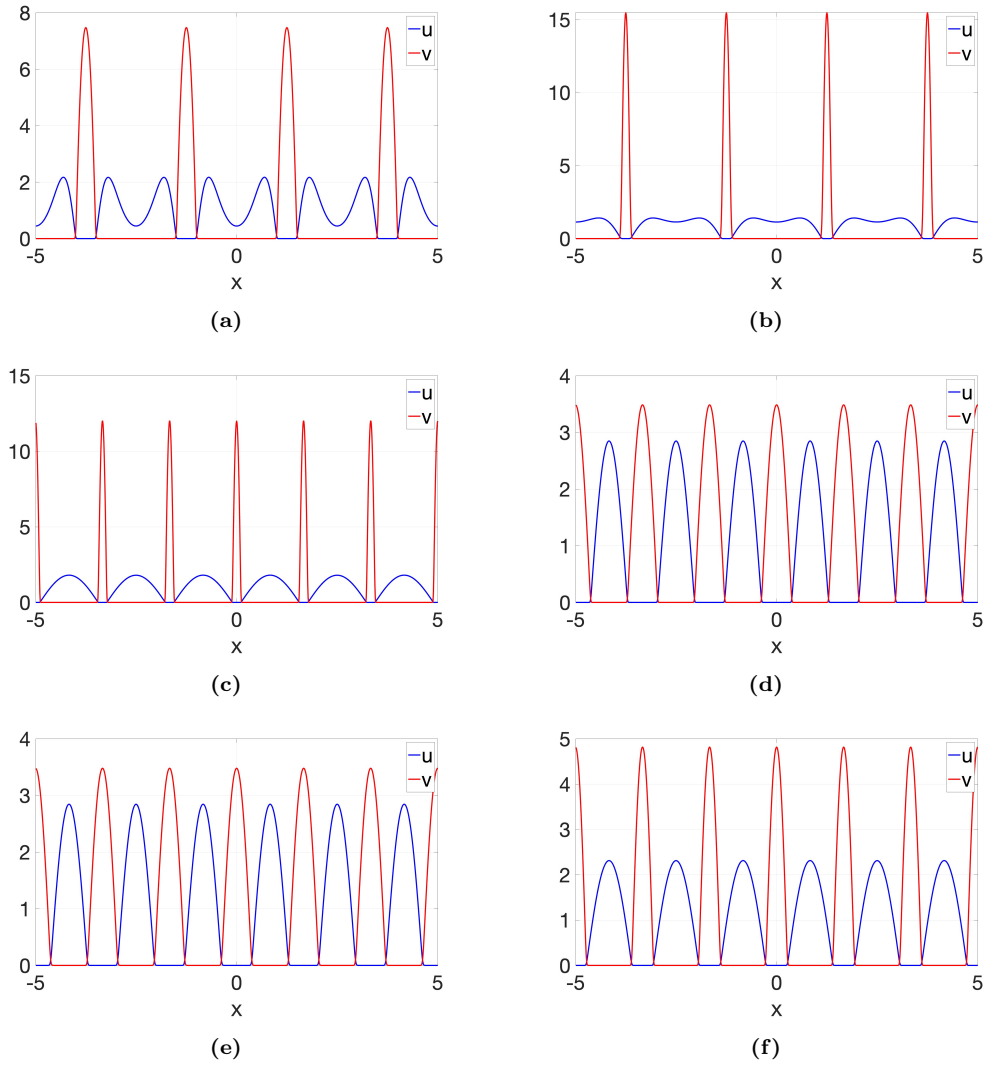


Figure 6.2: *IVP solutions from (6.1) at large t_{end} for $\phi = \Phi_\infty$. (a) $t_{end} = 4 \times 10^4$ from video 1a(i). (b) $t_{end} = 5000$ from video 1b(i). (c) $t_{end} = 8 \times 10^4$ from video 1c(i). (d) $t_{end} = 2 \times 10^4$ from video 1d(i). (e) $t_{end} = 2 \times 10^4$ from video 1e(i). (e) $t_{end} = 2 \times 10^4$ from video 1f(i). The parameter values can be found in Table 6.1.*

When $\phi_1 = \phi_2 = \phi = \Phi_1$

We now change both kernels to $\phi = \Phi_1$ and use the same parameter values in 2a as in 1a. Then, we vary one parameter from 2b to 2f and analyse the evolution of solutions in each case. The large-time solutions at $t = t_{end}$ are plotted in Figure 6.3.

When comparing solutions from cases 2b to 2f with 2a, similar observations can be drawn as before. For instance, solutions in 2c arrive at a steady state at a much larger t_{end} due to the smaller $D_2 = 10^{-6}$. Besides, $D_2 < D_1$ in 2b and 2c results in larger local maxima in v and smaller local maxima in u. Moreover,

Videos	t_{end}	D_1	D_2	α	β	λ	Amplitude in (i)	Λ in (i)
2a(i)	9×10^4	10^{-5}	10^{-5}	0.2	0.9	1	$u = 1.85$ $v = 6.47$	0.835
2a(ii)	200							
2b(i)	8×10^4	10^{-4}	10^{-5}	0.2	0.9	1	$u = 1.37$ $v = 14.03$	1
2b(ii)	100							
2c(i)	5×10^5	10^{-5}	10^{-6}	0.2	0.9	1	$u = 1.4$ $v = 16.39$	0.625
2c(ii)	1000							
2d(i)	8×10^4	10^{-5}	10^{-5}	0.6	0.9	1	$u = 2.37$ $v = 3.29$	0.415
2d(ii)	200							
2e(i)	8×10^4	10^{-5}	10^{-5}	0.2	0.3	1	$u = 2.2$ $v = 3.22$	0.454
2e(ii)	700							
2f(i)	7×10^4	10^{-5}	10^{-5}	0.2	0.9	1.2	$u = 1.82$ $v = 7.16$	0.835
2f(ii)	200							

Table 6.2: *Parameter values for the solutions of IVP (6.1) when $\phi = \Phi_1$. The varying parameters based on case 2a are highlighted in red.*

larger α in 2d and smaller β in 2e lead to smaller v and larger u. Finally, increasing λ increases v and reduces u slightly.

Compared with the solutions with Gaussian kernels, we find that the solutions of $\phi = \Phi_1$ kernel pair converge to steady-state solutions at a slower rate as the t_{end} for large-time solutions are larger. On top of that, the wavelengths of solutions with both $\phi = \Phi_1$ kernels are smaller for all of the parameter sets. We also observe the formation of more prominent peaks in Figure 6.3 compared to Figure 6.2, especially in v. At steady state, solutions u in Figures 6.3(c) and 6.3(f) form an extra peak in each wavelength as opposed to those in Figures 6.2(c) and 6.2(f). From cases 1c to 1f, the observed wavelength is 1.67. However, the solutions for $\phi = \Phi_1$ kernels converge to different wavelengths in $\Lambda \in [0.415, 0.835]$.

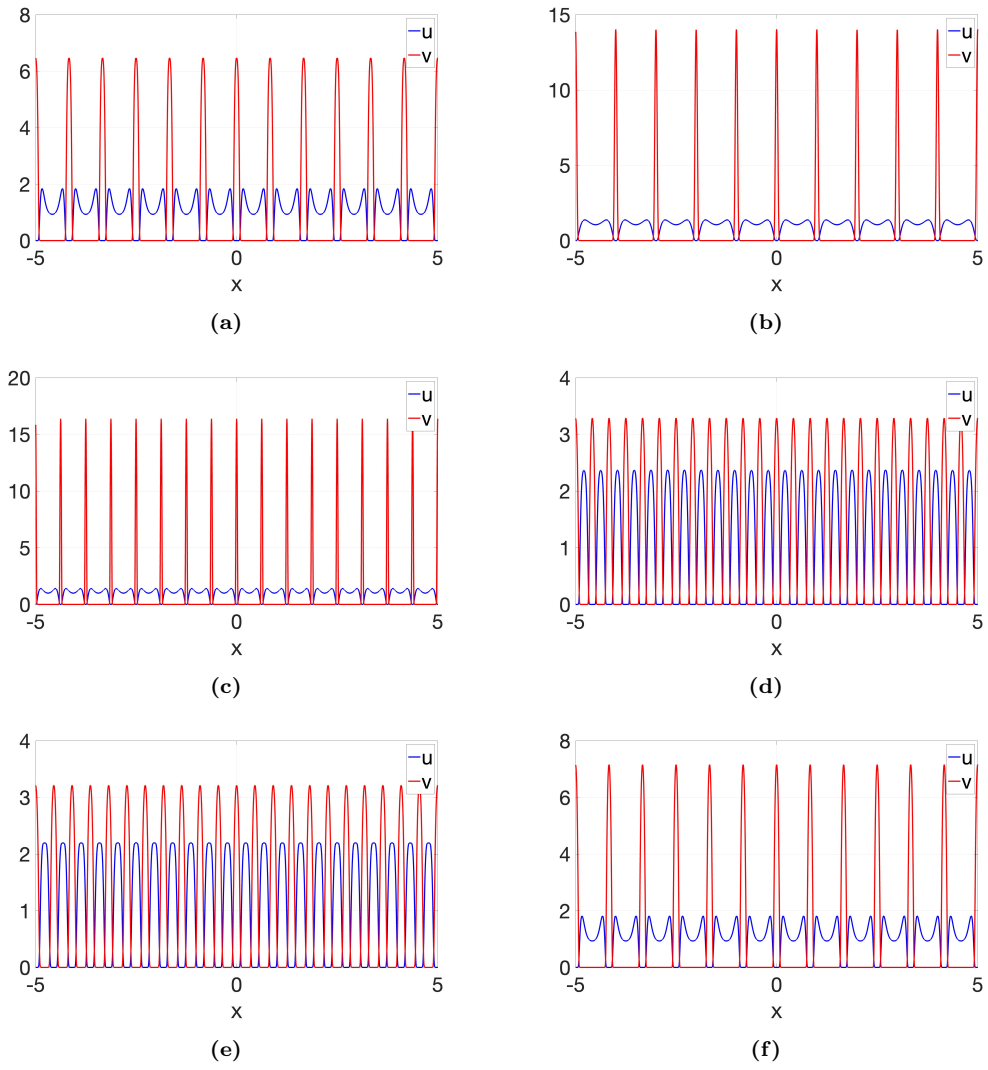


Figure 6.3: *IVP solutions from (6.1) at large t_{end} for $\phi = \Phi_1$. (a) $t_{end} = 9 \times 10^4$ from video 2a(i). (b) $t_{end} = 8 \times 10^4$ from video 2b(i). (c) $t_{end} = 5 \times 10^5$ from video 2c(i). (d) $t_{end} = 8 \times 10^4$ from video 2d(i). (e) $t_{end} = 8 \times 10^4$ from video 2e(i). (e) $t_{end} = 7 \times 10^4$ from video 2f(i). The parameter values can be found in Table 6.2.*

When $\phi_1 = \Phi_1$ and $\phi_2 = \Phi_\infty$

We now look at the solutions of the mixed kernel pair when $\phi_1 = \Phi_1$ and $\phi_2 = \Phi_\infty$. Despite having different kernels, all the solutions from 3a to 3f converge to a spatially oscillatory pattern. Again, the changes in amplitude and wavelength of the steady-state solutions are consistent with the conclusion drawn from Section 5.5. That being said, $D_1 < D_2$, increase in α and decrease in β reduces the amplitude of v and increases the amplitude of u, as shown in videos 3b(i), 3d(i) and 3e(i). The opposite behaviour is observed when $D_2 < D_1$ in video 3c(i). Increasing λ to 1.2, on the other hand, results in

similar amplitude and wavelength in the solutions compared to that of $\lambda = 1$ in case 3a.

Videos	t_{end}	D_1	D_2	α	β	λ	Amplitude in (i)	Λ in (i)
3a(i)	9×10^4	10^{-5}	10^{-5}	0.2	0.9	1	$u = 2.11$ $v = 17.41$	2.5
3a(ii)	200							
3b(i)	1×10^4	10^{-6}	10^{-5}	0.2	0.9	1	$u = 4.09$ $v = 12$	2.5
3b(ii)	1200							
3c(i)	1×10^4	10^{-5}	10^{-6}	0.2	0.9	1	$u = 1.55$ $v = 41.72$	2.5
3c(ii)	1200							
3d(i)	7.5×10^5	10^{-5}	10^{-5}	0.6	0.9	1	$u = 2.41$ $v = 9.19$	1.67
3d(ii)	400							
3e(i)	6.5×10^5	10^{-5}	10^{-5}	0.2	0.3	1	$u = 2.38$ $v = 9.22$	1.67
3e(ii)	700							
3f(i)	1×10^4	10^{-5}	10^{-5}	0.2	0.9	1.2	$u = 2.11$ $v = 17.5$	2.5
3f(ii)	600							

Table 6.3: *Parameter values for the solutions of IVP (6.1) when $\phi_1 = \Phi_1$ and $\phi_2 = \Phi_\infty$. The varying parameters based on case 3a are highlighted in red.*

Combining $\phi_1 = \Phi_1$ and $\phi_2 = \Phi_\infty$ generates some interesting behaviour in the solutions. One of the examples is when time increases from $t = 6.3 \times 10^5$ to $t = 6.35 \times 10^5$ in video 3d(i), v reduces from eight peaks to six peaks suddenly, before converging to solutions with wavelength 1.67 at $t = 7.5 \times 10^5$. A similar observation is also spotted in video 3e(i) from $t = 4.95 \times 10^5$ to $t = 4.97 \times 10^5$. It could be one of the research challenges that is addressed in future work.

Overall, the solutions converge to spatial oscillations much faster than the solutions of both Gaussian pair or slower than that of both $\phi = \Phi_1$ pair, depending on the random initial conditions. Apart from that, the solutions of the mixed kernel pair converge to solutions with wavelengths that are equal or greater to both Gaussian pair but larger than that of both $\phi = \Phi_1$ pair. It can also be seen from Figure 6.4 that the differences between the peaks of v and u are the largest among these three pair of kernels, hence producing the sharpest peaks.

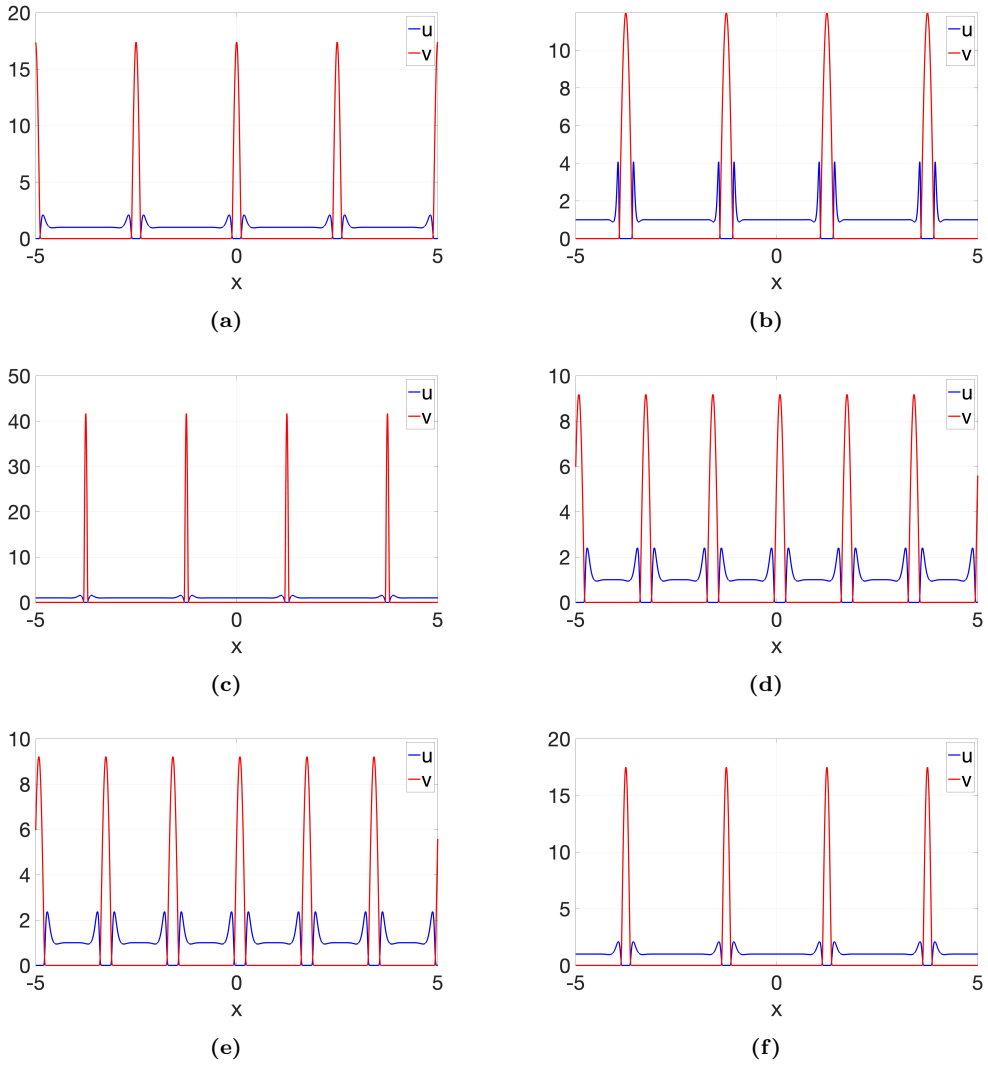


Figure 6.4: *IVP solutions from (6.1) at large t_{end} for $\phi_1 = \Phi_1$ and $\phi_2 = \Phi_\infty$. (a) $t_{end} = 9 \times 10^4$ from video 3a(i). (b) $t_{end} = 10^4$ from video 3b(i). (c) $t_{end} = 10^4$ from video 3c(i). (d) $t_{end} = 7.5 \times 10^5$ from video 3d(i). (e) $t_{end} = 6.5 \times 10^5$ from video 3e(i). (e) $t_{end} = 10^4$ from video 3f(i). The parameter values can be found in Table 6.3.*

6.3 Asymptotic structure of solution with small diffusivity

In the previous section, we have seen that solutions become segregated when the diffusion coefficients are sufficiently small. In the following few sections, we will examine the structure of these solutions by carrying out an asymptotic analysis and comparing the findings to the numerical solutions.

Figure 6.5 depicts an example of numerical solutions of the steady-state problem ((6.1) with time derivatives equal to zero) when both kernels are $\phi = \Phi_1$ in a

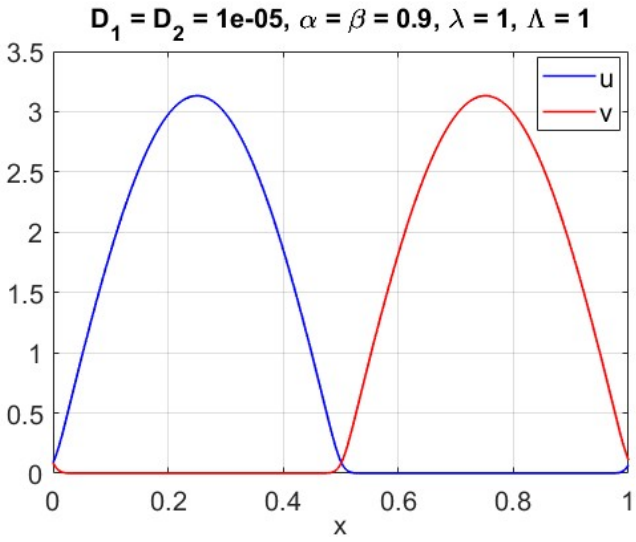


Figure 6.5: *Numerical solutions of a steady-state problem when both* $\phi = \Phi_1$.

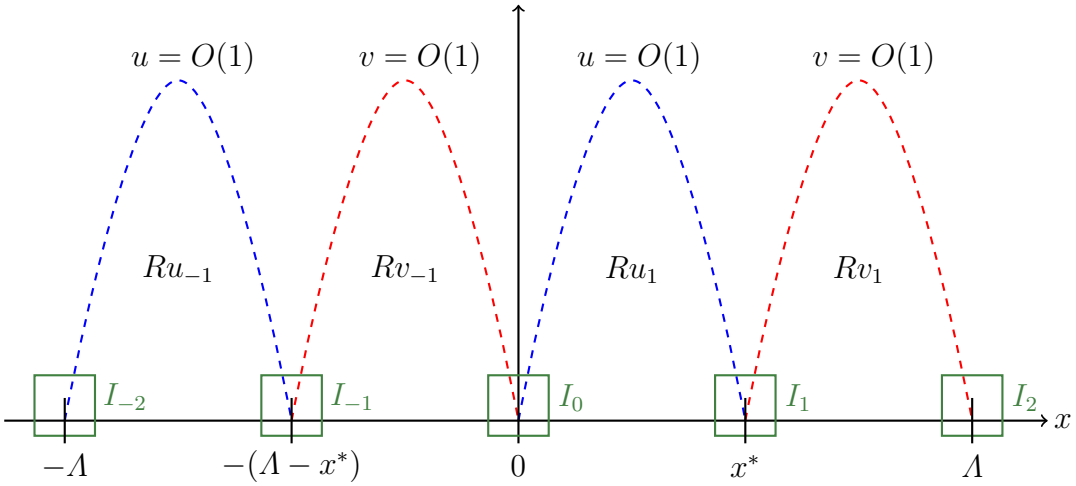


Figure 6.6: *Structure of asymptotic solutions.*

finite domain with periodic boundary conditions. The solution u is symmetric about $x = 0.25$ whereas v is symmetric about $x = 0.75$, with a wavelength equal to one.

Figure 6.6 illustrates the structure of periodic asymptotic solutions of a general kernel combination with wavelength Λ. Blue and red dashed lines represent the asymptotic outer solutions, while Ru_i and Rv_i denote the distinct regions where $v = 0$ and $u = 0$ at the leading order. The green boxes indicated by I_k represent the inner regions where $k = -2, -1, 0, 1, 2$. Finally, outer regions are anywhere outside the inner regions.

To study solutions in the domain $x \in [0, \Lambda]$, we construct asymptotic outer solutions in two distinct regions, Ru_1 and Rv_1. The former region consists of an asymptotic solution where $u = O(1)$ in $x \in [0, x^*]$ and the latter with $v = O(1)$ in $x \in [x^*, \Lambda]$ in the limit of $\epsilon \to 0$. We will see later how ϵ depends on the parameters of our NLLV system. The region where numerical u and v intersect at the junction will be studied asymptotically in the inner region I_1 where $|x - x^*| = O(\chi(\epsilon))$ with $\chi \to 0$ as $\epsilon \to 0$.

6.4 Approximation of convolution term

In the disjoint regions Ru_1 and Rv_1, the steady-state NLLV system (4.4) becomes an uncoupled system

$$\begin{aligned} 0 &= D_1 \frac{\mathrm{d}^2 u}{\mathrm{d}x^2} + u\left(1 - \int_{-\infty}^{\infty} \phi_1(x-y)u(y)\,\mathrm{d}y\right), \\ 0 &= D_2 \frac{\mathrm{d}^2 v}{\mathrm{d}x^2} + Rv\left(1 - \frac{1}{\lambda}\int_{-\infty}^{\infty} \phi_2\left(\frac{x-y}{\lambda}\right) v(y)\,\mathrm{d}y\right). \end{aligned} \tag{6.4}$$

In this section, we approximate each convolution term in the system by assuming periodicity in the solutions u and v. Doing so will simplify the construction of asymptotic outer solutions in later sections. For simplicity, we take $R = 1$ throughout the rest of the computations in this chapter as it gives the same effect as varying D_2 in the steady-state problem (6.4).

6.4.1 Effective periodic Gaussian kernel, Φ_∞, when $\lambda = 1$

We begin by looking at the convolution term where $\phi_1 = \Phi_\infty$ and $\lambda = 1$. Therefore, the approximation below applies to u and v that satisfy these parameters. To simplify the convolution term asymptotically, we first assume that the solution u is periodic with wavelength Λ by writing $u(y) = \sum_{m=-\infty}^{\infty} \overline{u}(y + m\Lambda)$ where $\overline{u}$ is a single hump with wavelength Λ and

$\overline{u}(x) = 0$ for $x \notin [0, \Lambda]$. Then, the convolution term in (6.4) becomes

$$\begin{aligned}\int_{-\infty}^{\infty} \phi_1(x-y)u(y)\,\mathrm{d}y &= \int_{-\infty}^{\infty} \phi_1(x-y) \sum_{m=-\infty}^{\infty} \overline{u}(y+m\Lambda)\,\mathrm{d}y, \\ &= \int_0^{\Lambda} \sum_{m=-\infty}^{\infty} \phi_1(x-y+m\Lambda)\overline{u}(y)\,\mathrm{d}y,\end{aligned} \tag{6.5}$$

by replacing $y + m\Lambda$ with y. Notice that (6.5) involves an infinite summation of shifted kernel ϕ_1. It is possible to represent the infinite series as a complex Fourier series to simplify the convolution term. For a general periodic kernel Φ with wavelength (or period) Λ, the infinite summation of the shifted kernel can be written as

$$P(x) = \sum_{m=-\infty}^{\infty} \Phi(x + m\Lambda). \tag{6.6}$$

The complex form of the Fourier series of the periodic function is

$$P(x) = \sum_{m=-\infty}^{\infty} C_m \mathrm{e}^{\frac{2mx\pi i}{\Lambda}}, \tag{6.7}$$

where

$$\begin{aligned} C_m &= \frac{1}{\Lambda}\int_{-\Lambda/2}^{\Lambda/2} P(x)\mathrm{e}^{-\frac{2mx\pi i}{\Lambda}}\,\mathrm{d}x, \\ &= \frac{1}{\Lambda}\int_{-\Lambda/2}^{\Lambda/2} \sum_{m'} \Phi(x+m'\Lambda)\mathrm{e}^{-\frac{2mx\pi i}{\Lambda}}\,\mathrm{d}x, \\ &= \frac{1}{\Lambda}\sum_{m'}\int_{(-\frac{1}{2}+m')\Lambda}^{(\frac{1}{2}+m')\Lambda} \Phi(y)\mathrm{e}^{-\frac{2m(y-m'\Lambda)\pi i}{\Lambda}}\,\mathrm{d}y, \qquad \text{by replacing } x = y - m'\Lambda, \\ &= \frac{1}{\Lambda}\sum_{m'}\int_{(-\frac{1}{2}+m')\Lambda}^{(\frac{1}{2}+m')\Lambda} \Phi(y)\mathrm{e}^{-\frac{2my\pi i}{\Lambda}}\mathrm{e}^{2mm'\pi i}\,\mathrm{d}y, \\ &= \frac{1}{\Lambda}\int_{-\infty}^{\infty} \Phi(y)\mathrm{e}^{-\frac{2my\pi i}{\Lambda}}\,\mathrm{d}y, \\ &= \frac{1}{\Lambda}\overline{\Phi}\left(\frac{2m\pi}{\Lambda}\right), \end{aligned} \tag{6.8}$$

is the complex Fourier coefficient and $\overline{\Phi}$ is the Fourier transform of Φ.

For Gaussian kernel $\phi_1(x) = \Phi(x) = \Phi_\infty(x) = \frac{1}{2\sqrt{\pi}}\mathrm{e}^{-x^2/4}$, the periodic function $P(x)$ becomes

$$\begin{aligned} P(x) &= \sum_{m=-\infty}^{\infty} \frac{1}{\Lambda}\overline{\Phi}\left(\frac{2m\pi}{\Lambda}\right)\left[\cos\left(\frac{2m\pi x}{\Lambda}\right) + i\sin\left(\frac{2m\pi x}{\Lambda}\right)\right], \\ &= \frac{1}{\Lambda} + \sum_{m=1}^{\infty} \frac{2}{\Lambda}\mathrm{e}^{-\left(\frac{2m\pi}{\Lambda}\right)^2}\cos\left(\frac{2m\pi x}{\Lambda}\right), \\ &= \frac{1}{\Lambda} + \sum_{m=1}^{\infty} Q_m(x), \end{aligned} \tag{6.9}$$

where the positive and negative m in sine terms cancel out each other.

When $m = 1$, $Q_m(x) = \frac{2}{\Lambda}\mathrm{e}^{-4\pi^2/\Lambda^2}\cos\left(\frac{2\pi x}{\Lambda}\right)$. When $m = 2$, $Q_m(x) = \frac{2}{\Lambda}\mathrm{e}^{-16\pi^2/\Lambda^2}\cos\left(\frac{4\pi x}{\Lambda}\right)$. Therefore, $Q_m(x)$ decreases with increasing m. By letting $\epsilon_\infty = 2\mathrm{e}^{-4\pi^2/\Lambda^2}$, we can then truncate (6.9) into $P(x) \approx \frac{1}{\Lambda} + \frac{\epsilon_\infty}{\Lambda}\cos\left(\frac{2\pi x}{\Lambda}\right)$ in the limit of $\epsilon_\infty \to 0$. For $\epsilon_\infty \ll 1$, we need Λ to be small. However, as we will see later, a good agreement between asymptotic and numerical solutions can be obtained when Λ is not too small. This is because when $\Lambda = 1$, $\epsilon_\infty = O(\mathrm{e}^{-4\pi^2}) \approx O(7 \times 10^{-18})$. Since the main idea of this analysis is to study the solutions in the limit of small diffusivity, we will later scale the diffusion coefficient $D_1 = O(\epsilon_\infty)$ as the distinguished limit for u.

For a Gaussian kernel, the convolution term from (6.5) becomes

$$\begin{aligned} \int_0^\Lambda \sum_{m=-\infty}^{\infty} \phi_1(x - y + m\Lambda)\overline{u}(y)\,\mathrm{d}y &= \int_0^\Lambda P(x-y)\overline{u}(y)\,\mathrm{d}y, \\ &\approx \int_0^\Lambda \left[\frac{1}{\Lambda} + \frac{\epsilon_\infty}{\Lambda}\cos\left(\frac{2\pi(x-y)}{\Lambda}\right)\right]\overline{u}(y)\,\mathrm{d}y. \end{aligned} \tag{6.10}$$

In short, we have shifted a periodic solution with a localised kernel to a solution with an effective periodic kernel (see (6.5)) and then transformed it into a solution on a finite domain (see (6.10)).

6.4.2 Effective periodic Gaussian kernel, Φ_∞, when $\lambda \neq 1$

When $\lambda \neq 1$, we require a slightly different approach to approximate the convolution term for v. We first eliminate the λ in (6.4) by letting $x = \lambda\tilde{x}$, $y = \lambda\tilde{y}$, $v(x) = v(\tilde{x})$ and $v(y) = v(\tilde{y})$ to obtain

$$0 = \frac{D_2}{\lambda^2}\frac{\mathrm{d}^2 v}{\mathrm{d}\tilde{x}^2} + Rv\left(1 - \int_{-\infty}^{\infty} \phi_2\left(\tilde{x} - \tilde{y}\right) v(\tilde{y})\,\mathrm{d}\tilde{y}\right). \tag{6.11}$$

Similar to solution u, we assume that the solution v is periodic with wavelength of Λ/λ by writing $v(\tilde{y}) = \sum_{m=-\infty}^{\infty} \overline{v}\left(\frac{\lambda\tilde{y}+m\Lambda}{\lambda}\right)$ where $\overline{v}$ is a single hump with wavelength Λ/λ. Finally, we let $\phi_2 = \Phi = \Phi_\infty$ to obtain the convolution term approximation

$$\begin{aligned}
\int_{-\infty}^{\infty} \phi_2(\tilde{x} - \tilde{y}) v(\tilde{y})\,\mathrm{d}\tilde{y} &= \int_{-\infty}^{\infty} \phi_2(\tilde{x} - \tilde{y}) \sum_{m=-\infty}^{\infty} \overline{v}\left(\frac{\lambda\tilde{y} + m\Lambda}{\lambda}\right) \mathrm{d}\tilde{y}, \\
&= \int_0^{\Lambda/\lambda} \sum_{m=-\infty}^{\infty} \phi_2\left(\tilde{x} - \tilde{y} + \frac{m\Lambda}{\lambda}\right) \overline{v}(\tilde{y})\,\mathrm{d}\tilde{y}, \\
&= \int_0^{\Lambda/\lambda} P_\lambda(\tilde{x} - \tilde{y})\overline{v}(\tilde{y})\,\mathrm{d}\tilde{y}, \\
&\approx \int_0^{\Lambda/\lambda} \left[\frac{\lambda}{\Lambda} + \frac{\lambda\epsilon_{\infty,\lambda}}{\Lambda}\cos\left(\frac{2\pi(\tilde{x} - \tilde{y})\lambda}{\Lambda}\right)\right] \overline{v}(\tilde{y})\,\mathrm{d}\tilde{y},
\end{aligned} \tag{6.12}$$

where $P_\lambda(x) = \sum_{m=-\infty}^{\infty} \Phi\left(x + \frac{m\Lambda}{\lambda}\right)$ and $\epsilon_{\infty,\lambda} = 2\mathrm{e}^{-4\pi^2\lambda^2/\Lambda^2}$ (see Appendix E.1 for more details).

6.4.3 Effective periodic exponential kernel, Φ_1, when $\lambda = 1$

When $\phi_1(x) = \Phi(x) = \mathrm{e}^{-|x|}/2$, the infinite summation of the shifted kernel $P(x) = \sum_{m=-\infty}^{\infty} \Phi(x + m\Lambda)$ is in the form

$$\begin{aligned} P(x) &= \sum_{m=-\infty}^{\infty} \frac{1}{\Lambda}\overline{\Phi}\left(\frac{2m\pi}{\Lambda}\right)\left[\cos\left(\frac{2m\pi x}{\Lambda}\right) + i\sin\left(\frac{2m\pi x}{\Lambda}\right)\right], \\ &= \frac{1}{\Lambda} + \sum_{m=1}^{\infty} \frac{2}{\Lambda\left(1 + \left(\frac{2m\pi}{\Lambda}\right)^2\right)} \cos\left(\frac{2m\pi x}{\Lambda}\right), \\ &\approx \frac{1}{\Lambda} + \frac{\Lambda}{2\pi^2}\sum_{m=1}^{\infty} \frac{1}{m^2}\cos\left(\frac{2m\pi x}{\Lambda}\right), \quad \text{as } \Lambda \to 0, \\ &= \frac{1}{\Lambda} + \frac{\Lambda}{4\pi^2}\left[\mathrm{Li}_2\left(\mathrm{e}^{-\frac{2i\pi x}{\Lambda}}\right) + \mathrm{Li}_2\left(\mathrm{e}^{\frac{2i\pi x}{\Lambda}}\right)\right], \end{aligned} \tag{6.13}$$

where $\sum_{m=1}^{\infty} \frac{1}{m^2}\cos\left(\frac{2m\pi x}{\Lambda}\right) = \frac{1}{2}\left[\mathrm{Li}_2\left(\mathrm{e}^{-\frac{2i\pi x}{\Lambda}}\right) + \mathrm{Li}_2\left(\mathrm{e}^{\frac{2i\pi x}{\Lambda}}\right)\right]$.

Here, $\mathrm{Li}_n(z)$ is a polylogarithm function of order n and argument z. Next, we make use of the relationship $\mathrm{Li}_n(z) + (-1)^n\mathrm{Li}_n(1/z) = -\frac{(2\pi i)^n}{n!}B_n\left(\frac{1}{2} + \frac{\ln(-z)}{2\pi i}\right)$ for integer n and complex z where $B_n(x)$ is a Bernoulli polynomials. Therefore, $P(x) \approx \frac{1}{\Lambda} + \frac{\Lambda}{4\pi^2}\left[2\pi^2 B_2\left(\frac{x}{\Lambda}\right)\right]$. For $n = 2$, the Bernoulli polynomial $B_2(x)$ can be expressed explicitly as $x^2 - x + 1/6$, thus simplifying $P(x)$ to $\frac{1}{\Lambda} + \frac{\Lambda}{4\pi^2}\left[2\pi^2\left(\frac{x^2}{\Lambda^2} - \frac{x}{\Lambda} + \frac{1}{6}\right)\right]$. Hence, the approximated convolution term for u becomes

$$\int_0^{\Lambda} P(x-y)\overline{u}(y)\,\mathrm{d}y \approx \int_0^{\Lambda}\left[\frac{1}{\Lambda} + \frac{2\pi^2\epsilon_1}{\Lambda}\left(\frac{x^2}{\Lambda^2} - \frac{|x|}{\Lambda} + \frac{1}{6}\right)\right]\overline{u}(y)\,\mathrm{d}y, \tag{6.14}$$

for a periodic exponential kernel symmetric at $x = 0$ and $\epsilon_1 = \Lambda^2/4\pi^2$. Note that $\epsilon_1 \to 0$ in the asymptotic limit of $\Lambda \to 0$. Specifically, $\epsilon_1 \ll 1$ when $\Lambda \ll 2\pi \approx 6.3$.

6.4.4 Effective periodic exponential kernel, Φ_1, when $\lambda \neq 1$

By making similar assumptions to the Gaussian case in subsection 6.4.2 and letting $\phi_2 = \Phi = \Phi_1$, we can approximate the convolution term for v as

$$\int_0^{\Lambda/\lambda} P_\lambda(\tilde{x}-\tilde{y})\overline{v}(\tilde{y})\,\mathrm{d}\tilde{y} \approx \int_0^{\Lambda/\lambda} \left[\frac{\lambda}{\Lambda} + \frac{2\pi^2\lambda\epsilon_{1,\lambda}}{\Lambda}\left(\frac{(\tilde{x}-\tilde{y})^2\lambda^2}{\Lambda^2} - \frac{|\tilde{x}-\tilde{y}|\lambda}{\Lambda} + \frac{1}{6}\right)\right]\overline{v}(\tilde{y})\,\mathrm{d}\tilde{y}, \tag{6.15}$$

in the limit of $\epsilon_{1,\lambda} \to 0$ where $P_\lambda(x) = \sum_{m=-\infty}^{\infty} \Phi\left(x + \frac{m\Lambda}{\lambda}\right)$ and $\epsilon_{1,\lambda} = \Lambda^2/4\pi^2\lambda^2$ (see Appendix E.2 for more details).

6.5 Inner region matching

In the outer regions (Ru_i and Rv_i for $i = -1, 1$ in Figure 6.6), either u or v are sufficiently small, hence the reaction terms αuv and βuv are equal to zero in (6.1). In the inner regions (I_k for $k = -2, -1, 0, 1, 2$ in Figure 6.6), however, the diffusion terms balance with the reaction terms, leading to a matching condition that matches the inner region with the outer solutions. In this section, we take a closer look at the disjoint regions Ru_1 and Rv_1 in Figure 6.6. In particular, we investigate the matching condition for the slopes of u and v at the inner region I_1 for general kernels ϕ_1 and ϕ_2 as well as general λ.

6.5.1 Ratio of slopes

Let us look at an example where both kernels are Gaussian functions and $\lambda \neq 1$. Suppose we asymptotically expand $u = \overline{u} = u_0 + \epsilon_\infty u_1 + \epsilon_\infty^2 u_2 + \dots$ and $v = \overline{v} = v_0 + \epsilon_{\infty,\lambda} v_1 + \epsilon_{\infty,\lambda} v_2 + \dots$ and substitute the approximated convolution

term into the uncoupled NLLV system (6.4) in the outer solution, i.e.

$$
\begin{aligned}
0 &= D_1 \frac{\mathrm{d}^2(u_0+\epsilon_\infty u_1)}{\mathrm{d}x^2} \\
&\quad + (u_0+\epsilon_\infty u_1)\left(1-\int_0^\Lambda \left[\frac{1}{\Lambda}+\frac{\epsilon_\infty}{\Lambda}\cos\left(\frac{2\pi(x-y)}{\Lambda}\right)\right](u_0(y)+\epsilon_\infty u_1(y))\,\mathrm{d}y\right), \\
0 &= D_2 \frac{\mathrm{d}^2(v_0+\epsilon_{\infty,\lambda} v_1)}{\mathrm{d}x^2} \\
&\quad + R(v_0+\epsilon_{\infty,\lambda} v_1)\left(1-\int_0^\Lambda \left[\frac{1}{\Lambda}+\frac{\epsilon_{\infty,\lambda}}{\Lambda}\cos\left(\frac{2\pi(x-y)}{\Lambda}\right)\right](v_0(\hat{y})+\epsilon_{\infty,\lambda} v_1(\hat{y}))\,\mathrm{d}y\right).
\end{aligned}
\tag{6.16}
$$

If we redefine $D_1 = \tilde{D}_1\epsilon_\infty$ and $D_2 = \tilde{D}_2\epsilon_{\infty,\lambda}$, it can be worked out that at leading order, the terms $1-\phi_1 * u$ and $1-\phi_2 * v$ in (6.16) are of $O(\epsilon_\infty)$ and $O(\epsilon_{\infty,\lambda})$ respectively. In other words, they are the same order as their corresponding diffusion coefficients.

Therefore, in the inner region, we will rescale the full steady-state system

$$
\begin{aligned}
0 &= D_1\frac{\mathrm{d}^2u}{\mathrm{d}x^2} + u\left(1-\int_{-\infty}^{\infty}\phi_1(x-y)u(y)\,\mathrm{d}y-\alpha v\right), \\
0 &= D_2\frac{\mathrm{d}^2v}{\mathrm{d}x^2} + Rv\left(1-\frac{1}{\lambda}\int_{-\infty}^{\infty}\phi_2\left(\frac{x-y}{\lambda}\right)v(y)\,\mathrm{d}y-\beta u\right),
\end{aligned}
$$

with $x=\epsilon^\gamma\check{x}$, $y=\epsilon^\gamma\check{y}$, $u=\epsilon^\gamma\check{u}$, $v=\epsilon^\gamma\check{v}$, $D_1=\check{D}_1\epsilon$, $D_2=\check{D}_2\epsilon$, $1-\phi_1*u=O(\epsilon)$ and $1-\phi_2*v=O(\epsilon)$ for small parameter ϵ that characterises the size of diffusion coefficients. Note that $\gamma>0$, $\check{x},\check{y},\check{u},\check{v},\check{D}_1,\check{D}_2=O(1)$ and we let $\lambda,R=1$. Here, x,y,u and v represent the variables of outer solutions whereas $\check{x},\check{y},\check{u}$ and $\check{v}$ are the inner scalings. Upon rescaling the system, we arrive at the system

$$
\begin{aligned}
0 &= \epsilon^{1-\gamma}\check{D}_1\frac{\mathrm{d}^2\check{u}}{\mathrm{d}\check{x}^2} + \check{u}O(\epsilon^{1+\gamma}) - \epsilon^{2\gamma}\alpha\check{u}\check{v}, \\
0 &= \epsilon^{1-\gamma}\check{D}_2\frac{\mathrm{d}^2\check{v}}{\mathrm{d}\check{x}^2} + \check{v}O(\epsilon^{1+\gamma}) - \epsilon^{2\gamma}\beta\check{u}\check{v}.
\end{aligned}
\tag{6.17}
$$

At leading order where $\epsilon\to 0$, we balance the dominating terms in (6.17) and

deduce that $\gamma = 1/3$. At $O(\epsilon^{2/3})$, the system (6.17) becomes

$$\begin{aligned} 0 &= \check{D}_1 \frac{\mathrm{d}^2\check{u}}{\mathrm{d}\check{x}^2} - \alpha\check{u}\check{v}, \\ 0 &= \check{D}_2 \frac{\mathrm{d}^2\check{v}}{\mathrm{d}\check{x}^2} - \beta\check{u}\check{v}. \end{aligned} \tag{6.18}$$

Then, we take a linear combination of (6.18) and integrate it to obtain

$$K = \beta\check{D}_1 \frac{\mathrm{d}\check{u}}{\mathrm{d}\check{x}} - \alpha\check{D}_2 \frac{\mathrm{d}\check{v}}{\mathrm{d}\check{x}}, \tag{6.19}$$

for constant K. As $\check{x} \to \infty$, $\check{u} \to 0$ and therefore $v = \epsilon^{1/3}\check{v}$, resulting in the matching condition

$$K = -\alpha\check{D}_2 \left.\frac{\mathrm{d}\check{v}}{\mathrm{d}\check{x}}\right|_{\check{x}\to\infty} = -\alpha\check{D}_2 \left.\frac{\mathrm{d}v}{\mathrm{d}x}\right|_{x=0^-}. \tag{6.20}$$

Similarly, as $\check{x} \to -\infty$, $\check{v} \to 0$ and hence we obtain the matching condition

$$K = \beta\check{D}_1 \left.\frac{\mathrm{d}\check{u}}{\mathrm{d}\check{x}}\right|_{\check{x}\to-\infty} = \beta\check{D}_1 \left.\frac{\mathrm{d}u}{\mathrm{d}x}\right|_{x=0^+}. \tag{6.21}$$

Equating both K terms gives rise to the ratio of slope

$$\frac{\beta}{\alpha} = -\left.\frac{D_2 \frac{\mathrm{d}v}{\mathrm{d}x}}{D_1 \frac{\mathrm{d}u}{\mathrm{d}x}}\right|_{x=0}, \tag{6.22}$$

in the outer scalings. Note that the ratio above works for all kernel combinations as balancing the dominating terms in (6.17) gets rid of the convolution terms.

6.6 Asymptotic outer solution

In this section, we derive the asymptotic outer solutions u and v using the approximated convolution terms and the ratio of slopes derived in sections 6.4 and 6.5. We begin the section with the case of $\phi_1 = \phi_2 = \phi = \Phi_\infty$ and then

proceed to $\phi = \Phi_1$ and finally, the combination of $\phi_1 = \Phi_1$ and $\phi_2 = \Phi_\infty$. We derive their asymptotic outer solutions for these kernel pairs and compare them with their numerical simulations. For $\phi = \Phi_\infty$ in particular, we demonstrate how the outer solutions are matched in the inner regions. In addition, we illustrate the comparison of outer solutions when the slope of u and v is the same at the intersection point where $u = v$ (when $\alpha = \beta$) and the cases otherwise.

6.6.1 Asymptotic outer solution when $\Phi = \Phi_\infty$

When $\lambda = 1$

From (6.16), we adopt the scalings of $x = \Lambda\hat{x}$, $y = \Lambda\hat{y}$, $u_0(x) = u_0(\hat{x})$ and $u_1(x) = u_1(\hat{x})$ where $\Lambda \ll 1$, $0 < \hat{x} < 1$ and $0 < \hat{y} < 1$. The rescaled equation can be written as

$$0 = \frac{D_1}{\Lambda^2}\frac{\mathrm{d}^2 u_0}{\mathrm{d}\hat{x}^2} + \frac{\epsilon_\infty D_1}{\Lambda^2}\frac{\mathrm{d}^2 u_1}{\mathrm{d}\hat{x}^2} + (u_0 + \epsilon_\infty u_1)\left(1 - \int_0^1 (1 + \epsilon_\infty \cos(2\pi(\hat{x} - \hat{y})))\,(u_0(\hat{y}) + \epsilon_\infty u_1(\hat{y}))\,\mathrm{d}\hat{y}\right). \tag{6.23}$$

Then, we let $D_1/\Lambda^2 = \epsilon_\infty \hat{D}_1 = O(\epsilon_\infty)$ which gives

$$\hat{D}_1 = \frac{D_1}{2\Lambda^2 \mathrm{e}^{-\frac{4\pi^2}{\Lambda^2}}}. \tag{6.24}$$

At $O(1)$, (6.23) returns $u_0 = 0$ or $\int_0^1 u_0(\hat{y})\,\mathrm{d}\hat{y} = 1$. At $O(\epsilon_\infty)$, we have

$$0 = \hat{D}_1\frac{\mathrm{d}^2 u_0}{\mathrm{d}\hat{x}^2} - u_0\int_0^1 \cos(2\pi(\hat{x} - \hat{y}))\,u_0(\hat{y})\,\mathrm{d}\hat{y} - u_0\int_0^1 u_1(\hat{y})\,\mathrm{d}\hat{y}. \tag{6.25}$$

By applying trigonometric identity $\cos(a - b) = \cos(a)\cos(b) + \sin(a)\sin(b)$,

(6.25) becomes

$$0 = \hat{D}_1 \frac{\mathrm{d}^2 u_0}{\mathrm{d}\hat{x}^2} + u_0 \Big[-\sin(2\pi\hat{x}) \int_0^1 \sin(2\pi\hat{y}) u_0(\hat{y})\,\mathrm{d}\hat{y} - \cos(2\pi\hat{x}) \int_0^1 \cos(2\pi\hat{y}) u_0(\hat{y})\,\mathrm{d}\hat{y} - \int_0^1 u_1(\hat{y})\,\mathrm{d}\hat{y} \Big]. \tag{6.26}$$

Next, we assume the leading term u_0 to be zero at $\hat{x} = 0$ for matching and solve for u_0 in Ru_1 with a rescaled domain $\hat{x} \in [0, b]$ where $0 < b < 1$. Therefore, the boundary conditions are $u_0 = 0$ when $\hat{x} = 0$ and $\hat{x} = b$. By rescaling $\hat{x} = b\overline{x}$, $\hat{y} = b\overline{y}$, $u_0(\hat{x}) = \overline{u}_0(\overline{x})$ and $u_1(\hat{x}) = \overline{u}_1(\overline{x})$ for $0 < \overline{x} < 1$, we can rewrite (6.26) as

$$0 = \frac{\hat{D}_1}{b^2} \frac{\mathrm{d}^2 \overline{u}_0}{\mathrm{d}\overline{x}^2} + \overline{u}_0 \Big[-b\sin(2\pi b\overline{x}) \int_0^1 \sin(2\pi b\overline{y}) \overline{u}_0(\overline{y})\,\mathrm{d}\overline{y} - b\cos(2\pi b\overline{x}) \int_0^1 \cos(2\pi b\overline{y}) \overline{u}_0(\overline{y})\,\mathrm{d}\overline{y} - b\int_0^1 \overline{u}_1(\overline{y})\,\mathrm{d}\overline{y} \Big], \tag{6.27}$$

which is a nonlinear Mathieu equation (see Subsection 2.3) of the form

$$0 = \frac{\hat{D}_1}{b^2} \frac{\mathrm{d}^2 \overline{u}_0}{\mathrm{d}\overline{x}^2} + \overline{u}_0 \left[a - 2q\cos(2\pi b\overline{x}) - 2p\sin(2\pi b\overline{x}) \right], \tag{6.28}$$

where

$$\begin{aligned} a &= -b \int_0^1 \overline{u}_1(\overline{y})\,\mathrm{d}\overline{y}, \\ 2q &= b \int_0^1 \cos(2\pi b\overline{y}) \overline{u}_0(\overline{y})\,\mathrm{d}\overline{y}, \\ 2p &= b \int_0^1 \sin(2\pi b\overline{y}) \overline{u}_0(\overline{y})\,\mathrm{d}\overline{y}. \end{aligned} \tag{6.29}$$

Note that the nonlinear Mathieu equation (6.28) is subjected to the boundary conditions of $\overline{u}_0(0) = 0$ and $\overline{u}_0(1) = 0$. We can easily derive the asymptotic solutions for v_0 in Rv_1 using a similar approach. By replacing b with $1 - b$ and scaling $D_2/\Lambda^2 = \epsilon_\infty \hat{D}_2 = O(\epsilon_\infty)$, we obtain

$$\hat{D}_2 = \frac{D_2}{2\Lambda^2 \mathrm{e}^{-\frac{4\pi^2}{\Lambda^2}}}. \tag{6.30}$$

The asymptotic outer equation for v is another nonlinear Mathieu equation

$$0 = \frac{\hat{D}_2}{(1-b)^2}\frac{\mathrm{d}^2\overline{v}_0}{\mathrm{d}\overline{x}^2} + R\overline{v}_0\left[a - 2q\cos(2\pi(1-b)\overline{x}) - 2p\sin(2\pi(1-b)\overline{x})\right], \quad (6.31)$$

where

$$\begin{aligned} a &= -(1-b)\int_0^1 \overline{v}_1(\overline{y})\,\mathrm{d}\overline{y}, \\ 2q &= (1-b)\int_0^1 \cos(2\pi(1-b)\overline{y})\overline{v}_0(\overline{y})\,\mathrm{d}\overline{y}, \\ 2p &= (1-b)\int_0^1 \sin(2\pi(1-b)\overline{y})\overline{v}_0(\overline{y})\,\mathrm{d}\overline{y}. \end{aligned} \quad (6.32)$$

Similarly, the boundary conditions for the nonlinear Mathieu equation (6.31) are $\overline{v}_0(0) = 0$ and $\overline{v}_0(1) = 0$.

When $\lambda \neq 1$

When $\lambda \neq 1$ in ϕ_2, We substitute the periodic convolution term from (6.12) into (6.11) to give

$$0 = \frac{D_2}{\lambda^2}\frac{\mathrm{d}^2 v}{\mathrm{d}\tilde{x}^2} + Rv\left(1 - \lambda\int_0^{\Lambda/\lambda}\left[\frac{1}{\Lambda} + \frac{\epsilon_{\infty,\lambda}}{\Lambda}\cos\left(\frac{2\pi(\tilde{x}-\tilde{y})\lambda}{\Lambda}\right)\right]\overline{v}(\tilde{y})\,\mathrm{d}\tilde{y}\right). \quad (6.33)$$

Then, we rescale $\tilde{x} = \Lambda\hat{x}/\lambda$, $\tilde{y} = \Lambda\hat{y}/\lambda$, $v(\tilde{x}) = v(\hat{x})$, $\overline{v}(\tilde{y}) = \overline{v}(\hat{y})$ and expand v and $\overline{v}$ asymptotically to obtain

$$\begin{aligned} 0 = {} & \frac{D_2}{\Lambda^2}\frac{\mathrm{d}^2 v_0}{\mathrm{d}\hat{x}^2} + \frac{\epsilon_{\infty,\lambda}D_2}{\Lambda^2}\frac{\mathrm{d}^2 v_1}{\mathrm{d}\hat{x}^2} \\ & + R(v_0 + \epsilon_{\infty,\lambda}v_1)\left(1 - \int_0^1 (1 + \epsilon_{\infty,\lambda}\cos(2\pi(\hat{x}-\hat{y})))\,(v_0(\hat{y}) + \epsilon_{\infty,\lambda}v_1(\hat{y}))\,\mathrm{d}\hat{y}\right). \end{aligned} \quad (6.34)$$

Finally, we choose $D_2/\Lambda^2 = \epsilon_{\infty,\lambda}\hat{D}_2 = O(\epsilon_{\infty,\lambda})$ such that

$$\hat{D}_2 = \frac{D_2}{2\Lambda^2 \mathrm{e}^{\frac{-4\pi^2\lambda^2}{\Lambda^2}}}. \quad (6.35)$$

Notice that the λ term in the convolution term is absorbed into the $\hat{D}_2$ term. Therefore, we expect that upon balancing terms at powers of $\epsilon_{\infty,\lambda}$ in (6.34) and rescaling $\hat{x} = (1-b)\overline{x}$, $\hat{y} = (1-b)\overline{y}$, $v_0(\hat{x}) = \overline{v}_0(\overline{x})$ and $v_1(\hat{x}) = \overline{v}_1(\overline{x})$, we will obtain the same nonlinear Mathieu equation as the one for $\overline{v}_0$ when $\lambda = 1$ in (6.31), with $\hat{D}_2$ now a function of λ (See Appendix E.3 for detailed workings).

6.6.2 Computation of asymptotic outer solutions when $\Phi = \Phi_\infty$

To solve the asymptotic solution $\overline{u}_0$ from (6.28) numerically, we first represent the equation as a system of fifth-order equations

$$\begin{aligned}
\overline{u}_0'(\overline{x}) &= \overline{w}(\overline{x}),\\
\overline{w}'(\overline{x}) &= -\frac{b^2\overline{u}_0(\overline{x})}{\hat{D}_1}\left[a - 2q\cos(2\pi b\overline{x}) - 2p\sin(2\pi b\overline{x})\right],\\
\overline{I}_1'(\overline{x}) &= \overline{u}_0(\overline{x}),\\
\overline{I}_2'(\overline{x}) &= \frac{b}{2}\cos(2\pi b\overline{x})\overline{u}_0(\overline{x}),\\
\overline{I}_3'(\overline{x}) &= \frac{b}{2}\sin(2\pi b\overline{x})\overline{u}_0(\overline{x}),
\end{aligned} \tag{6.36}$$

where $\overline{I}_1(\overline{x}) = \int_0^{\overline{x}} \overline{u}_0(\overline{y})\,\mathrm{d}\overline{y}$, $\overline{I}_2(\overline{x}) = \frac{b}{2}\int_0^{\overline{x}} \cos(2\pi b\overline{y})\overline{u}_0(\overline{y})\,\mathrm{d}\overline{y}$, and $\overline{I}_3(\overline{x}) = \frac{b}{2}\int_0^{\overline{x}} \sin(2\pi b\overline{y})\overline{u}_0(\overline{y})\,\mathrm{d}\overline{y}$. Note that a is the eigenvalue, whereas p and q are the unknown parameters of the system defined in (6.29). Therefore, we require eight boundary conditions to solve the system (6.36), i.e. $\overline{u}_0(1) = 0$, $\overline{u}_0(0) = 0$, $\overline{I}_1(1) = 1/b$, $\overline{I}_1(0) = 0$, $\overline{I}_2(1) = q$, $\overline{I}_2(0) = 0$, $\overline{I}_3(1) = p$, and $\overline{I}_3(0) = 0$. Here, we make use of the boundary conditions of the Mathieu equation in (6.28), the definition of p and q in (6.29), as well as the condition $\int_0^1 \overline{u}_0(\overline{y})\,\mathrm{d}\overline{y} = 1/b$ obtained from the equation (6.23) at order 1 (by rescaling $\hat{y} = b\overline{y}$ in $\int_0^1 u_0(\hat{y})\,\mathrm{d}\hat{y} = 1$). Then, we can solve the fifth-order system numerically using *bvp5c* on MATLAB to obtain $\overline{u}_0$ in terms of $\overline{x}$. Computing the solutions of the simplest case where the leading order periodic solutions $\overline{u}_0$ and $\overline{v}_0$ have the same slope at the intersection point requires that $b = 0.5$. Suitable initial guesses that satisfy all

the boundary conditions in the system (6.36) are, therefore

$$\begin{aligned}
\overline{u}_0(\overline{x}) &= \pi \sin(\pi\overline{x}),\\
\overline{w}(\overline{x}) &= \pi^2 \cos(\pi\overline{x}),\\
\overline{I}_1(\overline{x}) &= 1 - \cos(\pi\overline{x}),\\
\overline{I}_2(\overline{x}) &= \frac{1}{16}\left[1 - \cos(2\pi\overline{x})\right],\\
\overline{I}_3(\overline{x}) &= \frac{\pi}{8}\left[\overline{x} - \frac{1}{2\pi}\sin(2\pi\overline{x})\right].
\end{aligned} \tag{6.37}$$

At $b = 0.5$, the boundary conditions involving b, q and p can be computed analytically as $\overline{I}_1(1) = 2$, $\overline{I}_2(1) = q = 0$ and $\overline{I}_3(1) = p = 0.3927$.

The same method will also be employed to solve for the asymptotic solution $\overline{v}_0$ from (6.31) numerically by replacing b with $1 - b$ in the fifth order system and its boundary conditions. At $b = 0.5$, the same initial guesses from (6.37) will be used to solve for the asymptotic solution $\overline{v}_0$ from (6.31) numerically.

To compute the asymptotic solutions when $\lambda \neq 1$, we repeat the steps above but with $\hat{D}_1$ and $\hat{D}_2$ in (6.24) and (6.35) instead.

6.6.3 Inner region solution

To demonstrate how the rescaled system (6.18) in the inner region matches the outer solutions, we solve the system numerically and show that the solutions converge to the slopes of the outer solutions at both ends. We choose the simplest case where $D_1 = D_2 = D$ and therefore $\check{D}_1 = \check{D}_2 = \check{D}$. From (6.19), we obtain $\beta\check{u} - \alpha\check{v} = K\check{x} + H$ for constant H, where $K = \beta \left.\frac{\mathrm{d}u}{\mathrm{d}x}\right|_{x=0^+}$. Then, we rewrite $\check{v}$ as $(\beta\check{u} - K\check{x} - H)/\alpha$ and substitute it into the first equation in the system (6.18) to obtain the second order ODE

$$0 = \check{D}\frac{\mathrm{d}^2\check{u}}{\mathrm{d}\check{x}^2} - \check{u}(\beta\check{u} - K\check{x} - H), \tag{6.38}$$

that solves for $\check{u}$ in the inner region.

Numerical method

By solving the fifth-order system (6.36) for asymptotic outer solution $\overline{u}_0(\overline{x})$, we obtain the slope $\overline{u}_0'$ at the origin. We then rescale the slope to the outer scalings to obtain $K = \beta\overline{u}_0'/(\Lambda b)$. Since it is not straightforward to calculate H analytically, we assume that $H = 0$. In the inner region, the matching conditions are $\check{u}' \sim K/\beta$ as $\check{x} \to -\infty$ and $\check{u} \sim 0$ as $\check{x} \to \infty$. Then, we solve the second order ODE (6.38) using *bvp5c* in MATLAB with the boundary conditions $\check{u}'(-L) = K/\beta$ and $\check{u}(L) = 0$ in the domain $\check{x} \in [-L, L]$. The initial guesses that satisfy these boundary conditions are $\check{u}(\check{x}) = 0.5K\check{x}(1 - \tanh\check{x})/\beta$ and $\check{u}'(\check{x}) = (-0.5K\check{x}\,\mathrm{sech}^2(\check{x}) + 0.5K(1 - \tanh\check{x}))/\beta$. By setting $L = 5$ in the inner region, we can solve for the inner solutions $\check{u}$ and $\check{v}$. Figure 6.7 illustrates how the inner region matches the outer region of symmetric solutions with Gaussian kernels.

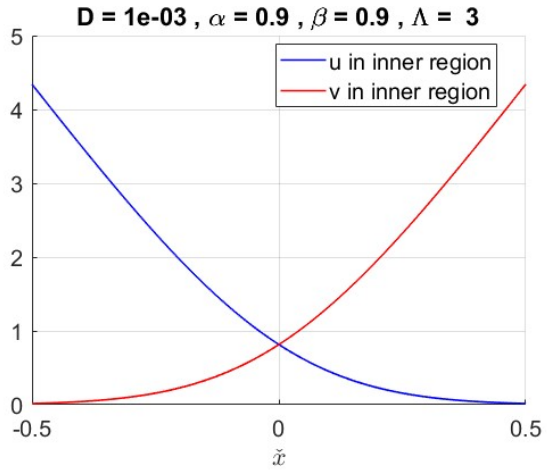


Figure 6.7: *Magnified inner region from solving (6.38) when both* $\phi = \Phi = \Phi_\infty$.

From Figure 6.7, we see that both $\check{u}$ and $\check{v}$ increase linearly from $\check{u}, \check{v} \ll 1$ and intersect at $\check{x} = 0$. Then, they continue to grow above the intersection point to match the slopes of the outer solutions.

6.6.4 Comparison with numerical solution when $\Phi = \Phi_\infty$

We are now ready to compare the asymptotic solutions $\overline{u}_0(\overline{x})$ and $\overline{v}_0(\overline{x})$ from the nonlinear Mathieu equations (6.28) and (6.31) with the numerical solutions

in the fully nonlinear steady-state problem. We begin by comparing the outer solutions with the same slopes in u and v at the intersection point, i.e. when $D_1 = D_2$, $\alpha = \beta$, $b = 0.5$ and $\lambda = 1$. Then, we compare the outer solutions when the slopes of u and v at the junction are different when $\alpha \neq \beta$ or/and $\lambda \neq 1$.

Outer solutions with the same slope

We first plot the numerical solution with a fixed set of parameters $[D_1, D_2, \alpha, \beta, \lambda, \Lambda]$. Next, we use the same set of parameter values to compute $\hat{D}_1$ from (6.24), which is in turn used to solve the fifth-order system (6.36) to obtain the asymptotic outer solution $\overline{u}_0(\overline{x})$. To compare it with the numerical solutions u in the fully nonlinear NLLV system in the same scaling, we plot the asymptotic solution u by rescaling $x = \overline{x}b\Lambda$, as shown in Figure 6.8. We then repeat the same process to plot the asymptotic solution $\overline{v}_0$ by shifting $b\Lambda$ in x, i.e.$x = b\Lambda + \overline{x}(1-b)\Lambda$.

	$D_1 = D_2$	$\alpha = \beta$	λ	Λ	$\hat{D}_1$
(a)	10^{-4}	0.1	1	2	0.242
(b)	10^{-5}	0.1	1	2	0.0242
(c)	10^{-4}	0.3667	1	1	6.99×10^{12}
(d)	10^{-5}	0.3667	1	1	6.99×10^{11}
(e)	10^{-3}	0.9	1	3	4.46×10^{-3}
(f)	10^{-4}	0.9	1	3	4.46×10^{-4}

Table 6.4: *Parameter values for asymptotic solutions of u and v from solving (6.28) and (6.31) where $\phi_1 = \phi_2 = \phi = \Phi_\infty$ and $\alpha = \beta$. The asymptotic solutions can be found in Figure 6.8.*

We first plot some solutions with the parameter values in Table 6.4. From Figure 6.8, the asymptotic outer solutions u and v agree with the numerical solutions to a good extent. Notice that the outer solutions in Figures 6.8(b), 6.8(d), and 6.8(f) have better agreement compared to those in Figures 6.8(a), 6.8(c) and 6.8(e). This could be explained by the diffusion coefficients of the former group being ten times smaller than the latter group. This observation is supported by our assumption of small diffusivity when deriving the Mathieu equation earlier.

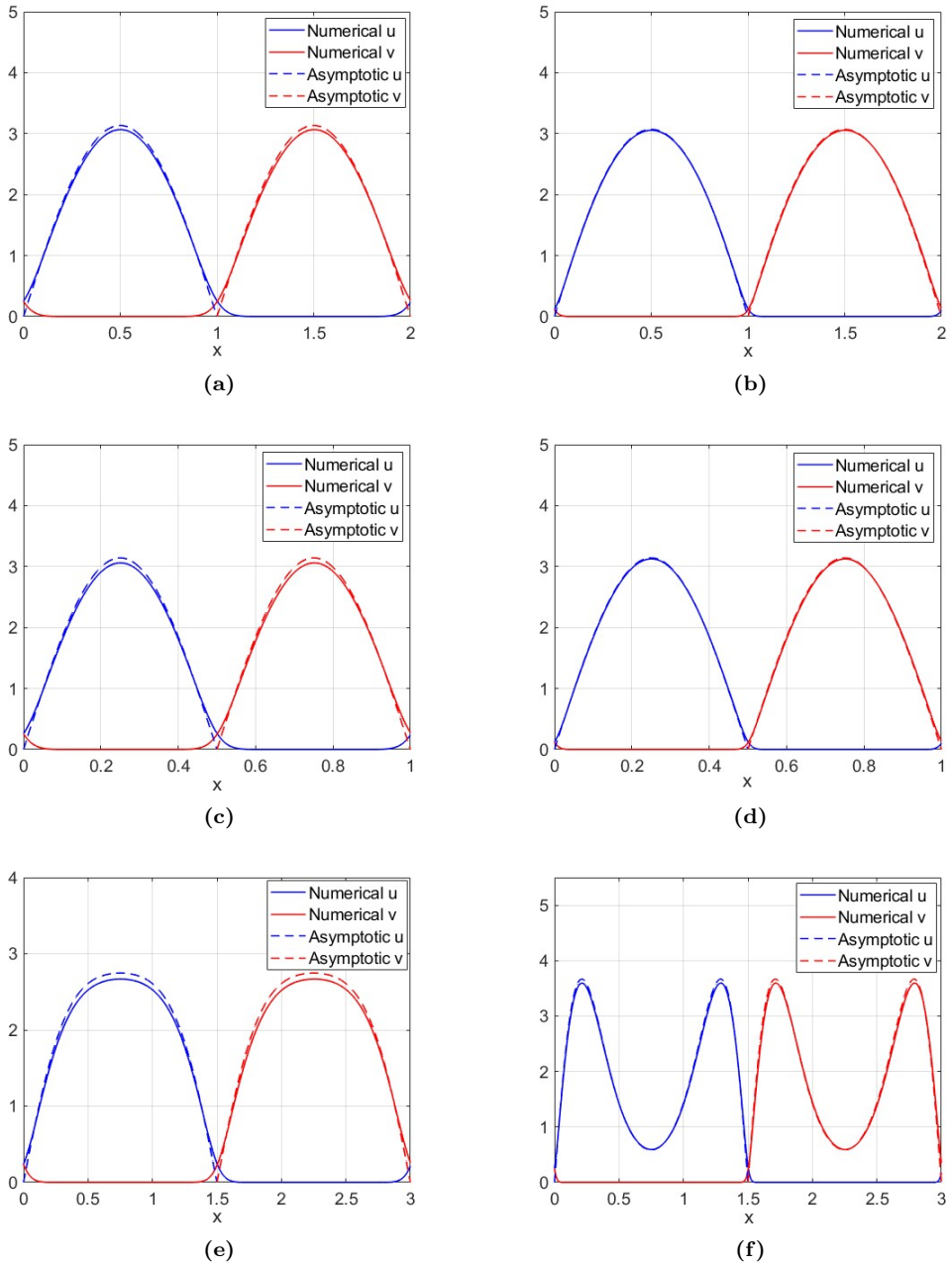


Figure 6.8: *Plots of asymptotic and numerical solutions u and v for $\phi_1 = \phi_2 = \phi = \Phi_\infty$ when $D_1 = D_2$, $\lambda = 1$ and $b = 0.5$. The details of the parameter values can be found in Table 6.4. (a) $D_1 = D_2 = 10^{-4}, \alpha = \beta = 0.1, \lambda = 1, \Lambda = 2, \hat{D}_1 = 0.242$, (b) $D_1 = D_2 = 10^{-5}, \alpha = \beta = 0.1, \lambda = 1, \Lambda = 2, \hat{D}_1 = 0.0242$, (c) $D_1 = D_2 = 10^{-4}, \alpha = \beta = 0.3667, \lambda = 1, \Lambda = 1, \hat{D}_1 = 6.99 \times 10^{12}$, (d) $D_1 = D_2 = 10^{-5}, \alpha = \beta = 0.3667, \lambda = 1, \Lambda = 1, \hat{D}_1 = 6.99 \times 10^{11}$, (e) $D_1 = D_2 = 10^{-3}, \alpha = \beta = 0.9, \lambda = 1, \Lambda = 3, \hat{D}_1 = 4.46 \times 10^{-3}$, and (f) $D_1 = D_2 = 10^{-4}, \alpha = \beta = 0.9, \lambda = 1, \Lambda = 3, \hat{D}_1 = 4.46 \times 10^{-4}$.*

Then, we plot some solutions with decreasing α and β in Figure 6.9. It can be seen that the larger the values of α and β, the better the agreement between the asymptotic and the numerical outer solutions, provided that the other parameters remain the same.

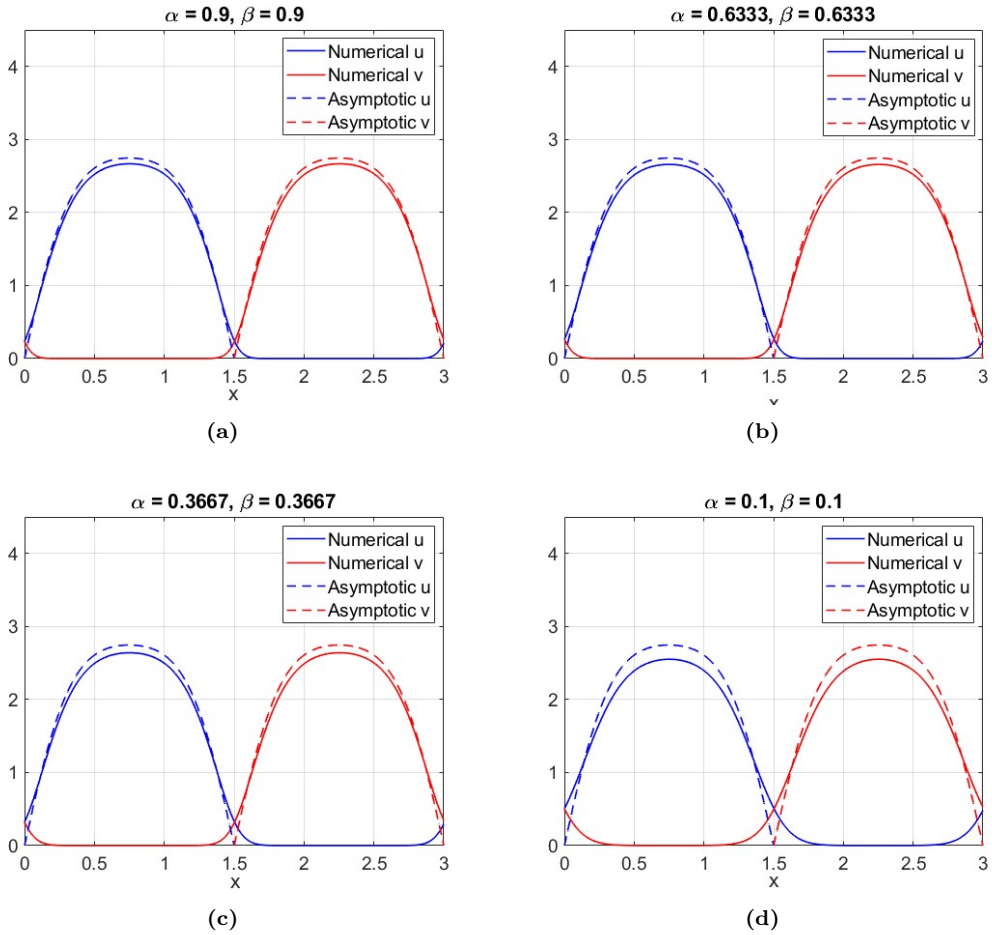


Figure 6.9: *Plots of asymptotic and numerical solutions u and v for $\phi_1 = \phi_2 = \phi = \Phi_\infty$ when $D_1 = D_2 = 10^{-3}$, $\lambda = 1$, $\Lambda = 3$ and $b = 0.5$. The values of α and β decrease from (a) to (d).*

Outer solutions with different slopes

We first compute the outer solutions with the same slopes from the Mathieu equations (6.28) for u and (6.31) or (E.8) for v depending on the λ value. Then, we apply the continuation method in b from $b = 0.5$ to a new parameter b such that $0 < b < 1$ and $b \neq 0.5$. Once we have computed the leading order outer solutions asymptotically, we can work out the slopes of u ($u \approx \overline{u}_0$) and v ($v \approx \overline{v}_0$) as $\mathrm{d}u/\mathrm{d}\overline{x}$ and $\mathrm{d}v/\mathrm{d}\overline{x}$. Next, we substitute them into the slope ratio in the inner region (6.22) to obtain

$$\frac{\beta}{\alpha} = -\frac{D_2 b \frac{\mathrm{d}v}{\mathrm{d}\overline{x}}}{D_1(1-b)\frac{\mathrm{d}u}{\mathrm{d}\overline{x}}}, \tag{6.39}$$

and use it to determine the pair of α and β to simulate the numerical outer

solutions for comparison.

For the rest of the asymptotic outer solutions, we define $D_1/\Lambda^2 = \hat{D}_1\epsilon_u$ and $D_1/\Lambda^2 = \hat{D}_1\epsilon_v$ for general ϵ_u and ϵ_v. When both of the kernels are Gaussian functions, we have $\epsilon_u = 2\mathrm{e}^{-4\pi^2/\Lambda^2}$ and $\epsilon_v = 2\mathrm{e}^{-4\pi^2\lambda^2/\Lambda^2}$.

When $\lambda = 1$

We begin by looking at the case where $\lambda = 1$ and $\alpha \neq \beta$. Table 6.5 shows all the parameter values used to plot Figure 6.10. We choose $\Lambda < 4$ so that $\epsilon_u = \epsilon_v < 0.01$. The last column of Table 6.5 represents the ratio of β over α from (6.39).

	$D_1 = D_2$	α	β	λ	Λ	$\hat{D}_1 = \hat{D}_2$	b	Ratio
(a)	10^{-5}	0.9	0.427	1	2	0.0242	0.4	0.474
(b)	10^{-5}	0.9	0.01346	1	2	0.0242	0.1	0.015
(c)	10^{-5}	0.02078	0.1	1	2	0.0242	0.7	0.208
(d)	10^{-4}	0.9	0.2006	1	3	4.46×10^{-4}	0.2	0.223

Table 6.5: *Parameter values for asymptotic solutions of u and v from solving (6.28) and (6.31) where $\phi_1 = \phi_2 = \phi = \Phi_\infty$ and $\lambda = 1$. The asymptotic solutions can be found in Figure 6.10.*

It is observed that the asymptotic solutions coincide with the numerical solutions in Figure 6.10(a), and the agreement between solutions is reasonably good in Figure 6.10(c). In Figures 6.10(b) and 6.10(d), the solutions v coincide, but a slight discrepancy exists between the peaks of solutions u due to smaller b. When $b < 0.5$, the peaks of solutions u are higher than that of v, and vice versa when $b > 0.5$. Overall, it is found that the asymptotic solutions from Mathieu equations are able to describe the numerical solutions in disjoint regions in the asymmetric case when the disjoint regions are matched by the ratio of slopes of solutions.

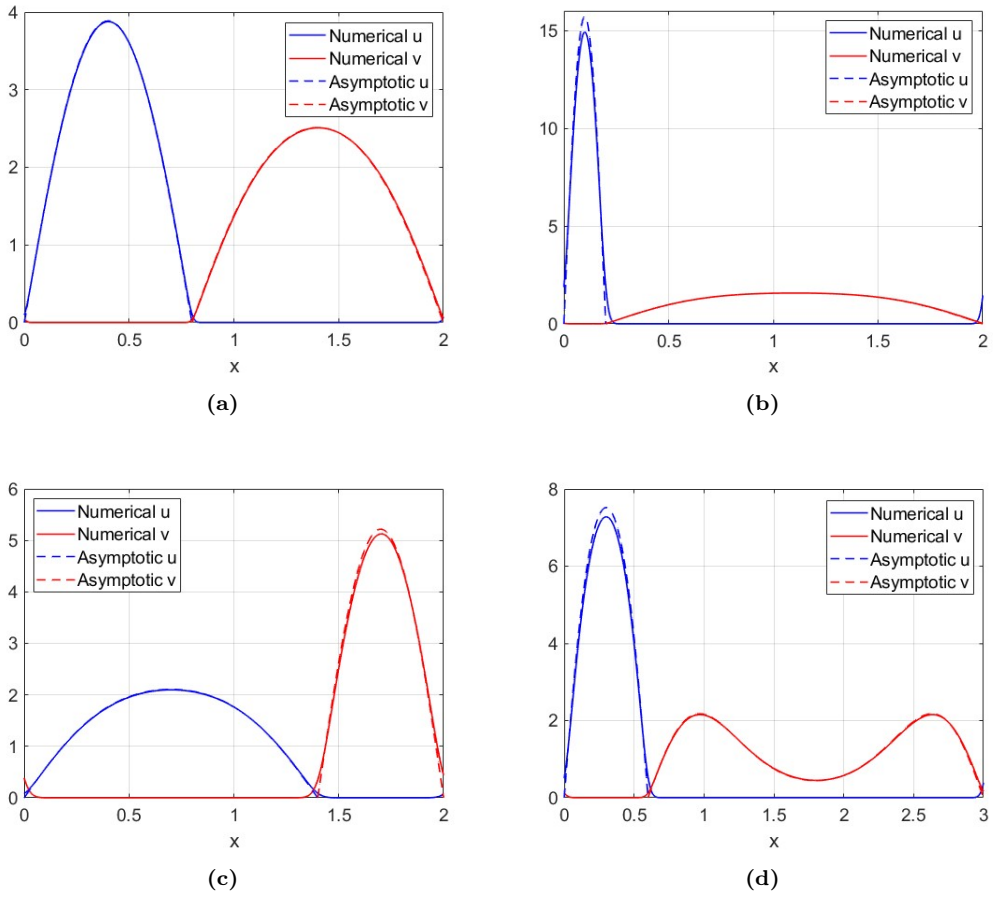


Figure 6.10: *Plots of asymptotic and numerical outer solutions u and v for $\phi_1 = \phi_2 = \phi = \Phi_\infty$ when $\lambda = 1$. The details of the parameter values can be found in Table 6.5. (a) $D_1 = D_2 = 10^{-5}, \alpha = 0.9, \beta = 0.427, \lambda = 1, \Lambda = 2, \hat{D}_1 = \hat{D}_2 = 0.0242, b = 0.4$, (b) $D_1 = D_2 = 10^{-5}, \alpha = 0.9, \beta = 0.01346, \lambda = 1, \Lambda = 2, \hat{D}_1 = \hat{D}_2 = 0.0242, b = 0.1$, (c) $D_1 = D_2 = 10^{-5}, \alpha = 0.02078, \beta = 0.1, \lambda = 1, \Lambda = 2, \hat{D}_1 = \hat{D}_2 = 0.0242, b = 0.7$, (d) $D_1 = D_2 = 10^{-4}, \alpha = 0.9, \beta = 0.2006, \lambda = 1, \Lambda = 3, \hat{D}_1 = \hat{D}_2 = 4.46 \times 10^{-4}, b = 0.2$.*

When $\lambda \neq 1$

We fix $\lambda \in [0.9, 1.2]$ and choose Λ value based on the restriction that $\epsilon_v < 0.01$. The parameter values in Table 6.6 are used to plot Figure 6.11. We fix $b = 0.4$ for all four cases to better study the effect of varying the other parameters on the agreement between the outer solutions.

First, we observe that the solutions in Figures 6.11(a) and 6.11(b) are in excellent agreement. However, the outer solutions in Figures 6.11(c) and 6.11(c) agree less, especially in solution u. The common features of these two plots are larger wavelength and smaller $\hat{D}_1$ compared to the first two plots.

	$D_1 = D_2$	α	β	λ	Λ	$\hat{D}_1$	$\hat{D}_2$	b	Ratio
(a)	10^{-5}	0.9	0.164	1.2	2	0.0242	1.8587	0.4	0.182
(b)	10^{-5}	0.9	0.321	0.9	2	0.0242	0.0037	0.4	0.357
(c)	10^{-3}	0.9	0.376	1.2	3	4.46×10^{-3}	0.0307	0.4	0.418
(d)	10^{-4}	0.9	0.1348	2	3	4.46×10^{-4}	231.65	0.4	0.15

Table 6.6: *Parameter values for asymptotic solutions of u and v from solving (6.28) and (E.8) where $\phi_1 = \phi_2 = \phi = \Phi_\infty$ and $\lambda \neq 1$. The asymptotic solutions can be found in Figure 6.11.*

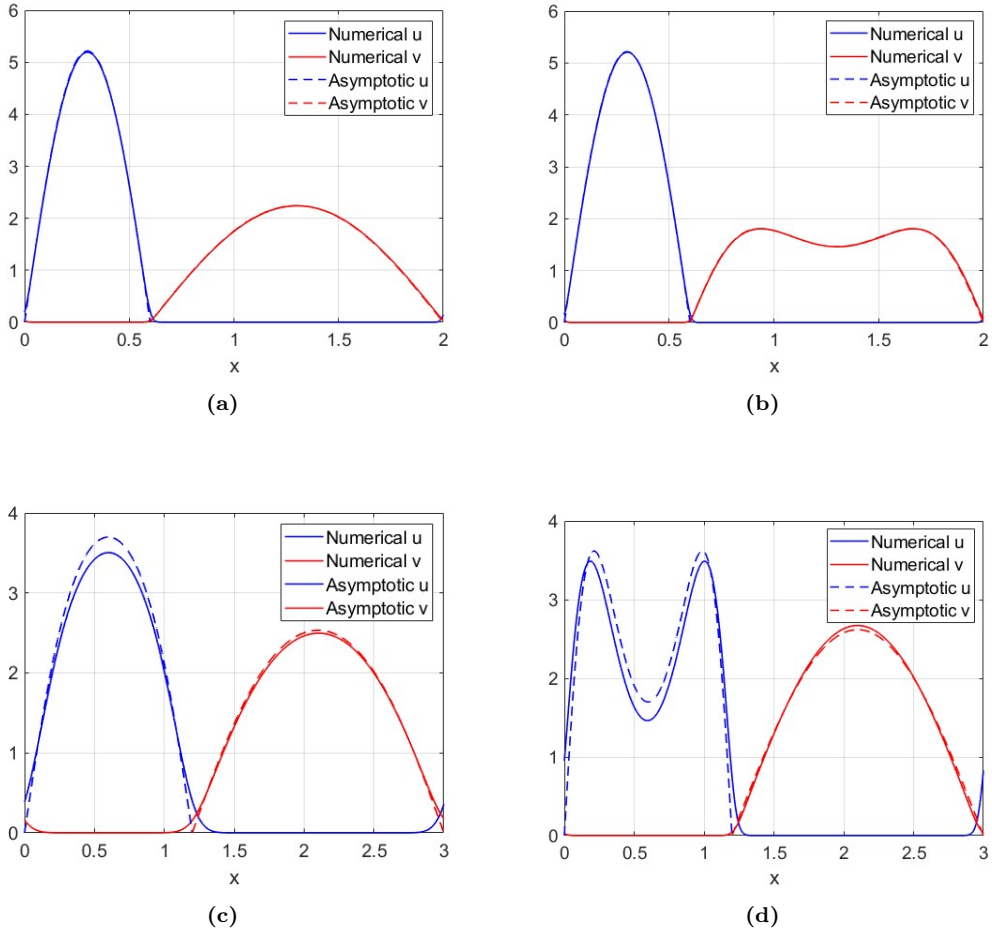


Figure 6.11: *Plots of asymptotic and numerical outer solutions u and v for $\phi_1 = \phi_2 = \phi = \Phi_\infty$ when $\lambda \neq 1$. The details of the parameter values can be found in Table 6.6. (a) $D_1 = D_2 = 10^{-5}, \alpha = 0.9, \beta = 0.164, \lambda = 1.2, \Lambda = 2, \hat{D}_1 = 0.0242, \hat{D}_2 = 1.8587, b = 0.4$, (b) $D_1 = D_2 = 10^{-5}, \alpha = 0.9, \beta = 0.321, \lambda = 0.9, \Lambda = 2, \hat{D}_1 = 0.0242, \hat{D}_2 = 3.7 \times 10^{-3}, b = 0.4$, (c) $D_1 = D_2 = 10^{-3}, \alpha = 0.9, \beta = 0.376, \lambda = 1.2, \Lambda = 3, \hat{D}_1 = 4.46 \times 10^{-3}, \hat{D}_2 = 0.0307, b = 0.4$, (d) $D_1 = D_2 = 10^{-4}, \alpha = 0.9, \beta = 0.1348, \lambda = 2, \Lambda = 3, \hat{D}_1 = 4.46 \times 10^{-4}, \hat{D}_2 = 231.65, b = 0.4$.*

To understand this, we look at the ϵ_u and ϵ_v values of these four plots in Table 6.7. We see that the values of ϵ_u are bigger in combinations (c) and (d) compared to combinations (a) and (b). Therefore, we conclude that the larger

	λ	Λ	ϵ_u	ϵ_v
(a)	1.2	2	1.03×10^{-4}	1.35×10^{-6}
(b)	0.9	2	1.03×10^{-4}	6.75×10^{-4}
(c)	1.2	3	0.0249	3.6×10^{-3}
(d)	2	3	0.0249	4.8×10^{-8}

Table 6.7: *λ, Λ, ϵ_u and ϵ_v for asymptotic solutions in Figure 6.11* where $\phi_1 = \phi_2 = \phi = \Phi_\infty$ and $\lambda \neq 1$.

value of ϵ_u, the larger values of D_1 and D_2, combined with the larger difference between ϵ_u and ϵ_v in (d) contributed to the discrepancies in the asymptotic and numerical outer solutions in Figures 6.11(c) and 6.11(d).

6.6.5 Asymptotic outer solution when $\Phi = \Phi_1$

When $\lambda = 1$

Next, we move on to study solutions when both of the kernels ϕ_1 and ϕ_2 are in the exponential form, i.e. $\mathrm{e}^{-|x|}/2$. We first substitute the convolution term obtained from subsection 6.4.3 into (6.4) and expand u asymptotically to obtain

$$0 = D_1 \frac{\mathrm{d}^2(u_0 + \epsilon_1 u_1)}{\mathrm{d}x^2} + (u_0 + \epsilon_1 u_1)\left(1 - \int_0^\Lambda \left[\frac{1}{\Lambda} + \frac{2\pi^2\epsilon_1}{\Lambda}\left(\frac{(x-y)^2}{\Lambda^2} - \frac{|x-y|}{\Lambda} + \frac{1}{6}\right)\right](u_0(y) + \epsilon_1 u_1(y))\,\mathrm{d}y\right). \tag{6.40}$$

Then, we rescale $x = \Lambda\hat{x}$, $y = \Lambda\hat{y}$, $u_0(x) = u_0(\hat{x})$ and $u_1(x) = u_1(\hat{x})$ and rewrite (6.40) as

$$0 = \frac{D_1}{\Lambda^2}\frac{\mathrm{d}^2 u_0}{\mathrm{d}\hat{x}^2} + \frac{\epsilon_1 D_1}{\Lambda^2}\frac{\mathrm{d}^2 u_1}{\mathrm{d}\hat{x}^2} + (u_0 + \epsilon_1 u_1)\left(1 - \int_0^1 \left[1 + 2\pi^2\epsilon_1\left((\hat{x}-\hat{y})^2 - |\hat{x}-\hat{y}| + \frac{1}{6}\right)\right](u_0(\hat{y}) + \epsilon_1 u_1(\hat{y}))\,\mathrm{d}\hat{y}\right). \tag{6.41}$$

By letting $D_1/\Lambda^2 = \epsilon_1\hat{D}_1 = O(\epsilon_1)$, we obtain

$$\hat{D}_1 = \frac{4\pi^2 D_1}{\Lambda^4}. \tag{6.42}$$

At $O(\epsilon_1)$, (6.41) returns

$$0 = \frac{\hat{D}_1}{b^2}\frac{\mathrm{d}^2\overline{u}_0}{\mathrm{d}\overline{x}^2} + \overline{u}_0\left(-b\int_0^1 2\pi^2\left((b\overline{x}-b\overline{y})^2 - |b\overline{x}-b\overline{y}| + \frac{1}{6}\right)\overline{u}_0(\overline{y})\,\mathrm{d}\overline{y} - b\int_0^1 \overline{u}_1(\overline{y})\,\mathrm{d}\overline{y}\right), \tag{6.43}$$

where we have rescaled $\hat{x} = b\overline{x}$, $\hat{y} = b\overline{y}$, $u_0(\hat{x}) = \overline{u}_0(\overline{x})$ and $u_1(\hat{x}) = \overline{u}_1(\overline{x})$. The next step would be to expand the term $(b\overline{x} - b\overline{y})^2$ and split up the integral involving the term $|b\overline{x} - b\overline{y}|$ into two integrals with the limits from 0 to $\overline{x}$ and from $\overline{x}$ to 1. After some algebraic calculation, we arrive at the asymptotic equation of u in the form (see Appendix E.4 for more details)

$$\begin{aligned} 0 = \frac{\hat{D}_1}{b^2}\frac{\mathrm{d}^2\overline{u}_0}{\mathrm{d}\overline{x}^2} + \overline{u}_0\Big[a + (4\pi^2 b^3\overline{x} + 2b^2\pi^2)q - 2\pi^2 b^3 p - 4b^2\pi^2\overline{x}r \\ - 4b^2\pi^2 s - 2\pi^2 b^2\overline{x}^2 + 2b\pi^2\overline{x} - \frac{\overline{x}}{3}\Big], \end{aligned} \tag{6.44}$$

where

$$a = -b\int_0^1 \overline{u}_1(\overline{y})\,\mathrm{d}\overline{y}, \quad q = \int_0^1 \overline{u}_0(\overline{y})\overline{y}\,\mathrm{d}\overline{y}, \quad p = \int_0^1 \overline{u}_0(\overline{y})\overline{y}^2\,\mathrm{d}\overline{y}, \tag{6.45}$$

$$r = \int_{\overline{x}}^1 \overline{u}_0(\overline{y})\,\mathrm{d}\overline{y}, \quad s = \int_0^{\overline{x}} \overline{u}_0(\overline{y})\overline{y}\,\mathrm{d}\overline{y}, \tag{6.46}$$

with the boundary conditions of $\overline{u}_0(0) = 0$ and $\overline{u}_0(1) = 0$.

Similar equation is also obtained for $\overline{v}_0$ when $\lambda = 1$, by replacing b with $(1-b)$ and redefining $D_2/\Lambda^2 = \epsilon_1\hat{D}_2 = O(\epsilon_1)$, where $\hat{D}_2 = O(1)$ and (see Appendix E.5)

$$\hat{D}_2 = \frac{4\pi^2 D_2}{\Lambda^4}. \tag{6.47}$$

When $\lambda \neq 1$

To derive the asymptotic equation for v when $\lambda \neq 1$, we substitute the periodic convolution term (6.15) into the equation of v in disjoint region (see 6.11) and

rescale $\tilde{x} = \Lambda\hat{x}/\lambda$, $\tilde{y} = \Lambda\hat{y}/\lambda$, $v(\tilde{x}) = v(\hat{x})$ and $\overline{v}(\tilde{y}) = \overline{v}(\hat{y})$ to obtain

$$0 = \frac{D_2}{\Lambda^2}\frac{\mathrm{d}^2 v}{\mathrm{d}\hat{x}^2} + Rv\left(1 - \int_0^1 \left[1 + 2\pi^2\epsilon_{1,\lambda}\left((\hat{x}-\hat{y})^2 - |\hat{x}-\hat{y}| + \frac{1}{6}\right)\right]\overline{v}(\hat{y})\,\mathrm{d}\hat{y}\right). \tag{6.48}$$

Then, we expand v and $\overline{v}$ asymptotically by writing $v = \overline{v} = v_0(\hat{y}) + \epsilon_{1,\lambda}v_1(\hat{y}) + \cdots$, and choose $D_2/\Lambda^2 = \epsilon_{1,\lambda}\hat{D}_2 = O(\epsilon_{1,\lambda})$ which gives

$$\hat{D}_2 = \frac{4D_2\pi^2\lambda^2}{\Lambda^4}. \tag{6.49}$$

Finally, we balance the terms at powers of $\epsilon_{1,\lambda}$ and rescale $\hat{x} = (1-b)\overline{x}$, $\hat{y} = (1-b)\overline{y}$, $v_0(\hat{x}) = \overline{v}_0(\overline{x})$ and $v_1(\hat{x}) = \overline{v}_1(\overline{x})$, to obtain the same asymptotic equation as the one for $\overline{v}_0$ when $\lambda = 1$, but with $\hat{D}_2$ defined in (6.49) instead of (6.47) (See Appendix E.6).

6.6.6 Computation of asymptotic outer solution when $\Phi = \Phi_1$

Using a similar method as before, the asymptotic equation for u in (6.44) can be written as a fifth-order system

$$\begin{aligned}
\overline{u}_0'(\overline{x}) &= \overline{w}(\overline{x}),\\
\overline{w}'(\overline{x}) &= -\frac{b^2\overline{u}_0(\overline{x})}{\hat{D}_1}\Big[a + (4\pi^2b^3\overline{x} + 2b^2\pi^2)q - 2\pi^2b^3p - 4b^2\pi^2\overline{x}\overline{I}_1\\
&\qquad - 4b^2\pi^2\overline{I}_2 - 2\pi^2b^2\overline{x}^2 + 2b\pi^2\overline{x} - \frac{\overline{x}}{3}\Big],\\
\overline{I}_1'(\overline{x}) &= -\overline{u}_0(\overline{x}),\\
\overline{I}_2'(\overline{x}) &= \overline{x}\overline{u}_0(\overline{x}),\\
\overline{I}_3'(\overline{x}) &= \overline{x}^2\overline{u}_0(\overline{x}),
\end{aligned} \tag{6.50}$$

where $\overline{I}_(\overline{x}) = \int_{\overline{x}}^1 \overline{u}_0(\overline{y})\,\mathrm{d}\overline{y} = -\int_1^{\overline{x}} \overline{u}_0(\overline{y})\,\mathrm{d}\overline{y}$, $\overline{I}_2(\overline{x}) = \int_0^{\overline{x}} \overline{u}_0(\overline{y})\overline{y}\,\mathrm{d}\overline{y}$, and $\overline{I}_3(\overline{x}) = \int_0^{\overline{x}} \overline{u}_0(\overline{y})\overline{y}^2\,\mathrm{d}\overline{y}$. The eight boundary conditions can be deduced from subsection

6.6.5 to be $\overline{u}_0(1) = 0$, $\overline{u}_0(0) = 0$, $\overline{I}_1(1) = 0$, $\overline{I}_1(0) = 1/b$, $\overline{I}_2(1) = q$, $\overline{I}_2(0) = 0$, $\overline{I}_3(1) = p$, and $\overline{I}_3(0) = 0$. The initial guesses for $b = 0.5$ are

$$\begin{aligned}
\overline{u}_0(\overline{x}) &= \pi \sin(\pi\overline{x}),\\
\overline{w}(\overline{x}) &= \pi^2 \cos(\pi\overline{x}),\\
\overline{I}_1(\overline{x}) &= 1 + \cos(\pi\overline{x}),\\
\overline{I}_2(\overline{x}) &= \frac{\sin(\pi\overline{x}) - \pi\overline{x}\cos(\pi\overline{x})}{\pi},\\
\overline{I}_3(\overline{x}) &= \frac{2\pi\overline{x}\sin(\pi\overline{x}) + (2 - \pi^2\overline{x}^2)\cos(\pi\overline{x}) - 2}{\pi^2}.
\end{aligned} \tag{6.51}$$

A similar system (E.21) is also obtained for $\overline{v}_0$ with similar boundary conditions and identical initial guesses, with $\hat{D}_2 = 4\pi^2 D_2/\Lambda^4$ (see Appendix E.6.1).

6.6.7 Comparison with numerical solution when $\Phi = \Phi_1$

When $\lambda = 1$, the asymptotic outer solutions u and v are computed using asymptotic equations (6.44) and (E.13). On the other hand, when $\lambda \neq 1$ in v, the asymptotic equation (E.19) is used to compute solution v instead.

When $\lambda = 1$

In general, we observe from Figure 6.12 that the outer solutions agree pretty well as long as D_1 and D_2 are sufficiently small, and $\epsilon_u = \epsilon_v < 0.1$. In other words, we require that wavelength to be $0 < \Lambda < 1.99$ for $\epsilon_u = \epsilon_v = \Lambda^2/(4\pi^2)$.

	$D_1 = D_2$	α	β	λ	Λ	$\hat{D}_1 = \hat{D}_2$	b	Ratio
(a)	10^{-5}	0.9	0.546	1	0.5	6.32×10^{-3}	0.4	0.607
(b)	10^{-5}	0.9	0.604	1	0.8	9.6×10^{-4}	0.4	0.671
(c)	10^{-6}	0.9	0.525	1	0.9	6×10^{-5}	0.4	0.583
(b)	10^{-5}	0.9	0.546	1	1.2	1.9×10^{-4}	0.4	0.606

Table 6.8: *Parameter values for asymptotic solutions of u and v from solving (6.44) and (E.13) where $\phi_1 = \phi_2 = \phi = \Phi_1$ and $\lambda = 1$. The asymptotic solutions can be found in Figure 6.12.*

Combinations (a), (b) and (d) have the same D_1 and D_2 values, with increasing wavelength, Λ. The ϵ_u (or ϵ_v) of these combinations increases from 0.006, 0.016

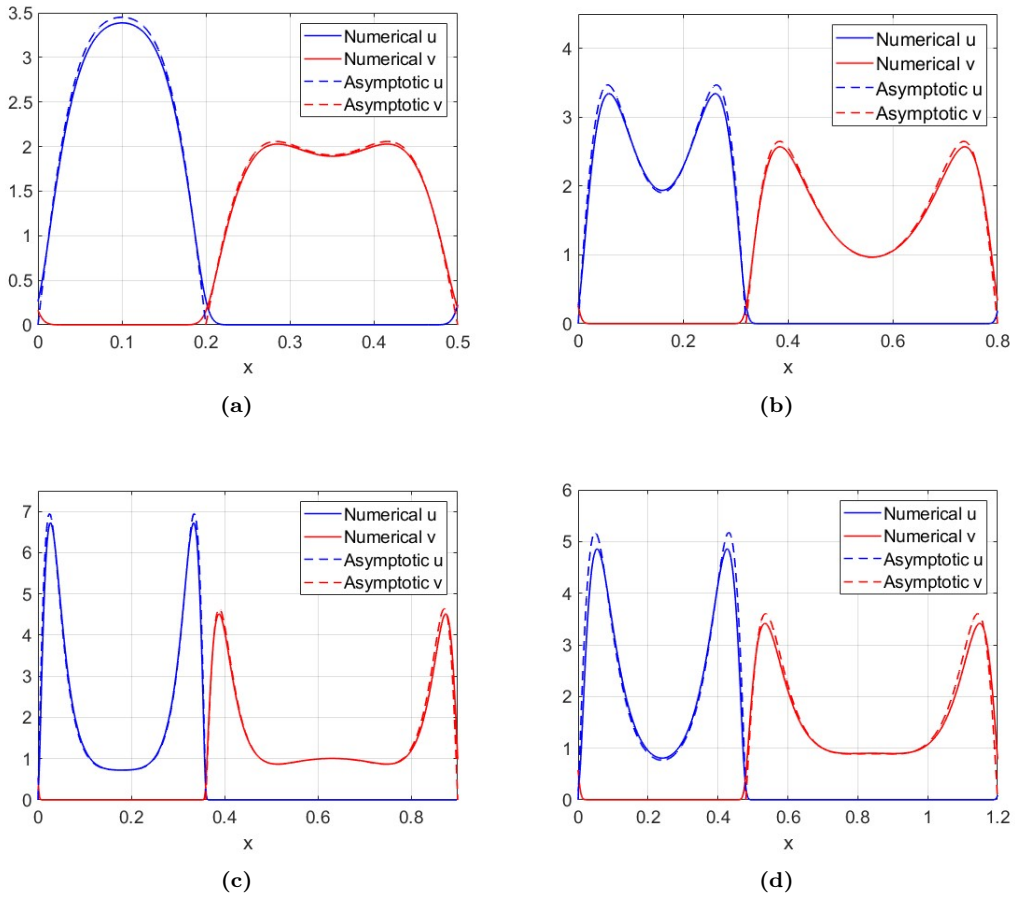


Figure 6.12: *Plots of asymptotic and numerical outer solutions u and v for $\phi_1 = \phi_2 = \phi = \Phi_1$ when $\lambda = 1$. The details of the parameter values can be found in Table 6.8. (a) $D_1 = D_2 = 10^{-5}, \alpha = 0.9, \beta = 0.546, \lambda = 1, \Lambda = 0.5, \hat{D}_1 = \hat{D}_2 = 6.32 \times 10^{-3}, b = 0.4$, (b) $D_1 = D_2 = 10^{-5}, \alpha = 0.9, \beta = 0.604, \lambda = 1, \Lambda = 0.8, \hat{D}_1 = \hat{D}_2 = 9.6 \times 10^{-4}, b = 0.4$, (c) $D_1 = D_2 = 10^{-6}, \alpha = 0.9, \beta = 0.525, \lambda = 1, \Lambda = 0.9, \hat{D}_1 = \hat{D}_2 = 6 \times 10^{-5}, b = 0.4$, (d) $D_1 = D_2 = 10^{-5}, \alpha = 0.9, \beta = 0.546, \lambda = 1, \Lambda = 1.2, \hat{D}_1 = \hat{D}_2 = 1.9 \times 10^{-4}, b = 0.4$.*

to 0.036, resulting in the increasing difference between the peaks of the outer solutions.

When $\lambda \neq 1$

In this subsection, we use the same D_1, D_2, α and Λ values as the case when $\lambda = 1$ in Table 6.8. We let $\lambda \in [0.8, 1.2]$ and $b = 0.3$. The values of β are calculated based on the ratio obtained in (6.39).

Since $b < 0.4$, we expect the outer solutions in Figure 6.13 to have smaller agreement compared to those in Figure 6.12. However, the asymptotic solutions are able to capture the shape of the outer solutions in general.

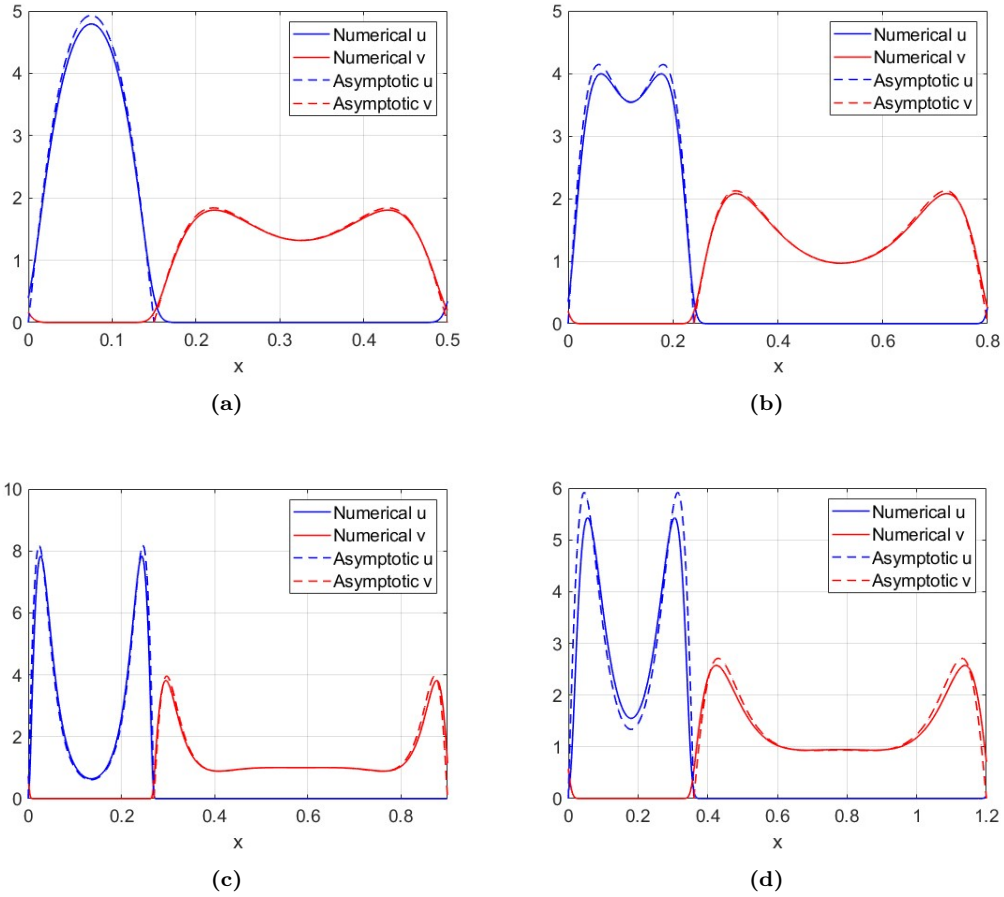


Figure 6.13: *Plots of asymptotic and numerical outer solutions u and v for $\phi_1 = \phi_2 = \phi = \Phi_1$ when $\lambda \neq 1$. The details of the parameter values can be found in Table 6.9. (a) $D_1 = D_2 = 10^{-5}, \alpha = 0.9, \beta = 0.351, \lambda = 0.8, \Lambda = 0.5, \hat{D}_1 = 6.3 \times 10^{-3}, \hat{D}_2 = 4 \times 10^{-3}, b = 0.3$, (b) $D_1 = D_2 = 10^{-5}, \alpha = 0.9, \beta = 0.329, \lambda = 1.2, \Lambda = 0.8, \hat{D}_1 = 1.9 \times 10^{-4}, \hat{D}_2 = 1.22 \times 10^{-4}, b = 0.3$, (c) $D_1 = D_2 = 10^{-6}, \alpha = 0.9, \beta = 0.38, \lambda = 0.8, \Lambda = 0.9, \hat{D}_1 = 6 \times 10^{-5}, \hat{D}_2 = 3.85 \times 10^{-5}, b = 0.3$, (d) $D_1 = D_2 = 10^{-5}, \alpha = 0.9, \beta = 0.274, \lambda = 1.2, \Lambda = 1.2, \hat{D}_1 = 1.9 \times 10^{-4}, \hat{D}_2 = 2.74 \times 10^{-4}, b = 0.3$.*

	$D_1 = D_2$	α	β	λ	Λ	$\hat{D}_1$	$\hat{D}_2$	b	Ratio
(a)	10^{-5}	0.9	0.351	0.8	0.5	6.3×10^{-3}	4×10^{-3}	0.3	0.39
(b)	10^{-5}	0.9	0.329	1.2	0.8	1.9×10^{-4}	1.22×10^{-4}	0.3	0.366
(c)	10^{-6}	0.9	0.38	0.8	0.9	6×10^{-5}	3.85×10^{-5}	0.3	0.423
(b)	10^{-5}	0.9	0.274	1.2	1.2	1.9×10^{-4}	2.74×10^{-4}	0.3	0.305

Table 6.9: *Parameter values for asymptotic solutions of u and v from solving (6.44) and (E.19) where $\phi_1 = \phi_2 = \phi = \Phi_1$ and $\lambda \neq 1$. The asymptotic solutions can be found in Figure 6.13.*

6.6.8 Comparison with numerical solution when $\phi_1 = \Phi_1$ and $\phi_2 = \Phi_\infty$

We now examine the outer solutions in the limit of small diffusivity when ϕ_1 is an exponential kernel and ϕ_2 is a Gaussian kernel. We use the asymptotic equation (6.44) derived in subsection 6.6.5 for u, and the nonlinear Mathieu equation (6.31) derived in subsection 6.6.1 for v when $\lambda = 1$. When $\lambda \neq 1$, we use the nonlinear Mathieu equation (E.8) in Appendix E.3 instead.

Similar methods from the previous sections are employed to compute the asymptotic outer solutions. So far, we have been letting α and β be less than one when comparing outer solutions with identical kernel pairs. However, the values of ϵ_u for exponential kernel and ϵ_v for Gaussian kernel vary significantly due to their different nature. Therefore, we require much larger α and β values for better agreement between outer solutions, as seen in subsection 6.6.4. Note that $\alpha, \beta > 1$ remains valid in our study of the fully nonlinear problem.

When $\lambda = 1$

For the parameter values in Table 6.10, $\epsilon_u = \Lambda^2/(4\pi^2) = 0.0253$ for u and $\epsilon_v = 2\mathrm{e}^{-\frac{4\pi^2\lambda^2}{\Lambda^2}} = 1.43 \times 10^{-17}$ for v. The significantly smaller value of ϵ_v leads to a much better solution agreement in v in Figure 6.14. For each combination, we choose α and β large enough while maintaining the same ratio of β over α to generate outer solutions with a better agreement with each other.

	D_1	D_2	α	β	λ	Λ	$\hat{D}_1$	$\hat{D}_2$	b	Ratio
(a)	10^{-4}	10^{-4}	6	0.9	1	1	3.95×10^{-3}	6.99×10^{12}	0.3	0.15
(b)	10^{-5}	10^{-5}	16.1	0.9	1	1	3.95×10^{-4}	6.99×10^{11}	0.3	0.056
(c)	10^{-5}	10^{-4}	3.58	2	1	1	3.95×10^{-4}	6.99×10^{12}	0.3	0.559
(d)	10^{-6}	10^{-5}	6.576	0.9	1	1	3.95×10^{-5}	6.99×10^{11}	0.3	0.137

Table 6.10: *Parameter values for asymptotic solutions of u and v from (6.44) and (6.31) where $\phi_1 = \Phi_1$, and $\phi_2 = \Phi_\infty$ and $\lambda = 1$. The asymptotic solutions can be found in Figure 6.14.*

Another observation is that as $D_1 = D_2$ decreases from 10^{-4} in Figure 6.14(a)

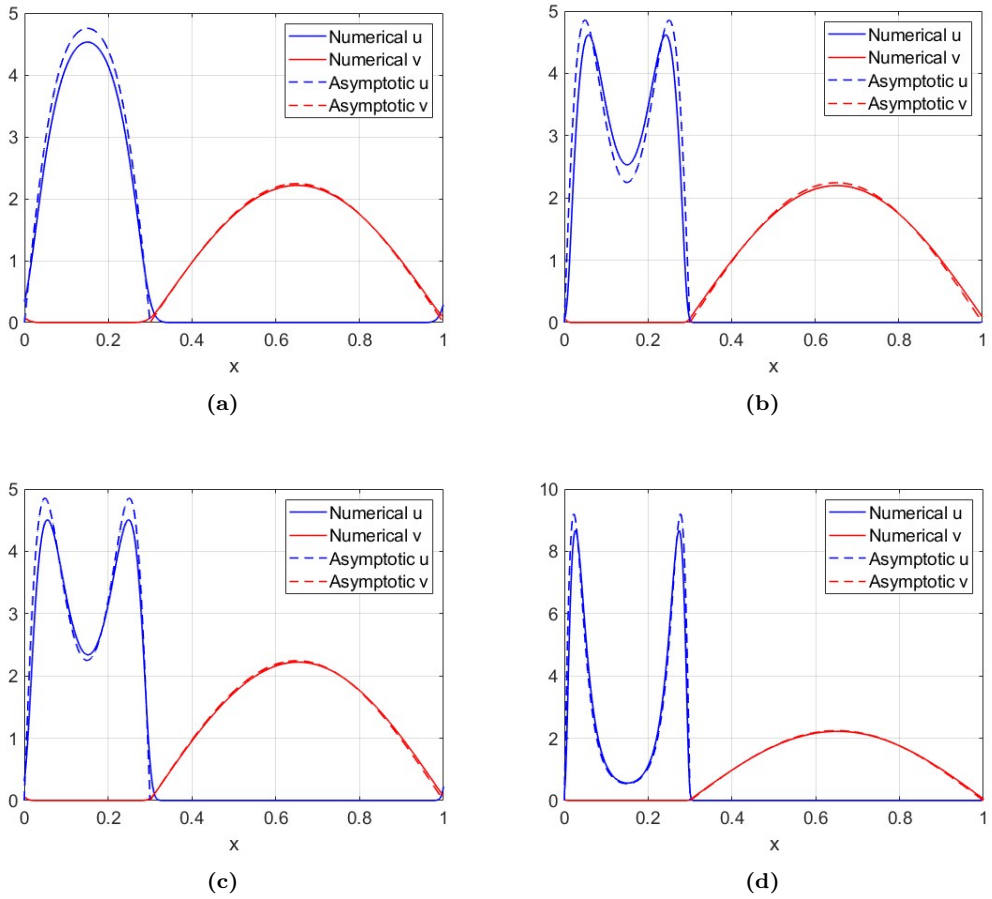


Figure 6.14: *Plots of asymptotic and numerical outer solutions u and v for $\phi_1 = \Phi_1$, and $\phi_2 = \Phi_\infty$ when $\lambda = 1$. The details of the parameter values can be found in Table 6.10. (a) $D_1 = D_2 = 10^{-4}, \alpha = 6, \beta = 0.9, \lambda = 1, \Lambda = 1, \hat{D}_1 = 3.95 \times 10^{-3}, \hat{D}_2 = 6.99 \times 10^{12}, b = 0.3$, (b) $D_1 = D_2 = 10^{-5}, \alpha = 16.1, \beta = 0.9, \lambda = 1, \Lambda = 1, \hat{D}_1 = 3.95 \times 10^{-4}, \hat{D}_2 = 6.99 \times 10^{11}, b = 0.3$, (c) $D_1 = 10^{-5}, D_2 = 10^{-4}, \alpha = 3.58, \beta = 2, \lambda = 1, \Lambda = 1, \hat{D}_1 = 3.95 \times 10^{-4}, \hat{D}_2 = 6.99 \times 10^{12}, b = 0.3$, (d) $D_1 = 10^{-6}, D_2 = 10^{-5}, \alpha = 6.576, \beta = 0.9, \lambda = 1, \Lambda = 1, \hat{D}_1 = 3.95 \times 10^{-5}, \hat{D}_2 = 6.99 \times 10^{11}, b = 0.3$.*

to 10^{-5} in Figure 6.14(b), the number of peaks in u increases, as we have seen in Section 6.2 that solutions with exponential kernel generate more distinct peaks than that of Gaussian kernel. Finally, in Figures 6.14(c) and 6.14(d), although D_1 is ten times smaller than D_2, the asymptotic solutions are still able to capture the structure of the outer solutions, despite some discrepancies in u.

When $\lambda \neq 1$:

The parameter values D_1, D_2, β and b in Table 6.11 are the same as the ones in Table 6.10. We now fix $\lambda = \Lambda$ to be 0.8 or 0.9. Since $\lambda = \Lambda$, the value of ϵ_v

remains the same as before, i.e. 1.43×10^{-17}. On the other hand, the ϵ_u for $\lambda = \Lambda = 0.9$ and 0.8 becomes 0.0205 and 0.0162.

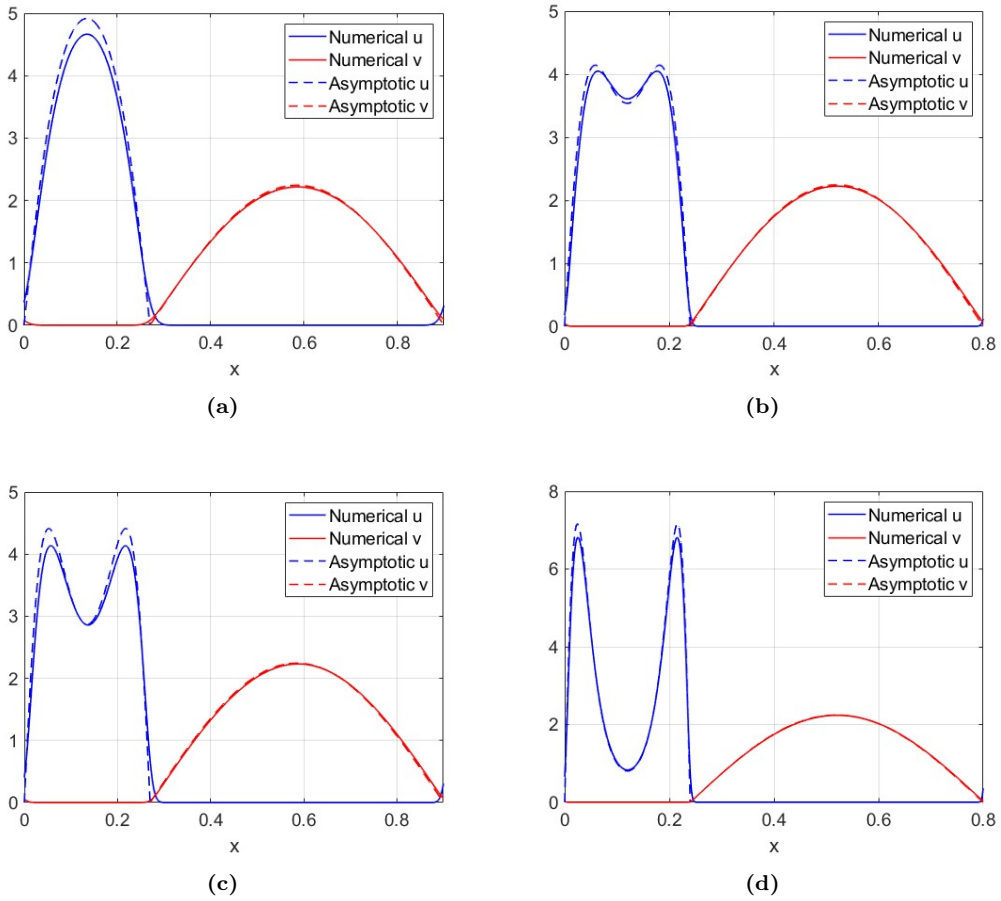


Figure 6.15: *Plots of asymptotic and numerical outer solutions u and v for $\phi_1 = \Phi_1$ and $\phi_2 = \Phi_\infty$ when $\lambda \neq 1$. The details of the parameter values can be found in Table 6.11. (a) $D_1 = D_2 = 10^{-4}, \alpha = 5.62, \beta = 0.9, \lambda = 0.9, \Lambda = 0.9, \hat{D}_1 = 6 \times 10^{-3}, \hat{D}_2 = 8.62 \times 10^{12}, b = 0.3$, (b) $D_1 = D_2 = 10^{-5}, \alpha = 9.7, \beta = 0.9, \lambda = 0.8, \Lambda = 0.8, \hat{D}_1 = 9.64 \times 10^{-4}, \hat{D}_2 = 1.1 \times 10^{12}, b = 0.3$, (c) $D_1 = 10^{-5}, D_2 = 10^{-4}, \alpha = 2.79, \beta = 2, \lambda = 0.9, \Lambda = 0.9, \hat{D}_1 = 6 \times 10^{-4}, \hat{D}_2 = 8.6 \times 10^{12}, b = 0.3$, (d) $D_1 = 10^{-6}, D_2 = 10^{-5}, \alpha = 3.81, \beta = 0.9, \lambda = 0.8, \Lambda = 0.8, \hat{D}_1 = 9.64 \times 10^{-5}, \hat{D}_2 = 1.1 \times 10^{12}, b = 0.3$.*

	D_1	D_2	α	β	λ	Λ	$\hat{D}_1$	$\hat{D}_2$	b	Ratio
(a)	10^{-4}	10^{-4}	5.62	0.9	0.9	0.9	6×10^{-3}	8.62×10^{12}	0.3	0.16
(b)	10^{-5}	10^{-5}	9.7	0.9	0.8	0.8	9.64×10^{-4}	1.1×10^{12}	0.3	0.093
(c)	10^{-5}	10^{-4}	2.79	2	0.9	0.9	6×10^{-4}	8.6×10^{12}	0.3	0.718
(d)	10^{-6}	10^{-5}	3.81	0.9	0.8	0.8	9.64×10^{-5}	1.1×10^{12}	0.3	0.236

Table 6.11: *Parameter values for asymptotic solutions of u and v from (6.44) and (E.8) in Figure 6.15 where $\phi_1 = \Phi_1$ and $\phi_2 = \Phi_\infty$ and $\lambda \neq 1$. The asymptotic solutions can be found in Figure 6.15.*

In general, there is no significant difference in the agreement in outer solutions compared to the case when $\lambda = 1$. It is observed that the outer solutions for v agree very well. The asymptotic outer solutions for u can capture the behaviour of numerical solutions to a reasonable degree.

6.6.9 Comparison with solution of IVP

In this subsection, we compare the asymptotic outer solutions for all three kernel combinations from subsections 6.6.4, 6.6.7 and 6.6.8 with the solutions of the fully nonlinear system (6.1) at large t. We set the initial condition of the IVP by introducing a small perturbation to the coexisting state, i.e. $(u_0, v_0) = (u_e, v_e) + 0.1 \sin\left(\frac{2\pi x}{\Lambda}\right)$ in (6.2), where Λ is the wavelength obtained from the asymptotic outer solutions. Then, we simulate the solutions of IVP with the same parameter values from $t = 0$ to $t = \min(D_1^{-1}, D_2^{-1})$. The solutions at $t = \min(D_1^{-1}, D_2^{-1})$ will then be compared against the outer solutions in terms of their amplitude and wavelength. For this subsection, we define amplitude as the maximum value of solutions over one period.

When both kernels are Φ_∞

Figures 6.16(b) and 6.16(d) show that at $t = 100000$, the solutions of IVP settle down to periodic solutions that oscillate in the spatial domain. Another observation is that the shapes of these solutions are captured by the asymptotic solutions in Figures 6.16(a) and 6.16(c) with the same parameter values. The amplitude and wavelength of all these solutions are tabulated in Table 6.12.

λ		Asymptotic solutions	IVP solutions	Difference
1	Amplitude of u	3.885	3.877	0.008
	Amplitude of v	2.512	2.509	0.003
	Wavelength	2	2	0
0.9	Amplitude of u	5.217	5.207	0.01
	Amplitude of v	1.809	1.806	0.003
	Wavelength	2	2	0

Table 6.12: *Amplitude and wavelength of the asymptotic and numerical solutions in Figure 6.16.*

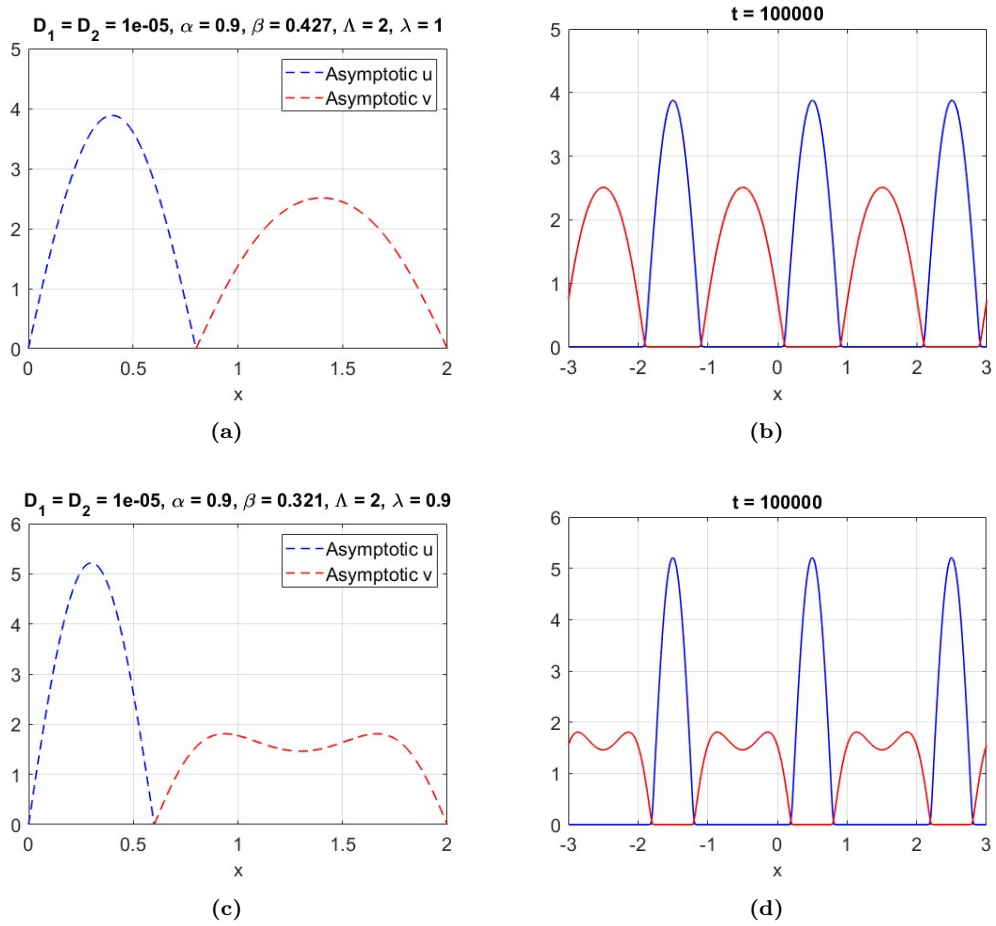


Figure 6.16: *Plots of asymptotic solutions from (6.28) and (6.31) in (a), asymptotic solutions from (6.28) and (E.8) in (c) and IVP solutions from (6.1) in (b) and (d) for* $\phi_1 = \phi_2 = \Phi_\infty$.

From Table 6.12, we see that the amplitudes of the asymptotic solutions are very close to the IVP solutions, with the largest error of 0.01 in the amplitude of u when $\lambda = 0.9$. Another observation is that all of the solutions have the same wavelength.

When both kernels are Φ_1

Again, we repeat the same procedures to compare the asymptotic solutions with IVP solutions for exponential kernel pairs. From Figure 6.17, we see that the asymptotic solutions from Figures 6.17(a) and 6.17(c) do exist in the large-time IVP solutions in Figures 6.17(b) and 6.17(d).

A closer look at the values of amplitudes reveals that the differences between asymptotic and numerical amplitudes are more significant than those of

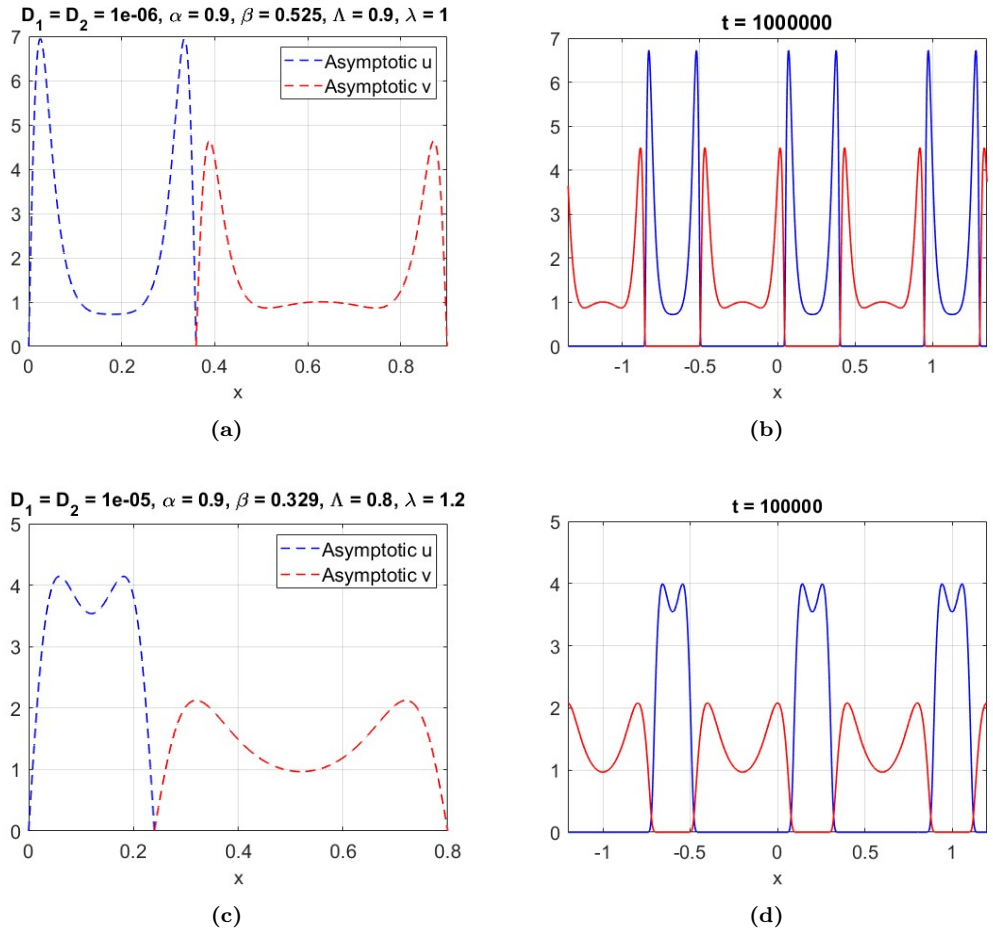


Figure 6.17: *Plots of asymptotic solutions from (6.44) and (E.13) in (a), asymptotic solutions from (6.44) and (E.19) in (c) and IVP solutions from (6.1) in (b) and (d) for* $\phi_1 = \phi_2 = \Phi_1$.

Gaussian kernel pairs, with the largest difference being 0.222. However, both the asymptotic and numerical wavelengths of the solutions are identical.

λ		Asymptotic solutions	IVP solutions	Difference
1	Amplitude of u	6.945	6.723	0.222
	Amplitude of v	4.639	4.513	0.126
	Wavelength	0.9	0.9	0
1.2	Amplitude of u	4.142	3.994	0.148
	Amplitude of v	2.125	2.08	0.045
	Wavelength	0.8	0.8	0

Table 6.13: *Amplitude and wavelength of the asymptotic and numerical solutions in Figure 6.17.*

When $\phi_1 = \Phi_1$ **and** $\phi_2 = \Phi_\infty$

Like the other two kernel pairs, the IVP solutions converge to the asymptotic solutions in Figure 6.18.

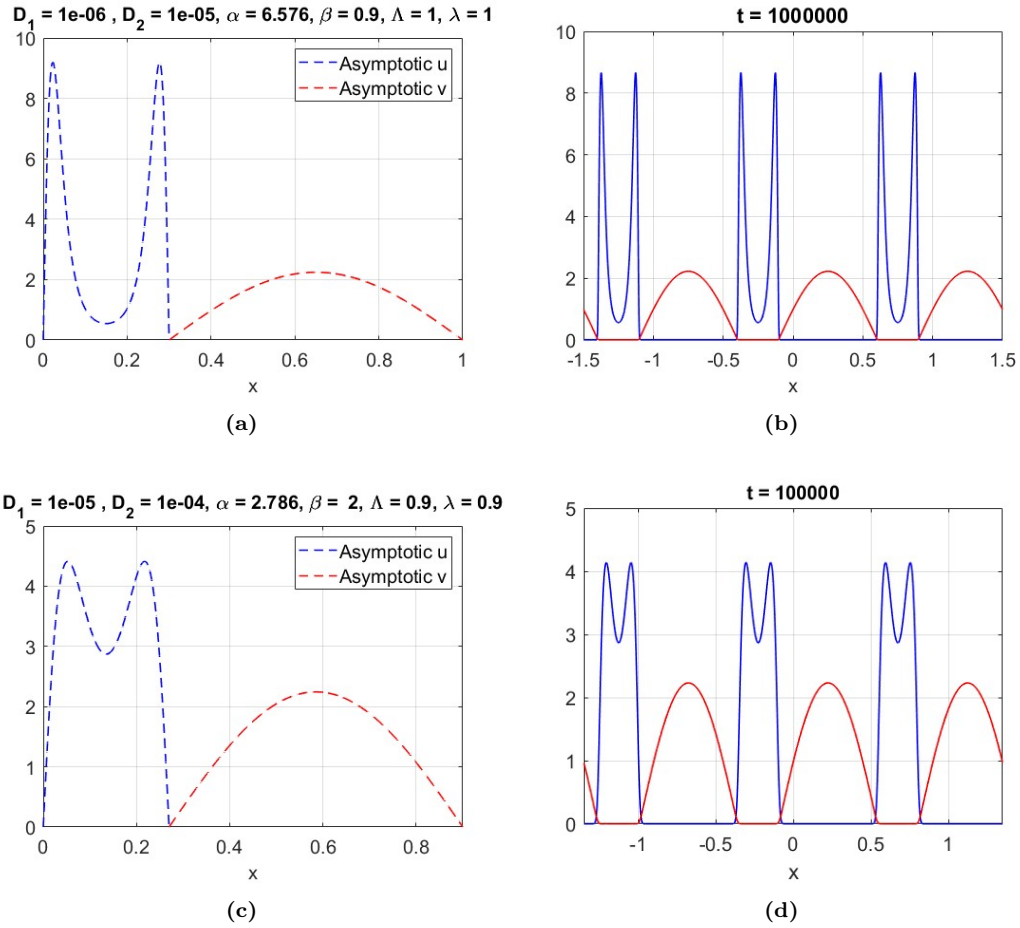


Figure 6.18: *Plots of asymptotic solutions from (6.44) and (6.31) in (a), asymptotic solutions from (6.44) and (E.8) in (c) and IVP solutions from (6.1) in (b) and (d) for* $\phi_1 = \Phi_1$ *and* $\phi_2 = \Phi_\infty$.

λ		Asymptotic solutions	IVP solutions	Difference
1	Amplitude of u	9.197	8.67	0.528
	Amplitude of v	2.244	2.222	0.022
	Wavelength	1	1	0
0.9	Amplitude of u	4.412	4.137	0.275
	Amplitude of v	2.244	2.231	0.013
	Wavelength	0.9	0.9	0

Table 6.14: *Amplitude and wavelength of the asymptotic and numerical solutions in Figure 6.18.*

Table 6.14 shows that the difference in the amplitudes of u is approximately 20 times larger than that of v. This is due to the exponential kernel ϕ_1 in u. However, the wavelengths in asymptotic and numerical solutions are in excellent agreement.

6.7 Conclusion

In this chapter, we have studied pattern formation for the fully nonlinear problem (6.1) as D_1 and/or $D_2 \to 0$ for Φ_1 and Φ_∞ kernel combinations. We have shown some animations in which the solutions of IVP with random initial conditions converge to oscillatory solutions with fixed amplitudes and wavelengths at their steady states. The behaviour of those solutions in relation to parameter change is predicted by the analysis from Section 5.5.

The main contribution of this chapter stems from the asymptotic analysis of the mathematical structure of the fully nonlinear solutions at steady states. In particular, we have analytically approximated the effective periodic kernels using truncated Fourier Series based on the assumption that the solutions are periodic on a finite domain. The estimated effective periodic kernels have greatly simplified the steady state problem 6.4 in the outer regions. We have also defined the ratio of the slope of solutions at their intersection point by matching the inner region with the outer region. The slope ratio, combined with the asymptotic effective periodic kernels, has allowed us to analytically construct the asymptotic solutions for outer solutions, which can then be solved numerically.

In general, a good agreement is found between the asymptotic and numerical outer solutions for small diffusivity, large α and large β at the leading order as $\epsilon_u, \epsilon_v \to 0$. Although the epsilon terms are functions of wavelength, Λ, we have found from numerical solutions that good agreement between solutions can be obtained even for $\Lambda = O(1)$.

In conclusion, we have found that the asymptotic solutions are able to capture the shape of the steady-state solutions as well as the IVP solutions despite some slight differences in the amplitudes of the solutions.

Chapter 7

Conclusion and Future Work

In this thesis, we have studied the asymptotic and numerical solutions of two different nonlocal reaction-diffusion models, motivated by the mathematical interest in the solution structure of nonlocal models. We focused on a local-nonlocal Fisher-KPP equation in Chapter 3 and a nonlocal Lotka-Volterra system in Chapters 4 to 6.

7.1 Local-Nonlocal Fisher-KPP equation

In Chapter 3, we studied the TW solution of

$$-cU_z = DU_{zz} + U\left(1 - \alpha U - (1-\alpha)\int_{-\infty}^{\infty} \phi(z-y)U(y)\,\mathrm{d}y\right), \tag{7.1}$$

with a primary focus on $\phi = \Phi_2$ and $\phi = \Phi_\infty$. We observed that the numerical solutions for $c \ll 1$ and $c = O(\alpha)$ show a finite number of spikes followed by decaying oscillations behind the wavefront. In particular, the TW solutions for $\phi = \Phi_\infty$ exhibit more spikes and oscillations behind the wavefront than that of $\phi = \Phi_2$. Moreover, the spikes in our numerical solutions resemble smoothed triangles instead of Gaussian functions in the nonlocal Fisher-KPP in [31] where $\alpha = 0$. In the limit of $c \to 0$ and $\alpha \to 0$, we expect similar behaviour in the

spikes formation as the work in [31], but with smoothed triangle spikes instead. More explicitly, we expect the appearance of infinitely many spikes within a finite region behind the wavefront for $\phi = \Phi_2$ and an infinite number of spikes that fill the domain behind the wavefront for $\phi = \Phi_\infty$.

In the far field of the solution when U oscillates towards one as $z \to -\infty$, we investigated five different kernels including $\phi = \Phi_1, \Phi_2, \Phi_3, \Phi_\infty$, and Φ_{alg}. By linearising the TW equation (7.1) around $U = 1$, we showed that the asymptotic solutions for those kernels are able to capture the frequency of the oscillations of TW solutions in the far field. Moreover, they predicted that the decay rate of oscillations for $\phi = \Phi_2$ is much higher than that of $\phi = \Phi_\infty$, which agrees with our observation in the numerical TW solutions.

In Section 3.5, we looked at the mathematical structure of the first spikes of solutions for $\phi = \Phi_2$ and $\phi = \Phi_\infty$. In the outer region with $O(1)$ scaling, the spikes behave like Dirac delta functions. In the inner region, we rescaled (7.1) such that the height of the spikes is of $O(\alpha^{-1/2})$ and the width of $O(\alpha^{1/2})$ as $\alpha \to 0$. We found that $c = O(\alpha)$ is the distinguished limit that shows how the spike changes from smoothed triangles to Gaussian functions by fixing c and decreasing α. We obtained analytical expressions of the asymptotic solutions with different scalings in both cases. We obtained the asymptotic solutions numerically and found that they agree with the numerical spikes to a good extent.

When $c \ll 1$ and $\alpha = O(1)$, we constructed an analytical expression for the asymptotic solution U for $\phi = \Phi_2$ and numerically solved for the asymptotic solution for $\phi = \Phi_\infty$ from a linear system. Both asymptotic solutions agree well with the numerical solutions, with higher maximum values at the wavefront due to the much smaller c. When $c \ll 1$, $\alpha \ll 1$ and $c \ll \alpha$, we solved a linear system to obtain an asymptotic solution for $\phi = \Phi_\infty$ with 21 regions of $U \ll 1$. It is able to predict the location and the width of the numerical spikes and the

distance between successive spikes.

7.2 Nonlocal Lotka-Volterra system

In Chapter 4, we studied the NLLV system

$$\begin{aligned} \frac{\partial u}{\partial t} &= D_1 \frac{\partial^2 u}{\partial x^2} + u\left(1 - \int_{-\infty}^{\infty} \phi_1(x-y)u(y)\,\mathrm{d}y - \alpha v\right), \\ \frac{\partial v}{\partial t} &= D_2 \frac{\partial^2 v}{\partial x^2} + Rv\left(1 - \frac{1}{\lambda}\int_{-\infty}^{\infty} \phi_2\left(\frac{x-y}{\lambda}\right) v(y)\,\mathrm{d}y - \beta u\right), \end{aligned} \tag{7.2}$$

where $D_1, D_2, R, \lambda, \alpha$ and β are nonnegative dimensionless parameters.

More specifically, this chapter covered the linear stability of the coexisting state of the NLLV system, both numerically and asymptotically. We found that by introducing nonlocal interactions into the intraspecific competitions in the typical local Lokta-Volterra system, the coexisting state loses its stability when $\alpha, \beta < 1$, depending on the values of parameters $D_1, D_2, R, \lambda, \alpha$ and β. To gain a deeper understanding of the stability of the coexisting state, we constructed asymptotic neutral curves in (α, β) parameter space to investigate the relation between the stability and the parameters for different kernels. For simplicity, we assumed that the ratio of growth rate, R, and the ratio of length scale, λ, are both one. Our analysis focused on three kernels, i.e. Φ_1, Φ_2, and Φ_∞, with increasing regularity around $x = 0$. The cases when u and v have the same kernel and different combinations of kernels were studied in detail. We found that in both cases, the asymptotic neutral curves reproduce the numerical neutral curves provided that $D \ll 1$. This is because $k \to \infty$ at leading order is only satisfied when D is sufficiently small based on the leading order equations we constructed above.

In addition, we found that the stability of the coexisting state in (α, β) parameter space, and subsequently the structure of the solutions, depend on two key factors. For the same kernel function, the smaller the value of D_1

and D_2, the larger the instability region. On the other hand, if we fix D_1 and D_2, we showed that the stability of the coexisting state depends crucially on the behaviour of the kernels in the neighbourhood around the origin at $x = 0$. The higher the smoothness of the kernel, the larger the instability region in (α, β) parameter space.

For each of the combinations of kernels, we investigated the numerical solutions of the IVPs with sufficiently localised initial conditions. In particular, we focused on the case when $\alpha = 0.6$ and $\beta = 0.5$ where the coexisting state is unstable. The common feature found in the numerical solutions is the existence of oscillations with similar oscillatory patterns in all the cases above. In addition, the wavelength of the oscillations correlates closely with the wavelength predicted from the linear stability analysis, $2\pi/k_{max}$. We found that the closer the σ is to the neutral curve, the closer the wavelength is to the predicted wavelength.

We also conducted a brief study on the case where σ is close to the neutral curve, which means that the growth rate of the coexisting state is small and positive in the system. By introducing a random initial condition to the coexisting state, the solutions converge to a spatially-oscillatory state when t is large enough. This behaviour is expected when we conduct the weakly nonlinear analysis in the next chapter.

Chapter 5 covered the weakly nonlinear analysis of the coexisting state of the redefined NLLV system

$$\begin{aligned} \frac{\partial u}{\partial t} &= D_1 \frac{\partial^2 u}{\partial x^2} + u\left(1 - \int_{-\infty}^{\infty} \phi_1(x-y)u(y)\,\mathrm{d}y - \alpha v\right), \\ \frac{\partial v}{\partial t} &= D_2 \frac{\partial^2 v}{\partial x^2} + Rv\left(1 - \int_{-\infty}^{\infty} \phi_2\left(x-y\right)v(y)\,\mathrm{d}y - \beta u\right), \end{aligned} \tag{7.3}$$

such that $\phi_2 = \phi_2(x;\lambda)$ and

$$\phi_2(x;\lambda) = \frac{1}{\lambda}\psi\left(\frac{x}{\lambda}\right), \tag{7.4}$$

for some function ψ. We carried out the analysis using the multiple-scale expansion method, showing no secondary bifurcation. In this chapter, u and v were assumed to have the same kernel, i.e. $\phi_1 = \psi = \Phi_1$, Φ_2 or Φ_∞.

In the weakly nonlinear analysis, we used λ as a bifurcation parameter λ to derive a cubic amplitude equation of the Ginzburg-Landau type. The standard approaches, including multiple-scale analysis, Taylor series expansion, and Fredholm alternative, were used to derive a set of solvability conditions, which is then applied to the system to arrive at the amplitude equation for the complex amplitude Z. We conducted a linear stability analysis of the steady states of the amplitude equation and found that for all the kernel pairs, the weakly nonlinear amplitudes of the coexisting state, (u_e, v_e), exhibit supercritical bifurcations when $\beta < 0.89$ and subcritical bifurcations when $\beta > 0.92$. However, no secondary bifurcations were observed.

We studied the numerical amplitudes of the oscillations generated by small perturbations to the coexisting state for all three kernel pairs. We found that the weakly nonlinear amplitudes from the weakly nonlinear solutions are in good agreement with the numerical amplitudes around the neighbourhood of the bifurcation point $\lambda_c = 1$. Apart from that, weakly nonlinear and numerical amplitudes change from supercritical bifurcation to subcritical bifurcation as β increases from 0.25 to 0.95 along the neutral curve in (α, β) parameter space.

Beyond the bifurcation point, the weakly nonlinear amplitudes no longer capture the numerical amplitudes when $\lambda > 1.1$ for $\beta = 0.5$. The numerical amplitudes converge to smaller values compared to the diverged weakly nonlinear amplitudes. For $\beta = 0.95$, the weakly nonlinear amplitudes agree well with the smaller numerical amplitudes from $\lambda = 1$ to 0.98 but could not

predict the behaviour of the increasing numerical amplitude of v. We focused on the $\phi_1 = \psi = \Phi_1$ case, but similar behaviour was also observed in both numerical amplitudes for $\phi_1 = \psi = \Phi_2$ and $\phi_1 = \psi = \Phi_\infty$ in Appendix C.

In the final section of this chapter, we studied the numerical solutions of the fully nonlinear problem for the $\phi_1 = \psi = \Phi_1$ case. We found that decreasing D_1 or increasing α while fixing the rest of the parameters results in similar changes in the solutions, where the amplitude of u increases—on the other hand, decreasing D_2 or increasing β leads to the same effect but in v instead. Besides, we noticed that the solution u increases in the number of peaks with increasing Λ. When λ increases, the amplitudes of u and v increase slightly. In general, we found the formation of sharp peaks in solutions when either D_1 or D_2 tends to zero. In particular, when both D_1 and D_2 are small, the fully nonlinear numerical solutions segregate into regions where either u or v are very close to zero. Similar observations can also be made to the solutions for $\phi_1 = \psi = \Phi_2$ and $\phi_1 = \psi = \Phi_\infty$ (see Appendix D). The only exception is that increasing λ has little effect on the amplitudes of the solutions. Moreover, the solutions have smoother peaks than that of $\phi_1 = \psi = \Phi_1$.

In Chapter 6, we generated some animations to illustrate the solutions of IVP (7.2) with random initial conditions in the limit of small diffusivity. We found that the solutions for $\phi_1 = \phi_2 = \phi = \Phi_1, \Phi_\infty$ and $\phi_1 = \Phi_1$ with $\phi_2 = \Phi_\infty$ converge to oscillatory patterns with fixed amplitudes and wavelengths. All solutions change with parameters as predicted in the analysis in Section 5.5. In general, we observed segregated regions where $u = O(1)$ or $v = O(1)$ in all the solutions. Besides, we also deduced that the solutions for both $\phi = \Phi_1$ kernels have the highest number of peaks within a fixed domain and that the solutions for the mixed kernel pair generate the sharpest peaks among all.

In addition to that, we asymptotically analysed the disjoint regions of solutions when diffusion coefficients are significantly small. We studied the cases where

both ϕ_1 and ϕ_2 are Φ_∞ and Φ_1, as well as the case when $\phi_1 = \Phi_1$ and $\phi_2 = \Phi_\infty$. In each of these cases, we looked into some examples when $\lambda = 1$ and also when $\lambda \neq 1$. To study the solutions u in the disjoint regions analytically, the effective periodic kernels were approximated by using the truncated Fourier series. Before constructing the asymptotic outer solutions, we first studied the inner regions to match the outer regions of the solutions. In particular, the ratio of slopes obtained from inner regions determines the ratio of β over α in the numerical solutions.

Later, we computed the outer solutions with the same slopes at the junction for Gaussian kernels (and similarly for v) and showed that they agree with the numerical outer solutions for large $\alpha = \beta$, or small $D_1 = D_2$. For the outer solutions with different slopes at the junction, we found that the asymptotic equation for v when $\lambda \neq 1$ is in the same form as when $\lambda = 1$, with $\hat{D}_2$ as a function of λ. In general, the asymptotic solutions for both Gaussian kernels agree well provided that the values of ϵ_u and ϵ_v, the difference between ϵ_u and ϵ_v, as well as the values of D_1 and D_2, are small. Coincidentally, the asymptotic solutions for Gaussian kernels are nonlinear Mathieu equations.

Furthermore, we derived the asymptotic equations for u and v when both kernels are $\phi_1 = \Phi_2 = \Phi_1$. In both $\lambda = 1$ and $\lambda \neq 1$ cases, we observed that the asymptotic outer solutions can capture the behaviour of the numerical outer solutions for $\epsilon_u = \epsilon_v < 0.1$.

The comparison of the asymptotic and numerical outer solutions when $\phi_1 = \Phi_1$ and $\phi_2 = \Phi_\infty$ demonstrates that the agreement between asymptotic and numerical outer solutions is preserved for large α and β. Apart from that, $\epsilon_v \ll \epsilon_u$ results in much better agreement in v than u.

Finally, in subsection 6.6.9, we compared the asymptotic outer solutions for all three kernel pairs with the solutions of IVP at large t. For initial conditions with fixed wavelength, all the IVP solutions converge to the same wavelength

as the steady asymptotic solutions. Besides, the structure of the IVP solutions converges to that of the outer solutions. However, some discrepancies are observed regarding the amplitudes of solutions, with more significant differences for exponential kernel and u.

7.3 Future work

Based on our findings, some possible extensions of our work for future research involve investigating how the smoothness of kernel functions affects the behaviour of our solutions. For instance, in the study of the TW solutions of the local-nonlocal Fisher-KPP equation (3.1) in Chapter 3, we illustrated that the solutions become more oscillatory as the kernel gets smoother. Later in Chapter 4, we showed that near the neutral curve, the instability region of the coexisting state of the NLLV system (7.2) increases with the smoothness of our kernels. In Chapter 6, we demonstrated that the fully nonlinear solutions of the NLLV IVP displayed a higher number of oscillations with larger amplitude with decreasing smoothness in the kernels. However, these are purely visual observations, and there is no obvious mathematical intuition to explain the underlying relationship. This thesis emphasises on the asymptotic analysis of the solutions and their pattern formations. Therefore, a possible next step would be to study the mathematical relationship between the number of oscillations and the smoothness of the kernels around $x = 0$. Some existing work proved that kernels with negative Fourier transform result in the nonmonotonic TW solutions of the nonlocal Fisher-KPP equation [8, 27]. However, since the Fourier transform of our kernels is positive, we require a different direction of investigation.

As mentioned in Section 5.6 before, there seems to be a hysteresis bifurcation in the numerical amplitudes in terms of λ when $\beta = 0.95$. Such a phenomenon could be investigated further in the future by studying the stability of the

patterning of the numerical solutions away from the bifurcation point $\lambda_c = 1$.

In Section 6.2, we observed in the animations of the IVP solution that the number of peaks reduces suddenly when the kernels, $\phi_1 = \Phi_1$ and $\phi_2 = \Phi_\infty$. For example, when $t \approx 6.33 \times 10^5$ in video 3d(i) and when $t \approx 4.96 \times 10^5$ in video 3e(i). Some asymptotic analysis could be carried out for solutions with those parameters set to understand such changes in mathematical structure in detail.

In general, we could investigate the solutions of local-nonlocal Fisher-KPP or the pattern formation of NLLV system for kernels with compact support, such as the top hat function. For instance, recent work by Needham and Billingham [109] studied the classical nonlocal Fisher-KPP equation with a top hat kernel and showed the existence of multipeak steady states for sufficiently small D. Another interesting kernel is the Mexican hat function which has negative values. Such kernel is usually found in the neural field modelling [110]. Other extensions include the analysis of fractional kernel functions Φ_n for non-integer n and the analysis of the solution in two spatial dimensions of either of our models. More specifically, weakly nonlinear analysis of two-dimensional models usually generates solutions with patterns such as stripes or rolls or hexagons [76, 80]. Furthermore, it would be interesting to extend our NLLV model to incorporate both nonlocal intraspecific and interspecific interactions (see [9, 22]) and conduct an asymptotic analysis on the neutral curve or the structure of the solutions. Finally, it would be great to collaborate with some laboratories to apply our model in real-life studies, such as the study of the invasion speed of grey squirrels in the habitats of red squirrels in Britain by Okubo et al. [43].

Appendix A

Neural Field Model

A.1 Bifurcation Point β_c at $D = 0$

Consider the dispersion relation

$$\sigma(k) = -Dk^2 - 1 + f'(u_0)\overline{w}(k).$$

When $D = 0$, bifurcation occurs at $\sigma(k_c) = 0$ i.e. $\overline{w}(k_c) = 1/f'(0)$. We can derive $\overline{w}(k)$ analytically. Recall that $w(x) = (1 - |x|)\mathrm{e}^{-|x|}$, which can be represented as

$$w(x) = \left(1 + \frac{\mathrm{d}}{\mathrm{d}a}\right) \mathrm{e}^{-a|x|}\Big|_{a=1}. \tag{A.1}$$

Hence,

$$\begin{aligned} \overline{w}(k) &= \int_{-\infty}^{\infty} w(\overline{y})\mathrm{e}^{-ik\overline{y}}\,\mathrm{d}\overline{y}, \\ &= \left(1 + \frac{\mathrm{d}}{\mathrm{d}a}\right) \int_{-\infty}^{\infty} \mathrm{e}^{-a|\overline{y}|}\Big|_{a=1} \mathrm{e}^{-ik\overline{y}}\,\mathrm{d}\overline{y}. \end{aligned} \tag{A.2}$$

The integral term in (A.2) can be simplified by

$$\begin{aligned} \int_{-\infty}^{\infty} \mathrm{e}^{-a|\overline{y}|}\Big|_{a=1} \mathrm{e}^{-ik\overline{y}}\,\mathrm{d}\overline{y} &= \left(\int_{-\infty}^{0} + \int_{0}^{\infty}\right) \mathrm{e}^{-a|\overline{y}|}\Big|_{a=1} \mathrm{e}^{-ik\overline{y}}\,\mathrm{d}\overline{y} \\ &= \int_{0}^{\infty} \mathrm{e}^{-a\overline{y}}\Big|_{a=1} \left(\mathrm{e}^{-ik\overline{y}} + \mathrm{e}^{ik\overline{y}}\right)\,\mathrm{d}\overline{y} \\ &= \left(\frac{1}{a - ih} + \frac{1}{a + ih}\right)\Big|_{a=1} \\ &= \frac{2a}{a^2 + k^2}\Big|_{a=1} \end{aligned} \tag{A.3}$$

Substituting this into (A.2), we obtain

$$\overline{w}(k) = \frac{2}{1+k^2} + \left[\frac{2(a^2+k^2)-4a^2}{(a^2+k^2)^2}\right]\Bigg|_{a=1} = \frac{4k^2}{(1+k^2)^2} \tag{A.4}$$

It is straightforward to obtain k_c from $\sigma'(k_c) = 0$. When $D = 0$ in $D(k_c^2+1)^3 + 4f'(0)(k_c^2-1) = 0$, $k_c = 1$. From $f(u) = 1/(1+\mathrm{e}^{-\beta u})$, we can easily work out $f'(u) = \beta f(u)(1-f(u))$ and therefore $f'(0) = \beta/4$. Finally, substituting all these into $\overline{w}(k_c) = 1/f'(0)$ returns $\beta_c = 4$ when $D = 0$.

Appendix B

Derivation of Amplitude Equation for NLLV System

B.1 $\overline{a}(k_c)$

Note that

$$\frac{\partial \phi_c(x)}{\partial \lambda} = \frac{\partial}{\partial \lambda}\left[\frac{1}{\lambda}\psi\left(\frac{x}{\lambda}\right)\right] = \frac{1}{\lambda}\psi'\left(\frac{x}{\lambda}\right)\left(-\frac{x}{\lambda^2}\right) + \psi\left(\frac{x}{\lambda}\right)\left(-\frac{1}{\lambda^2}\right) = -\frac{1}{\lambda^2}\left[\frac{x}{\lambda}\psi'\left(\frac{x}{\lambda}\right) + \psi\left(\frac{x}{\lambda}\right)\right]. \tag{B.1}$$

Therefore,

$$\begin{aligned}
\overline{a}(k_c) &= \int_{-\infty}^{\infty} \left.\frac{\partial \phi_c(y)}{\partial \lambda}\right|_{\lambda=\lambda_c} \mathrm{e}^{-ik_c y}\,\mathrm{d}y \\
&= -\frac{1}{\lambda_c^2}\int_{-\infty}^{\infty} \mathrm{d}y \left[\frac{y}{\lambda_c}\psi'\left(\frac{y}{\lambda_c}\right) + \psi\left(\frac{y}{\lambda_c}\right)\right] \mathrm{e}^{-ik_c y} \\
&= -\frac{1}{\lambda_c}\int_{-\infty}^{\infty} \mathrm{d}x \left(x\psi'(x) + \psi(x)\right) \mathrm{e}^{-ik_c\lambda_c x}, \\
&= -\frac{1}{\lambda_c^2}\frac{\mathrm{d}}{\mathrm{d}k_c}\int_{-\infty}^{\infty} \mathrm{d}x\, \psi'(x)\mathrm{e}^{-ik_c\lambda_c x} - \frac{1}{\lambda_c}\overline{\psi}(k_c\lambda_c) \\
&= -\frac{i}{\lambda_c^2}\frac{\mathrm{d}}{\mathrm{dk_c}}\left[ik_c\lambda_c\overline{\psi}(k_c\lambda_c)\right] - \frac{1}{\lambda_c}\overline{\psi}(k_c\lambda_c) = k_c\overline{\psi}'(k_c\lambda_c).
\end{aligned} \tag{B.2}$$

B.2 Projections when $n = 3$

Here we give details of the calculation of the projection of equation (B.13). Note that we could write a vector as a matrix-vector multiplication such that

$$\left\langle \mathrm{e}^{ik_c x}b, \begin{bmatrix} -u_1\phi_1 * u_2 \\ -Rv_1\phi_c * v_2 \end{bmatrix} \right\rangle = \left\langle \mathrm{e}^{ik_c x}b, -\begin{bmatrix} u_1\phi_1 * & 0 \\ 0 & Rv_1\phi_c * \end{bmatrix} \begin{bmatrix} u_2 \\ v_2 \end{bmatrix} \right\rangle, \tag{B.3}$$

where $\omega_2 = (u_2, v_2)$. The property $\langle \mathrm{e}^{imk_c x} b, \mathrm{e}^{ink_c x}\omega_c\rangle = \delta_{m,n}$ suggests that the projection (B.3) yields nonzero value only when the coefficients of the matrix-vector multiplication are of the order of $\mathrm{e}^{ik_c x}b$. By substituting $\omega_2 = \omega_+\mathrm{e}^{2ik_c x} + \omega_-\mathrm{e}^{-2ik_c x} + \omega_0 + \xi\omega_1$ (see (5.32) into (B.3), the right-hand side is equals to

$$
\begin{aligned}
&\left\langle \mathrm{e}^{ik_c x}b, -\begin{bmatrix} u_1\phi_1 * & 0 \\ 0 & Rv_1\phi_c * \end{bmatrix}\left(\omega_+\mathrm{e}^{2ik_c x} + \omega_0\right)\right\rangle \\
&= \left\langle \mathrm{e}^{ik_c x}b, -\left\{\begin{bmatrix} u_1\overline{\phi}_1(2k_c) & 0 \\ 0 & Rv_1\overline{\phi}_c(2k_c)\end{bmatrix}\omega_+\mathrm{e}^{2ik_c x} + \begin{bmatrix} u_1\overline{\phi}_1(0) & 0 \\ 0 & Rv_1\overline{\phi}_c(0)\end{bmatrix}\omega_0\right\}\right\rangle \\
&= \left\langle \mathrm{e}^{ik_c x}b, -\left\{\begin{bmatrix} \overline{\phi}_1(2k_c) & 0 \\ 0 & Rv_1\overline{\phi}_c(2k_c)\end{bmatrix}\begin{bmatrix} u_0 & 0 \\ 0 & v_0\end{bmatrix}\left(Z\mathrm{e}^{ik_c x} + Z^*\mathrm{e}^{-ik_c x}\right)\omega_+\mathrm{e}^{2ik_c x}\right.\right. \\
&\qquad \left.\left. + \begin{bmatrix} \overline{\phi}_1(0) & 0 \\ 0 & R\overline{\phi}_c(0)\end{bmatrix}\begin{bmatrix} u_c & 0 \\ 0 & v_c\end{bmatrix}\left(Z\mathrm{e}^{ik_c x} + Z^*\mathrm{e}^{-ik_c x}\right)\omega_0\right\}\right\rangle \\
&= \left\langle \mathrm{e}^{ik_c x}b, -\left\{\begin{bmatrix} \overline{\phi}_1(2k_c) & 0 \\ 0 & Rv_1\overline{\phi}_c(2k_c)\end{bmatrix}\begin{bmatrix} u_c & 0 \\ 0 & v_c\end{bmatrix}Z^*\omega_+\mathrm{e}^{ik_c x}\right\}\right\rangle \\
&\qquad + \left\langle \mathrm{e}^{ik_c x}b, -\left\{\begin{bmatrix} \overline{\phi}_1(0) & 0 \\ 0 & R\overline{\phi}_c(0)\end{bmatrix}\begin{bmatrix} u_c & 0 \\ 0 & v_c\end{bmatrix}Z\omega_0\mathrm{e}^{ik_c x}\right\}\right\rangle,
\end{aligned}
\tag{B.4}
$$

where $(u_1, v_1) = \left(\left(Z\mathrm{e}^{ik_c x} + \text{c.c.}\right)u_c, \left(Z\mathrm{e}^{ik_c x} + \text{c.c.}\right)v_c\right)$ and the linearity of dot product is applied in the last line. Substitute the equation (B.4) into Euclidean dot product formula to obtain

$$
\begin{aligned}
&\left\langle \mathrm{e}^{ik_c x}b, \begin{bmatrix} -u_1\phi_1 * u_2 \\ -Rv_1\phi_c * v_2\end{bmatrix}\right\rangle \\
&= -b\cdot\left\{\begin{bmatrix} \overline{\phi}_1(2k_c) & 0 \\ 0 & R\overline{\phi}_c(2k_c)\end{bmatrix}\begin{bmatrix} u_c & 0 \\ 0 & v_c\end{bmatrix}Z^*\omega_+ + \begin{bmatrix} \overline{\phi}_1(0) & 0 \\ 0 & R\overline{\phi}_c(0)\end{bmatrix}\begin{bmatrix} u_c & 0 \\ 0 & v_c\end{bmatrix}Z\omega_0\right\},
\end{aligned}
\tag{B.5}
$$

where the first term on the right hand side of (B.5) is obtained by

$$
\frac{k_c}{2\pi}\int_0^{\frac{2\pi}{k_c}}(\mathrm{e}^{-ik_c x}b)\cdot -\left\{\begin{bmatrix} \overline{\phi}_1(2k_c) & 0 \\ 0 & R\overline{\phi}_c(2k_c)\end{bmatrix}\begin{bmatrix} u_c & 0 \\ 0 & v_c\end{bmatrix}Z^*\omega_+\mathrm{e}^{ik_c x}\right\}\mathrm{d}x. \tag{B.6}
$$

Similarly, we can write

$$\begin{aligned}
&\left\langle \mathrm{e}^{ik_c x} b, \begin{bmatrix} -u_2\phi_1 * u_1 \\ -Rv_2\phi_c * v_1 \end{bmatrix} \right\rangle \\
&= \left\langle \mathrm{e}^{ik_c x} b, -\begin{bmatrix} u_2\phi_1 * & 0 \\ 0 & Rv_2\phi_c * \end{bmatrix} \begin{bmatrix} u_1 \\ v_1 \end{bmatrix} \right\rangle \\
&= \left\langle \mathrm{e}^{ik_c x} b, -\begin{bmatrix} u_2\phi_1 * & 0 \\ 0 & Rv_2\phi_c * \end{bmatrix} \omega_c \left(Z\mathrm{e}^{ik_c x} + Z^* \mathrm{e}^{-ik_c x} \right) \right\rangle \\
&= \left\langle \mathrm{e}^{ik_c x} b, -\begin{bmatrix} u_2\overline{\phi}_1(k_c) * & 0 \\ 0 & Rv_2\overline{\phi}_c(k_c) * \end{bmatrix} \left(Z\omega_c \mathrm{e}^{ik_c x} + Z^* \omega_c \mathrm{e}^{-ik_c x} \right) \right\rangle \\
&= \left\langle \mathrm{e}^{ik_c x} b, -\begin{bmatrix} \overline{\phi}_1(k_c) * & 0 \\ 0 & R\overline{\phi}_c(k_c) * \end{bmatrix} \begin{bmatrix} u_c & 0 \\ 0 & v_c \end{bmatrix} \left(Z\omega_2 \mathrm{e}^{ik_c x} + Z^* \omega_2 \mathrm{e}^{-ik_c x} \right) \right\rangle \\
&= \left\langle \mathrm{e}^{ik_c x} b, -\begin{bmatrix} \overline{\phi}_1(k_c) * & 0 \\ 0 & R\overline{\phi}_c(k_c) * \end{bmatrix} \begin{bmatrix} u_c & 0 \\ 0 & v_c \end{bmatrix} \left(Z\omega_0 \mathrm{e}^{ik_c x} + Z^* \omega_+ \mathrm{e}^{-ik_c x} \right) \right\rangle
\end{aligned} \tag{B.7}$$

Then, we substitute the equation (B.7) into Euclidean dot product formula to obtain

$$\left\langle \mathrm{e}^{ik_c x} b, \begin{bmatrix} -u_2\phi_1 * u_1 \\ -Rv_2\phi_c * v_1 \end{bmatrix} \right\rangle = -b \cdot \left\{ \begin{bmatrix} \overline{\phi}_1(k_c) & 0 \\ 0 & R\overline{\phi}_c(k_c) \end{bmatrix} \begin{bmatrix} u_c & 0 \\ 0 & v_c \end{bmatrix} \left(Z\omega_0 + Z^* \omega_+ \right) \right\} \tag{B.8}$$

Similarly,

$$\begin{aligned}
\left\langle \mathrm{e}^{ik_c x} b, \begin{bmatrix} -\alpha u_1 v_2 \\ -R\beta v_1 u_2 \end{bmatrix} \right\rangle &= \left\langle \mathrm{e}^{ik_c x} b, -\begin{bmatrix} 0 & \alpha u_1 \\ R\beta v_1 & 0 \end{bmatrix} \begin{bmatrix} u_2 \\ v_2 \end{bmatrix} \right\rangle \\
&= \left\langle \mathrm{e}^{ik_c x} b, -\begin{bmatrix} 0 & \alpha u_c \\ R\beta v_c & 0 \end{bmatrix} \begin{bmatrix} u_2 \\ v_2 \end{bmatrix} \left(Z\mathrm{e}^{ik_c x} + Z^* \mathrm{e}^{-ik_c x} \right) \right\rangle \\
&= \left\langle \mathrm{e}^{ik_c x} b, -\begin{bmatrix} 0 & \alpha u_c \\ R\beta v_c & 0 \end{bmatrix} \left(Z\omega_0 \mathrm{e}^{ik_c x} + Z^* \omega_+ \mathrm{e}^{ik_c x} \right) \right\rangle .
\end{aligned} \tag{B.9}$$

We then substitute the equation (B.9) into Euclidean dot product formula to obtain

$$\left\langle \mathrm{e}^{ik_c x} b, \begin{bmatrix} -\alpha u_1 v_2 \\ -R\beta v_1 u_2 \end{bmatrix} \right\rangle = -b \cdot \left\{ \begin{bmatrix} 0 & \alpha u_c \\ R\beta v_c & 0 \end{bmatrix} \left(Z\omega_0 + Z^* \omega_+ \right) \right\} . \tag{B.10}$$

Similarly, the final projection term is such that

$$\begin{aligned}
&\left\langle \mathrm{e}^{ik_c x} b, \begin{bmatrix} -\alpha u_2 v_1 \\ -R\beta v_2 u_1 \end{bmatrix} \right\rangle \\
&= \left\langle \mathrm{e}^{ik_c x} b, - \begin{bmatrix} \alpha v_1 & 0 \\ 0 & R\beta u_1 \end{bmatrix} \begin{bmatrix} u_2 \\ v_2 \end{bmatrix} \right\rangle \\
&= \left\langle \mathrm{e}^{ik_c x} b, - \begin{bmatrix} \alpha v_c & 0 \\ 0 & R\beta u_c \end{bmatrix} \begin{bmatrix} u_2 \\ v_2 \end{bmatrix} \left(Z\mathrm{e}^{ik_c x} + Z^* \mathrm{e}^{-ik_c x} \right) \right\rangle \\
&= \left\langle \mathrm{e}^{ik_c x} b, - \begin{bmatrix} \alpha v_c & 0 \\ 0 & R\beta u_c \end{bmatrix} \left(Z\omega_0 \mathrm{e}^{ik_c x} + Z^* \omega_+ \mathrm{e}^{ik_c x} \right) \right\rangle .
\end{aligned} \tag{B.11}$$

Finally, we substitute the equation (B.11) into Euclidean dot product formula to obtain

$$\left\langle \mathrm{e}^{ik_c x} b, \begin{bmatrix} -\alpha u_2 v_1 \\ -R\beta v_2 u_1 \end{bmatrix} \right\rangle = -b \cdot \left\{ \begin{bmatrix} \alpha v_c & 0 \\ 0 & R\beta u_c \end{bmatrix} \left(Z\omega_0 + Z^* \omega_+ \right) \right\} . \tag{B.12}$$

Finally, adding all the terms (B.5,B.8,B.10,B.12) together yield

$$\begin{aligned}
&\left\langle \mathrm{e}^{ik_c x} b, \begin{bmatrix} -u_1 \phi_1 * u_2 - \alpha u_1 v_2 - u_2 \phi_1 * u_1 - \alpha u_2 v_1 \\ -Rv_1 \phi_c * v_2 - R\beta v_1 u_2 - Rv_2 \phi_c * v_1 - R\beta v_2 u_1 \end{bmatrix} \right\rangle \\
&= -b \cdot \left\{ \begin{bmatrix} \overline{\phi}_1(0) + \overline{\phi}_1(k_c) & 0 \\ 0 & R\left(\overline{\phi}_c(0) + \overline{\phi}_c(k_c) \right) \end{bmatrix} \begin{bmatrix} u_c & 0 \\ 0 & v_c \end{bmatrix} Z\omega_0 \right. \\
&\quad + \begin{bmatrix} \overline{\phi}_1(2k_c) + \overline{\phi}_1(k_c) & 0 \\ 0 & R\left(\overline{\phi}_c(2k_c) + \overline{\phi}_c(k_c) \right) \end{bmatrix} \begin{bmatrix} u_c & 0 \\ 0 & v_c \end{bmatrix} Z^* \omega_+ \\
&\quad \left. + \begin{bmatrix} \alpha v_c & \alpha u_c \\ R\beta v_c & R\beta u_c \end{bmatrix} \left(Z^* \omega_+ + Z\omega_0 \right) \right\} \\
&= -b \cdot \left\{ Z \begin{bmatrix} u_c \left(\overline{\phi}_1(0) + \overline{\phi}_1(k_c) \right) + \alpha v_c & \alpha u_c \\ R\beta v_c & v_c R\left[\overline{\phi}_c(0) + \overline{\phi}_c(k_c) \right] + R\beta u_c \end{bmatrix} \omega_0 \right. \\
&\quad \left. + Z^* \begin{bmatrix} u_c \left(\overline{\phi}_1(2k_c) + \overline{\phi}_1(k_c) \right) + \alpha v_c & \alpha u_c \\ R\beta v_c & v_c R\left[\overline{\phi}_c(2k_c) + \overline{\phi}_c(k_c) \right] + R\beta u_c \end{bmatrix} \omega_+ \right\} .
\end{aligned} \tag{B.13}$$

Appendix C

Numerical Amplitude Away from Bifurcation Point

C.1 When $\beta = 0.5$

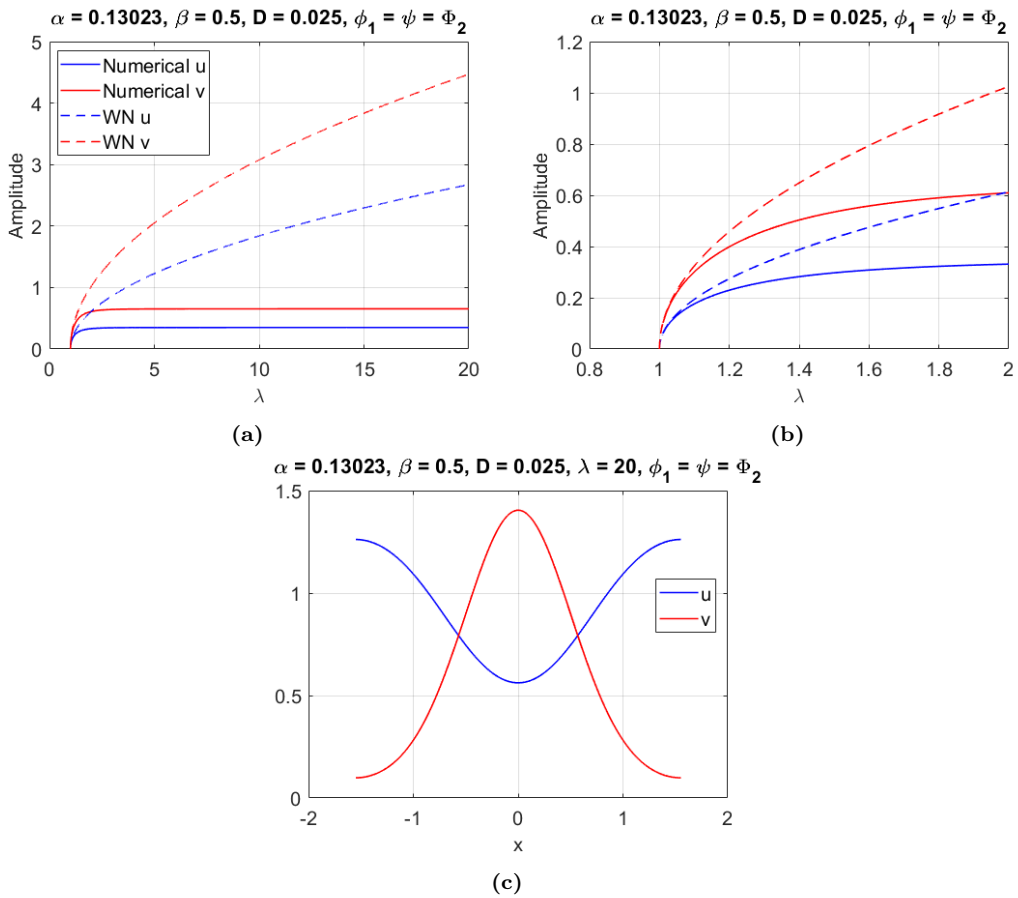


Figure C.1: *(a) The numerical amplitudes from (5.50) and weakly nonlinear (WN) amplitudes of $\phi_1 = \psi = \Phi_2$ for large λ. (b) is the magnified image of (a). (c) The numerical solutions at $\lambda = 20$.*

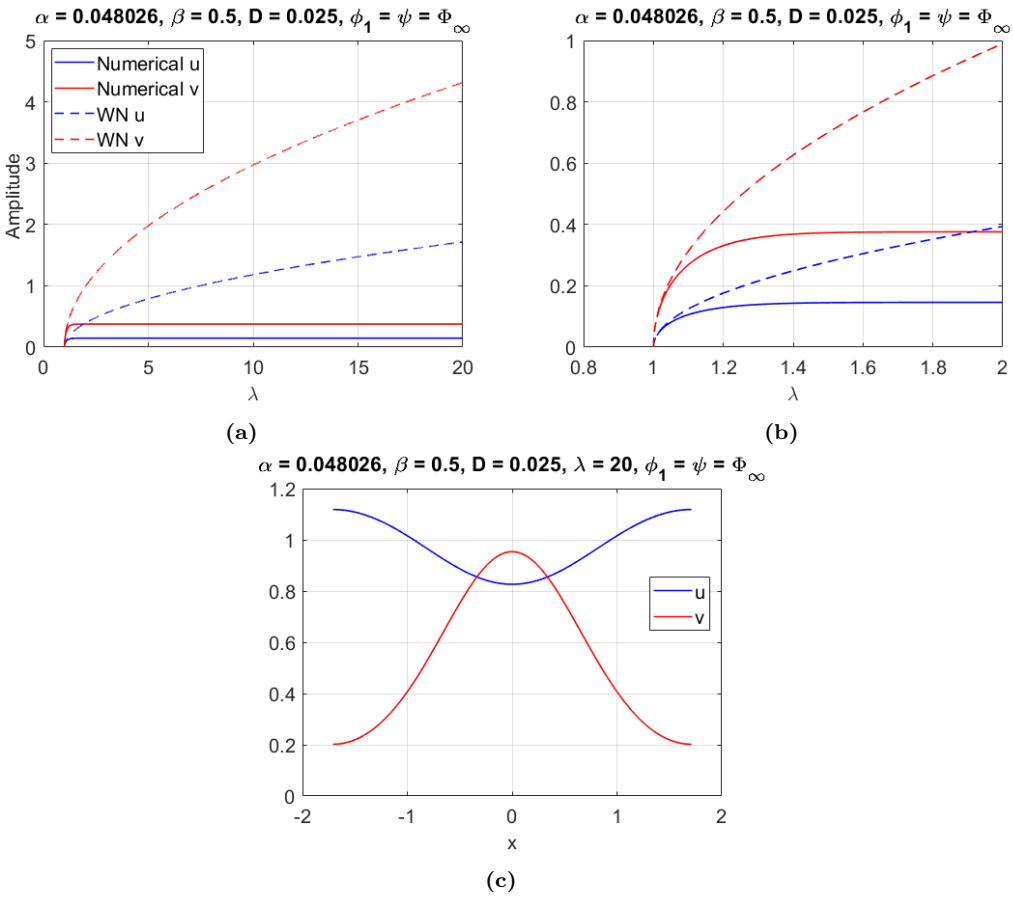


Figure C.2: *(a) The numerical amplitudes from (5.50) and weakly nonlinear (WN) amplitudes of $\phi_1 = \psi = \Phi_\infty$ for large λ. (b) is the magnified image of (a). (c) The numerical solutions at $\lambda = 20$.*

C.2 When $\beta = 0.95$

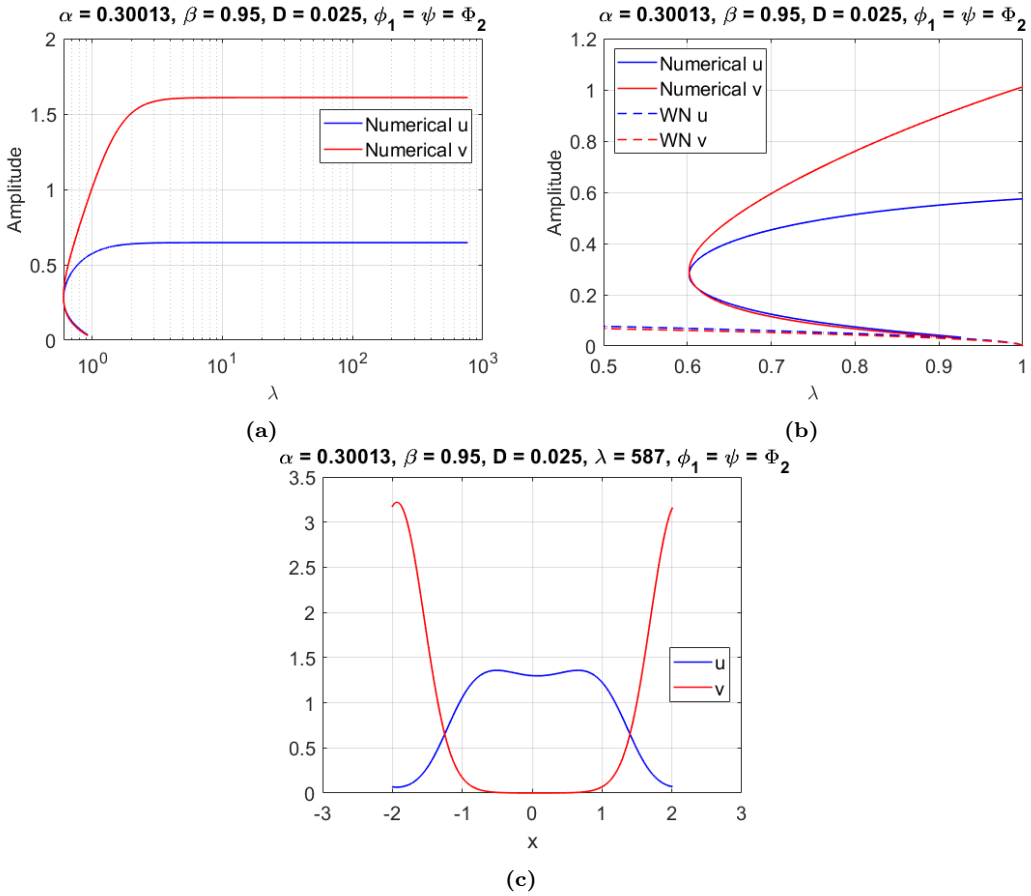


Figure C.3: *(a) The numerical amplitude of u and v from (5.50) for $\phi_1 = \psi = \Phi_2$ solved by fixing amplitude. (b) The analytical and numerical amplitudes in a smaller λ domain. (c) The numerical solutions u and v solved by fixing amplitude.*

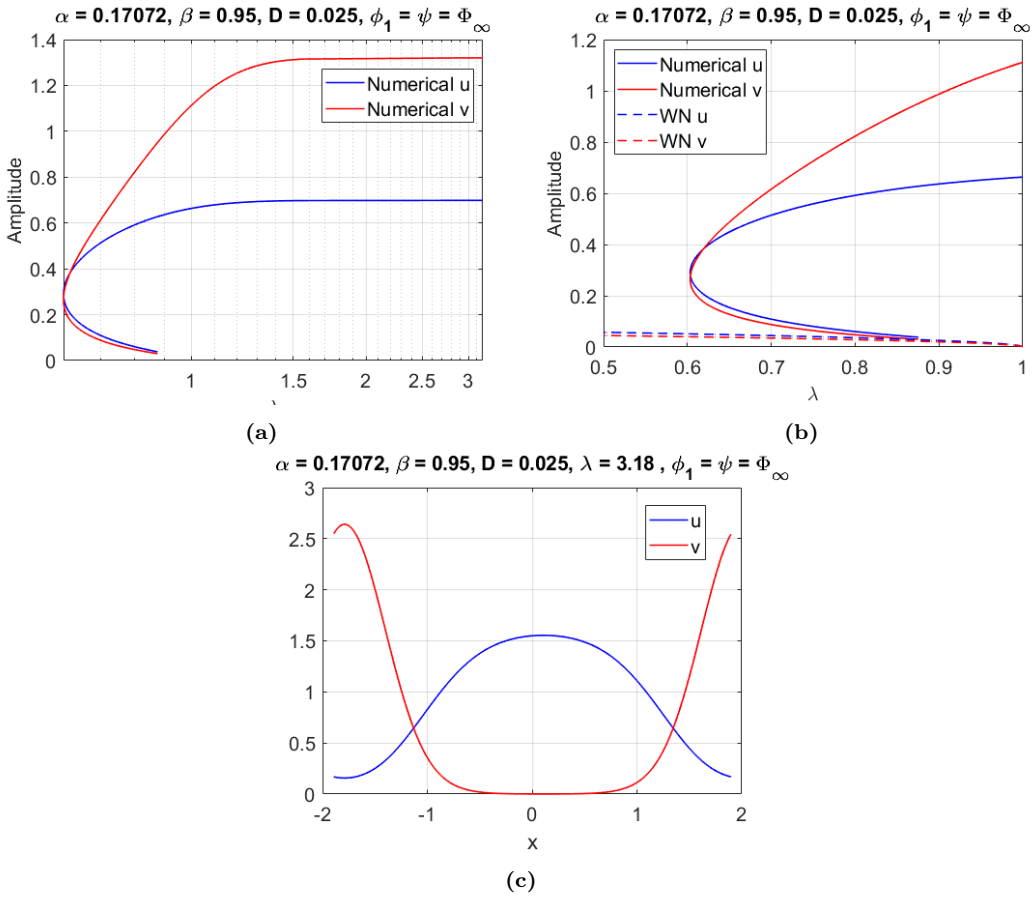
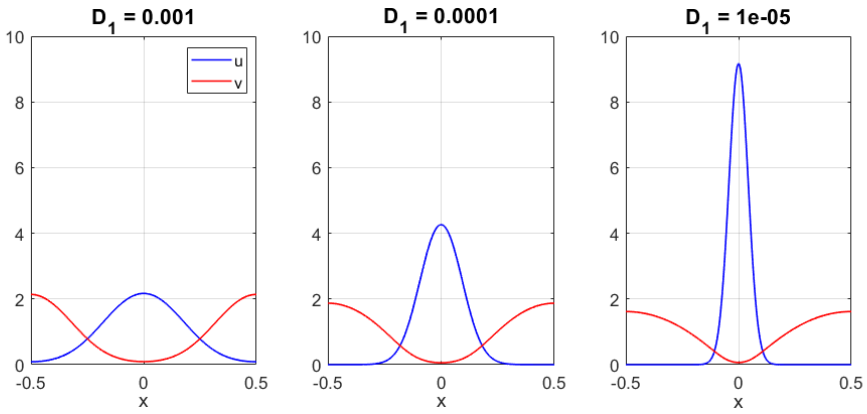


Figure C.4: *(a) The numerical amplitude of u and v from (5.50) for $\phi_1 = \psi = \Phi_\infty$ solved by fixing amplitude. (b) The analytical and numerical amplitudes in a smaller λ domain. (c) The numerical solutions u and v solved by fixing amplitude.*

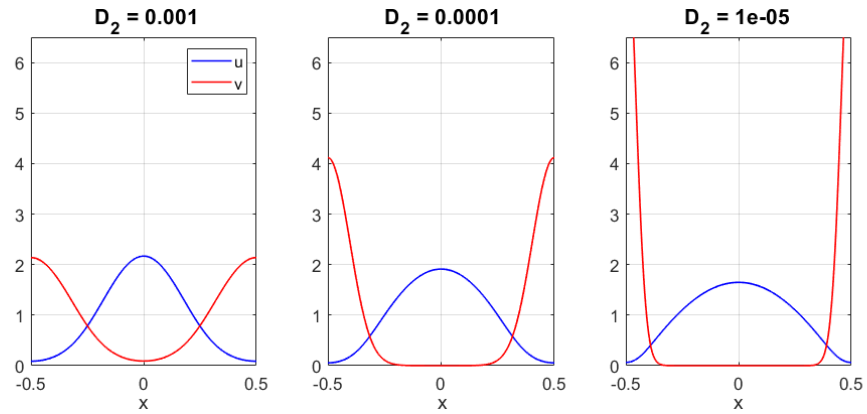
Appendix D

Fully Nonlinear Numerical Solutions

D.1 When $\phi_1 = \psi = \Phi_2$

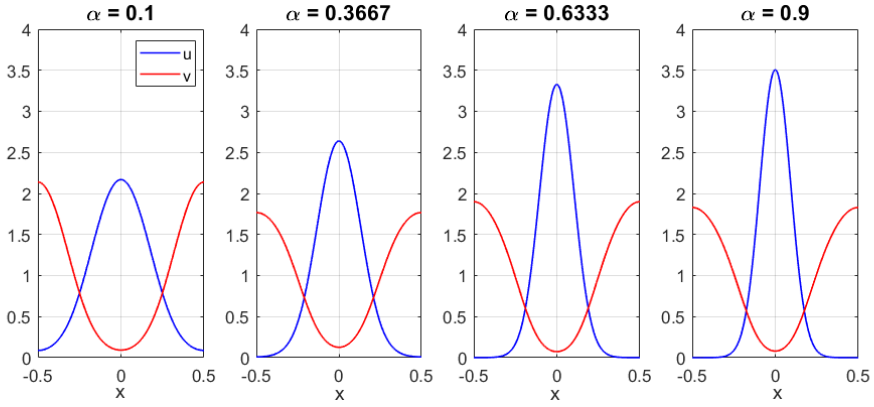


(a) $D_2 = 0.001$, $\alpha = \beta = 0.1$, $\lambda = 0.8$, $\Lambda = 1$.

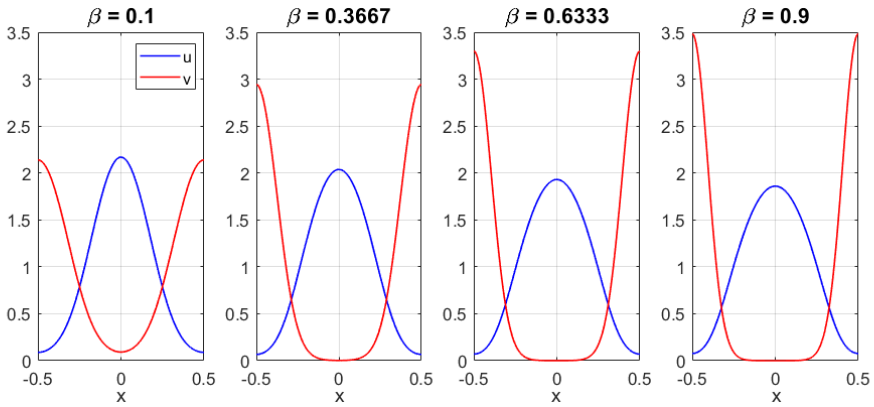


(b) $D_1 = 0.001$, $\alpha = \beta = 0.1$, $\lambda = 0.8$, $\Lambda = 1$.

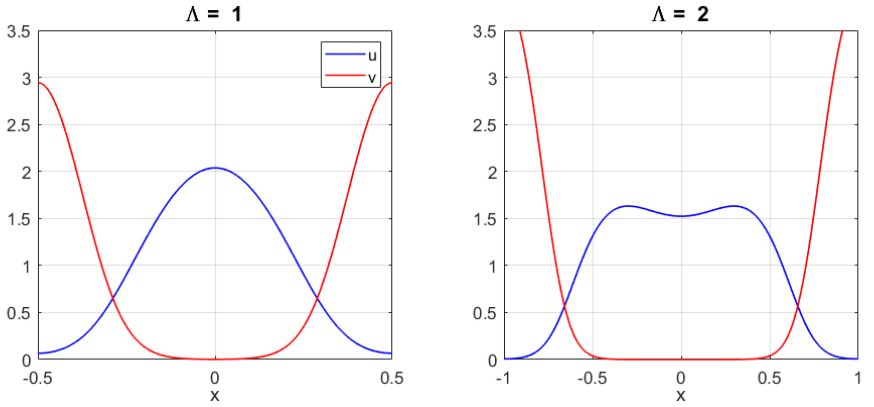
Figure D.1: *Fully nonlinear solutions from (5.50) for $\phi_1 = \psi = \Phi_2$ for (a) decreasing D_1 and (b) decreasing D_2.*



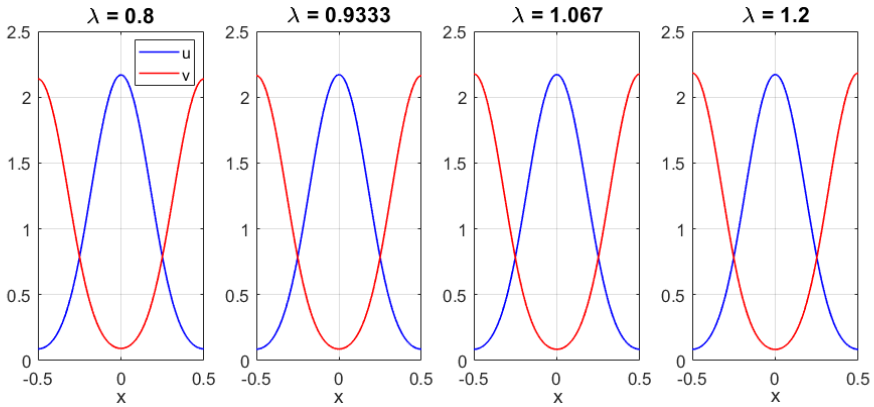
(c) $D_1 = D_2 = 0.001$, $\beta = 0.1$, $\lambda = 0.8$, $\Lambda = 1$.



(d) $D_1 = D_2 = 0.001$, $\alpha = 0.1$, $\lambda = 0.8$, $\Lambda = 1$.



(e) $D_1 = D_2 = 0.001$, $\alpha = 0.1$, $\beta = 0.3667$, $\lambda = 0.8$.



(f) $D_1 = D_2 = 0.001$, $\alpha = \beta = 0.1$, $\Lambda = 1$.

Figure D.1: *(cont.) Fully nonlinear solutions from (5.50) for $\phi_1 = \psi = \Phi_2$ for (c) increasing α, (d) increasing β, (e) increasing Λ, and (f) increasing λ.*

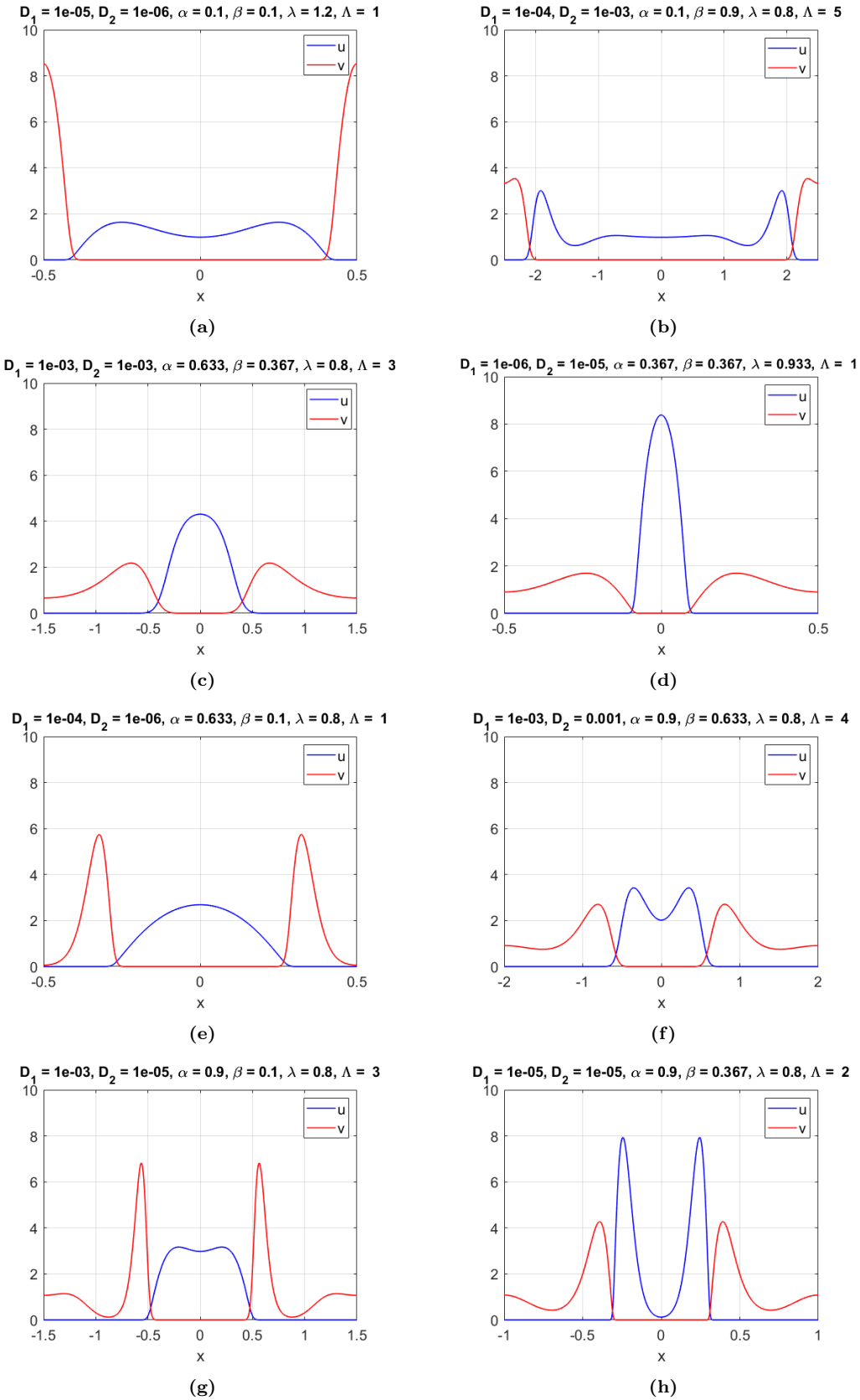
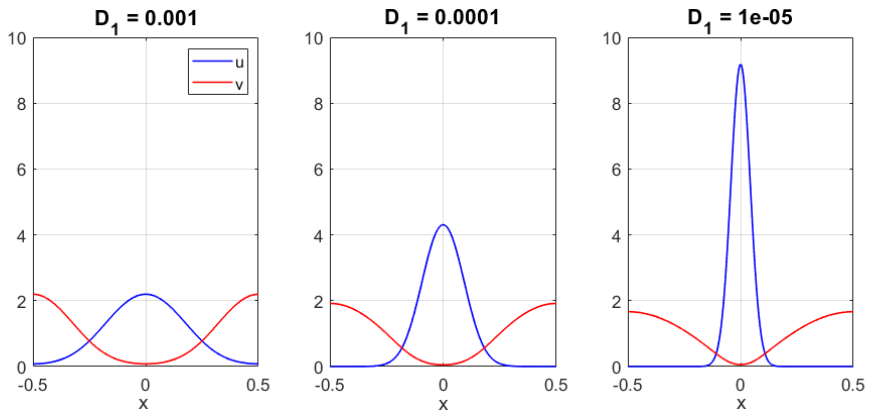
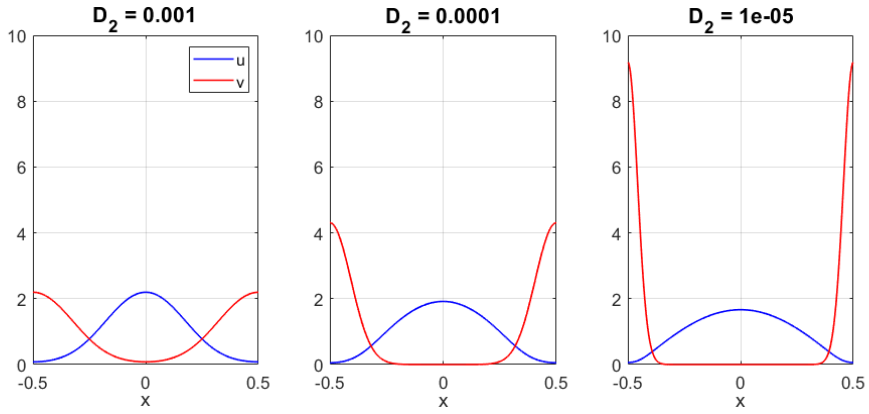


Figure D.2: *Plots of the fully nonlinear solutions from (5.50) for $\phi = \Phi_2$. (a) The maximum amplitude of v is greater than that of u as $D_2 < D_1$. (b) The effect of $\beta > \alpha$ is greater than $D_1 < D_2$, hence larger peak in v. More than two peaks due to $\Lambda = 5$. (c) $\alpha > \beta$ and therefore larger peak in u. (d) Larger peak in u as $D_1 < D_2$. (e) The effect of $D_2 < D_1$ is larger than $\alpha > \beta$. (f) $\max u > \max v$ as $\alpha > \beta$. Solution u has two peaks due to $\Lambda = 4$. (g) The effect of $D_2 < D_1$ is greater than $\alpha > \beta$. Solution v has more than two peaks. (h) $\alpha > \beta$ leads to larger amplitude in u.*

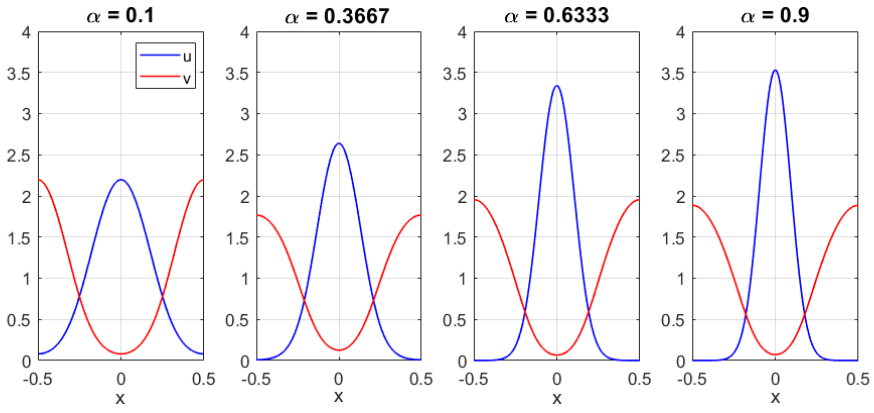
D.2 When $\phi_1 = \psi = \Phi_\infty$



(a) $D_2 = 0.001$, $\alpha = \beta = 0.1$, $\lambda = 0.8$, $\Lambda = 1$.

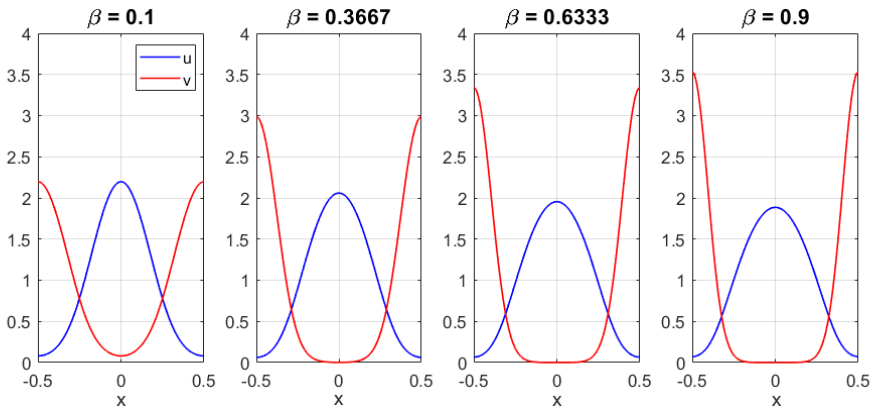


(b) $D_1 = 0.001$, $\alpha = \beta = 0.1$, $\lambda = 0.8$, $\Lambda = 1$.

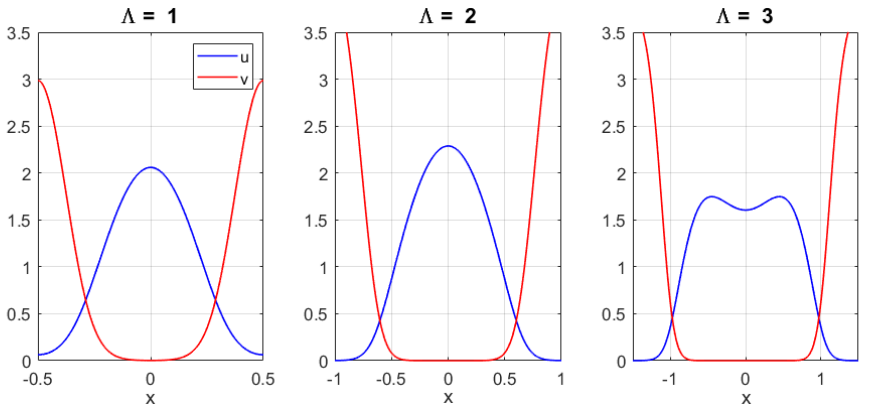


(c) $D_1 = D_2 = 0.001$, $\beta = 0.1$, $\lambda = 0.8$, $\Lambda = 1$.

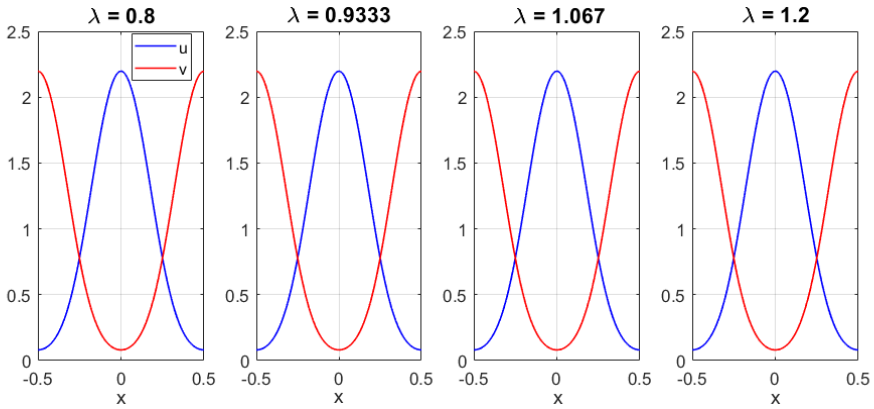
Figure D.3: *Fully nonlinear solutions from (5.50) for $\phi_1 = \psi = \Phi_\infty$ for (a) decreasing D_1, (b) decreasing D_2 and (c) increasing α.*



(d) $D_1 = D_2 = 0.001$, $\alpha = 0.1$, $\lambda = 0.8$, $\Lambda = 1$.



(e) $D_1 = D_2 = 0.001$, $\alpha = 0.1$, $\beta = 0.3667$, $\lambda = 0.8$.



(f) $D_1 = D_2 = 0.001$, $\alpha = \beta = 0.1$, $\Lambda = 1$.

Figure D.3: *Fully nonlinear solutions from (5.50) for $\phi_1 = \psi = \Phi_\infty$ for (d) increasing β, (e) increasing Λ, and (f) increasing λ.*

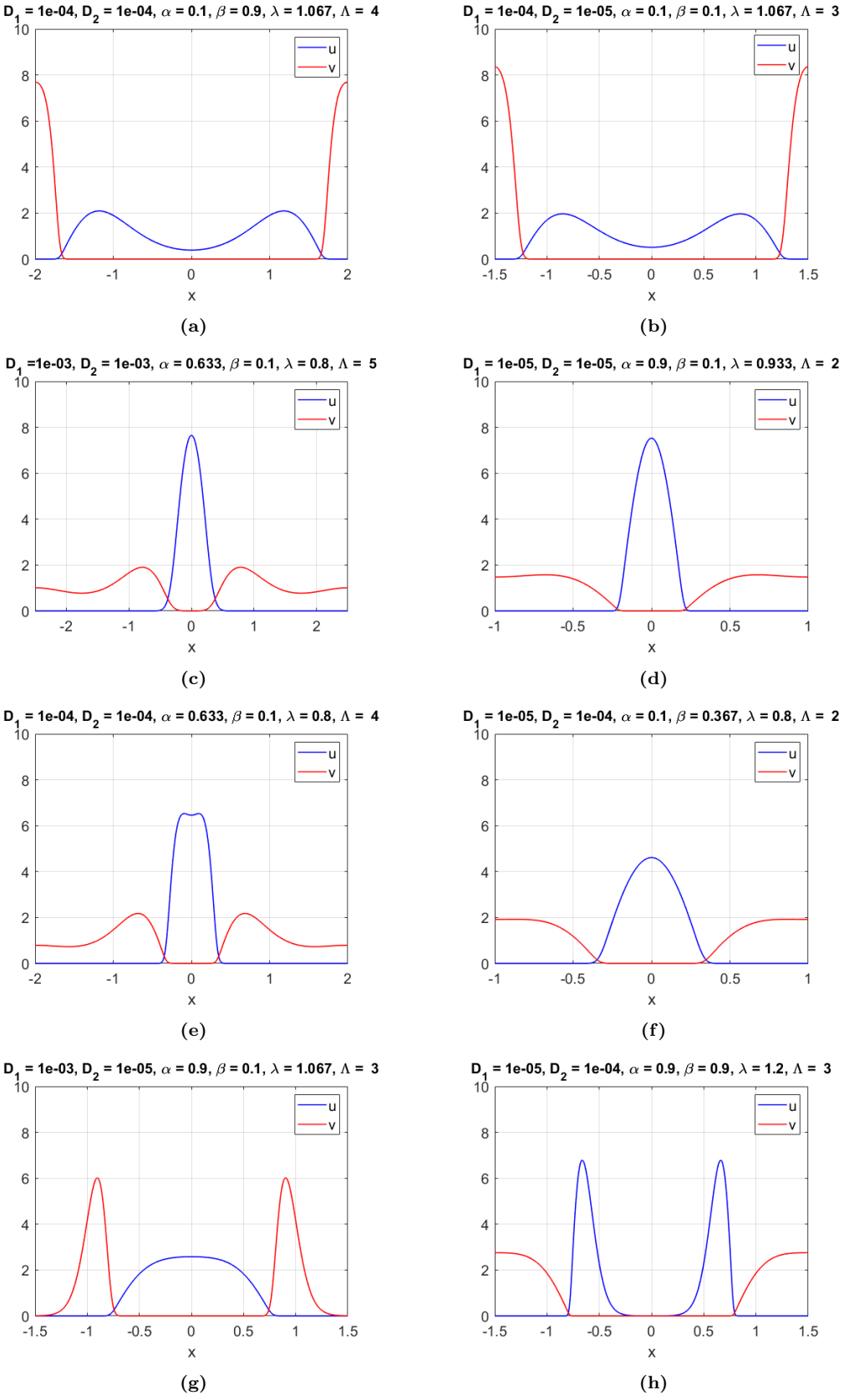


Figure D.4: *Plots of the fully nonlinear solutions from (5.50) for* $\phi_1 = \psi = \Phi_\infty$. *(a)* $\beta > \alpha$ *results in larger peak in* v. $\Lambda = 4$ *leads to two peaks in* u. *(b)* $D_2 < D_1$ *and hence* $\max v > \max u$. *(c)* $\max u > \max v$ *as* $\alpha > \beta$.*Solution* v *has more than two peaks as* $\Lambda > 1$. *(d) The maximum amplitude of* u *is larger as* $\alpha > \beta$. *(e)* $\max u > \max v$ *as* $\alpha > \beta$. *Solution* u *forms two peaks as* $\Lambda > 1$. *(f) The effect of* $D_1 < D_2$ *is larger than* $\beta > \alpha$. *(g) The effect of* $D_2 < D_1$ *is larger than* $\alpha > \beta$. *(h) Solution* u *has larger maximum amplitude than that of* v *as* $D_1 < D_2$.

Appendix E

Fully Nonlinear Pattern Formation in a NLLV System with Small Diffusivity

E.1 Effective periodic kernel when $\Phi = \Phi_\infty$ and $\lambda \neq 1$

For a general kernel Φ with wavelength $\Lambda = \Lambda/\lambda$, the infinite summation of the shifted kernel can be written as

$$\begin{aligned} P_\lambda(x) &= \sum_{m=-\infty}^{\infty} \Phi\left(x + \frac{m\Lambda}{\lambda}\right) \\ &= \sum_{m=-\infty}^{\infty} C_m \mathrm{e}^{\frac{2mx\pi\lambda i}{\Lambda}}, \end{aligned} \tag{E.1}$$

where

$$\begin{aligned} C_m &= \frac{\lambda}{\Lambda}\int_{-\Lambda/2\lambda}^{\Lambda/2\lambda} P_\lambda(x)\mathrm{e}^{-\frac{2mx\pi\lambda i}{\Lambda}}\,\mathrm{d}x, \\ &= \frac{\lambda}{\Lambda}\int_{-\Lambda/2\lambda}^{\Lambda/2\lambda} \sum_{m'} \Phi\left(x + \frac{m'\Lambda}{\lambda}\right)\mathrm{e}^{-\frac{2mx\pi\lambda i}{\Lambda}}\,\mathrm{d}x, \\ &= \frac{\lambda}{\Lambda}\sum_{m'}\int_{(-\frac{1}{2}+m')\frac{\Lambda}{\lambda}}^{(\frac{1}{2}+m')\frac{\Lambda}{\lambda}} \Phi(y)\mathrm{e}^{-\frac{2m\left(y-\frac{m'\Lambda}{\lambda}\right)\pi\lambda i}{\Lambda}}\,\mathrm{d}y, \qquad \text{by replacing } x = y - \frac{m'\Lambda}{\lambda}, \\ &= \frac{\lambda}{\Lambda}\sum_{m'}\int_{(-\frac{1}{2}+m')\frac{\Lambda}{\lambda}}^{(\frac{1}{2}+m')\frac{\Lambda}{\lambda}} \Phi(y)\mathrm{e}^{-\frac{2my\pi\lambda i}{\Lambda}}\mathrm{e}^{2mm'\pi i}\,\mathrm{d}y, \\ &= \frac{\lambda}{\Lambda}\int_{-\infty}^{\infty} \Phi(y)\mathrm{e}^{-\frac{2my\pi\lambda i}{\Lambda}}\,\mathrm{d}y, \\ &= \frac{\lambda}{\Lambda}\hat{\Phi}\left(\frac{2m\pi\lambda}{\Lambda}\right), \end{aligned} \tag{E.2}$$

are the complex Fourier coefficients.

For Gaussian kernel $\Phi(x) = \Phi_\infty = \frac{1}{2\sqrt{\pi}}\mathrm{e}^{-x^2/4}$ and a wavelength of Λ/λ, the periodic function $P_\lambda(x)$ becomes

$$\begin{aligned} P_\lambda(x) &= \sum_{m=-\infty}^{\infty} \frac{\lambda}{\Lambda}\overline{\Phi}\left(\frac{2m\pi\lambda}{\Lambda}\right)\left[\cos\left(\frac{2m\pi\lambda x}{\Lambda}\right) + i\sin\left(\frac{2m\pi\lambda x}{\Lambda}\right)\right], \\ &= \frac{\lambda}{\Lambda} + \sum_{m=1}^{\infty} \frac{2\lambda}{\Lambda}\mathrm{e}^{-\left(\frac{2m\pi\lambda}{\Lambda}\right)^2}\cos\left(\frac{2m\pi\lambda x}{\Lambda}\right) \\ &= \frac{\lambda}{\Lambda} + \sum_{m=1}^{\infty} Q_\lambda(x), \end{aligned} \tag{E.3}$$

where the positive and negative m in sine terms cancel out each other. When $m = 1$, $Q_\lambda(x) = \frac{2\lambda}{\Lambda}\mathrm{e}^{-4\pi^2\lambda^2/\Lambda^2}\cos\left(\frac{2\pi\lambda x}{\Lambda}\right)$. When $m = 2$, $Q_\lambda(x) = \frac{2\lambda}{\Lambda}\mathrm{e}^{-16\pi^2\lambda^2/\Lambda^2}\cos\left(\frac{4\pi\lambda x}{\Lambda}\right)$, which is smaller. Therefore, we approximate $P_\lambda(x) \approx \frac{\lambda}{\Lambda} + \frac{\lambda\epsilon_{\infty,\lambda}}{\Lambda}\cos\left(\frac{2\pi\lambda x}{\Lambda}\right)$ as $\epsilon_{\infty,\lambda} \to 0$ where $\epsilon_{\infty,\lambda} = 2\mathrm{e}^{-4\pi^2\lambda^2/\Lambda^2}$.

E.2 Effective periodic kernel when $\Phi = \Phi_1$ and $\lambda \neq 1$

For exponential kernel $\Phi(x) = \Phi_1 = \mathrm{e}^{-|x|/2}$, the periodic function $P_\lambda(x)$ with wavelength Λ/λ becomes

$$\begin{aligned} P_\lambda(x) &= \sum_{m=-\infty}^{\infty} \frac{\lambda}{\Lambda}\overline{\Phi}\left(\frac{2m\pi\lambda}{\Lambda}\right)\left[\cos\left(\frac{2m\pi\lambda x}{\Lambda}\right) + i\sin\left(\frac{2m\pi\lambda x}{\Lambda}\right)\right], \\ &= \frac{\lambda}{\Lambda} + \sum_{m=1}^{\infty} \frac{2\lambda}{\Lambda\left(1 + \left(\frac{2m\pi\lambda}{\Lambda}\right)^2\right)}\cos\left(\frac{2m\pi\lambda x}{\Lambda}\right), \\ &\approx \frac{\lambda}{\Lambda} + \frac{\Lambda}{2\pi^2\lambda}\sum_{m=1}^{\infty}\frac{1}{m^2}\cos\left(\frac{2m\pi\lambda x}{\Lambda}\right), \quad \text{as } \Lambda \to 0, \\ &= \frac{\lambda}{\Lambda} + \frac{\Lambda}{4\pi^2\lambda}\left[\mathrm{Li}_2\left(\mathrm{e}^{-\frac{2i\pi\lambda x}{\Lambda}}\right) + \mathrm{Li}_2\left(\mathrm{e}^{\frac{2i\pi\lambda x}{\Lambda}}\right)\right], \\ &= \frac{\lambda}{\Lambda} + \frac{\Lambda}{4\pi^2\lambda}\left[2\pi^2 B_2\left(\frac{x\lambda}{\Lambda}\right)\right], \\ &= \frac{\lambda}{\Lambda} + \frac{\Lambda}{4\pi^2\lambda}\left[2\pi^2\left(\frac{x^2\lambda^2}{\Lambda^2} - \frac{|x|\lambda}{\Lambda} + \frac{1}{6}\right)\right], \\ &= \frac{\lambda}{\Lambda} + \frac{2\pi^2\lambda\epsilon_{1,\lambda}}{\Lambda}\left(\frac{x^2\lambda^2}{\Lambda^2} - \frac{|x|\lambda}{\Lambda} + \frac{1}{6}\right), \end{aligned} \tag{E.4}$$

where $\epsilon_{1,\lambda} = \Lambda^2/4\pi^2\lambda^2$. Note that $\epsilon_{1,\lambda} \to 0$ as $\Lambda \to 0$.

E.3 Derivation of nonlinear Mathieu equation for v when $\phi_2 = \Phi_\infty$ and $\lambda \neq 1$

At $O(1)$, (6.34) returns $1 = \int_0^1 v_0(\hat{y})\,\mathrm{d}\hat{y}$. At $O(\epsilon_{\infty,\lambda})$, (6.34) yields

$$0 = \hat{D}_2 \frac{\mathrm{d}^2 v_0}{\mathrm{d}\hat{x}^2} - R v_0 \int_0^1 \cos\left(2\pi(\hat{x}-\hat{y})\right) v_0(\hat{y})\,\mathrm{d}\hat{y} - R v_0 \int_0^1 u_1(\hat{y})\,\mathrm{d}\hat{y}. \tag{E.5}$$

Again, we apply trigonometric identity to rewrite (E.5) as

$$\begin{aligned} 0 = \hat{D}_2 \frac{\mathrm{d}^2 v_0}{\mathrm{d}\hat{x}^2} + R v_0 \Big[&- \sin(2\pi\hat{x}) \int_0^1 \sin(2\pi\hat{y}) v_0(\hat{y})\,\mathrm{d}\hat{y} \\ &- \cos(2\pi\hat{x}) \int_0^1 \cos(2\pi\hat{y}) v_0(\hat{y})\,\mathrm{d}\hat{y} - \int_0^1 v_1(\hat{y})\,\mathrm{d}\hat{y} \Big]. \end{aligned} \tag{E.6}$$

Similar as the case for u, we rescale $\hat{x} = (1-b)\overline{x}$, $\hat{y} = (1-b)\overline{y}$, $v_0(\hat{x}) = \overline{v}_0(\overline{x})$ and $v_1(\hat{x}) = \overline{v}_1(\overline{x})$ for $0 < \overline{x} < 1$ and $0 < b < 1$. Therefore, equation (E.6) becomes

$$\begin{aligned} 0 = \frac{\hat{D}_2}{(1-b)^2} \frac{\mathrm{d}^2 \overline{v}_0}{\mathrm{d}\overline{x}^2} + R\overline{v}_0 \Big[&- (1-b)\sin(2\pi(1-b)\overline{x}) \int_0^1 \sin(2\pi(1-b)\overline{y})\overline{v}_0(\overline{y})\,\mathrm{d}\overline{y} \\ &- (1-b)\cos(2\pi(1-b)\overline{x}) \int_0^1 \cos(2\pi(1-b)\overline{y})\overline{v}_0(\overline{y})\,\mathrm{d}\overline{y} - (1-b)\int_0^1 \overline{v}_1(\overline{y})\,\mathrm{d}\overline{y} \Big]. \end{aligned} \tag{E.7}$$

Equation (E.7) is a nonlinear Mathieu equation in the form of

$$0 = \frac{\hat{D}_2}{(1-b)^2} \frac{\mathrm{d}^2 \overline{v}_0}{\mathrm{d}\overline{x}^2} + R\overline{v}_0 \left[a - 2q\cos(2\pi(1-b)\overline{x}) - 2p\sin(2\pi(1-b)\overline{x})\right], \tag{E.8}$$

where

$$\begin{aligned} a &= -(1-b)\int_0^1 \overline{v}_1(\overline{y})\,\mathrm{d}\overline{y}, \\ 2q &= (1-b)\int_0^1 \cos(2\pi(1-b)\overline{y})\overline{v}_0(\overline{y})\,\mathrm{d}\overline{y}, \\ 2p &= (1-b)\int_0^1 \sin(2\pi(1-b)\overline{y})\overline{v}_0(\overline{y})\,\mathrm{d}\overline{y}, \end{aligned} \tag{E.9}$$

with $\hat{D}_2$ term defined in (6.35).

Same as the case when $\lambda = 1$, the boundary conditions for Mathieu equation (E.8) are also $\overline{v}(0) = 0$ and $\overline{v}(1) = 0$.

E.4 Derivation of asymptotic equation for u when $\phi_1 = \Phi_1$

From (6.43), we expand the $(b\overline{x} - b\overline{y})^2$ term and split the integral of $|b\overline{x} - b\overline{y}|$ term to obtain

$$0 = \frac{\hat{D}_1}{b^2}\frac{\mathrm{d}^2\overline{u}_0}{\mathrm{d}\overline{x}^2} - 2\pi^2 b\overline{u}_0 \int_0^1 \left(b^2\overline{x}^2 - 2b^2\overline{x}\overline{y} + b^2\overline{y}^2 + \frac{1}{6}\right)\overline{u}_0(\overline{y})\,\mathrm{d}\overline{y} - \overline{u}_0 b\int_0^1 \overline{u}_1(\overline{y})\,\mathrm{d}\overline{y} + 2\pi^2 b\overline{u}_0\left[\int_0^{\overline{x}}(b\overline{x} - b\overline{y})\overline{u}_0(\overline{y})\,\mathrm{d}\overline{y} + \int_{\overline{x}}^1 (b\overline{y} - b\overline{x})\overline{u}_0(\overline{y})\,\mathrm{d}\overline{y}\right]. \tag{E.10}$$

The terms in squared bracket in (E.10) can be simplified by making use of the result that

$$\begin{aligned}\int_0^{\overline{x}} \overline{u}_0(\overline{y})\,\mathrm{d}\overline{y} - \int_{\overline{x}}^1 \overline{u}_0(\overline{y})\,\mathrm{d}\overline{y}, &= \left(\int_0^1 \overline{u}_0(\overline{y})\,\mathrm{d}\overline{y} - \int_{\overline{x}}^1 \overline{u}_0(\overline{y})\,\mathrm{d}\overline{y}\right) - \int_{\overline{x}}^1 \overline{u}_0(\overline{y})\,\mathrm{d}\overline{y},\\ &= \frac{1}{b} - 2\int_{\overline{x}}^1 \overline{u}_0(\overline{y})\,\mathrm{d}\overline{y},\end{aligned} \tag{E.11}$$

since $\int_0^1 \overline{u}_0(\overline{y})\,\mathrm{d}\overline{y} = 1/b$. Therefore, (E.10) becomes

$$\begin{aligned}0 = {} & \frac{\hat{D}_1}{b^2}\frac{\mathrm{d}^2\overline{u}_0}{\mathrm{d}\overline{x}^2} - 2\pi^2\overline{u}_0(\overline{x})\left(b^2\overline{x}^2 + \frac{1}{6}\right) + 4\pi^2 b^3\overline{u}_0\overline{x}\int_0^1 \overline{y}\overline{u}_0(\overline{y})\,\mathrm{d}\overline{y}\\ & - 2\pi^2 b^3\overline{u}_0\int_0^1 \overline{y}^2\overline{u}_0(\overline{y})\,\mathrm{d}\overline{y} - \overline{u}_0 b\int_0^1 \overline{u}_1(\overline{y})\,\mathrm{d}\overline{y}\\ & + 2\pi^2 b\overline{u}_0\left[\overline{x} - 2b\overline{x}\int_{\overline{x}}^1 \overline{u}_0(\overline{y})\,\mathrm{d}\overline{y} - b\int_0^{\overline{x}} \overline{y}\overline{u}_0(\overline{y})\,\mathrm{d}\overline{y} + b\int_{\overline{x}}^1 \overline{y}\overline{u}_0(\overline{y})\,\mathrm{d}\overline{y}\right],\\ = {} & \frac{\hat{D}_1}{b^2}\frac{\mathrm{d}^2\overline{u}_0}{\mathrm{d}\overline{x}^2} + \overline{u}_0\Bigg[-b\int_0^1 \overline{u}_1(\overline{y})\,\mathrm{d}\overline{y} + (4\pi^2 b^3\overline{x} + 2\pi^2 b^2)\int_0^1 \overline{y}\overline{u}_0(\overline{y})\,\mathrm{d}\overline{y}\\ & - 2\pi^2 b^3\int_0^1 \overline{y}^2\overline{u}_0(\overline{y})\,\mathrm{d}\overline{y} - 4\pi^2 b^2\overline{x}\int_{\overline{x}}^1 \overline{u}_0(\overline{y})\,\mathrm{d}\overline{y} - 4\pi^2 b^2\int_0^{\overline{x}} \overline{y}\overline{u}_0(\overline{y})\,\mathrm{d}\overline{y}\\ & - 2\pi^2 b^2\overline{x}^2 + 2\pi^2 b\overline{x} - \frac{\pi^2}{3}\Bigg].\end{aligned} \tag{E.12}$$

E.5 Asymptotic equation for v when $\phi_2 = \Phi_1$ and $\lambda = 1$

By repeating the derivation steps in Appendix E.4 above, but replacing b by $1-b$ and $\overline{u}_0$ by $\overline{v}_0$, we obtain the asymptotic equation of v in a similar form

$$0 = \frac{\hat{D}_2}{(1-b)^2}\frac{\mathrm{d}^2\overline{v}_0}{\mathrm{d}\overline{x}^2} + R\overline{v}_0\Bigg[a + (4\pi^2(1-b)^3\overline{x} + 2(1-b)^2\pi^2)q - 2\pi^2(1-b)^3 p \\ - 4(1-b)^2\pi^2\overline{x}r - 4(1-b)^2\pi^2 s - 2\pi^2(1-b)^2\overline{x}^2 + 2(1-b)\pi^2\overline{x} - \frac{\overline{x}}{3}\Bigg], \tag{E.13}$$

where

$$a = -(1-b)\int_0^1 \overline{v}_1(\overline{y})\,\mathrm{d}\overline{y}, \quad q = \int_0^1 \overline{v}_0(\overline{y})\overline{y}\,\mathrm{d}\overline{y}, \tag{E.14}$$

$$p = \int_0^1 \overline{u}_0(\overline{y})\overline{y}^2\,\mathrm{d}\overline{y}, \quad r = \int_{\overline{x}}^1 \overline{v}_0(\overline{y})\,\mathrm{d}\overline{y}, \quad s = \int_0^{\overline{x}} = \overline{v}_0(\overline{y})\overline{y}\,\mathrm{d}\overline{y}, \tag{E.15}$$

with the boundary conditions of $\overline{v}_0(0) = 0$ and $\overline{v}_0(1) = 0$.

E.6 Derivation of asymptotic equation for v when $\phi_2 = \Phi_1$ and $\lambda \neq 1$

Once we expand v and $\overline{v}$ in (6.48) asymptotically in terms of $\epsilon_{1,\lambda}$, we obtain

$$0 = \frac{D_2}{\Lambda^2}\frac{\mathrm{d}^2 v_0}{\mathrm{d}\hat{x}^2} + \frac{\epsilon_{1,\lambda}D_2}{\Lambda^2}\frac{\mathrm{d}^2 v_1}{\mathrm{d}\hat{x}^2} + +R(v_0 + \epsilon_{1,\lambda}v_1)\Bigg\{1 \\ - \int_0^1 \left[1 + 2\pi^2\epsilon_{1,\lambda}\left((\hat{x}-\hat{y})^2 - |\hat{x}-\hat{y}| + \frac{1}{6}\right)\right](v_0(\hat{y}) + \epsilon_{1,\lambda}v_1(\hat{y}))\,\mathrm{d}\hat{y}\Bigg\}. \tag{E.16}$$

Then, we rescale $D_2/\Lambda^2 = \hat{D}_2\epsilon_{1,\lambda}$ where $\hat{D}_2 = O(1)$. At $O(1)$, (E.16) returns $1 = \int_0^1 v_0(\hat{y})\,\mathrm{d}\hat{y}$. At $O(\epsilon_{1,\lambda})$, (E.16) yields

$$0 = \hat{D}_2\frac{\mathrm{d}^2 v_0}{\mathrm{d}\hat{x}^2} + Rv_0\left[-\int_0^1 2\pi^2\left((\hat{x}-\hat{y})^2 - |\hat{x}-\hat{y}| + \frac{1}{6}\right)v_0(\hat{y})\,\mathrm{d}\hat{y} - \int_0^1 v_1(\hat{y})\,\mathrm{d}\hat{y}\right]. \tag{E.17}$$

Upon rescaling $\hat{x} = (1-b)\overline{x}$, $\hat{y} = (1-b)\overline{y}$, $v_0(\hat{x}) = \overline{v}_0(\overline{x})$ and $v_1(\hat{x}) = \overline{v}_1(\overline{x})$ for

$0 < \overline{x} < 1$, we can rewrite (E.17) as

$$\begin{aligned} 0 = {} & \frac{\hat{D}_2}{(1-b)^2}\frac{\mathrm{d}^2\overline{v}_0}{\mathrm{d}\overline{x}^2} \\ & + R\overline{v}_0\Bigg[-(1-b)\int_0^1 2\pi^2\left(\Big((1-b)(\overline{x}-\overline{y})\Big)^2 - |(1-b)(\overline{x}-\overline{y})| + \frac{1}{6}\right)\overline{v}_0(\overline{y})\,\mathrm{d}\overline{y} \\ & - (1-b)\int_0^1 \overline{v}_1(\overline{y})\,\mathrm{d}\overline{y}\Bigg]. \end{aligned} \tag{E.18}$$

Finally, we expand the $\Big((1-b)(\overline{x}-\overline{y})\Big)^2$ term, split the integral of $|(1-b)(\overline{x}-\overline{y})|$, and repeat all the steps in Appendix E.4 to obtain the exact same form of nonlinear Mathieu equation as (E.13) which satisfies (E.14), except that $\hat{D}_2 = 4D_2\pi^2\lambda^2/\Lambda^4$, i.e.

$$\begin{aligned} 0 = \frac{\hat{D}_2}{(1-b)^2}\frac{\mathrm{d}^2\overline{v}_0}{\mathrm{d}\overline{x}^2} + R\overline{v}_0\Bigg[& a + (4\pi^2(1-b)^3\overline{x} + 2(1-b)^2\pi^2)q - 2\pi^2(1-b)^3 p \\ & - 4(1-b)^2\pi^2\overline{x}r - 4(1-b)^2\pi^2 s - 2\pi^2(1-b)^2\overline{x}^2 + 2(1-b)\pi^2\overline{x} - \frac{\overline{x}}{3}\Bigg], \end{aligned} \tag{E.19}$$

where

$$\begin{aligned} a &= -(1-b)\int_0^1 \overline{v}_1(\overline{y})\,\mathrm{d}\overline{y}, \\ q &= \int_0^1 \overline{y}\overline{v}_0(\overline{y})\,\mathrm{d}\overline{y}, \\ p &= \int_0^1 \overline{y}^2\overline{v}_0(\overline{y})\,\mathrm{d}\overline{y}, \\ r &= \int_{\overline{x}}^1 \overline{v}_0(\overline{y})\,\mathrm{d}\overline{y}, \\ s &= \int_0^{\overline{x}} \overline{y}\overline{v}_0(\overline{y})\,\mathrm{d}\overline{y}, \end{aligned} \tag{E.20}$$

with the boundary conditions of $\overline{v}_0(0) = 0$ and $\overline{v}_0(1) = 0$.

E.6.1 Fifth order system for v when $\phi_2 = \Phi_1$ when $\lambda = 1$

The fifth order system of (E.13) is then

$$\begin{aligned}
\overline{v}_0'(\overline{x}) &= \overline{w}(\overline{x}),\\
\overline{w}'(\overline{x}) &= -\frac{(1-b)^2 R\overline{v}_0(\overline{x})}{\hat{D}_2}\Big[a + (4\pi^2(1-b)^3\overline{x} + 2(1-b)^2\pi^2)q - 2\pi^2(1-b)^3 p\\
&\qquad - 4(1-b)^2\pi^2\overline{x}\overline{I}_1 - 4(1-b)^2\pi^2\overline{I}_2 - 2\pi^2(1-b)^2\overline{x}^2 + 2(1-b)\pi^2\overline{x} - \frac{\overline{x}}{3}\Big],\\
\overline{I}_1'(\overline{x}) &= -\overline{v}_0(\overline{x}),\\
\overline{I}_2'(\overline{x}) &= \overline{x}\overline{v}_0(\overline{x}),\\
\overline{I}_3'(\overline{x}) &= \overline{x}^2\overline{v}_0(\overline{x}),
\end{aligned} \tag{E.21}$$

where $\overline{I}_(\overline{x}) = \int_{\overline{x}}^1 \overline{v}_0(\overline{y})\,\mathrm{d}\overline{y} = -\int_1^{\overline{x}} \overline{v}_0(\overline{y})\,\mathrm{d}\overline{y}$, $\overline{I}_2(\overline{x}) = \int_0^{\overline{x}} \overline{v}_0(\overline{y})\overline{y}\,\mathrm{d}\overline{y}$, and $\overline{I}_3(\overline{x}) = \int_0^{\overline{x}} \overline{v}_0(\overline{y})\overline{y}^2\,\mathrm{d}\overline{y}$. The boundary conditions are $\overline{v}_0(1) = 0$, $\overline{v}_0(0) = 0$, $\overline{I}_1(1) = 0$, $\overline{I}_1(0) = 1/(1-b)$, $\overline{I}_2(1) = q$, $\overline{I}_2(0) = 0$, $\overline{I}_3(1) = p$, and $\overline{I}_3(0) = 0$.

Bibliography

[1] Nicholas F Britton. *Reaction-diffusion equations and their applications to biology.* Academic Press, 1986.

[2] Vitaly Volpert and Sergei Petrovskii. Reaction–diffusion waves in biology. *Physics of Life Reviews*, 6(4):267–310, 2009.

[3] Ronald A Fisher. The wave of advance of advantageous genes. *Annals of Eugenics*, 7(4):355–369, 1937.

[4] Matthieu Alfaro and Jérôme Coville. Rapid traveling waves in the nonlocal fisher equation connect two unstable states. *Applied Mathematics Letters*, 25(12):2095–2099, 2012.

[5] Matthieu Alfaro and Dongyuan Xiao. Lotka–volterra competition-diffusion system: the critical competition case. *Communications in Partial Differential Equations*, 48(2):182–208, 2023.

[6] Nicholas F Britton. Aggregation and the competitive exclusion principle. *Journal of Theoretical Biology*, 136(1):57–66, 1989.

[7] Nicholas F Britton. Spatial structures and periodic travelling waves in an integro-differential reaction-diffusion population model. *SIAM Journal on Applied Mathematics*, 50(6):1663–1688, 1990.

[8] François Hamel and Lenya Ryzhik. On the nonlocal Fisher–KPP equation: steady states, spreading speed and global bounds. *Nonlinearity*, 27(11):2735, 2014.

[9] Gabriel A Maciel and Ricardo Martinez-Garcia. Enhanced species coexistence in Lotka-Volterra competition models due to nonlocal interactions. *Journal of Theoretical Biology*, 530:110872, 2021.

[10] Ricardo Martínez-García, Justin M Calabrese, Emilio Hernández-García, and Cristóbal López. Vegetation pattern formation in semiarid systems without facilitative mechanisms. *Geophysical Research Letters*, 40(23):6143–6147, 2013.

[11] Miguel A Fuentes, Marcelo N Kuperman, and Vasudev M Kenkre. Nonlocal interaction effects on pattern formation in population dynamics. *Physical Review Letters*, 91(15):158104, 2003.

[12] Miguel A Fuentes, Marcelo N Kuperman, and Vasudev M Kenkre. Analytical considerations in the study of spatial patterns arising from nonlocal interaction effects. *The Journal of Physical Chemistry B*, 108(29):10505–10508, 2004.

[13] Manfred Milinski. Competitive resource sharing: an experimental test of a learning rule for esss. *Animal Behaviour*, 32(1):233–242, 1984.

[14] Xiaoqing He and Wei-Ming Ni. The effects of diffusion and spatial variation in Lotka–Volterra competition–diffusion system I: heterogeneity vs. homogeneity. *Journal of Differential Equations*, 254(2):528–546, 2013.

[15] Georg Hetzer, Anotida Madzvamuse, and Wenxian Shen. Characterization of Turing diffusion-driven instability on evolving domains. *Discrete & Continuous Dynamical Systems*, 32(11):3975, 2012.

[16] Razvan A Satnoianu, Michael Menzinger, and Philip K Maini. Turing instabilities in general systems. *Journal of Mathematical Biology*, 41(6):493–512, 2000.

[17] Alan M Turing. The chemical basis of morphogenesis. *Philosophical Transactions of the Royal Society of London. Series B, Biological Sciences*, 237(641):37–72, 1952.

[18] Mario I Simoy and Marcelo N Kuperman. Nonlocal interaction effects in models of interacting populations. *Chaos, Solitons & Fractals*, 167:112993, 2023.

[19] Henri Berestycki, Grégoire Nadin, Benoit Perthame, and Lenya Ryzhik. The nonlocal Fisher–KPP equation: travelling waves and steady states. *Nonlinearity*, 22(12):2813, 2009.

[20] Stephen A Gourley. Travelling front solutions of a nonlocal Fisher equation. *Journal of Mathematical Biology*, 41(3):272–284, 2000.

[21] Jian Fang and Xiao-Qiang Zhao. Monotone wavefronts of the nonlocal Fisher–KPP equation. *Nonlinearity*, 24(11):3043, 2011.

[22] Benjamin L Segal, Vladimir A Volpert, and Alvin Bayliss. Pattern formation in a model of competing populations with nonlocal interactions. *Physica D: Nonlinear Phenomena*, 253:12–22, 2013.

[23] Wenjie Ni, Junping Shi, and Mingxin Wang. Global stability and pattern formation in a nonlocal diffusive Lotka–Volterra competition model. *Journal of Differential Equations*, 264(11):6891–6932, 2018.

[24] Wen Wang and Shutang Liu. Nonlocal delay driven spatiotemporal patterns in a single-species reaction–diffusion model. *Communications in Nonlinear Science and Numerical Simulation*, 117:106899, 2023.

[25] Vitaly Volpert. *Elliptic Partial Differential Equations: Volume 2: Reaction-Diffusion Equations*, volume 104. Springer, 2014.

[26] Akira Sasaki. Clumped distribution by neighbourhood competition. *Journal of Theoretical Biology*, 186(4):415–430, 1997.

[27] Benoît Perthame and Stephane Génieys. Concentration in the nonlocal Fisher equation: the Hamilton-Jacobi limit. *Mathematical Modelling of Natural Phenomena*, 2(4):135–151, 2007.

[28] Stéphane Genieys, Vitaly Volpert, and Pierre Auger. Pattern and waves for a model in population dynamics with nonlocal consumption of resources. *Mathematical Modelling of Natural Phenomena*, 1(1):63–80, 2006.

[29] Sarah Penington. The spreading speed of solutions of the nonlocal Fisher–KPP equation. *Journal of Functional Analysis*, 275(12):3259–3302, 2018.

[30] Henri Berestycki, Tianling Jin, and Luis Silvestre. Propagation in a nonlocal reaction-diffusion equation with spatial and genetic trait structure. *Nonlinearity*, 29(4), 2016.

[31] John Billingham. Slow travelling wave solutions of the nonlocal Fisher-KPP equation. *Nonlinearity*, 33(5):2106, 2020.

[32] Grégoire Nadin, Benoît Perthame, and Min Tang. Can a traveling wave connect two unstable states? the case of the nonlocal Fisher equation. *Comptes Rendus Mathematique*, 349(9-10):553–557, 2011.

[33] Peter Grindrod. *The theory and applications of reaction-diffusion equations: Patterns and Wave*. Clarendon Press, 1996.

[34] Philip K Maini, DL Sean McElwain, and David I Leavesley. Traveling wave model to interpret a wound-healing cell migration assay for human peritoneal mesothelial cells. *Tissue Engineering*, 10(3-4):475–482, 2004.

[35] Lawrence K Forbes. A two-dimensional model for large-scale bushfire spread. *The ANZIAM Journal*, 39(2):171–194, 1997.

[36] Stephen A Gourley and Nicholas F Britton. Instability of travelling wave solutions of a population model with nonlocal effects. *IMA Journal of Applied Mathematics*, 51(3):299–310, 1993.

[37] Zhi-Cheng Wang, Wan-Tong Li, and Shigui Ruan. Travelling wave fronts in reaction–diffusion systems with spatio-temporal delays. *Journal of Differential Equations*, 222(1):185–232, 2006.

[38] Alfred J Lotka. *Elements of physical biology*. Williams & Wilkins, 1925.

[39] Vito Volterra. Variations and fluctuations of the number of individuals in animal species living together. *Animal Ecology*, pages 409–448, 1926.

[40] Simon A Levin and Lee A Segel. Hypothesis for origin of planktonic patchiness. *Nature*, 259(5545):659–659, 1976.

[41] Alan Hastings. Global stability in Lotka-Volterra systems with diffusion. *Journal of Mathematical Biology*, 6:163–168, 1978.

[42] F Rothe. Convergence to the equilibrium state in the Volterra-Lotka diffusion equations. *Journal of Mathematical Biology*, 3(3-4):319–324, 1976.

[43] Akira Okubo, Philip Kumar Maini, Mark H Williamson, and James Dickson Murray. On the spatial spread of the grey squirrel in britain. *Proceedings of the Royal Society of London. B. Biological Sciences*, 238(1291):113–125, 1989.

[44] Jérôme Mounier, Christophe Monnet, Tatiana Vallaeys, Roger Arditi, Anne-Sophie Sarthou, Arnaud Hélias, and Françoise Irlinger. Microbial interactions within a cheese microbial community. *Applied and Environmental Microbiology*, 74(1):172–181, 2008.

[45] Arietta Fleming-Davies, Sara Jabbari, Suzanne L Robertson, Tri Sri Noor Asih, Cristina Lanzas, Suzanne Lenhart, and Casey M Theriot. Mathematical modeling of the effects of nutrient competition and bile acid metabolism by the gut microbiota on colonization resistance against clostridium difficile. In *Women in Mathematical Biology: Research Collaboration Workshop, NIMBioS, Knoxville, June 2015*, pages 137–161. Springer, 2017.

[46] Seong-Joon Lee, Deok-Joo Lee, and Hyung-Sik Oh. Technological forecasting at the korean stock market: A dynamic competition analysis using Lotka–Volterra model. *Technological Forecasting and Social Change*, 72(8):1044–1057, 2005.

[47] Su-Yun Chiang, Gwo-Gauang Wong, Yiming Li, and Hsiao-Cheng Yu. A dynamic competition analysis on the personal computer shipments in taiwan using lotka-volterra model. In *2008 IEEE Asia-Pacific Services Computing Conference*, pages 1412–1417. IEEE, 2008.

[48] Hui-Chih Hung, Yu-Chih Chiu, Huang-Chen Huang, and Muh-Cherng Wu. An enhanced application of Lotka–Volterra model to forecast the sales of two competing retail formats. *Computers & Industrial Engineering*, 109:325–334, 2017.

[49] Rui Dilão. Mathematical models in population dynamics and ecology. In *Biomathematics: modelling and simulation*, pages 399–449. World Scientific, 2006.

[50] Steven R Dunbar. Travelling wave solutions of diffusive Lotka–Volterra equations. *Journal of Mathematical Biology*, 17(1):11–32, 1983.

[51] Yuzo Hosono. The minimal speed of traveling fronts for a diffusive Lotka-Volterra competition model. *Bulletin of Mathematical Biology*, 60(3):435–448, 1998.

[52] Jianhua Huang and Xingfu Zou. Traveling wavefronts in diffusive and cooperative Lotka–Volterra system with delays. *Journal of Mathematical Analysis and Applications*, 271(2):455–466, 2002.

[53] Andrei Kolmogorov, Ivan Petrovsky, and Nikolai Piskunov. Study of the equation of diffusion with growth of the quantity of material and its application to a biological problem. *Bulletin of Moscow State University Series A: Mathematics and Mechanics*, 1:1–25, 1937.

[54] Min Ming Tang and Paul C Fife. Propagating fronts for competing species equations with diffusion. *Archive for Rational Mechanics and Analysis*, 73(1):69–77, 1980.

[55] Yukio Kan-On. Parameter dependence of propagation speed of travelling waves for competition-diffusion equations. *SIAM Journal on Mathematical Analysis*, 26(2):340–363, 1995.

[56] Ahmad Alhasanat and Chunhua Ou. Minimal-speed selection of traveling waves to the Lotka–Volterra competition model. *Journal of Differential Equations*, 266(11):7357–7378, 2019.

[57] Ahmad Alhasanat and Chunhua Ou. On the conjecture for the pushed wavefront to the diffusive Lotka–Volterra competition model. *Journal of Mathematical Biology*, 80(5):1413–1422, 2020.

[58] Jong-Shenq Guo and Xing Liang. The minimal speed of traveling fronts for the Lotka–Volterra competition system. *Journal of Dynamics and Differential Equations*, 23(2):353–363, 2011.

[59] Andrea Cangiani, Emmanuil H Georgoulis, A Yu Morozov, and Oliver J Sutton. Revealing new dynamical patterns in a reaction–diffusion model with cyclic competition via a novel computational framework. *Proceedings of the Royal Society A: Mathematical, Physical and Engineering Sciences*, 474(2213):20170608, 2018.

[60] Sergei Petrovskii, Kohkichi Kawasaki, Fugo Takasu, and Nanako Shigesada. Diffusive waves, dynamical stabilization and spatio-temporal chaos in a community of three competitive species. *Japan Journal of Industrial and Applied Mathematics*, 18(2):459–481, 2001.

[61] Chueh-Hsin Chang, Chiun-Chuan Chen, Li-Chang Hung, Masayasu Mimura, and Toshiyuki Ogawa. Existence and stability of non-monotone travelling wave solutions for the diffusive Lotka–Volterra system of three competing species. *Nonlinearity*, 33(10):5080, 2020.

[62] Masayasu Mimura and Makoto Tohma. Dynamic coexistence in a three-species competition–diffusion system. *Ecological complexity*, 21:215–232, 2015.

[63] Changjin Xu, Maoxin Liao, and Xiaofei He. Stability and Hopf bifurcation analysis for a lotka-volterra predator-prey model with two delays. *International Journal of Applied Mathematics and Computer Science*, 21(1):97–107, 2011.

[64] Xue-zhong He. Stability and delays in a predator-prey system. *Journal of Mathematical Analysis and Applications*, 198(2):355–370, 1996.

[65] Teresa Faria. Stability and bifurcation for a delayed predator–prey model and the effect of diffusion. *Journal of Mathematical Analysis and Applications*, 254(2):433–463, 2001.

[66] Jian Gao, Changgui Gu, and Huijie Yang. Spiral waves with interfacial oscillatory chemical reactions emerge in a model of reaction-diffusion systems. *Chemical Physics*, 528:110507, 2020.

[67] Kishore Dutta. Reaction-diffusion dynamics and biological pattern formation. *Journal of Applied Nonlinear Dynamics*, 6(4):547–564, 2017.

[68] Stefanie Sick, Stefan Reinker, Jens Timmer, and Thomas Schlake. WNT and DKK determine hair follicle spacing through a reaction-diffusion mechanism. *Science*, 314(5804):1447–1450, 2006.

[69] Alfred Gierer and Hans Meinhardt. A theory of biological pattern formation. *Kybernetik*, 12(1):30–39, 1972.

[70] Vincent Castets, Etiennette Dulos, Jacques Boissonade, and Patrick De Kepper. Experimental evidence of a sustained standing Turing-type nonequilibrium chemical pattern. *Physical Review Letters*, 64(24):2953, 1990.

[71] Edmund J Crampin, Eamonn A Gaffney, and Philip K Maini. Reaction and diffusion on growing domains: scenarios for robust pattern formation. *Bulletin of Mathematical Biology*, 61(6):1093–1120, 1999.

[72] John T Stuart. On the nonlinear mechanics of wave disturbances in stable and unstable parallel flows part 1. the basic behaviour in plane poiseuille flow. *Journal of Fluid Mechanics*, 9(3):353–370, 1960.

[73] J Watson. On the non-linear mechanics of wave disturbances in stable and unstable parallel flows part 2. the development of a solution for plane poiseuille flow and for plane couette flow. *Journal of Fluid Mechanics*, 9(3):371–389, 1960.

[74] Lee A Segel. Distant side-walls cause slow amplitude modulation of cellular convection. *Journal of Fluid Mechanics*, 38(1):203–224, 1969.

[75] Zhen-Gang Ji and Cesar Mendoza. Weakly nonlinear stability analysis for dune formation. *Journal of Hydraulic Engineering*, 123(11):979–985, 1997.

[76] Rachel Nicks, Abigail Cocks, Daniele Avitabile, Alan Johnston, and Stephen Coombes. Understanding sensory induced hallucinations: From neural fields to amplitude equations. *SIAM Journal on Applied Dynamical Systems*, 20(4):1683–1714, 2021.

[77] Simon A Levin and Lee A Segel. Pattern generation in space and aspect. *SIAM Review*, 27(1):45–67, 1985.

[78] Alan C Newell and John A Whitehead. Finite bandwidth, finite amplitude convection. *Journal of Fluid Mechanics*, 38(2):279–303, 1969.

[79] Mark C Cross and Pierre C Hohenberg. Pattern formation outside of equilibrium. *Reviews of Modern Physics*, 65(3):851, 1993.

[80] Rebecca Hoyle. *Pattern formation: an introduction to methods*. Cambridge University Press, 2006.

[81] David Morgan and Jonathan HP Dawes. The Swift–Hohenberg equation with a nonlocal nonlinearity. *Physica D: Nonlinear Phenomena*, 270:60–80, 2014.

[82] Stefano Garlaschi, Deepak Gupta, Amos Maritan, and Sandro Azaele. Ginzburg-Landau amplitude equation for nonlinear nonlocal models. *Physical Review E*, 103(2):022210, 2021.

[83] Leonard C Maximon. *Differential and Difference Equations*. Springer, 2016.

[84] Michael Cross and Henry Greenside. *Pattern formation and dynamics in nonequilibrium systems*. Cambridge University Press, 2009.

[85] Matthew Cartmell, Spencer W Ziegler, Raya Khanin, and David Forehand. Multiple scales analyses of the dynamics of weakly nonlinear mechanical systems. *Applied Mechanics Review*, 56(5):455–492, 2003.

[86] Ju Swift and Pierre C Hohenberg. Hydrodynamic fluctuations at the convective instability. *Physical Review A*, 15(1):319, 1977.

[87] David C Bentley and Alastair M Rucklidge. Localized patterns in a generalized Swift–Hohenberg equation with a quartic marginal stability curve. *IMA Journal of Applied Mathematics*, 86(5):944–983, 2021.

[88] Moira L Steyn-Ross, D Alistair Steyn-Ross, Marcus T Wilson, and James W Sleigh. Gap junctions mediate large-scale turing structures in a mean-field cortex driven by subcortical noise. *Physical Review E*, 76(1):011916, 2007.

[89] Émile Mathieu. Mémoire sur le mouvement vibratoire d'une membrane de forme elliptique. *Journal de Mathématiques Pures et Appliquées*, 13:137–203, 1868.

[90] Edmund T Whittaker. On the functions associated with the elliptic cylinder in harmonic analysis. In *Proceedings of the Fifth International Congress of Mathematicians*, volume 1, pages 366–371, 1912.

[91] Chris Brimacombe, Robert M Corless, and Mair Zamir. Computation and applications of Mathieu functions: A historical perspective. *SIAM Review*, 63(4):653–720, 2021.

[92] Harold Jeffreys. The free oscillations of water in an elliptical lake. *Proceedings of the London Mathematical Society*, 2(1):455–476, 1925.

[93] Lawrence Ruby. Applications of the Mathieu equation. *American Journal of Physics*, 64(1):39–44, 1996.

[94] Milton Abramowitz and Irene A. Stegun, editors. *Handbook of Mathematical Functions with Formulas, Graphs, and Mathematical Tables*. U.S. Government Printing Office, Washington, DC, USA, tenth printing edition, 1972.

[95] Norman W McLachlan. Theory and application of Mathieu functions. *Publisher to the University Geoffrey Cumberlege, Oxford University Press*, 1951.

[96] Peter J Olver et al. *Introduction to Partial Differential Equations*, volume 1. Springer, 2014.

[97] Yajun Yang and Sheldon P Gordon. Interpolation and polynomial curve fitting. *The Mathematics Teacher*, 108(2):132–141, 2014.

[98] Edmund T Whittaker and George Robinson. *The Calculus of observations: a treatise on numerical mathematics*. Blackie and Son limited, 1924.

[99] S.P. Venkateshan and Prasanna Swaminathan. *Computational methods in engineering*. Elsevier, 2013.

[100] Sandip Mazumder. *Numerical methods for Partial Differential Equations: finite difference and finite volume methods*. Academic Press, 2015.

[101] David Kahaner, Cleve Moler, and Stephen Nash. *Numerical methods and software*. Prentice-Hall, Inc., 1989.

[102] E. Oran Brigham. *The Fast Fourier Transform and its applications*. Prentice-Hall, Inc., 1988.

[103] James W Cooley and John W Tukey. An algorithm for the machine calculation of complex Fourier series. *Mathematics of Computation*, 19(90):297–301, 1965.

[104] Jack Dongarra and Francis Sullivan. Guest editors introduction to the top 10 algorithms. *Computing in Science & Engineering*, 2(01):22–23, 2000.

[105] Ron Bracewell and Peter B Kahn. The Fourier Transform and its applications. *American Journal of Physics*, 34(8):712–712, 1966.

[106] David J Needham, John Billingham, Nikos M Ladas, and John C Meyer. The evolution problem for the 1D nonlocal Fisher-KPP equation with a top hat kernel. Part 1. The cauchy problem on the real line. *arXiv preprint arXiv:2304.10922*, 2023.

[107] Alan M Turing. The chemical basis of morphogenesis. *Philosophical Transactions of the Royal Society of London. Series B: Biological Sciences*, 237(641):37–72, 1952.

[108] Silviu Filip, Aurya Javeed, and Lloyd N Trefethen. Smooth random functions, random odes, and Gaussian processes. *SIAM Review*, 61(1):185–205, 2019.

[109] David J Needham and John Billingham. The evolution problem for the 1D nonlocal Fisher-KPP equation with a top hat kernel. Part 2. The cauchy problem on a finite interval. *arXiv preprint arXiv:2304.10935*, 2023.

[110] Nikola A Venkov, Stephen Coombes, and Paul C Matthews. Dynamic instabilities in scalar neural field equations with space-dependent delays. *Physica D: Nonlinear Phenomena*, 232(1):1–15, 2007.